

**CREEP OF PLAIN WEAVE POLYMER MATRIX
COMPOSITES**

By

ABHISHEK GUPTA

**A Thesis submitted to the Faculty of Graduate Studies of the
University of Manitoba in partial fulfillment of the requirements of the
degree of**

DOCTOR OF PHILOSOPHY

Department of Mechanical and Manufacturing Engineering

University of Manitoba

Winnipeg, Manitoba, Canada

Copyright © 2009 by Abhishek Gupta

ABSTRACT

Polymer matrix composites are increasingly used in various industrial sectors to reduce structural weight and improve performance. Woven (also known as textile) composites are one class of polymer matrix composites with increasing market share mostly due to their lightweight, their flexibility to form into desired shape, their mechanical properties and toughness. Due to the viscoelasticity of the polymer matrix, time-dependent degradation in modulus (creep) and strength (creep rupture) are two of the major mechanical properties required by engineers to design a structure reliably when using these materials. Unfortunately, creep and creep rupture of woven composites have received little attention by the research community and thus, there is a dire need to generate additional knowledge and prediction models, given the increasing market share of woven composites in load bearing structural applications. Currently, available creep models are limited in scope and have not been validated for any loading orientation and time period beyond the experimental time window. In this thesis, an analytical creep model, namely the Modified Equivalent Laminate Model (MELM), was developed to predict tensile creep of plain weave composites for any orientation of the load with respect to the orientation of the fill and warp fibers, using creep of unidirectional composites. The ability of the model to predict creep for any orientation of the load is a “first” in this area. The model was validated using an extensive experimental involving the tensile creep of plain weave composites under varying loading orientation and service conditions.

Plain weave epoxy (F263)/ carbon fiber (T300) composite, currently used in aerospace applications, was procured as fabrics from Hexcel Corporation. Creep tests were conducted under two loading conditions: on-axis loading (0^0) and off-axis loading (45^0). Constant load creep, in the temperature range of $80\text{--}240^0\text{C}$ and stress range of 1-70% UTS of the composites, was experimentally evaluated for time periods ranging from 1–120 hours under both loading conditions. The composite showed increase in creep with increase in temperature and stress. Creep of composite increased with increase in angle of loading, from 1% under on-axis loading to 31% under off-axis loading, within the tested time window. The experimental creep data for plain weave composites were superposed using TTSP (Time Temperature Superposition Principle) to obtain a master curve of experimental data extending to several years and was compared with model predictions to validate the model. The experimental and model results were found in good agreement within an error range of $\pm 1\text{--}3\%$ under both loading conditions. A parametric study was also conducted to understand the effect of microstructure of plain weave composites on its on-axis and off-axis creep. Generation of knowledge in this area is also “first”. Additionally, this thesis generated knowledge on time-dependent damage in woven composites and its effect on creep and tensile properties and their prediction.

ACKNOWLEDGEMENT

I would like to express my sincere gratitude to my thesis advisor **Dr. Raghavan Jayaraman**, for his invaluable guidance, academic support and financial assistance throughout my thesis work.

I would like to thank **Natural Sciences and Engineering Research Council of Canada** for funding this research work.

I would like to thank the **Faculty of Graduate Studies, University of Manitoba** for awarding me a graduate fellowship to pursue my thesis work.

I would like to thank **Anand Birur** for training me on various instruments in the composites laboratory as well as providing me with valuable suggestions during the course of my thesis. I would like to thank **Amir Asadi** for his help and support during my thesis work and other group colleagues for making my stay a memorable one.

My sincere thanks to **Mike Boskwick, John VanDorp** (Mechanical Engineering) and **Liting** (Civil Engineering) for providing me technical assistance during my research.

Last, but not the least, my very special thanks to **my family and friends** for their constant support and encouragement during my graduate studies.

TABLE OF CONTENTS

ABSTRACT.....	I
ACKNOWLEDGEMENT.....	III
TABLE OF CONTENTS	IV
LIST OF FIGURES	VII
LIST OF TABLES	XXI
LIST OF SYMBOLS	XXIII
1. INTRODUCTION.....	1
1.1 BACKGROUND	2
1.2 THESIS MOTIVATION AND SCOPE	10
1.3 THESIS ORGANIZATION	12
2. LITERATURE REVIEW	13
2.1 INTRODUCTION.....	13
2.2 FACTORS AFFECTING CREEP AND CREEP RUPTURE OF WOVEN COMPOSITES	15
2.2.1 Microstructure.....	15
2.2.2 Environmental / Service Factors.....	22
2.3 PUBLISHED STUDIES ON CREEP & CREEP RUPTURE OF WOVEN COMPOSITES	34
2.3.1 On Creep	34
2.3.2 On Creep- Rupture	39

2.4 SUMMARY & LIMITATIONS OF PUBLISHED STUDIES ON CREEP & CREEP RUPTURE OF WOVEN COMPOSITES	40
2.5 THESIS OBJECTIVES	41
2.6 RESEARCH APPROACH	42
3. MODEL FOR CREEP OF PLAIN WEAVE POLYMER COMPOSITES	44
3.0 INTRODUCTION.....	44
3.1 PUBLISHED MODELS FOR <i>TIME-INDEPENDENT</i> PROPERTIES OF WOVEN COMPOSITES ..	44
3.2 Published models for <i>time-dependent</i> properties (creep) of woven composites	48
3.3 MODIFIED EQUIVALENT LAMINATE MODEL (MELM) FOR CREEP OF PLAIN WEAVE COMPOSITES	50
3.3.1 Model assumptions	52
3.3.2 Model Description	53
3.3.3 MATLAB Program for Simulation of Creep of Woven Composites..	64
4. EXPERIMENTAL & SIMULATION DETAILS.....	71
4.1 Introduction.....	71
4.2 EXPERIMENTAL DETAILS	71
4.2.1 Material	71
4.2.2 Manufacturing of test coupons.....	72
4.2.3 Tensile test	87
4.2.4 Tensile creep tests	90
4.2.5 Damage analysis	94
4.2.6 Microscopic analysis.....	96
4.2.7 Data Acquisition System (DAQ)	96
4.2.8 Rationale for selection of creep test parameters	99

4.2.9 Precision, resolution and repeatability of test results.....	107
4.2.10 Experimental procedure for unidirectional composites	112
4.3 SIMULATION APPROACH	115
4.3.1 Microstructural input parameters.....	116
4.3.2 Creep data for unidirectional composites	116
4.3.3 Simulation parameters	139
5. RESULTS AND DISCUSSION	143
5.1 INTRODUCTION.....	143
5.2 MICROSTRUCTURAL CHARACTERIZATION OF PLAIN WEAVE COMPOSITES	143
5.3 TENSILE BEHAVIOR OF PLAIN WEAVE COMPOSITES.....	151
5.3.1 On-axis loading.....	151
5.3.2 Off-axis loading	154
5.4 CREEP OF PLAIN WEAVE COMPOSITES.....	163
5.4.1 On-axis loading.....	163
5.4.2 Off-axis loading	203
5.4.3 Discussion	222
6. CONCLUSIONS, THESIS CONTRIBUTIONS & RECOMMENDATIONS FOR FUTURE WORK	234
REFERENCES.....	239
APPENDIX.....	250
APPENDIX A	251
APPENDIX B	261

LIST OF FIGURES

Figure 1.1: Schematic of a tape lamina.....	3
Figure 1.2: Schematic of a fabric lamina.....	3
Figure 1.3: Schematic of a unidirectional laminate/ composite.....	3
Figure 1.4: Schematic of a woven laminate/ composite.	3
Figure 1.5: A Schematic of global and principle coordinate system [2].	5
Figure 1.6: Schematics of (a) multidirectional non-woven laminate and (b) multidirectional woven laminate.....	5
Figure 1.7: Various weave patters for (a) 2-harness plain weave, (b) 3-harness weave, (c) 5-harness weave and (d) 8-harness satin weave fabric.	6
Figure 1.8: Application of woven composites as (a) fuselage structural part, (b) curved frames for fuselage keel structure, and (c) lower fuselage side panel perform [3].....	8
Figure 1.9: Illustration of creep in polymer matrix composites; Variation of (a) applied stress, (b) time-dependent strain in response to (a), and (c) time-dependent compliance, with time	9
Figure 1.10: Illustration of creep rupture.....	9
Figure 2.1: Illustration of (a) stress profile, (b) elastic behavior and (c) viscoelastic behavior.....	14
Figure 2.2: Two-dimensional schematics of plain weave with and without gap.....	16
Figure 2.3: Schematics of various stacking configurations of laminae within a woven laminate.....	19

Figure 2.4: Effect of temperature on compliance of [90] ₈ composites at a stress level of 10 MPa.....	24
Figure 2.5: Effect of temperature and stress on creep-rupture time of [90] ₁₂ composites [4].....	24
Figure 2.6: Time-Temperature Superposition Principle (TTSP) for long-term creep characterization.....	25
Figure 2.7: Effect of stress on creep of polymer matrix composites.	27
Figure 2.8: Effect of physical aging [4].....	30
Figure 3.1: A flow chart on time-dependent models for woven composites.	45
Figure 3.2: Comparison of (a)transverse and (b) shear creep compliance for unidirectional composites obtained experimentally and through simulation using modified rules of mixtures at 5MPa and 80 °C.	49
Figure 3.3: Plain weave fabric.	51
Figure 3.4: Schematic overview of modified equivalent laminate model (MELM) for predicting creep of plain weave composites.	54
Figure 3.5: Schematic overview of section (1) laminate.	57
Figure 3.6: Schematic overview of section (2) laminate.	59
Figure 3.7: Flow chart representing proposed modified equivalent laminate creep model (MELM) for plain weave polymer woven composites.	66
Figure 3.8: Schematic of a plain weave laminate under a constant applied stress.	68
Figure 3.9: A plot of load distribution between fill and warp lamina of a plain weave laminate.....	68

Figure 4.1: Schematic of the mold assembly & vacuum bag used in simulated autoclave curing of composite panels.	73
Figure 4.2: Cure cycle used in manufacturing of the composite panels.	73
Figure 4.3: DSC plot of thermal analysis of post cured plain weave composite panel. ...	75
Figure 4.4: Test coupon geometry for tests using (a) DMA and (b) Instron testing machine.	81
Figure 4.5: (a) Size of unit cell and (b) strain gage size used for experiment.	82
Figure 4.6: (a) Fiber breakage due to surface abrasion and (b) Cracking of strain gage backing during test due to broken surface fibers in the test coupon.	83
Figure 4.7: Comparison of on-axis tensile test results at a temperature of 120 $^{\circ}\text{C}$ using extensometer and strain gage.	85
Figure 4.8: Instron 8562 servo-electric frame with environmental chamber.....	88
Figure 4.9: Dynamic Mechanical Analyzer 2980	91
Figure 4.10: Instron 5500R screw- driven tensile and creep test machine.	92
Figure 4.11a: Micrograph of polished edge of post cured [0, 90] ₆ plain weave composite coupon (X 100).	95
Figure 4.11b: Micrograph of polished edge of post cured and conditioned [0, 90] ₆ plain weave composite coupon with vertical cracks (X 100).	95
Figure 4.12: (a) Nikon's LV100 Eclipse optical microscope, and (b) Xradia MicroXCT microscope.	97
Figure 4.13: Data acquisition system with Labview software.....	98
Figure 4.14: Time-Temperature Superposition Principal (TTSP) procedure.	100
Figure 4.15: Time and steps used for each creep test.	100

Figure 4.16: Micrograph of cross-ply laminate [0/90 ₂] _s with transverse and vertical cracks (X 100) [78].	102
Figure 4.17: Stress-strain plots for [0, 90] ₆ plain weave composite coupon tested under repeated loading- unloading at room temperature.	104
Figure 4.18: Stress-strain plots for [0, 90] ₆ plain weave composite coupon tested at 160 ⁰ C and 240 ⁰ C.....	104
Figure 4.19: Creep-recovery plots for [0, 90] ₆ plain weave composite coupons subjected to on-axis loading (100MPa) at various temperatures	106
Figure 4.20: Micrograph of polished edge of a [0, 90] ₆ plain weave composite coupon after creep test at 180 ⁰ C and 100MPa stress.....	106
Figure 4.21: Fluctuation in acquired strain data from DAQ.....	108
Figure 4.22: Stress and strain variation at a given applied stress and temperature.	109
Figure 4.23: Comparison of on-axis strain measured at 7MPa and 80 ⁰ C using DMA and Instron testing machine.....	110
Figure 4.24: Comparison of creep test results at 200MPa and 80 ⁰ C using two different test coupons under on-axis loading.....	110
Figure 4.25: Test coupon configurations used to measure S ₁₁ (t), S ₂₂ (t) and S ₆₆ (t).....	114
Figure 4.26: Schematic of one - dimensional plain weave unit cell with identified microstructural parameters required as input to the creep model.	117
Figure 4.27: Creep and recovery test	119
Figure 4.28: A typical strain-time curve generated during a creep-recovery test.....	119
Figure 4.29: Longitudinal creep compliance (S ₁₁) plots at various temperatures and at a constant stress of 200MPa.	126

Figure 4.30: Master creep compliance (S_{11}) plots at various stress levels and a reference temperature of 80 $^{\circ}\text{C}$	126
Figure 4.31: Transverse creep compliance (S_{22}) plots at various stress levels and a constant temperature of 80 $^{\circ}\text{C}$	127
Figure 4.32: Creep and recovery data for [90 $^{\circ}$] ₈ test coupon at various temperatures ranging 80- 160 $^{\circ}\text{C}$ and at a stress level of 10MPa.....	127
Figure 4.33: Plot of nonlinear parameters for transverse compliance (S_{22}) at various stress levels and a temperature of 80 $^{\circ}\text{C}$	128
Figure 4.34: Plot of constants A and B at various temperatures and a stress level of 10MPa.....	129
Figure 4.35: Shear creep compliance (S_{66}) plots at various stress levels and at a constant temperature of 80 $^{\circ}\text{C}$	131
Figure 4.36: Shear creep and recovery data for [10 $^{\circ}$] ₈ test coupon at various temperatures ranging 80- 160 $^{\circ}\text{C}$ and at a stress level of 15MPa.....	131
Figure 4.37: Plot of nonlinear parameters for shear compliance (S_{66}) at various stress levels and a constant temperature of 80 $^{\circ}\text{C}$	132
Figure 4.38: Plot of constants A and B at various temperatures and a shear stress level of 15MPa.....	133
Figure 4.39: Comparison of predicted and experimental transverse creep compliance (S_{22}) at various stresses and at a constant temperature of 140 $^{\circ}\text{C}$	137
Figure 4.40: Comparison of predicted and experimental shear creep compliance (S_{66}) at various stresses and at a constant temperature of 140 $^{\circ}\text{C}$	137

Figure 4.41: Variation of warp stress (σ_{22}) and nonlinear parameter (a_6) with time at applied stress of 100MPa and temperature of 80 ^0C	141
Figure 4.42: Comparison of experimental creep compliance (S_{22}) of unidirectional composites with predicted creep compliance derived using nonlinear parameters and KWW equation at 3MPa and 80 ^0C	142
Figure 4.43: Comparison of experimental creep compliance (S_{66}) of unidirectional composites with predicted creep compliance derived using nonlinear parameters and KWW equation at 5MPa and 80 ^0C	142
Figure 5.1: Micrographs of a single-ply lamina used for measurement of undulation parameters (X50).	144
Figure 5.2: Micrographs of a multi-ply laminate used for measurement of undulation parameters (X50).	145
Figure 5.3: Micrograph of a multi-ply laminate showing nesting(X50).....	149
Figure 5.4: Image analysis method used to measure the volume fraction of fiber in plain weave composite coupons using its micrograph at X500.....	149
Figure 5.5: Tensile stress- strain plots for [0, 90] ₆ plain weave composite coupons at various temperatures.	152
Figure 5.6: Fractured edges of [0, 90] ₆ plain weave composite coupons after tensile test at various temperatures.	153
Figure 5.7: Tensile stress- strain plots for [45, -45] ₆ plain weave composite coupons at various temperatures.	155
Figure 5.8: Fractured edges of [+45, -45] ₆ plain weave composite coupons after tensile test at various temperatures.....	156

Figure 5.9: Stress-strain plots of loading-unloading tests for $[+45, -45]_6$ plain weave composite coupons at various temperatures.	159
Figure 5.10: Radiographs of $[+45, -45]_6$ plain weave composite coupons inspected non-destructively after loading-unloading tests at various temperatures (X10).	162
Figure 5.11: Experimental creep results for $[0, 90]_6$ plain weave composite test coupons loaded to 200 MPa along fill and warp directions at 80°C	164
Figure 5.12: Experimental creep results for $[0, 90]_6$ plain weave composite test coupons at various temperatures and at a stress level of 100MPa.	166
Figure 5.13: Master creep plot for $[0, 90]_6$ plain weave composite test coupons at a reference temperature of 80°C and at a stress level of 100MPa.	166
Figure 5.14: Comparison of master creep plot and experimental creep data of $[0, 90]_6$ plain weave composite test coupon at a temperature of 80°C and stress of 100MPa....	167
Figure 5.15: Experimental creep plots for $[0, 90]_6$ plain weave composite test coupons at various temperatures and at a stress level of 5MPa.	169
Figure 5.16: Master creep plot for $[0, 90]_6$ plain weave composite test coupon at a reference temperature of 80°C and at a stress level of 5MPa.	169
Figure 5.17: Variation of storage modulus of $[0, 90]$ plain weave composites with temperature obtained using DMA at 10Hz frequency.	170
Figure 5.18: Horizontal shift factors for $[0, 90]_6$ plain weave composites as a function of inverse of temperature at various stress levels.....	172
Figure 5.19: Vertical shift factors for $[0, 90]_6$ plain weave composites as a function of inverse of temperature at various stress levels.....	172

Figure 5.20: Experimental creep results for [0, 90] ₆ plain weave composite test coupons at various stress levels and at a temperature of 80 ⁰ C.....	176
Figure 5.21: Master creep plots for [0, 90] ₆ plain weave composite test coupons at various stress levels and at a temperature of 80 ⁰ C.	176
Figure 5.22: Micrographs of [0, 90] ₆ plain weave composite test coupons after creep test at the highest temperature tested for various stress levels.	178
Figure 5.23: Master creep plots for [0, 90] ₆ plain weave composite test coupons at various stress levels and at a temperature of 80 ⁰ C.	178
Figure 5.24: Variation of instantaneous compliance of plain weave composites with undulation length (l_u) under on-axis loading.	181
Figure 5.25: Variation of instantaneous compliance of plain weave composites with crimp angle under on-axis loading.....	181
Figure 5.26: Schematic of a plain weave unit cell.	182
Figure 5.27: Variation of modulus with volume fraction of undulation region in a plain weave composite.....	182
Figure 5.28: Predicted creep compliance of plain weave composites under on-axis loading at 80 ⁰ C, using three sets of undulation parameters.	186
Figure 5.29: Comparison of model predictions with experimental creep results obtained at a stress of 100MPa and temperature of 80 ⁰ C for plain weave composites under on-axis loading.....	189
Figure 5.30: Comparison of model predictions with master plot obtained at a stress of 100MPa and temperature of 80 ⁰ C for plain weave composites under on-axis loading. 189	

Figure 5.31: Comparison of model predictions with experimental creep results obtained at a stress of 200MPa and temperature of 80 $^{\circ}$ C for plain weave composites under on-axis loading.....	191
Figure 5.32: Comparison of model predictions with master plot obtained at a stress of 200MPa and temperature of 80 $^{\circ}$ C for plain weave composites under on-axis loading.	191
Figure 5.33: Comparison of model predictions with experimental creep results obtained at a stress of 300MPa and temperature of 80 $^{\circ}$ C for plain weave composites under on-axis loading.....	193
Figure 5.34: Comparison of model predictions with master plot obtained at a stress of 300MPa and temperature of 80 $^{\circ}$ C for plain weave composites under on-axis loading.	193
Figure 5.35: Comparison of model predictions with experimental creep results obtained at a stress of 400MPa and temperature of 80 $^{\circ}$ C for plain weave composites under on-axis loading.....	195
Figure 5.36: Comparison of model predictions with master plot obtained at a stress of 400MPa and temperature of 80 $^{\circ}$ C for plain weave composites under on-axis loading.	195
Figure 5.37: Comparison of model predictions with experimental creep results obtained at a stress of 450MPa and temperature of 80 $^{\circ}$ C for plain weave composites under on-axis loading.....	196
Figure 5.38: Comparison of model predictions with master plot obtained at a stress of 450MPa and temperature of 80 $^{\circ}$ C for plain weave composites under on-axis loading.	196
Figure 5.39: Comparison of model predictions with master plot obtained at a stress of 3MPa and temperature of 80 $^{\circ}$ C for plain weave composites under on-axis loading....	199

Figure 5.40: Comparison of model predictions with master plot obtained at a stress of 5MPa and temperature of 80 $^{\circ}\text{C}$ for plain weave composites under on-axis loading.....	199
Figure 5.41: Comparison of model predictions with master plot obtained at a stress of 7MPa and temperature of 80 $^{\circ}\text{C}$ for plain weave composites under on-axis loading.....	200
Figure 5.42: Comparison of MELM, CM and EqM model predictions with master plot obtained at a stress of 3MPa and temperature of 80 $^{\circ}\text{C}$ for plain weave composites under on-axis loading.....	202
Figure 5.43: Comparison of shifted MELM, CM and EqM model predictions with master plot obtained at a stress of 3MPa and temperature of 80 $^{\circ}\text{C}$ for plain weave composites under on-axis loading.....	202
Figure 5.44: Creep-recovery plot for $[+45, -45]_6$ plain weave composite test coupon at various temperatures and a stress level of 7MPa.....	205
Figure 5.45: Creep-recovery plot for $[+45, -45]_6$ plain weave composite test coupon at various temperatures and a stress level of 50MPa.....	205
Figure 5.46: Creep-recovery plot for $[+45, -45]_6$ plain weave composite test coupon at various temperatures and a stress level of 100MPa.....	206
Figure 5.47: Compliance of $[+45, -45]_6$ plain weave composites at 7MPa and at various test temperatures.....	208
Figure 5.48: Master creep plot for $[+45, -45]_6$ plain weave composites at a reference temperature of 80 $^{\circ}\text{C}$ and at a stress level of 7MPa.....	208
Figure 5.49: Comparison of master creep plot and 2-days experimental creep plot for $[+45, -45]_6$ plain weave composites at a reference temperature of 80 $^{\circ}\text{C}$ and at a stress level of 7MPa.....	210

Figure 5.50: Experimental creep plot for [+45, -45] ₆ plain weave composites at a temperature of 80 ⁰ C and at a stress level of 50MPa for 2 days.....	210
Figure 5.51: Comparison of long-term creep of [+45, -45] ₆ plain weave composites at 7 & 50MPa stress levels and at a temperature of 80 ⁰ C.....	212
Figure 5.52: Variation of instantaneous compliance with undulation length for plain weave composites under 45 ⁰ off-axis loading.....	214
Figure 5.53: Variation of instantaneous compliance of plain weave composites with crimp angle under 45 ⁰ off-axis loading.....	214
Figure 5.54: Predicted creep compliance of plain weave composites under off-axis loading for three sets of undulation parameters.....	217
Figure 5.55: Comparison of model predictions with experimental creep plot obtained at a stress of 7MPa and temperature of 80 ⁰ C for plain weave composites under off-axis loading.....	220
Figure 5.56: Comparison of model predictions with experimental results obtained at a stress of 50MPa and temperature of 80 ⁰ C for plain weave composites under off-axis loading.....	220
Figure 5.57: Comparison of MELM and EqM model predictions with experimental results obtained at a stress of 7MPa and temperature of 80 ⁰ C for plain weave composites under off-axis loading.....	221
Figure 5.58: Comparison of MELM and EqM model predictions with experimental results obtained at a stress of 50MPa and temperature of 80 ⁰ C for plain weave composites under off-axis loading.....	221

Figure 5.59: Comparison of creep of [0 ⁰], [90 ⁰], [0/90] cross-ply and [0, 90] plain weave composite to illustrate effect of crimp.	223
Figure 5.60: Comparison of experimental creep of plain weave composites under on-axis (0 ⁰) loading and off-axis (45 ⁰) loading at a stress of 20% UTS and a temperature of 80 ⁰ C.	225
Figure 5.61: Comparison of experimental and predicted creep results obtained using approach 1 and approach 2 for plain weave composites under on-axis loading at 5MPa and 80 ⁰ C.....	227
Figure 5.62: Schematic of a section of unit cell of plain weave composite used to calculate the fiber volume fraction.	233
Figure A.1: 2-dimensional and 1-dimensional representation of the plain weave unit cell for crimp model.....	253
Figure A.2: Schematic overview of equivalent laminate model for predicting creep of plain weave composites.	256
Figure B.1: Experimental creep results for [0, 90] ₆ plain weave composite test coupons at various temperatures and at a stress level of 200MPa.	262
Figure B.2: Master creep curve for [0, 90] ₆ plain weave composite test coupons at a reference temperature of 80 ⁰ C and at a stress level of 200MPa.	262
Figure B.3: Experimental creep results for [0, 90] ₆ plain weave composite test coupons at various temperatures and at a stress level of 300MPa.	263
Figure B.4: Master creep curve for [0, 90] ₆ plain weave composite test coupons at a reference temperature of 80 ⁰ C and at a stress level of 300MPa.	263

Figure B.5: Experimental creep results for [0, 90] ₆ plain weave composite test coupons at various temperatures and at a stress level of 400MPa	264
Figure B.6: Master creep curve for [0, 90] ₆ plain weave composite test coupons at a reference temperature of 80 ⁰ C and at a stress level of 400MPa	264
Figure B.7: Experimental creep results for [0, 90] ₆ plain weave composite test coupons at various temperatures and at a stress level of 450MPa	265
Figure B.8: Master creep curve for [0, 90] ₆ plain weave composite test coupons at a reference temperature of 80 ⁰ C and at a stress level of 450MPa	265
Figure B.9: Experimental creep results for [0, 90] ₆ plain weave composite test coupons at various temperatures and at a stress level of 3MPa	266
Figure B.10: Master creep curve for [0, 90] ₆ plain weave composite test coupons at a reference temperature of 80 ⁰ C and at a stress level of 3MPa	266
Figure B.11: Experimental creep results for [0, 90] ₆ plain weave composite test coupons at various temperatures and at a stress level of 7MPa	267
Figure B.12: Master creep curve for [0, 90] ₆ plain weave composite test coupons at a reference temperature of 80 ⁰ C and at a stress level of 7MPa	267
Figure B.13: Experimental creep results for [0, 90] ₆ plain weave composite test coupons at various stress levels and at a temperature of 100 ⁰ C.....	268
Figure B.14: Experimental creep results for [0, 90] ₆ plain weave composite test coupons at various stress levels and at a temperature of 120 ⁰ C.....	268
Figure B.15: Experimental creep results for [0, 90] ₆ plain weave composite test coupons at various stress levels and at a temperature of 140 ⁰ C.....	269

Figure B.16: Experimental creep results for [0, 90]₆plain weave composite test coupons at various stress levels and at a temperature of 160 ⁰C..... 269

LIST OF TABLES

Table 2.1: Summary of published literature on creep of woven composites.....	35
Table 4.1: Summary of fiber volume fraction test results (step 1 & 2) for the manufactured woven composite panel.....	77
Table: 4.2 Test coupon dimensions for on-axis and off-axis tests.....	82
Table 4.3: Test plans for on-axis and off-axis tensile tests.....	89
Table 4.4: Plan for On-axis creep testing using DMA.....	91
Table 4.5: Test plans for on-axis and off-axis creep testing using Instron testing machine.	
.....	92
Table 4.6: Test coupon dimensions for various coupon configurations.	113
Table 4.7: Creep and recovery test scheme for unidirectional composites in nonlinear viscoelastic region of matrix.....	113
Table 4.8: Constants for modified KWW equation used in simulating the time-dependent compliance of unidirectional tape lamina at a reference temperature of 80 $^{\circ}$ C in linear viscoelastic range of its polymer matrix.	117
Table 4.9: Nonlinear parameters for transverse creep at various stresses and temperatures.	
.....	135
Table 4.10: Nonlinear parameters for shear creep at various stresses and temperatures.	136
Table 5.1: Undulation parameters measured using micrograph of a single-ply lamina shown in Figure 5.1.....	146

Table 5.2: Undulation parameters measured using micrographs of multi-ply laminates shown in Figure 5.2.....	146
Table 5.3: Tensile test results for [0, 90] ₆ plain weave composite coupons at various temperatures tested at a strain rate of 10^{-4} sec ⁻¹	152
Table 5.4: Tensile test results for [45, -45] ₆ plain weave composite coupons at various temperatures tested at a strain rate of 10^{-4} sec ⁻¹	155
Table 5.5: Instantaneous modulus and permanent recovery strain in [+45, -45] ₆ plain weave composite coupons obtained through loading-unloading tests at various temperatures.....	160
Table 5.6: Activation energies and pre-exponential factors for [0, 90] ₆ plain weave composites at various stress levels.....	173
Table 5.7: Average, upper bound, and lower bound values for the undulation parameters	185
Table 5.8: Comparison of on-axis experimental and predicted instantaneous compliance and modulus at various stress levels and at temperature of 80 °C.....	190
Table 5.9: Comparison of on-axis experimental and predicted instantaneous compliance and modulus at various stress levels and at temperature of 80 °C.....	200
Table 5.10: Recovery strain after creep tests at various stresses and temperatures for [+45, -45] ₆ plain weave composite test coupons.	206

LIST OF SYMBOLS

- θ orientation of the fiber in a lamina with respect to the loading direction (X-axis).
 σ_0 applied stress.
 ε_0 instantaneous strain.
 $\varepsilon(t)$ time-dependent strain.
 ϕ undulation or crimp angle of plain weave fabric.
 μ aging shift rate.
 $\nu_{12}^k(t)$ time-dependent Poisson's ratio of unidirectional lamina.
 $\varepsilon_{xy}(t)$ time-dependent strain on equivalent plain weave laminate.
 $\varepsilon_{xx}^k(t, \phi^k)$ time-dependent longitudinal strain of infinitesimal segment of equivalent fill/warp lamina.
 $\varepsilon_{yy}^k(t, \phi^k)$ time-dependent transverse strain of infinitesimal segment of equivalent fill/warp lamina.
 $\bar{\varepsilon}_{xx}^k(t)$ average time-dependent longitudinal strain in equivalent fill/warp lamina.
 $\bar{\varepsilon}_{yy}^k(t)$ average time-dependent transverse strain in equivalent fill/warp lamina.
 $\nu_{xy}^k(t, \phi^k)$ time-dependent Poisson's ratio of infinitesimal segment of equivalent fill/warp lamina.
 $\nu_{xy}^k(t)$ average time-dependent Poisson's ratio of equivalent fill/warp lamina.

- n_g harness of woven fabric.
 S_0 instantaneous compliance.
 $S(t)$ time-dependent compliance.
 t_R creep rupture time.
 l length of plain weave unit cell.
 $2a, 2b$ cross-sectional dimensions of elliptical fill or warp yarn in a plain weave.
 h_0 thickness of plain weave fabric.
 l_u undulation or crimp length of plain weave fabric.
 T_g glass- transition temperature of polymer.
 a_T temperature dependent shift factor.
 A_0 pre-exponential constant for Arrhenius equation.
 ΔH activation energy.
 T service temperature
 T_{ref} reference temperature.
 R gas constant (8.314 J/K.mole)
 a_{ta} aging time shift factor.
 t_a aging time.
 t_{aref} reference aging time.
 N_X applied force per unit length on equivalent plain weave laminate along X-axis.
 $a_{xy}(t)$ time-dependent compliance of equivalent plain weave laminate.
 $a_{xy}^1(t)$ time-dependent compliance of section (1) of equivalent plain weave laminate.
 $a_{xy}^2(t)$ time-dependent compliance of section (2) of equivalent plain weave laminate.

l_0 length of section (1) of equivalent plain weave laminate.

$Q_{ij}^k(t)$ time-dependent stiffness matrix of unidirectional lamina along principal directions of fiber.

$E_{11}^k(t)$ time-dependent longitudinal modulus of unidirectional lamina.

$S_{11}(t)$ time-dependent longitudinal compliance of unidirectional lamina.

$E_{22}^k(t)$ time-dependent transverse modulus of unidirectional lamina.

$S_{22}(t)$ time-dependent transverse compliance of unidirectional lamina.

$G_{12}^k(t)$ time-dependent shear modulus of unidirectional lamina.

$S_{66}(t)$ time-dependent shear compliance of unidirectional lamina.

T^k transformation matrix.

$Q_{II}^k(t)$ time-dependent stiffness matrix of unidirectional lamina in global coordinate system.

$A_{II}^1(t)$ time-dependent stiffness matrix per unit width of section (1) of equivalent laminate.

h_f, h_w Z coordinates of the centre line of the fill and warp laminae of plain weave.

$E_{xx}^k(t, \phi^k)$ time-dependent longitudinal modulus of infinitesimal segment of equivalent fill/ warp lamina.

$E_{yy}^k(t, \phi^k)$ time-dependent transverse modulus of infinitesimal segment of equivalent fill/ warp lamina.

$G_{xy}^k(t, \phi^k)$ time-dependent shear modulus of infinitesimal segment of equivalent fill/ warp

lamina.

$E_{xx}^k(t)$ average time-dependent longitudinal modulus of equivalent fill/ warp lamina.

$E_{yy}^k(t)$ average time-dependent transverse modulus of equivalent fill/ warp lamina.

$G_{xy}^k(t)$ average time-dependent shear modulus of equivalent fill/ warp lamina.

$Q_{ijeq}^k(t)$ time-dependent stiffness matrix of equivalent lamina along local directions of fiber (x, y, Z).

$Q_{Ijeq}^k(t)$ time-dependent stiffness matrix of equivalent lamina in global coordinate system.

$A_{II}^2(t)$ time-dependent stiffness matrix per unit width of section (2) of equivalent laminate.

$S_{XY}(t)$ time-dependent compliance of plain weave unit cell.

V_f volume fraction of fibers in composite.

X, B, C constants in modified KWW equation.

g_0, g_1, g_2, a_σ nonlinear parameters in Schapery's nonlinear viscoelastic model.

1. INTRODUCTION

A composite is a mixture of two or more constituents with properties superior to those of its constituents. A polymer matrix composite (PMC) comprises a polymer matrix reinforced with high strength fibers. Advantages of polymer matrix composites over metals/alloys are high specific strength (strength to density ratio), specific modulus (modulus to density ratio), corrosion resistance and better fatigue resistance. Due to these advantages, polymer matrix composites are increasingly used in structural applications as well as non-structural applications in aerospace, automotive, civil infrastructure, recreation, building/ construction and bio-medical industries. Forthcoming Boeing 787 Dreamliner is a perfect example of increasing use of PMCs in structural applications.

The current share of PMC in civilian aircraft is 10-12 % of the total structural weight of the aircraft. To date, PMCs have been mostly used to manufacture secondary structures, which are not the primary load bearing members of the aircraft. Horizontal and vertical stabilizers are the only primary structural applications for PMCs, known to date in civilian aircrafts. A composite elevator of Boeing 727 was designed, manufactured, and qualified almost three decades ago using the composite used in this study, . In forthcoming Boeing 787, the PMCs are applied for the first time in other primary load bearing structures such as the entire fuselage and wings (<http://www.boeing.com/commercial/787family/background.html>). The share of PMCs are about to increase to about 50% of the structural weight.

1.1 Background

Polymer matrix composites can be classified based on the shape of reinforcement as particulate composites, discontinuous fiber composites, and continuous fiber composites. Particulate composites contain reinforcement particles with aspect ratio (Length/Diameter) varying from 1 to 20, dispersed randomly within the matrix, while discontinuous fiber composites contain short fibers with aspect ratio varying from 20 to 1000. Continuous fiber composites consist of fibers with aspect ratio greater than 1000. Normally, a fiber reinforces the matrix of a PMC by sharing a major portion of the applied load. The percentage of the applied load, shared by the fibers, increases with increase in aspect ratio of the fiber. Hence, continuous fiber composites with highest reinforcing efficiency are normally used in structural applications. The composite material used in the present study is a continuous fiber composite.

Continuous fiber composites used in structural applications are made-up of basic building blocks, known as a *lamina* or a *ply*. Before lamination, this lamina is known as a pre-preg (*pre-impregnated*). The composites, also known as a laminates, are made by stacking these pre-pregs together and laminating them under heat and pressure in an autoclave (for aerospace applications). The pre-preg, made-up of continuous reinforcing fibers and matrix, is classified based on the fiber arrangement,

- A) *Tape Pre-preg*: A tape pre-preg is a single layer of parallel fibers impregnated with resin, as shown in *Figure 1.1*.
- B) *Fabric Pre-preg*: A fabric pre-preg is formed by weaving two fiber rovings (a roving is a bundle of parallel fibers) in orthogonal direction and impregnated with resin as shown in *Figure 1.2*.



Figure 1.1: Schematic of a tape lamina.

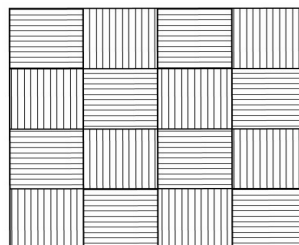


Figure 1.2: Schematic of a fabric lamina.

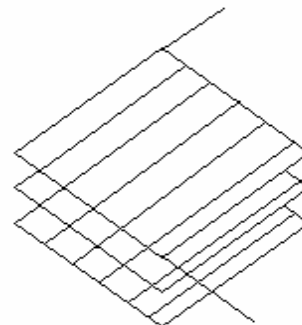


Figure 1.3: Schematic of a unidirectional laminate/ composite.

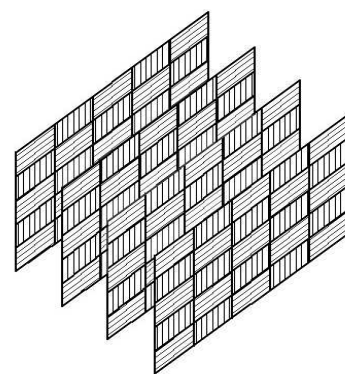


Figure 1.4: Schematic of a woven laminate/ composite.

Since a single lamina (tape or fabric) is difficult to test, normally a laminate, made up of several laminae with same fiber orientation in all layers, is manufactured and tested. Such a laminate is termed as either *Unidirectional composite / laminate* $[\theta]_n$ (made from tape pre-pregs) or *Woven composite/ laminate* $[\theta, \theta+90]_n$ (made from fabric pre-pregs) as shown in *Figures 1.3 & 1.4* respectively. n is the number of laminae in the laminate. Composites used in structural applications are usually multidirectional composites that are made up of several laminae with different fiber orientation in each layer with respect to loading direction X, as shown in *Figure 1.5*, to obtain the desired properties. 1-2-3 corresponds to the principle co-ordinate system of the ply, wherein, 1 coincides with the longitudinal axis of the fiber and 2 & 3 correspond to axes oriented perpendicular to 1 axis. X-Y-Z is the global coordinate system. θ is the angle of orientation of the fibers in a lamina with respect to the loading (global) X-axis. A multidirectional composite made using tape laminae is referred as *Multidirectional non-woven composite/ laminate* $[\theta_i/\theta_j]_s$, as shown in *Figure 1.6a*, while a multidirectional composite made using fabric laminae is referred as *Multidirectional woven composite/ laminate* $[\theta_i, (\theta_i+90)/\theta_j, (\theta_j+90)]_s$, as shown in *Figure 1.6b*. The subscript ‘s’ corresponds to ‘symmetric’ and $\theta_i, \theta_j = 0$ to 90° . A symmetric laminate is one in which the lamina lay-up on one side of a reference plane is a mirror image of the lamina lay-up on the other side. In other words, for each lamina layer on one side of the reference plane, there is a corresponding lamina layer on the other side at equal distance from the reference plane with identical thickness, orientation and properties. As an example, $[0/90]_s$ corresponds to $[0/90/90/0]$. *Present study deals with woven composites, similar to those shown in Figure 1.4.*

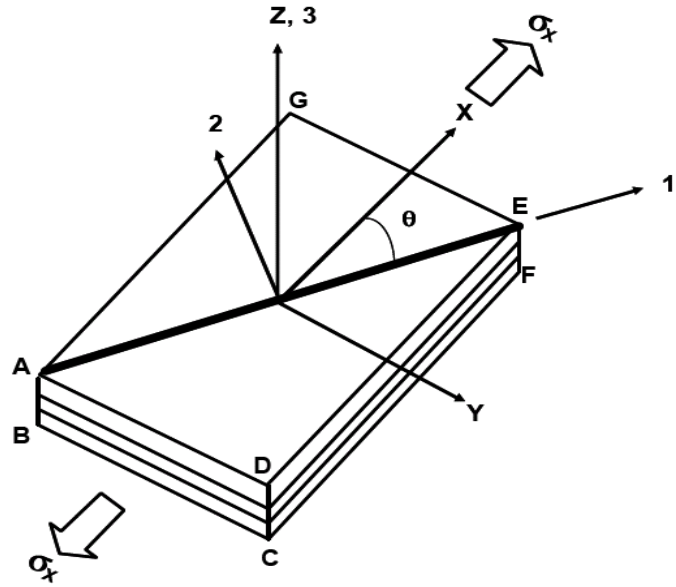


Figure 1.5: A Schematic of global and principle coordinate system [2].

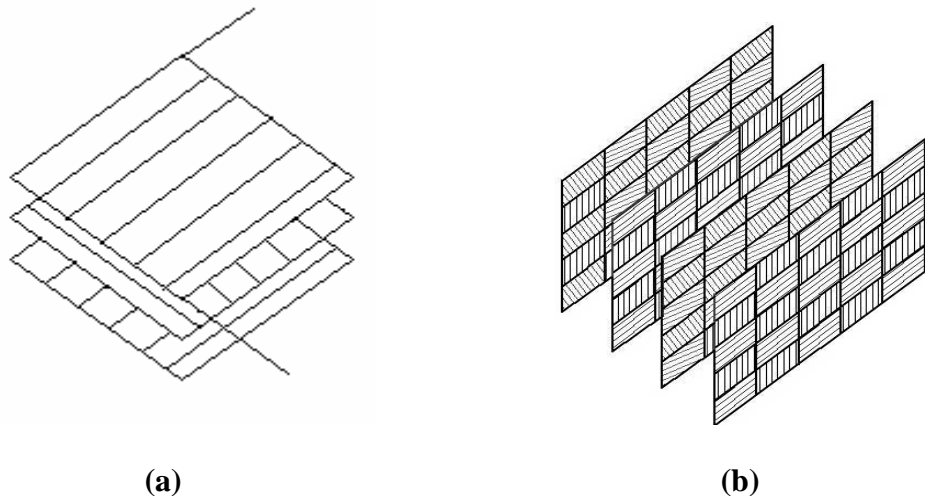
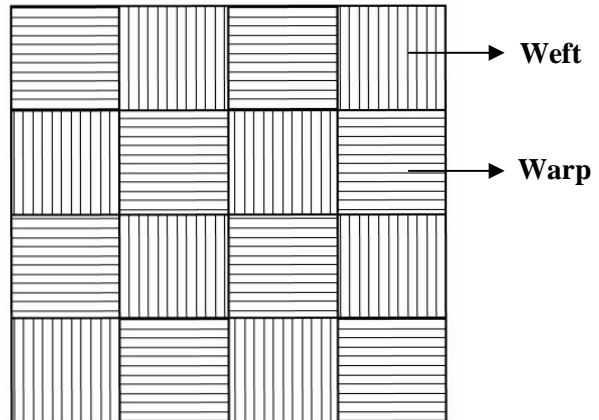
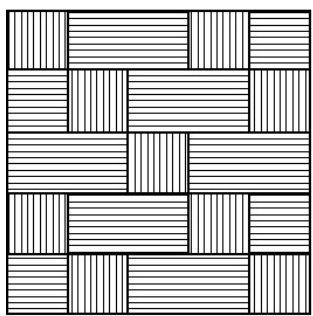


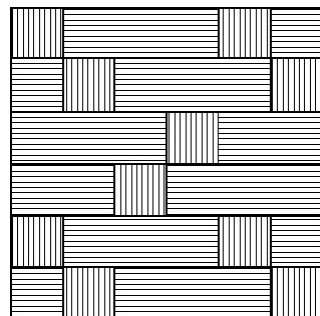
Figure 1.6: Schematics of (a) multidirectional non-woven laminate and (b) multidirectional woven laminate.



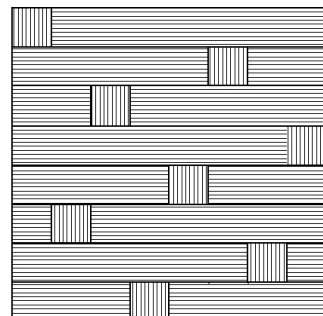
(a)



(b)



(c)



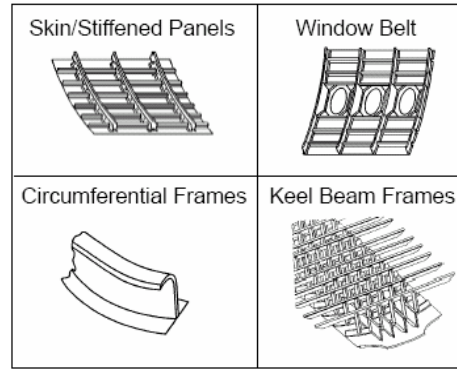
(d)

Figure 1.7: Various weave patterns for (a) 2-harness plain weave, (b) 3-harness weave, (c) 5-harness weave and (d) 8-harness satin weave fabric.

The woven fiber architecture in a fabric lamina is formed on a textile loom by interlacing two or more sets of fiber rovings. When two sets of rovings are interlaced at right angles, the lengthwise roving is known as the *warp*, and the widthwise roving is known as the *fill or weft*, as shown in *Figure 1.7a*. The woven fabric pattern varies with harness^{*} ($n_g = 2, 3, 5, 8$) as shown in *Figure 1.7. The woven pattern used in the present study has a harness of 2 and is known as plain weave*. It should be noted that “Textile composites” is a generic terminology used to refer to both woven as well as multidirectional woven composites.

Most of the aerospace structures utilize both multidirectional non-woven and woven composites. In the past, woven composites were primarily used for NASA spacecrafts and military aircrafts, due to their higher manufacturing cost. In recent years, woven composites have been gaining acceptance in civilian aerospace industries as well as in automobile, electronics, civil infra-structure industries. Woven architecture results in quasi-isotropic properties and offers good impact resistance and damage tolerance owing to high intra and inter-laminar strength. Typical fuselage structural parts of an aircraft such as stiffened side panels, circumferential frames, keel beam frames and window belts, shown in *Figure 1.8 [3]*, are made of woven composites. It also offers the ability to manufacture complex shaped parts, unlike tape pre-preg based composites.

* Harness of woven fabric pattern is defined as the number of warp/weft sections between the two successive weft / warp sections.



(a)

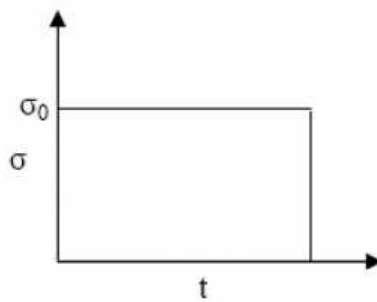


(b)

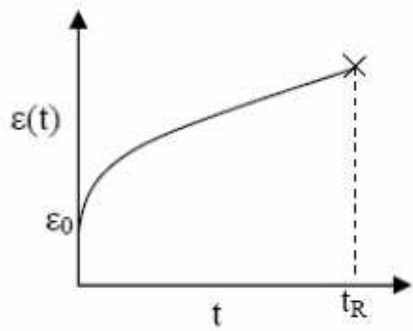


(c)

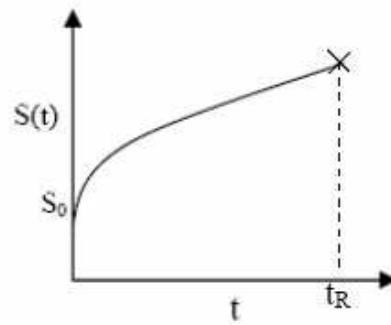
Figure 1.8: Application of woven composites as (a) fuselage structural part, (b) curved frames for fuselage keel structure, and (c) lower fuselage side panel perform [3].



(a)



(b)



(c)

Figure 1.9: Illustration of creep in polymer matrix composites; Variation of (a) applied stress, (b) time-dependent strain in response to (a), and (c) time-dependent compliance, with time

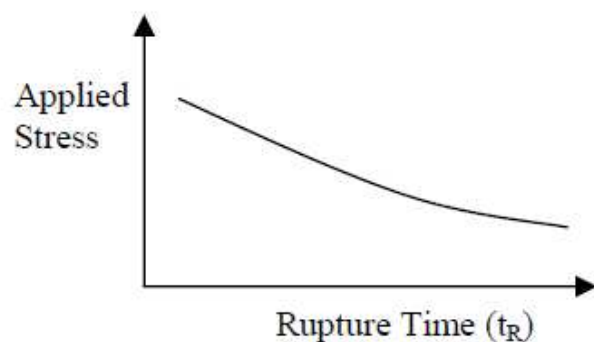


Figure 1.10: Illustration of creep rupture.

1.2 Thesis Motivation and Scope

Modulus and strength of PMCs degrade with time during service. The degradation in modulus is known as *Creep* while the degradation in strength is known as *Creep rupture*, as illustrated in *Figures 1.9* and *1.10* respectively. In response to an applied load σ_0 , which is less than the ultimate tensile strength of the material, at $t=0$, the composite would experience instantaneous strain ϵ_0 as shown in *Figure 1.9(a)*. If the load is maintained constant, the strain ($\epsilon(t)$) in the material increases with time as shown in *Figure 1.9(b)* and this response is known as creep. The ratio of creep strain to applied creep load is the creep compliance ($S(t)$) plotted in *Figure 1.9(c)*. It can be inferred that the compliance or alternatively the modulus of the PMC degrades with time. While creeping, the material suddenly fails, as illustrated in *Figure 1.9(b)*, even though the applied stress is lower than the ultimate tensile strength of the material. The time (t_R) for this delayed rupture, i.e. creep rupture depends on the magnitude of the applied load. The lower the load is the longer the time to rupture. The time t_R is plotted as a function of applied stress in *Figure 1.10* and it can be inferred that the strength of the PMC degrades with time. The cause of such time-dependent degradation in modulus and strength of PMC is the viscoelastic nature[†] of the polymer matrix. Since these composites are increasingly utilized in various structural parts with a typical service life of 20-30 years, there is a vital need to understand and characterize creep and creep rupture of these composites to prevent pre-mature failure during service.

[†] Discussed in Chapter 2.

During the past three decades, considerable research has been carried out to understand and model creep and creep rupture of a polymer matrix and its composites made from tape laminae i.e., both unidirectional and multidirectional non-woven composites. A comprehensive review on this can be found in references [4] & [5]. Researchers from the Composite Materials & Structures Research Group at the University of Manitoba have made significant contributions to this area during the past decade by characterizing the combined effect of temperature, stress, moisture and physical aging[‡] on creep and creep-rupture of unidirectional and multidirectional non-woven composites as well as the polymer matrix used in these composites [4, 5].

An extensive literature review indicates that studies on creep and creep rupture of woven composites are limited. Additionally, a critical review of these studies highlights a number of knowledge gaps, which are discussed in Chapter 2. Considering the increasing use of woven composites in load-bearing structural applications, additional concentrated efforts are required to bridge these knowledge gaps for safe design and use of PMCs in load bearing structural applications. This is the motivation for this thesis. A study of both creep and creep rupture, addressing all the knowledge gaps identified in Section 2.4, is beyond the scope of one PhD thesis. Hence, ***main focus in this thesis is creep of plain weave woven composites.***

[‡] Discussed in Chapter 2.

1.3 Thesis Organization

The thesis is organized as follows:

In Chapter 2, a brief introduction to factors influencing creep and creep rupture in polymer matrix composites, such as temperature, stress, physical aging and moisture is presented first, followed by a discussion on the microstructural factors that influence the creep of woven composites. Subsequently, a detailed literature review on creep and creep rupture in woven polymer matrix composites is presented and discussed. Knowledge gaps are identified supporting the objectives of this thesis.

In Chapter 3, a generalized model is proposed to simulate the creep of plain weave polymer matrix composites under on- and off-axis loading.

In Chapter 4, the creep experiments are presented first, followed by simulation.

In Chapter 5, experimental and simulation results are presented, compared and discussed to validate the creep model proposed in this thesis.

In Chapter 6, conclusions based on the results of this research are presented followed by future recommendations.

2. LITERATURE REVIEW

2.1 Introduction

Creep and creep rupture are two major concerns while using PMCs in load-bearing structural applications, as discussed in Chapter 1, even at room temperature due to viscoelastic nature of the polymer matrix. While excess deformation due to creep may cause a composite part's dimensions unfit for an application, creep rupture may lead to catastrophic failure of the structural part. Therefore, creep and creep rupture are major considerations in safe and reliable design of PMC structures.

As defined in Chapter 1, degradation in modulus with time is known as creep while degradation in strength with time is known as creep- rupture. The primary cause of creep and creep rupture of PMCs is the viscoelasticity of the polymer matrix. When a stress of σ_0 is applied to an elastic material, as shown in *Figure 2.1a*, it would deform elastically, in-phase with the applied stress, to a strain of ϵ_0 as shown in *Figure 2.1b*. This strain will remain constant with time and will return to zero strain state as soon as the applied stress is removed. In contrast, a viscoelastic material would exhibit a time-dependent increase in strain (ϵ_v), as shown in *Figure 2.1c*, in addition to the instantaneous strain (ϵ_0). Upon unloading, the elastic strain will recover immediately while the viscoelastic strain will recover over a period of time. A viscoelastic material exhibits both elastic and viscous behavior. In carbon fiber composites, such as the one studied in this thesis, the carbon fibers remain elastic and do not creep. Hence, the observed creep and final rupture in these composites is due to viscoelasticity of the polymer matrix, which is

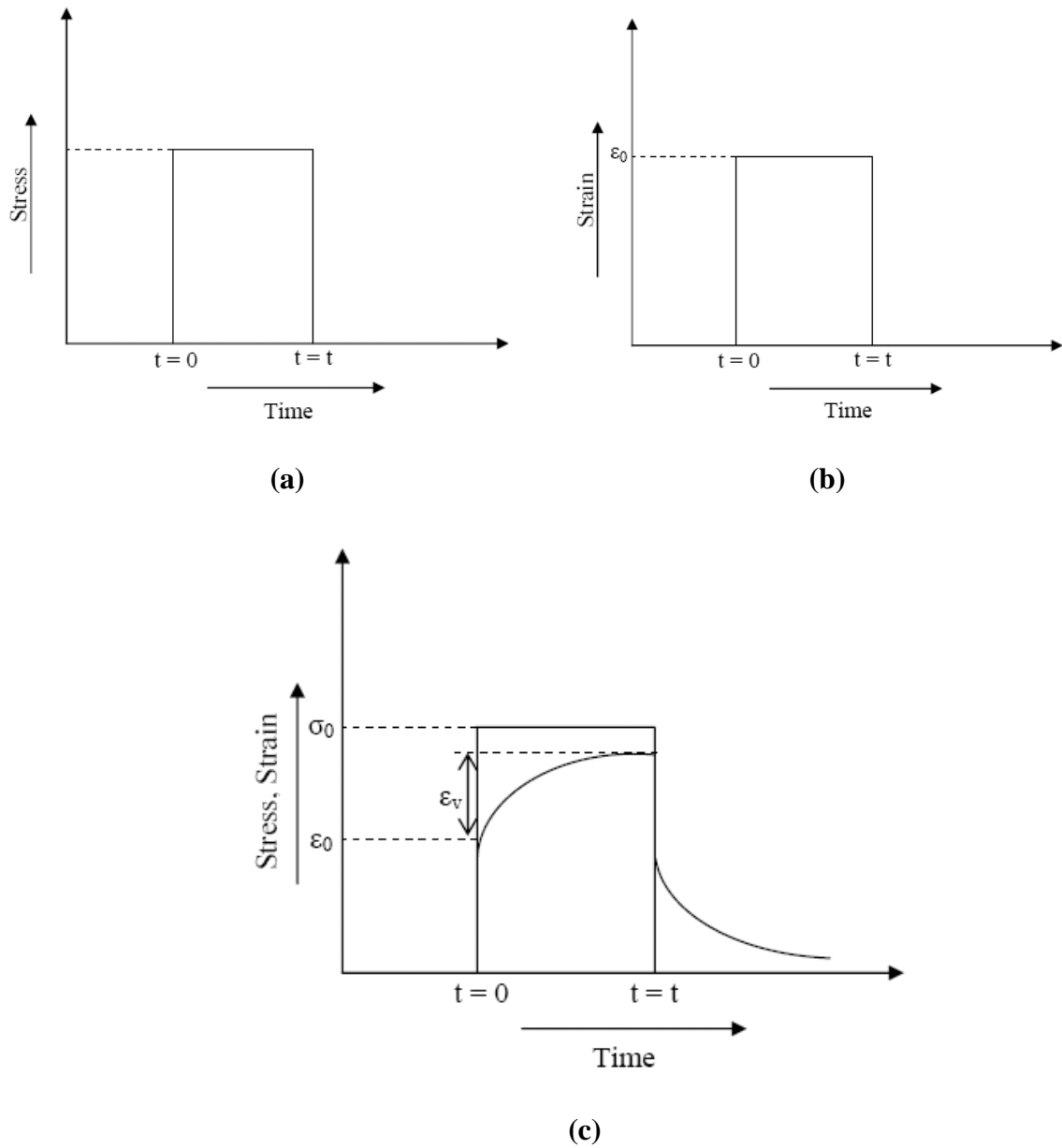


Figure 2.1: Illustration of (a) stress profile, (b) elastic behavior and (c) viscoelastic behavior.

affected by a number of factors.

A brief introduction of factors influencing the creep and creep rupture of polymer matrix composites is provided below followed by a thorough and critical literature review of published research in the area of creep and creep rupture of woven composites. Based on this critical review, the current knowledge gaps are identified and used to define the objectives of this thesis.

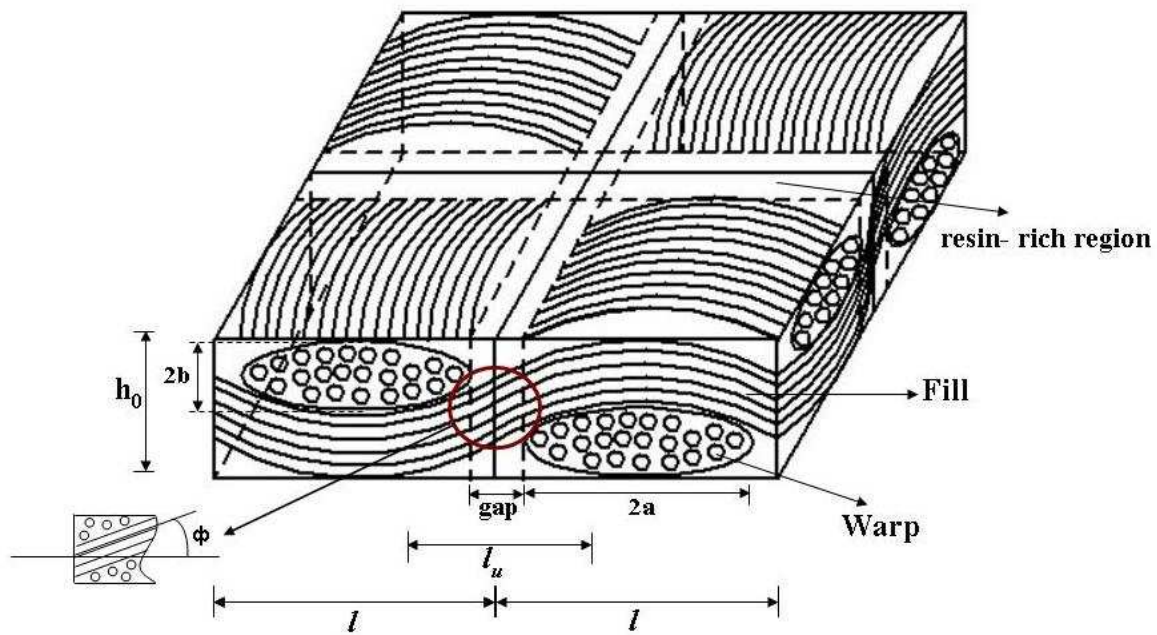
2.2 Factors affecting creep and creep rupture of woven composites

2.2.1 Microstructure

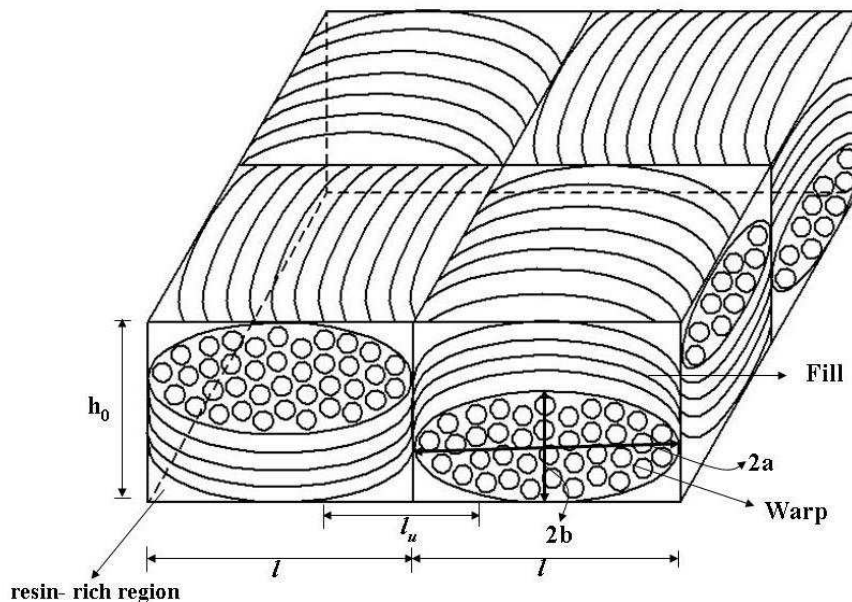
The microstructural features, at a lamina level, that affect mechanical behavior of woven composites are the fiber volume fraction and fiber architecture. The microstructural features of relevance at the laminate level are lamina orientation with respect to the loading direction and the phase shift among laminae. These microstructural features are introduced first. Subsequently, published literature on the study of effect these features on the properties of woven composites is presented and discussed.

2.2.1.1 Microstructural features of a woven lamina

A schematic of the microstructure of a plain weave lamina is shown in *Figure 2.2a*. The fill and warp yarns interlace with each other, over one yarn width at a time, resulting in a 2-harness (2H) plain weave geometry. The wavelength of undulation in the yarn is defined by $2l$. The cross-section of the yarn is typically ellipsoidal with dimensions of the major and minor axes defined by $2a$ and $2b$, respectively. The magnitude of these dimensions is decided by the number of fibers in a yarn and the yarn



(a) with gap



(b) without gap

Figure 2.2: Two-dimensional schematics of plain weave with and without gap.

tension during the weaving process. Spacing between two warp yarns or two fill yarns is defined by the yarn count, i.e. number of yarns per unit length. For example, the plain weave fabric used in the present thesis has a yarn count of 12.5 per inch in both fill and warp directions. Hence, the yarn spacing in both fill and warp directions is 2mm. This space, identified as l , in *Figure 2.2* can be equal to $2a$ of the yarn. In this case, there will not be any resin rich “gap” as shown in *Figure 2.2b*. If l is less than $2a$, then a fabric will have resin rich “gap” as shown in *Figure 2.2a*. Due to the presence of such resin-rich region, a yarn’s packing density (fiber volume fraction within a yarn) is always higher than the overall volume fraction of the plain weave fabric. In present thesis, a plain weave with zero gap is considered for modeling and will be discussed in detail in Chapter 3.

The representative unit cell shown in *Figure 2.2b* is used in modeling. The parameters of this unit cell used in modeling are defined by the microstructural features discussed above. These parameters are thickness of the lamina (h_0), undulation or crimp length (l_u), undulation or crimp angle (ϕ), the dimensions of the warp or fill yarn ($2a$ and $2b$).

2.2.1.2 Microstructural features of a woven laminate

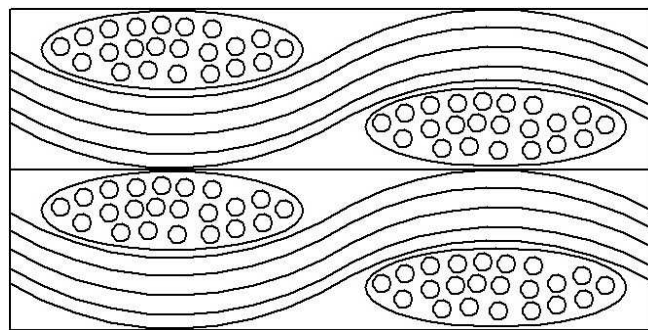
In addition to the microstructural features discussed in 2.2.1.1, the other microstructural features for a woven laminate are lamina orientation with respect to the loading direction and phase- shift among the laminae of the laminate.

As discussed in Chapter 1, multi-directional woven laminates are normally used in a given application and the mechanical behavior of these laminates depends on the orientation of each lamina within the laminate with respect to the loading direction.

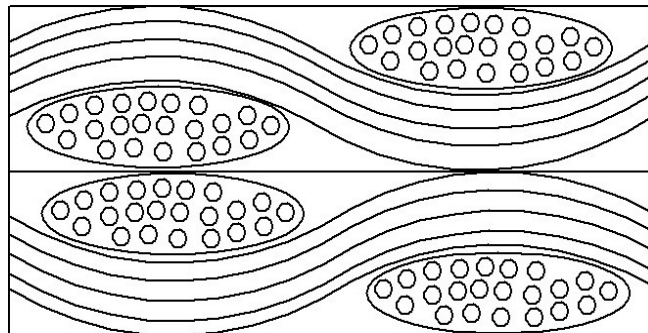
The phase shift among the laminae refers to the relative position of a lamina with respect to the other laminae within a laminate. This can be understood from *Figure 2.3*. Let us consider a woven laminate with all laminae oriented in the same direction. Three possible stacking configurations [6] are identified as: (i) Iso- phase stacking configuration, as shown in *Figure 2.3a*, with zero for all laminae; (ii) Out-of-phase stacking configuration, shown in *Figure 2.3b* with a phase shift of $\pm \pi$ for all laminae; and (iii) Random stacking configuration, shown in *Figure 2.3c*, with a phase shift that randomly varies between 0 to $\pm \pi$ from laminae to laminae. This phase shift is normally caused by error while laying-up as well as movement of laminae during autoclave manufacturing. Due to this phase shift, the undulation parameters of a lamina within a woven laminate could be different from that in a single woven lamina. Previous studies [7-10] have shown that the average lamina thickness decreases with increase in the number of laminae in a woven laminate during consolidation, under a given cure pressure. Lomov et al. [11, 12] studied the variation of lamina thickness in a laminate due to phase shifts using a mathematical model. For a given number of laminae in a laminate, the lamina thickness was found to decrease with increase in phase shift. Yurgartis et. al. [13, 14] developed computer-aided image analysis technique to measure crimp angles and its variation within a woven laminate using its micrographs, to assist micromechanical modeling used to predict properties of woven composites.

2.2.1.3 Effect of microstructure on elastic properties, creep and creep rupture of woven composites

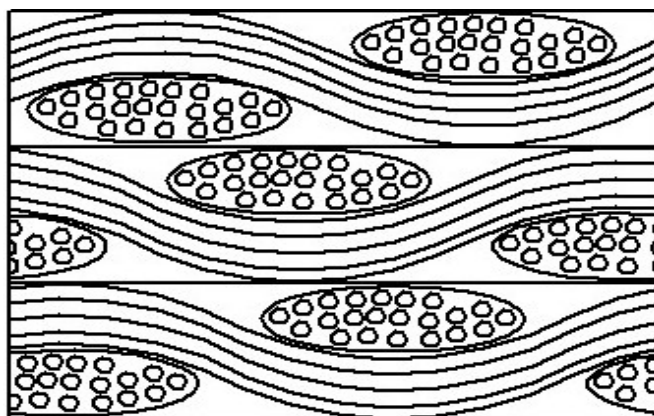
These microstructural features strongly influence both the elastic and time-dependent properties of woven composites. While there are no systematic studies



(a) Iso- phase



(b) Out- of- phase



(c) Random- phase

Figure 2.3: Schematics of various stacking configurations of laminae within a woven laminate.

correlating these microstructural features to creep and creep rupture, there are many publications that have related them to elastic properties and failure behavior of woven composites [15- 28]. Hence, the latter is reviewed here to underpin the efforts of this thesis to relate microstructure with creep of woven composites.

It is difficult to control these microstructural features during manufacturing of composite panels in order to experimentally study their effect on the elastic properties. Hence, most of the studies were conducted analytically. Ishikawa et al. [15] studied the effect of number of plies and crimp ratio (h_0/l) on on-axis and off-axis elastic modulus of plain weave composite laminates. The on-axis elastic modulus was found to increase with increase in number of plies or decrease in crimp ratio. The off-axis modulus, obtained for different orientation of laminae (0- 45⁰), was also found to increase with increase in number of plies.

Whitcomb et al. [16, 17] and Ito et al. [18] have studied the effect of phase shift and the crimp ratio on elastic modulus of woven laminate. The elastic modulus for iso-phase configuration was found to be lower than that for the out-of-phase configuration. These studies suggest that the deformation of a lamina is constrained more by the out-of-phase configuration than by iso-phase configuration resulting in larger flexural deformation of the laminate and lower modulus. The flexural modulus of a single lamina is the modulus of a woven laminate due to lack of such constraints. In this study, due to experimental difficulties, woven laminate is manufactured and tested to obtain the properties of a single lamina. The above result is significant in this context. The tensile elastic modulus has been found to increase with decrease in crimp ratio [15, 18-20].

However, the in-plane shear modulus has been found to be independent of phase shift and crimp ratio [17, 19].

Naik et al. [21-23] investigated in detail the effect of fabric microstructure on the failure behaviour of plain weave composites under on-axis loading. Similar to the observations of other researchers, they also recorded the lowest elastic modulus for iso-phase configuration. The failure strength of plain weave composites was found to increase with increase in fiber volume fraction and decrease with increase in crimp ratio. They have studied the effect of yarn gap on failure strength of plain weave composites. For a given fiber volume fraction and crimp ratio, the failure strength was found to first increase and then decrease with increase in yarn gap. With increase in yarn gap, the crimp ratio as well as the overall fiber volume fraction decreases. Decrease in crimp ratio increases the strength of the composite while decrease in fiber volume fraction decreases the strength of the composite. Thus, due to combined effect of crimp ratio and fiber volume fraction, the failure strength first increases at lower yarn gap while decreases at higher gap. They also studied the effect of these parameters on shear strength of plain weave composites [24]. The in-plane shear strength for a laminate with iso-phase configuration was found to be higher than other stacking configurations for lower crimp ratio while the opposite was observed for higher crimp ratio. The shear modulus did not show any dependence on crimp ratio. The effect of yarn gap on shear strength was not observed; however, an increase in yarn gap decreased the shear modulus.

In addition to the stacking configuration, process-induced damage during manufacturing of composite laminate could also result in variation of microstructural parameters. Process-induced damage has been previously reported in multidirectional

laminates [2] as well as in woven composites [29]. Similar process-induced damage was observed in the plain weave composites used in present thesis and will be discussed in detail in Chapter 4. However, no studies were found on the effect of process-induced damage on variation of microstructural parameters in woven composites.

Based on the above review, it is obvious that the microstructure of woven composites is dependent on various factors such as number of laminae, stacking configuration of laminae and damage. Variation of microstructural parameters due to these factors strongly influences the elastic and failure behavior of woven composites. Similar effect of microstructure on time-dependent properties of woven composites is obvious. However, the published studies [6-29] have not investigated this effect. Considering the importance of microstructure on time-dependent properties of woven composites, such investigation was carried out analytically in the present thesis and will be presented in Chapter 5.

2.2.2 Environmental / Service Factors

There are four major service or environment factors that affect creep and creep rupture of polymer matrix composites: a) Temperature, b) Stress, c) Physical Aging, and d) Moisture. A complete study of individual and combined effect of these service environmental factors is necessary to characterize creep and creep rupture of polymer matrix woven composites. Most of the published studies in this area have focused on the effect of one or more of these factors but not all. Moreover, these studies are predominantly on non-woven polymer matrix composites. These factors are discussed in general without any review of published literature since they are numerous to fit within the scope of this chapter.

2.2.2.1 Effect of Temperature

It is well known that an increase in temperature accelerates creep and creep rupture of polymer matrix composites. Under a constant load, an increase in test temperature reduces the modulus of the composite and increases its creep compliance as shown in *Figure 2.4*. Similarly, an increase in test temperature reduces the creep rupture time of the composite, for an applied stress, as shown in *Figure 2.5*.

In general, service life of a PMC at a service temperature would be from few years to few decades. However, it is not possible to characterize the complete creep (or creep rupture) behavior of the composite for its entire service life experimentally. Normally, allowable experimental test time would range from few hours to few days, as shown in *Figure 2.6*. The data beyond this experimental time window is generated using an accelerated characterization and superposition principle, known as Time-Temperature Superposition Principle (TTSP). According to this principle, creep compliance at a service temperature (T_{service}) for a time beyond the experimental time window (e.g. creep for the period of 5-10 years in *Figure 2.6*) can be generated within experimental time window by testing at temperatures higher than T_{service} [30]. These experimental creep data at temperatures T_1 to T_5 are then shifted horizontally along the time axis to superpose to yield the creep compliance curve at T_{service} , beyond the experimental time window, as shown in *Figure 2.6*. This shifting procedure assumes that the shape of the creep compliance curve (i.e. creep mechanism) does not change in the temperature range of T_{service} to T_5 . The shift factor (a_T) is defined as the ratio of the time (t) to reach a particular value of compliance/modulus at some higher temperature (e.g. T_3 in *Figure 2.6*) to the time (t_R) to reach the same compliance/modulus value at a reference temperature (T_{service}).

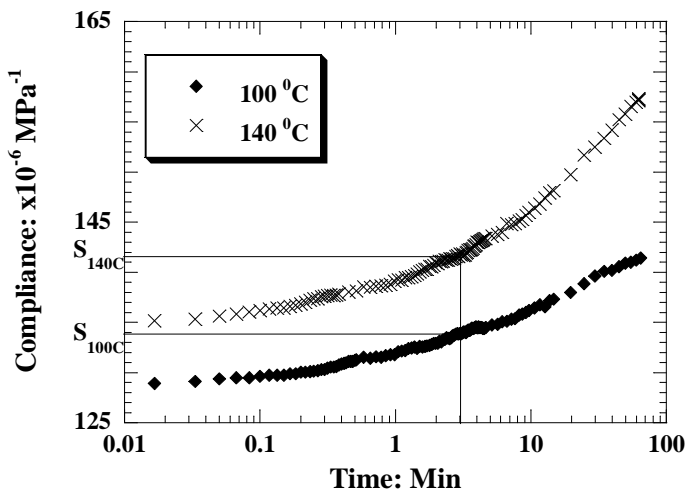


Figure 2.4: Effect of temperature on compliance of $[90]_8$ composites at a stress level of 10 MPa.

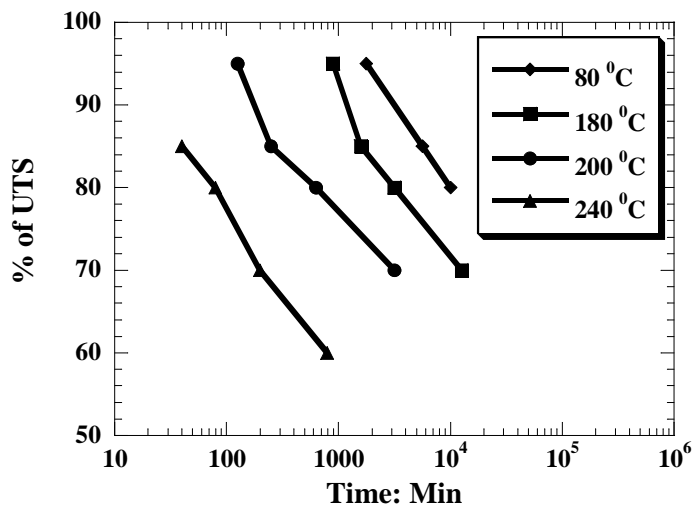


Figure 2.5: Effect of temperature and stress on creep-rupture time of $[90]_{12}$ composites [4].

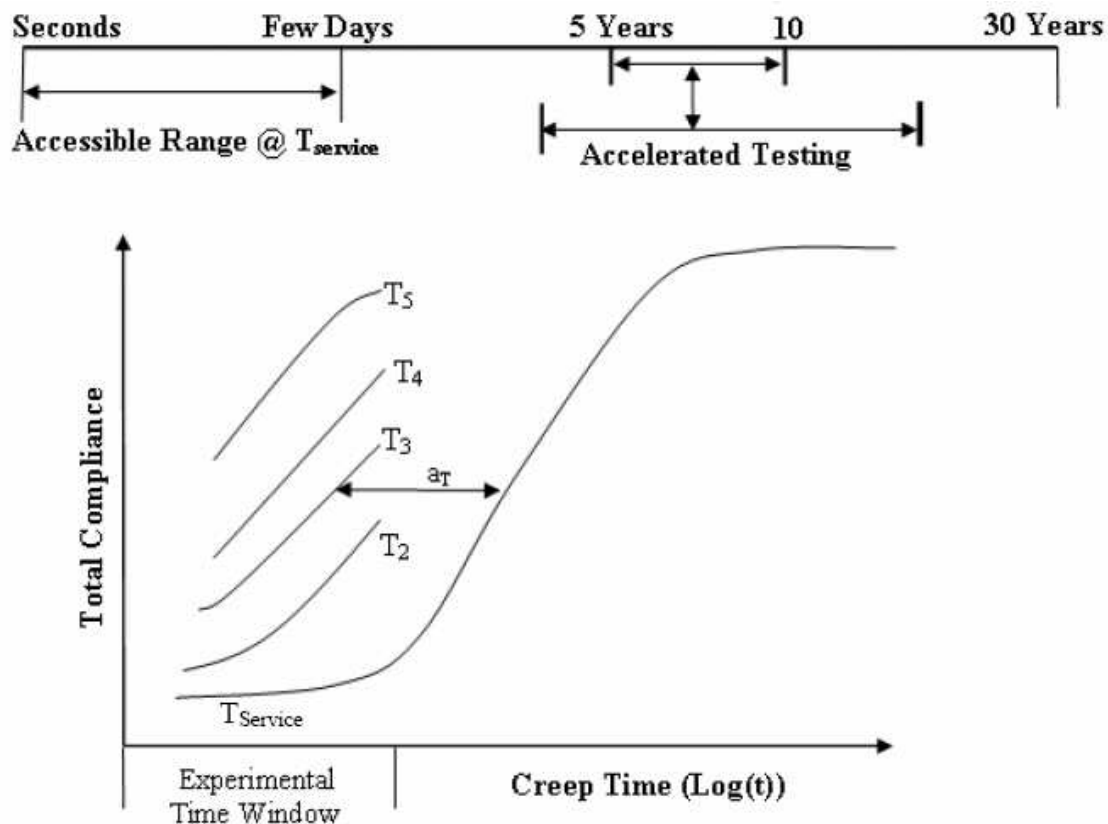


Figure 2.6: Time-Temperature Superposition Principle (TTSP) for long-term creep characterization.

$$a_T = \frac{t}{t_R} \quad (2.1)$$

The shift factor is temperature dependent and can be expressed using the Arrhenius equation for temperatures below the glass-to-rubber transition temperature of the polymer (T_g ; this is a temperature below which a polymer behaves like a brittle material and above which it behaves like a rubber):

$$a_T = A_0 \exp\left[-\frac{\Delta H}{RT}\right] \quad (2.2a)$$

In terms of $T_{\text{reference}}$, it can be expressed as,

$$a_T = \exp\left[\frac{\Delta H}{R}\left[\frac{1}{T_{\text{ref}}} - \frac{1}{T}\right]\right] \quad (2.2b)$$

where,

A_0 - Pre-exponential constant; ΔH - activation energy (J/mole)

T - Service temperature (K); T_{ref} - Reference temperature (K)

R - gas constant (8.314 J/K.mole)

This principle is used in this study to obtain creep data beyond the experimental time window.

2.2.2.2 Effect of Stress

Similar to temperature, an increase in stress accelerates the creep rate of PMCs resulting in increase in creep compliance as shown in *Figure 2.7*, and reduction in creep rupture time as shown in *Figure 2.5*. The creep behavior of a polymer matrix and its composites may be independent of the applied stress, and this is known as linear creep. Alternatively, the creep behavior may be a strong function of the applied stress and this is

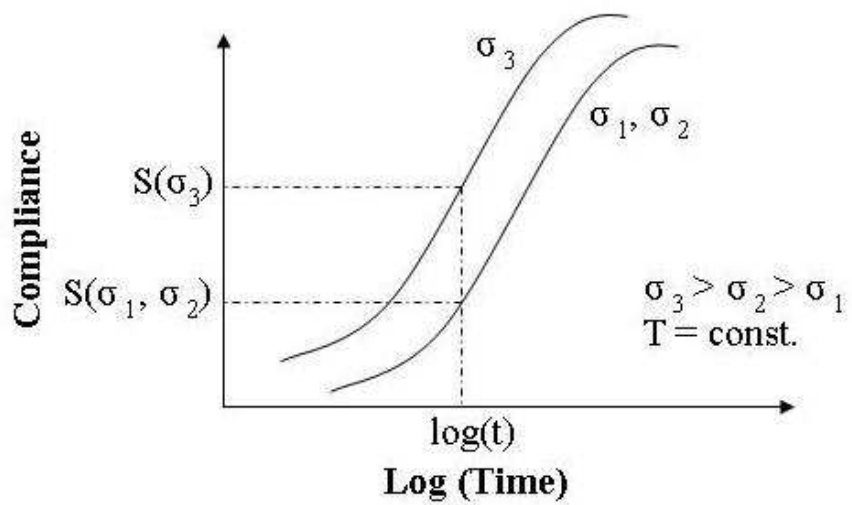


Figure 2.7: Effect of stress on creep of polymer matrix composites.

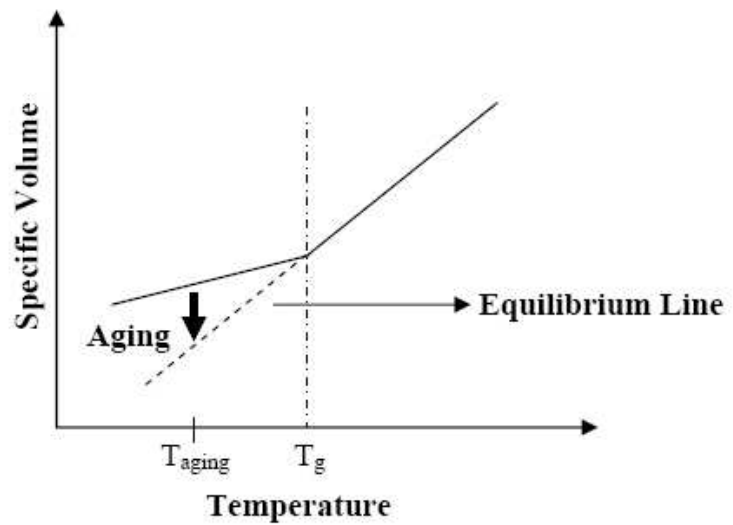
known as non-linear creep. This difference in creep behavior can be easily differentiated by plotting the creep compliance as a function of creep time at different stress levels. Since the compliance is defined as the ratio of creep strain to applied constant stress ($S(t) = \varepsilon(t)/\sigma$), the creep compliance would not increase with increase in stress, and the compliance curves would superimpose at those stress levels for which the material is *linearly viscoelastic*. In *Figure 2.7*, creep curves at stresses σ_1 and σ_2 superpose and hence, creep is linear at or below these stress levels. However, the creep compliance curves at various stress levels would not superpose if the material is *nonlinearly viscoelastic*. In *Figure 2.7*, creep curves at σ_2 and σ_3 do not superpose as the material's creep becomes nonlinear at stress levels above σ_2 . A previous study conducted by researchers of the Composite Structures & Research Group at the University of Manitoba, on Hexcel Corporation's F-263 epoxy resin and its composites (which are used in this study) shows that the compliance curves superpose up to 5MPa stress, while they deviate above 5MPa [4, 5]. Therefore, the PMC used in this study exhibit linear creep up to 5MPa and nonlinear creep above 5MPa.

The effect of stress on creep was modeled by Yeow et.al. [31] using a superposition methodology, known as Time-Stress-Superposition Principle (TSSP), that is similar to TTSP. Creep curves obtained at different stress levels and at a constant temperature are shifted horizontally to a reference stress value with respect to the time. Here, a shift factor (a_σ) is defined as the ratio of the time (t) to reach a particular value of compliance/modulus at some higher stress to the time (t_R) to reach the same compliance value at a reference stress level. Later, Griffith [32] proposed Time-Temperature-Stress-Superposition Principle (TTSSP) combining TTSP and TSSP together. A more detailed

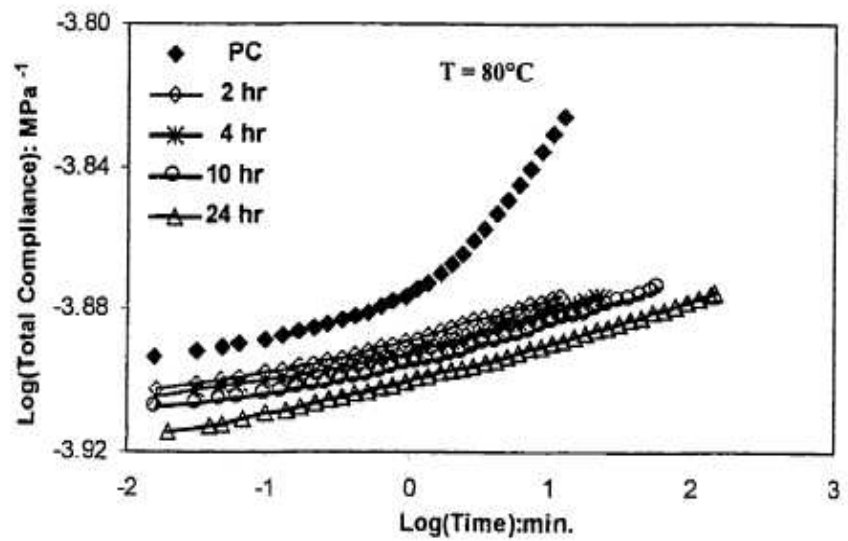
discussion on this procedure can be found in references [33, 34]. Another approach to model the effect of stress on creep of polymer matrix composites is Shapery's model [35]. This model is used in the present study and will be explained in detail in Chapter 4.

2.2.2.3 Effect of Physical Aging

When an amorphous polymer is heated above its T_g and then cooled rapidly to a temperature below T_g , the polymer will vitrify at T_g , i.e. the mobility of polymer chains will be severely restricted. The polymer will be in a thermodynamically non-equilibrium state below T_g and will be manifested as a deviation in the measured specific volume, away from the equilibrium volume, as illustrated in *Figure 2.8a*. When this polymer is held at a constant temperature (T_{aging}), it will slowly approach the thermodynamic equilibrium state and the specific volume in *Figure 2.8a* will decrease with time. This process of slow evolution towards an equilibrium state is known as *Physical Aging* [36], in contrast to the chemical aging, where additional cross-linking of polymeric chains occurs with time. The mechanical properties of the polymer would change due to physical aging. The polymer would become stiffer and more brittle with increase in time due to physical aging. In other words, the compliance of the polymer would decrease and the modulus would increase with aging time. The effect of physical aging on creep of [90]₈ composites tested at 5MPa is shown in *Figure 2.8b*. An increase in physical aging time decreases the creep compliance and creep rate at a given stress and temperature. Additionally, the physical aging causes increase in brittleness of the polymer matrix resulting in decrease in creep rupture time at a given stress and temperature when compared to the creep rupture time of a non-aged sample at the same stress and temperature.



(a)



(b)

Figure 2.8: Effect of physical aging [4].

An experimental method to quantify the effect of physical aging was proposed by Struik [36]. According to this method, a series of short term creep tests (also known as momentary creep test) are conducted for the test duration less than or equal to $1/10^{\text{th}}$ of the aging time. This short time period is suggested to avoid any aging during the test. Creep curves obtained at different aging time are shifted horizontally along the time axis to get a momentary master curve. By plotting the aging time shift factors (a_{ta}) as a function of aging time, a shift rate (μ) is calculated from the slope of the plot, which is given as [36],

$$\mu = -\frac{\partial \log a_{ta}}{\partial \log t_a} = \text{Shift rate} \quad (2.3)$$

and,

$$a_{ta} = \left(\frac{t_{a\text{ref}}}{t_a} \right)^\mu \quad (2.4)$$

This shift rate has been found to be dependent on temperature [37, 38]. Using the aging shift factor, the creep compliance of a polymer composite can be calculated at any aging time subjected to an arbitrary level of physical aging (t_a) using the creep compliance at a reference aging time ($t_{a\text{ref}}$) according to equation 2.5,

$$S(t_a) = S(a_{ta} t_{a\text{ref}}) \quad (2.5)$$

This equation predicts momentary creep response due to aging very well. However, for a creep time beyond the aging time, it over predicts the creep response, since it does not consider any decrease in creep rate due to physical aging occurring during the creep test. In order to account for this, Struik [36] proposed a modified theory

known as Effective Time Theory (ETT) considering the effect of physical aging during creep. Thus, at any given creep time (t), the shift factor will be expressed as,

$$a_{ta}(t) = \left(\frac{t_{aref}}{t_a + t} \right)^{\mu} \quad (2.6)$$

and, thus the creep compliance at any given creep time will be,

$$S(t) = S(a_{ta}(t)t_{ref}) \quad (2.5)$$

where, t_{ref} is the reference creep time.

Although most of the published studies on the effect of physical aging on creep of polymer matrix composites were focused on the linear viscoelastic creep [4], published work on the effect of physical aging on nonlinear creep as well as on creep rupture of polymer matrix composites is very limited [4, 36].

2.2.2.4 Effect of Moisture Content

Similar to temperature and stress, moisture also accelerates creep and creep rupture in polymers and polymer matrix composites. Diffusion of moisture plasticizes the polymer matrix, decreases its glass-transition temperature (T_g), and increases its specific volume. This, in turn, increases the creep rate as well as creep of the polymer and reduces its creep rupture time. A previous study on unidirectional composites has shown that the creep response of moisture conditioned composite at a lower temperature (T_2) is equal to the creep of a dry composite at a higher temperature (T_1) [4, 5]. It was found that the difference between test temperatures of a dry and wet sample ($T_1 - T_2$) is equal to the decrease in glass transition temperature ($T_{g,DRY} - T_{g,WET}$) due to plasticization of polymer matrix.

$$T_1 - T_2 = T_{g,DRY} - T_{g,WET} \quad (2.6)$$

It was also observed that the effect of moisture on the nonlinear creep is more than on linear creep. Physical aging limited the extent of plasticization when compared to a non-aged polymer and hence, reduced the creep rate [4]. It was also found that the presence of moisture decreased the creep rupture life of an epoxy resin and its composites when compared to the creep rupture life of a dry resin and its composites [4, 5].

2.2.2.5 Combined Effect of Temperature, Stress, Physical Aging and Moisture

In real life applications of polymer matrix composites, all service environmental parameters (temperature, stress, physical aging, and moisture) are present together. Hence, it is possible that one factor can affect the influence of other factor on creep and creep- rupture. While most of the published studies are limited to discussion of one or two of these parameters, a study on the interactive effect of all four parameters was conducted by the Composites Structures and Research Group at the University of Manitoba for unidirectional composites and its polymer matrix [4, 5]. This study demonstrated that the creep and creep rupture under combined effect of all these four parameters is entirely different and can not be predicted by just adding the individual effect.

As mentioned before, only the effects of temperature and stress are focused in the present study.

2.3 Published Studies on Creep & Creep rupture of Woven Composites

2.3.1 On Creep

Published literature on creep of polymer matrices, unidirectional and multidirectional non-woven composites is extensive and a detailed review can be found in references [4, 5]. However, the published literature on creep of polymer matrix woven composites is very limited. There are very few research groups around the world who have studied creep of woven composites [29, 39- 49]. These are summarized in *Table 2.1* and a detailed discussion on each of them is provided below.

Govindarajan et al. [39, 40] investigated the tensile creep behavior of plain weave graphite/ epoxy woven composites under on-axis loading through experimental study and analytical modeling. Tensile creep experiments were conducted at two different stresses (125 and 200MPa) and at three different temperatures (22, 65 and 93 °C) for a time period of 5 hours. The experimental results showed a small increase in creep strain. A maximum of 300microstrains was observed after 5.5 hours at 200MPa stress and 93 °C. The crimp model developed by Ishikawa and Chou [50] for predicting time-independent elastic properties of woven composites was extended to develop the creep model. This model used the elastic properties of the fibers and the creep of the polymer matrix, which was modeled using a Maxwell-Voight mechanical analog model. The effect of temperature on the creep of the matrix was modeled using the Arrhenius equation. The parameters of the creep model for the polymer matrix were obtained by fitting the experimentally measured creep data for the composite. The developed creep model fitted the experimental data well. However, the predictive capability of the model within and beyond experimental time frame (> 5.5 hours) was not evaluated. The effect of stress and

Table 2.1: Summary of published literature on creep of woven composites.

Reference	Weave type	Parameters Studied/ Considered	Experimental Analysis	Theoretical Analysis
Govindarajan, Langrana, Weng ^{39,40} (Rutgers University, USA)	Graphite/ epoxy plain weave fabric	Creep, effect of temperature	Yes	Yes
Shrotriya, Sottos ^{20, 41-43} (University of Illinois, USA)	Glass fiber/ epoxy, plain weave fabric	Creep and stress-relaxation behavior	Yes	Yes
Bathgate et.al ^{44, 45} (Australia) Pang & Wang ⁴⁶ (Australia)	Hybrid plain weave (glass, carbon/ epoxy)	Creep, effect of temperature and through-the-thickness stitching	Yes	No
	Hybrid plain weave (glass, carbon/ epoxy)	Creep, effect of through-the-thickness stitching	No	Yes
Gupta et. al. ^{47, 48} (University of Missouri-Rolla, USA)	5H satin woven composite	Long-term mechanical behavior	No	Yes
Ahcí & Talreja ²⁹ (A & M University, USA)	8H satin woven composite	Creep-recovery, damage	Yes	Yes

microstructure on the creep behavior of woven composites was not focused.

Shrotriya & Sottos [20, 41] characterized creep and stress-relaxation of plain weave glass/epoxy composite substrate for multilayer circuit board applications using a Dynamic Mechanical Analyzer (DMA). This composite had different crimp parameters and fiber volume fraction in fill and warp directions. Flexural creep compliance of neat resin was measured under 3-point bending at 1MPa for 20 minutes in the temperature range of 45- 135 $^{\circ}$ C. Tensile creep compliance of woven composite was measured in warp and fill directions using the DMA at 10MPa for 20 minutes and at temperatures ranging from 30 to 160 $^{\circ}$ C. Creep compliance data was shifted using TTSP to obtain a master creep curve extending to 10^{10} minutes. Creep compliance in the fill direction was significantly higher than creep compliance in the warp direction due to lower fiber volume fraction in the fill direction. Creep response of the composite was modeled using two different micromechanical models based on equivalent laminate model (EQLAM) and curved beam model, described in reference [41]. In EQLAM model, the woven composite was considered as an equivalent three-ply cross-ply laminate. The warp and fill yarns were separated and represented as three individual plies. These plies were arranged as a symmetric cross-ply laminate with a fill ply sandwiched between two warp plies with a thickness that is of 50% of the thickness of the fill ply. Properties of each ply were calculated using the fiber and the matrix properties utilizing micromechanical relationships developed using the self-consistent field model [51], similar to the efforts of Govindarajan et al. [39]. The properties of the equivalent cross-ply laminate were then obtained using classical lamination theory. Curved beam model was a one-dimensional model, where the woven fabric was separated into longitudinal (fill) and transverse

(warp) fibers. The fill fiber was modeled as wavy layer while the warp fiber and the matrix were modeled as a layer with homogenized properties, which were calculated using micromechanical relationships [51]. The properties of undulated fiber layer embedded in a homogenized layer were calculated using Lee and Harris model [52]. The time-dependence of the polymer matrix was obtained by fitting the experimental creep data to a prony series equation. Although the instantaneous modulus of the woven composite, predicted using these models, was close to the experimental value, the creep of the composite was under-predicted. Subsequently, a two-dimensional finite element model [42] and a three-dimensional finite element model [43] were also developed. However, there were significant differences between the simulated and experimental creep results. Effect of stress and microstructure on the creep behavior of woven composites was not focused.

An experimental investigation on creep of woven composites was conducted by *Bathgate et al.* [44, 45]. They studied the effect of temperature and through-the-thickness stitching on creep of carbon/glass fiber epoxy woven composites at temperatures of 35, 55 and 70 $^{\circ}\text{C}$ and stress levels of 30, 50 and 70 MPa. Creep strain was found to increase with increase in temperature and stress. Short-term creep data (33 hours) obtained for stitched and unstitched composite was shifted using Time-Temperature-Stress Superposition Principle (TTSSP) to obtain master creep curves for a longer time extending to 2 years. The vertical and horizontal shift factors were obtained by fitting the experimental creep data with Findley's equation. Subsequently, *Pang & Wang* [46] proposed a mechanistic creep model for woven composites. In this model, the change in waviness of the fill fibers with time was related to the creep of woven composites. A

relationship was developed to calculate the total creep in the composite using time-dependent change in undulation of the fiber and viscoelastic properties of the matrix. Predicted creep results compared well with experimental creep results obtained at room temperature for a time period of 80 hours. However, application of this model is limited to on-axis loading only and cannot be generalized to predict creep behavior under the off-axis loading. With the exception of undulation in the yarn, the effect of other microstructural features was not considered.

Gupta et al. [47, 48] developed a micromechanics based model to characterize the out-of-plane creep properties of 5H satin weave composites. Out-of-plane properties were determined using a finite element model. In-plane properties were considered to be time-independent due to dominance of fibers and were determined using the model developed by Raju & Wang [53]. However, other researchers have shown that in-plane properties of woven composites are also time-dependent [39-45]. Similar trend was also observed in the present study. Out-of-plane compliance was considered to be dominated by the matrix response. Schapery's nonlinear viscoelastic model was used to model the creep of the matrix and incorporated within the FEM model to predict the out-of-plane creep of the composite. Physical aging of the matrix was also included using effective time theory, proposed by Struik [36]. Numerical results were presented for out-of-plane creep compliances of satin weave composite in linear and nonlinear viscoelastic range for a time period of 40 years. However, their predictions were not validated with experimental data. They also studied the effect of various nesting (i.e. phase shift) configurations on out-of-plane properties through predictions.

Achi and Talreja [29] characterized the damage and creep of 8-harness satin weave carbon fiber/ polyamide resin at high temperatures, experimentally and by finite element modeling, under on-axis loading. The creep-recovery tests were conducted at 371 °C in the linear and nonlinear stress range of 75- 345MPa (up to 60% UTS). The composite was found to develop matrix cracking above 170MPa (30% UTS) stress. A thermodynamics based model for nonlinear creep of the composite with damage was developed using finite element method. The satin weave composite was idealized as equivalent cross-ply laminate with equally spaced transverse cracks in transverse plies of the laminate. The idealized laminate was used for finite element analysis. The comparison of model results with experimental results was not presented here. Effect of microstructure on creep was not considered.

2.3.2 On Creep- Rupture

To the best knowledge of the author, there has been only one published study on creep rupture of woven composites. Creep- rupture behavior of E-glass/carbon epoxy hybrid woven composites was studied experimentally by *Pang & Wang* [54]. They studied the effect of through-the-thickness stitching on creep rupture properties. Tests were conducted at stress levels in the range of 85-95% of ultimate tensile strength (UTS) of the composite at two temperatures, at ambient and 80 °C. It was found that through-the-thickness stitching improved rupture life. There are no published studies on modeling of creep rupture of woven composites.

2.4 Summary & Limitations of Published Studies on Creep & Creep rupture of Woven Composites

Based on the above literature review, it can be concluded that:

- Creep of woven composites has been studied by few researchers experimentally within experimental time periods of few hours to few days. Applying TTSP, some of these studies have generated master curves extending beyond the experimental time window to 2 years [44] and beyond 30 years [41] were obtained.
- With the exception of two studies that accounted for the effect of microstructure on creep [46, 47], none of the previous research focused on the effect of microstructural features on creep.
- A systematic study of the influence of various service environmental factors (temperature, stress, physical aging and moisture) is lacking. The previous studies have mostly focused on the experimental investigation of the effect of temperature with the exception of one study each on the effect of stress, physical aging and moisture. Knowledge on the combined effect of temperature, stress, physical aging and moisture on creep of woven composites is lacking.
- Various creep models developed in the past for the prediction of creep of woven composites under on-axis loading are modified crimp model, EQLAM, curved beam model, and FEM models. All of them used the elastic properties of the fiber and creep properties of the matrix to predict the creep of woven composites. These models were either not validated using experimental data or validated only for the experimental time window of few hours to few days. The maximum

difference between experimental data and predictions were found to be up to 15-20 %.

- These models did not simulate the effect of stress on creep of woven composites and validate the simulation.
- Creep of woven composites under off-axis loading has not been studied. Practically, multidirectional woven composite structures are normally made up of layers, in which, the orientation of fibers with respect to the loading axis will differ from layer to layer. All of the published studies have focused on creep of woven composites under on-axis loading only, parallel to either warp or fill fibers. Hence, creep of woven composites under off-axis loading is very important for practical applications.
- With the exception of one experimental study [54], there is no other experimental or theoretical study on creep rupture of woven composites.
- Experimental and theoretical study of creep and creep- rupture of multidirectional woven composites is lacking.

2.5 Thesis Objectives

It is obvious from previous section 2.4 that a number of knowledge gaps exist in the area of creep and creep rupture of woven composites. However, all of the knowledge gaps cannot be focused in one Ph.D. thesis work. Hence, only creep of woven composites was focused in this thesis. Specific objectives of this thesis, in this focus area, are:

1. To develop a model, extending the existing knowledge in the literature, to predict creep of plain weave polymer matrix woven composites, subjected to loading at varying orientations to the warp or fill fibers.
2. To experimentally study the creep of plain weave polymer matrix woven composites, subjected to tensile loading at an angle of 0^0 and 45^0 to the fill/ warp fibers, in a wide range of temperatures and stresses covering both linear and nonlinear creep.
3. Validation of a model, developed in objective 1 using data in objective 2 in both within and beyond experimental time window.
4. Study parametrically and develop an understanding of the effect of various microstructural features on the creep of plain weave polymer matrix woven composites.

2.6 Research Approach

Unlike previous studies, this thesis developed a creep model to predict creep of plain weave composites *using the experimental creep data for unidirectional composites, for any orientation of the load with respect to fill/ warp fibers*. The experimental creep data for unidirectional composites, generated in the linear region by previous researchers of the Composite Materials & Structures Research Group at the University of Manitoba, was augmented by additional tests by the author of this thesis in the nonlinear region. This data was modeled using Schapery's nonlinear model and used in the model for the creep of woven composites.

In order to validate the creep model for plain weave composites developed in this study, experimental tensile creep data using carbon fiber/epoxy plain weave composites, loaded at 0^0 and 45^0 to the warp fiber was generated in a wide range of temperatures and stresses. These data were used to validate the model predictions within the experimental time window. A master curve at a reference temperature, extending many decades of time, was generated by applying TTSP to the experimental creep data and was used to validate the predictive capability of the model beyond the experimental time window.

Finally, a systematic parametric study was completed to understand the effect of various microstructural features on the creep of plain weave composites.

3. MODEL FOR CREEP OF PLAIN WEAVE POLYMER COMPOSITES

3.0 Introduction

In this chapter, an analytical model, developed to simulate the creep of plain weave polymer composites, under in-plane tensile loading, is presented. Using this model, the creep of plain weave composites was predicted using the creep of unidirectional composites, obtained experimentally. A MATLAB program was written for simulation. The creep model and MATLAB program are described in this chapter.

3.1 Published models for *time-independent* properties of woven composites

Several modeling methodologies have been developed to simulate the *time-independent* elastic properties of woven composites by previous researchers [18, 20, 41, 50, 53, 55-58, 60-62]. These methodologies, summarized in *Figure 3.1* can be generally categorized as either analytical or numerical. In this thesis, an analytical modeling approach is used.

In published analytical models, the complex woven structure of the composite is idealized into a simple representative repeat unit cell, made up of unidirectional non-woven laminae. The properties of the idealized repeat unit cell are calculated using either a lamination theory based approach or a non-lamination theory based approach. The properties of the unidirectional tape (non-woven) lamina used in these models are

Models for Time- independent properties of woven composites

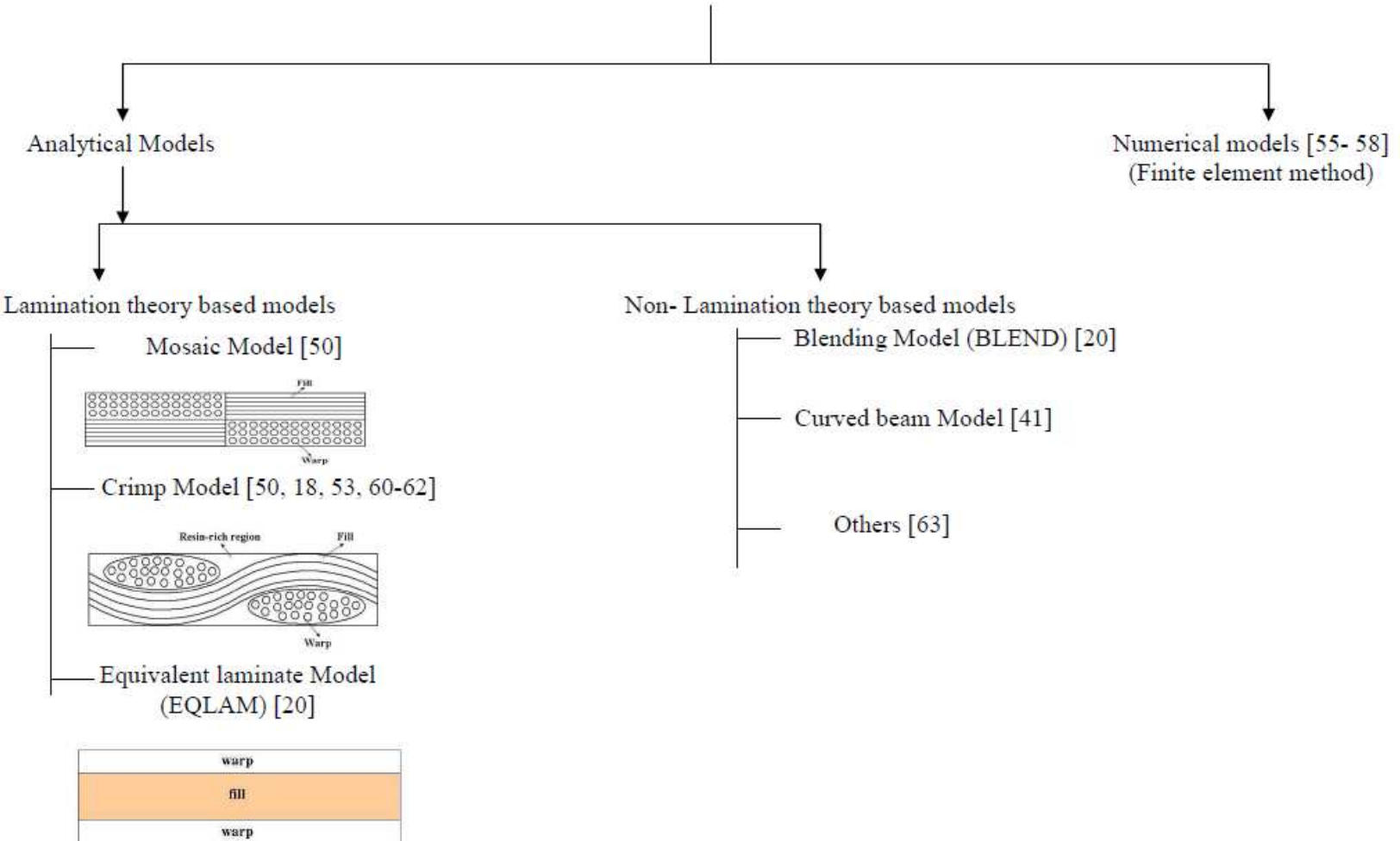


Figure 3.1: A flow chart on time-dependent models for woven composites.

calculated using the time-independent properties of fiber and resin, and modified rules of mixtures. These are subsequently used along with lamination model or other micromechanical relationships (such as Halpin-Tsai equations, curved beam model, volume averaging method) to determine the properties of the unit cell.

The various lamination theory based models are the mosaic model, the crimp model and the equivalent laminate model. In the mosaic model [50], the woven composite laminate is considered to be an assembly of cross-ply laminates, ignoring the undulation of fibers in a woven composite. The properties of unidirectional laminae are used to calculate the properties of cross-ply laminate using the classical lamination theory [64]. The crimp model [50] considers the undulation of the fibers. This is a one-dimensional model, where undulation is considered only in one direction. The properties of the unidirectional non-woven laminae and the undulation geometry are used along with the classical lamination theory to simulate the properties of woven composite laminate. Further extensions of the crimp model have been proposed [18, 53, 60-62] by considering the undulation in both the fill and the warp directions, i.e. a 2-D model. The equivalent laminate model (EQLAM), proposed by Sottos et al. [20], considers the woven composite to be a three-ply laminate, wherein the fill ply is sandwiched between two warp laminae (also known as plies). The undulated fill and warp plies are idealized as an equivalent lamina consisting of plies with straight fibers and angle fibers. The properties of the equivalent fill and warp plies are calculated using fiber and resin properties and a micromechanical relationship developed by Whitney and McCullough [51]. The classical lamination theory is then employed to predict the properties of the equivalent laminate using the lamina properties. While this model applies the lamination

theory to the entire unit cell, the models discussed above apply the lamination theory to infinitesimal segments of the idealized unit cell and sums their properties to obtain the properties of the unit cell. The predicted instantaneous moduli using EQLAM model compares well with experimental moduli of glass/epoxy fabric, than the predicted moduli obtained using the crimp model.

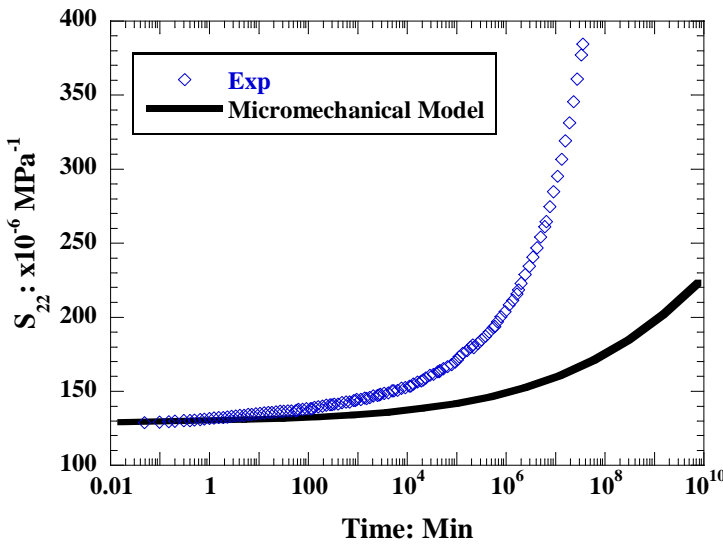
Non-lamination theory based models are the blending model and the curved beam model. In the blending model (BLEND) [20], the properties of fill and warp plies are calculated first, similar to the case for EQLAM. However, instead of using the lamination theory, the properties of the equivalent laminate (as described previously for EQLAM) are calculated using micromechanical relationships. The longitudinal properties of the equivalent laminate are calculated using the rules of mixtures, while the transverse properties of equivalent laminate are calculated using the Halpin-Tsai relationship. In the case of the curved beam model, the longitudinal fibers are modeled as a wavy layer, while the transverse fibers and polymer matrix are modeled as a homogenized layer in which the wavy fibers are embedded. The instantaneous moduli, predicted by Lee and Harris [52] using the curved beam model are found to be consistent with experimental results. Another model presented by *Hahn & Pandey* [63] calculates the time-independent moduli of plain weave fabric using volume averaging method for ceramic matrix composites.

In addition to analytical models, several numerical models have also been developed based on the finite element method [55-58] to calculate time-independent properties of woven composites. Accuracy of prediction of these models were no better than that of analytical models. However, the analytical models are relatively easier and

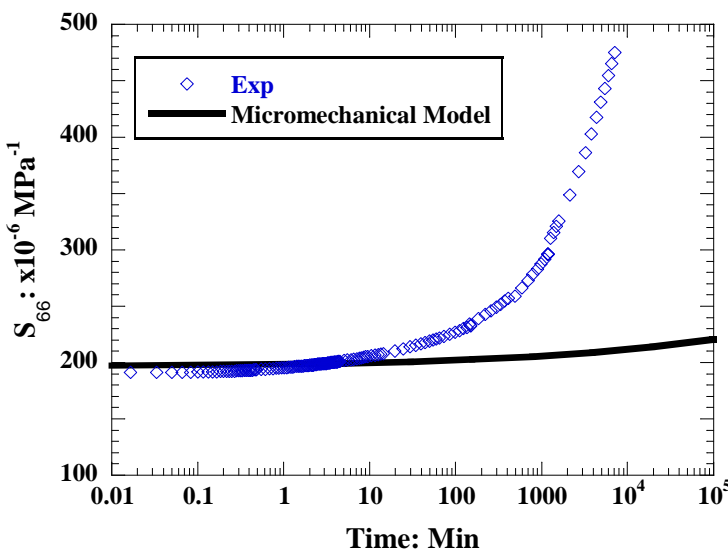
user friendly than FEM – based models since the latter requires substantial experience and knowledge to minimize the effect of various solution parameters such as element type, mesh density, representative volume size on the quality and accuracy of solution. Additionally, the analytical models are more physics based than numerical models; hence, the numerical modeling method is not considered in this thesis.. Hence, a detailed review of these models is beyond the scope of this chapter.

3.2 Published models for *time-dependent* properties (creep) of woven composites

The models discussed in the previous section developed to calculate *time-independent* properties of woven composites have been extended to calculate *creep* of woven composites by several researchers [39- 49], as discussed in Chapter 2. In lieu of time-independent properties, creep of unidirectional tape lamina were used in these models. There are two possible approaches to obtain the creep of unidirectional lamina. One approach involves the use of the elastic properties of fiber, creep of resin, and micromechanical models. The second approach is to determine the creep of unidirectional lamina, experimentally. Previous creep models [39- 49] have adopted the first approach. None of the published studies were found to adopt the latter approach. As a part of this thesis work, efforts were made to simulate the creep of unidirectional lamina using elastic properties of fiber and creep of resin by employing a modified rule of mixtures [51]. The predictions are compared with experimental transverse and shear compliance of the unidirectional lamina in *Figures 3.2a and b*. The predictions were significantly different from the experimental results in terms of both magnitude and curvature. This indicates that this approach will lead to erroneous creep predictions for plain weave composites. Hence, the second approach was used in this study. The superiority of second approach



(a)



(b)

Figure 3.2: Comparison of (a)transverse and (b) shear creep compliance for unidirectional composites obtained experimentally and through simulation using modified rules of mixtures at 5MPa and 80 °C.

over first approach is further discussed in Chapter 5, Section 5.4.3. Although, similar micromechanical relationships, using first approach, have been employed to calculate creep of unidirectional composites by several researchers [65-70] in the past, the model predictions are validated only for a short time period ($< 10^4$ minutes or 7 days). It can be inferred from *Figures 3.2a* and *b* that the long-term creep of unidirectional composites cannot be predicted accurately using micromechanical models. Hence, this approach was not adopted in the current work. Instead, the creep of unidirectional composites was obtained experimentally and used to predict creep of plain weave composites. The creep model developed as a part of this thesis work is presented below.

3.3 Modified Equivalent laminate model (MELM) for creep of plain weave composites

An analytical model is presented in this section to simulate the creep of plain weave composites under in-plane tensile loading. A schematic of a plain weave fabric lamina is shown in *Figure 3.3*. The lengthwise direction of the fabric is usually referred to as ‘warp’ and the widthwise direction of the fabric is referred to as ‘fill or weft’. Hence, the fibers along the warp and fill directions are known as warp fibers and fill fibers, respectively. It can be inferred from *Figure 3.3* that a plain weave fabric lamina can be constructed by stacking a repeating unit-cell side by side. Hence, the creep of the plain weave composites may be simulated by predicting the creep of this representative unit cell shown in *Figure 3.3*. While defining such a representative unit cell is possible for loading along either fill or warp directions (on-axis loading), identifying one for loading at an angle to either fill or warp directions (off-axis) is not possible [71].

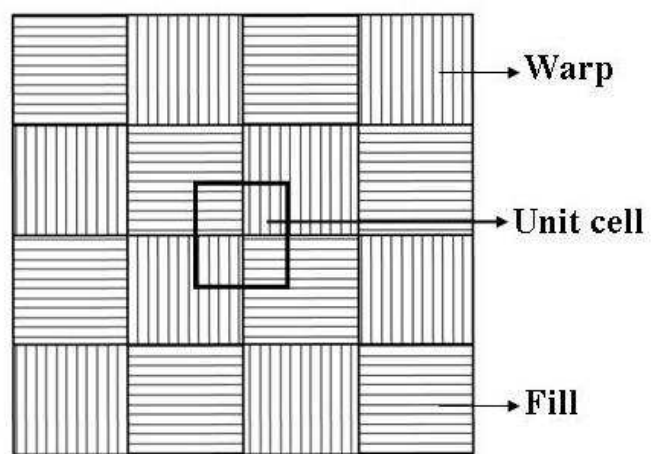


Figure 3.3: Plain weave fabric.

Numerical modeling may be one approach to predict creep of plain weave composites for off-axis loading. Another approach is the equivalent laminate approach similar to the one proposed by *Shrotriya & Sottos* [41]. While these authors developed the equivalent laminate model (EQLM) for on-axis loading, the present study extended this approach and developed a creep model, modified equivalent laminate model (MELM) for both on-axis and off-axis loading, which is presented below. Additionally, while *Shrotriya & Sottos* [41] used the predicted creep compliance of the unidirectional lamina (using modulus of fiber, creep of resin, and micromechanical relationships developed by Whitney and McCullough [51]), in this thesis the experimentally measured creep data for unidirectional lamina is used.

3.3.1 Model assumptions

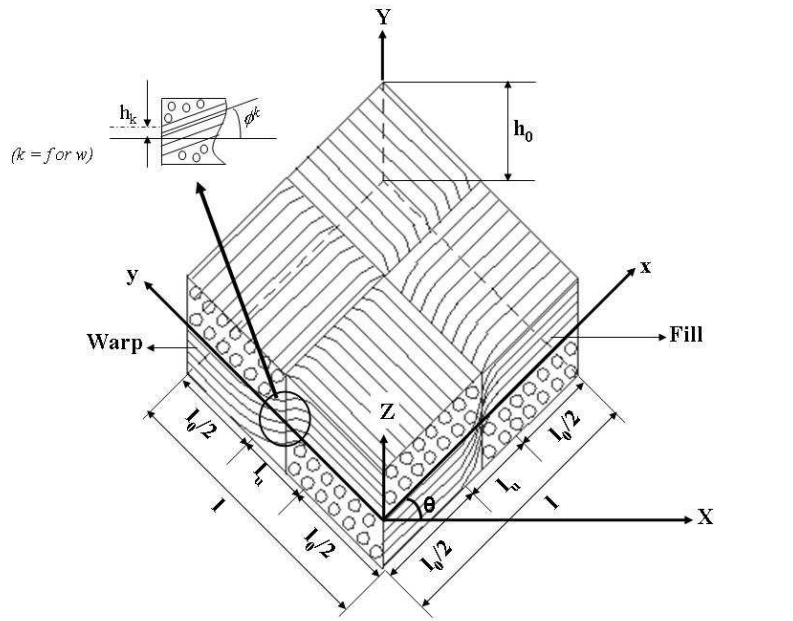
The assumptions of the creep model developed in this thesis are as follows. The impact of these assumptions on prediction is discussed in Chapter 5, Section 5.4.3.

1. The plain weave unit cell is assumed to be made of unidirectional laminae, interlaced orthogonally.
2. It is assumed that the creep of unidirectional lamina determined experimentally under uni-axial loading is applicable to determine the creep of the lamina under bi-axial state of stress within the laminate.
3. The unit cell is considered to have zero gap (refer to section 2.2.1.1). Hence, the average fiber volume fraction for the entire unit cell is assumed to be equal to the fiber volume fraction for the unidirectional lamina.
4. The undulation parameters in both fill and warp directions are considered to be same and this has been experimentally verified.

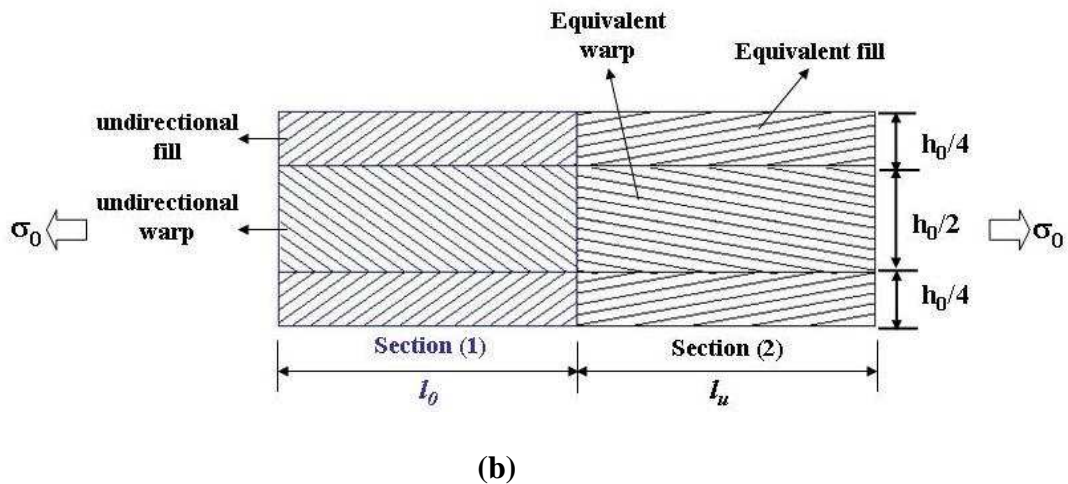
5. Since the measured creep strains are small, the undulation parameters are assumed not to change with time, temperature, and stress.
6. The composite is assumed to be an iso-phase plain weave laminate; i.e., the undulations in the various layers of the laminate are in-phase (refer to section 2.2.1.2). Since a single fabric lamina is difficult to test, a laminate made up of several layers of fabric lamina was tested in this research program. However, the orientation of each layer in the laminate, with respect to loading axis, is same.
7. Shear coupling (i.e. in-plane coupling between normal stress and shear strain and vice versa) is assumed to be absent.
8. In-plane – out-plane (tension – bending) coupling is also assumed to be absent.
9. The shape of the undulation in the unidirectional lamina (fill and warp) is assumed to be a sinusoidal.
10. The assumptions for classical lamination theory [64] are applicable to the current model.

3.3.2 Model Description

A schematic overview of MELM is presented in *Figure 3.4*. A 3-D representation of a unit cell is shown in *Figure 3.4a*. X,Y, Z represents global coordinate system (loading axes) and x, y, Z represents local coordinate system for the unit cell. The creep of this unit cell is determined using a 2-D section of an equivalent laminate shown in *Figure 3.4b*, consisting of two laminate sections in series. The laminate section (1) represents the straight portions of the fill and warp laminae i.e. sections of length $l_0/2$ in *Figure 3.4a*. The crimp section of length l_u in *Figure 3.4a* is replaced by an equivalent laminate, section (2). If the crimp geometry in *Figure 3.4a* is approximated to be sinusoidal, there



(a)



(b)

Figure 3.4: Schematic overview of modified equivalent laminate model (MELM) for predicting creep of plain weave composites.

will not be coupling between the in-plane and out-of-plane components (i.e. model assumption 8, $B_{ij} = 0$). In order to fulfill this requirement, the equivalent laminate in *Figure 3.4b* is considered to be symmetric. However, the volume fractions of warp and fill laminae in the equivalent laminate are same as that in the original unit cell.

The properties of the fill and warp laminae in section (1) correspond to the properties of the unidirectional laminae determined experimentally. The properties of the equivalent fill and warp laminae in section (2) correspond to an average of the properties of the crimp section of the fill and warp laminae shown in *Figure 3.4a*. The averaging procedure is presented later in this section. Applying lamination theory, given in *Appendix A*, the in-plane creep (ε) response of this equivalent laminate to an applied force per unit length (N_x), applied along X-axis, is given by equation 3.1,

$$[\varepsilon_{xy}(t)] = [a_{xy}(t)]^* N_x \quad (3.1)$$

where, $a_{xy}(t)$ is the compliance of the laminate given by,

$$[a_{xy}(t)] = \frac{[a_{xy}^1(t)]^* l_0 + [a_{xy}^2(t)]^* l_u}{l} \quad (3.2)$$

where, $a_{xy}^1(t)$ and $a_{xy}^2(t)$ are the compliance matrices for section (1) and section (2), respectively. l_0 and l_u are the lengths of section (1) and section (2), respectively, and l is the length of the equivalent plain weave laminate.

The determination of compliance matrices for section (1) and section (2) is described in the following sub-sections.

3.3.2.1 Determination of the compliance matrix for section (1) of composite laminate

A schematic overview to determine the compliance for section (1) is shown in *Figure 3.5*. Section (1) of the plain weave composite laminate is composed of

unidirectional laminae as fill and warp lamina. The compliance matrix for section (1), $a_{xy}^1(t)$, is determined as follows.

The stiffness matrix for unidirectional fill or warp lamina along its principal directions can be written as,

$$Q_{ij}^k(t) = \begin{bmatrix} E_{11}^k(t)/(1-\nu_{12}^k(t)*\nu_{21}^k(t)) & \nu_{21}^k(t)*E_{11}^k(t)/(1-\nu_{12}^k(t)*\nu_{21}^k(t)) & 0 \\ \nu_{12}^k(t)*E_{22}^k(t)/(1-\nu_{12}^k(t)*\nu_{21}^k(t)) & E_{22}^k(t)/(1-\nu_{21}^k(t)*\nu_{21}^k(t)) & 0 \\ 0 & 0 & G_{12}^k(t) \end{bmatrix}$$

(i, j = 1, 2, 6), (k = fill or warp) (3.3)

$E_{11}^k(t)$, $E_{22}^k(t)$, $G_{12}^k(t)$ are the time-dependent longitudinal, transverse and shear moduli of unidirectional lamina along its principle axes (1, 2, 6), respectively. $\nu_{12}^k(t)$ and $\nu_{21}^k(t)$ are the time-dependent Poisson's ratios of the unidirectional lamina along its principle axes (1, 2, 6). These properties were determined experimentally and discussed in Chapter 4.

The corresponding moduli of fill and warp laminae in the global coordinate system for a given angle of loading (θ) are obtained using a transformation matrix given by equation 3.4,

$$[T^k] = \begin{bmatrix} m^2 & n^2 & 2mn \\ n^2 & m^2 & -2mn \\ -mn & -mn & m^2 - n^2 \end{bmatrix}^k$$
(3.4)

where, $m = \cos \theta$; $n = \sin \theta$ for fill lamina, and, $m = \cos(90 + \theta)$; $n = \sin(90 + \theta)$ for warp lamina. The transformed moduli of fill or warp lamina is,

$$Q_{IJ}^k(t) = [T^k]^{-1} [Q_{ij}^k(t)] [T^k];$$
(3.5)

(I, J = X, Y, Z; i, j = x, y, Z)

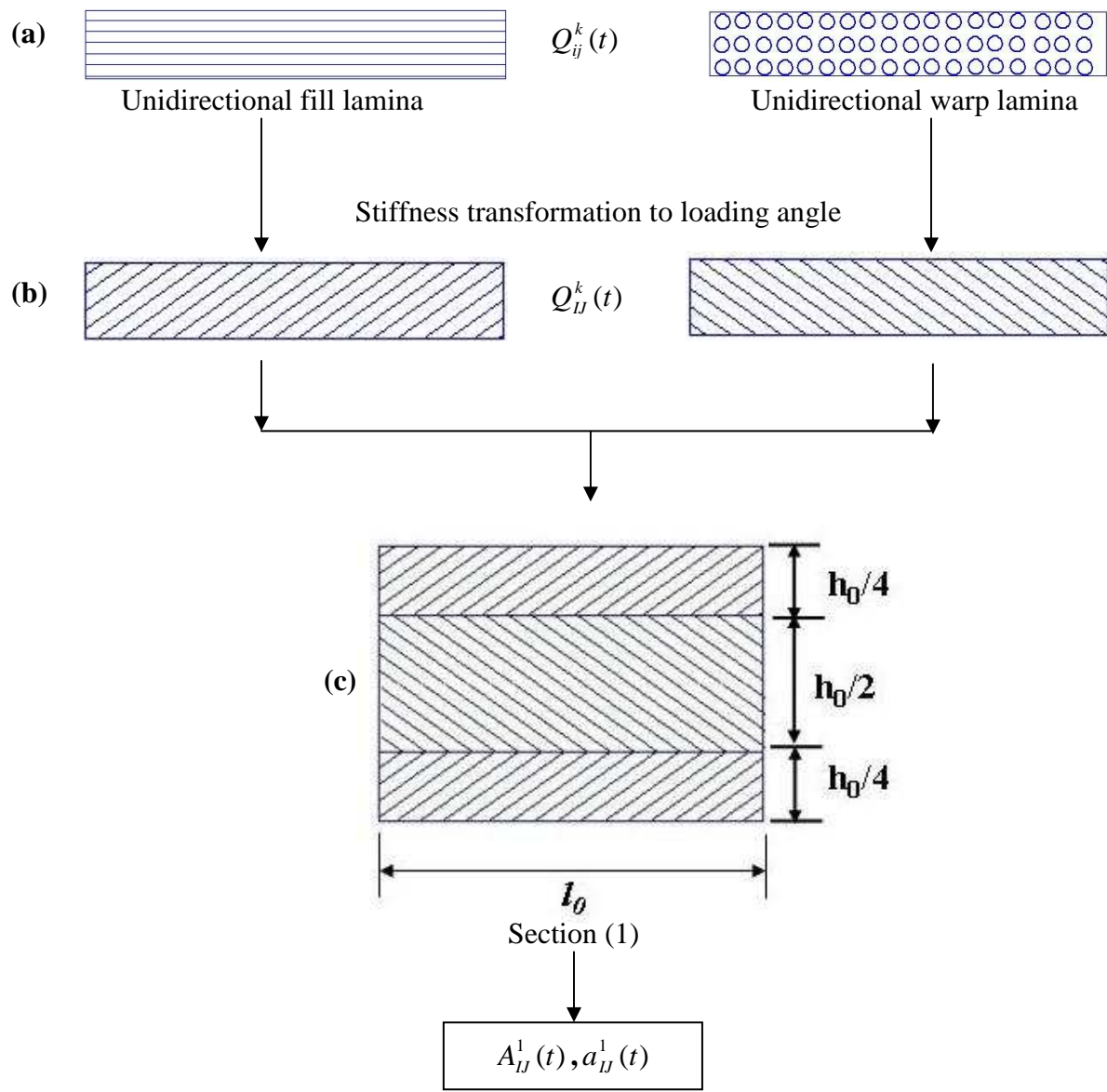


Figure 3.5: Schematic overview of section (1) laminate.

Using stiffness from equation 3.5 and classical lamination theory [64], given in *Appendix A*, the stiffness per unit width of the laminate, i.e. section (1) is determined as,

$$A_{IJ}^1(t) = \left[\frac{h_0}{4} (Q_{IJ}^{fill}(t)) \right]_a + \left[\frac{h_0}{2} (Q_{IJ}^{warp}(t)) \right]_b + \left[\frac{h_0}{4} (Q_{IJ}^{fill}(t)) \right]_c \quad (3.6)$$

By inverting equation 3.6, compliance matrix for the section (1) is obtained as,

$$[a_{XY}^1(t)] = [A_{XY}^1(t)]^{-1} \quad (3.7)$$

Using equation 3.7, all terms of the compliance matrix in equation 3.8, are determined and used in equation 3.2,

$$[a_{IJ}^1(t)] = \begin{bmatrix} a_{XX}(t) & a_{XY}(t) & a_{XZ}(t) \\ a_{YX}(t) & a_{YY}(t) & a_{YZ}(t) \\ a_{ZX}(t) & a_{ZY}(t) & a_{ZZ}(t) \end{bmatrix}^1 \quad (3.8)$$

3.3.2.2 Determination of the compliance for section (2) of composite laminate

Section (2) of the plain weave composite laminate is composed of equivalent unidirectional laminae - equivalent fill lamina and equivalent warp lamina. The compliance for section (2), $a_{XY}^2(t)$, is determined as follows.

Consider lamina and warp sections shown in *Figure 3.6a*, which are the undulated portions of length l_u , of fill and warp lamina in *Figure 3.4a*. ($h_0/2$) is the thickness of each lamina. The undulation shape of these laminae is defined by a sinusoidal function given in equation 3.9 and 3.10,

$$h_f = [1 + \sin\{(x - \frac{l_u}{2}) \frac{\pi}{l_u}\}] h_0 / 4 \quad (0 \leq x \leq l_u) \quad (3.9)$$

and,

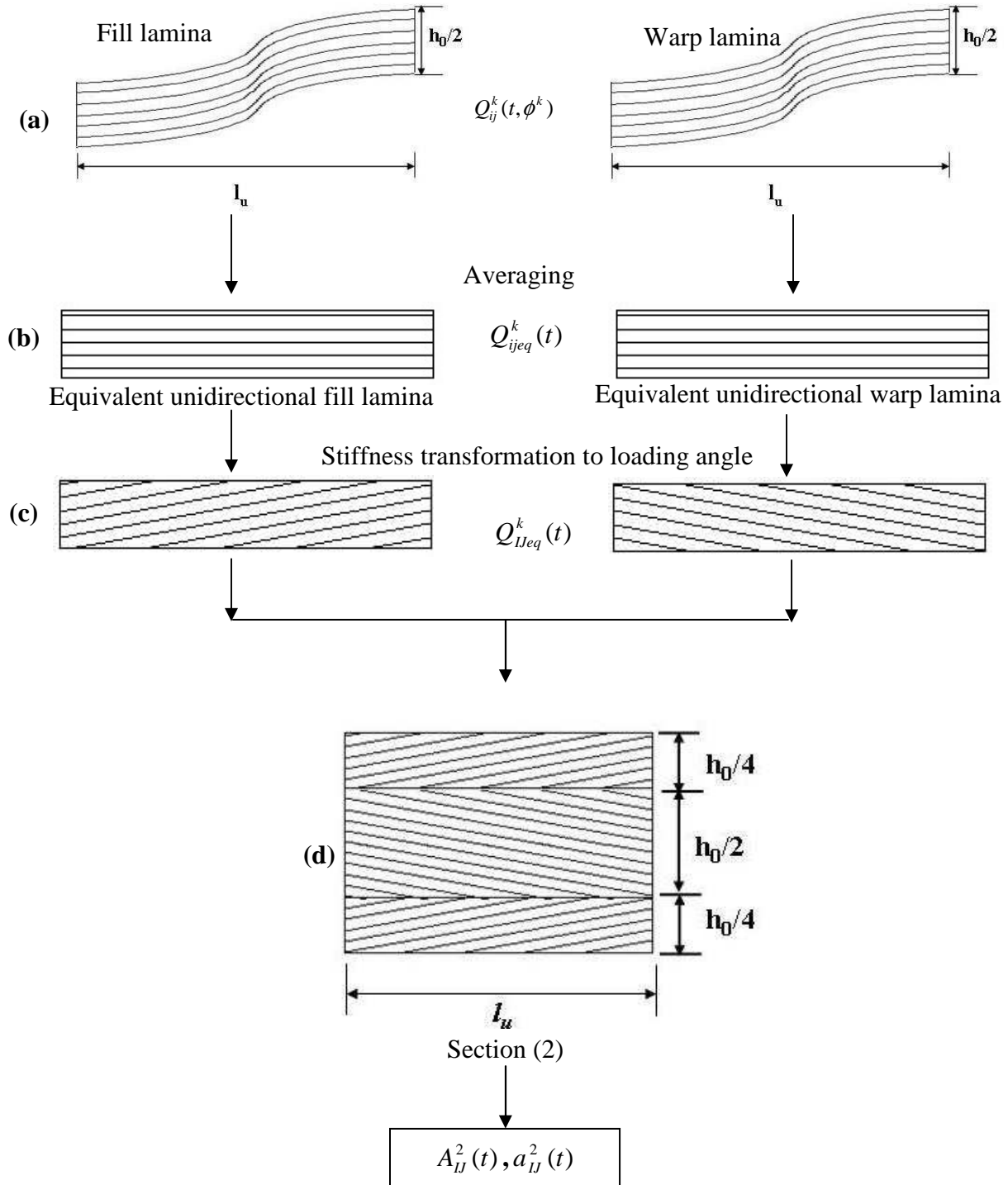


Figure 3.6: Schematic overview of section (2) laminate.

$$h_w = [1 + \sin\{(y - \frac{l_u}{2})\frac{\pi}{l_u}\}]h_0/4 \quad (0 \leq y \leq l_u) \quad (3.10)$$

where, subscript ‘f’ and ‘w’ denotes undulated fill and warp lamina, respectively. h_f and h_w are the Z coordinates of the centre-line of the fill and warp laminae, respectively. x, y and Z represent local coordinate system. The undulation angle (ϕ) at any location along x and y, for fill and warp laminae, are calculated using h_f and h_w as,

$$\tan(\phi^f) = \frac{\partial h_f(x)}{\partial x}; \quad \tan(\phi^w) = \frac{\partial h_w(y)}{\partial y} \quad (3.11)$$

Consider, the crimp section in *Figure 3.6a* subjected to a tensile stress (σ) along x or y axis. If the lamina is divided into infinitesimal sections along its length, the stress on each section will be same since they will be in series. However, the strain will be different. The strain in each segment within equivalent fill or warp lamina (k = fill or warp) is given as [50],

$$\begin{aligned} \varepsilon_{xx}^k(t, \phi^k) &= \frac{\sigma}{E_{xx}^k(t, \phi^k)} \\ \varepsilon_{yy}^k(t, \phi^k) &= -\nu_{xy}^k(t, \phi^k) \frac{\sigma}{E_{xx}^k(t, \phi^k)} \end{aligned} \quad (3.12)$$

where,

$$\begin{aligned} \frac{1}{E_{xx}^k(t, \phi^k)} &= \frac{\cos^4 \phi^k}{E_{11}(t)} + \left(\frac{1}{G_{12}(t)} - \frac{2\nu_{21}}{E_{22}(t)} \right) \cos^2 \phi^k \sin^2 \phi^k + \frac{\sin^4 \phi^k}{E_{22}(t)} \\ E_{yy}^k(t, \phi^k) &= E_{22}(t) \\ \nu_{yx}^k(t, \phi^k) &= \nu_{21}(t) \cos^2 \phi^k + \nu_{32} \sin^2 \phi^k \\ \nu_{xy}^k(t, \phi^k) &= \nu_{yx}^k(t, \phi^k) \frac{E_{xx}^k(t, \phi^k)}{E_{yy}^k(t, \phi^k)} \end{aligned} \quad (3.13)$$

$E_{xx}^k(t, \phi^k), E_{yy}^k(t, \phi^k)$ are the time-dependent longitudinal and transverse moduli of infinitesimal section within equivalent fill or warp lamina along local x, y, z axes.

$\nu_{xy}^k(t, \phi^k)$ and $\nu_{yx}^k(t, \phi^k)$ are the time-dependent Poisson's ratios of infinitesimal section within equivalent fill or warp lamina along local x, y, z axes.

The total average strain in the equivalent fill or warp lamina over its entire undulation length (l_u) along x and y directions will be,

$$\begin{aligned}\bar{\epsilon}_{xx}^k(t) &= \frac{1}{l_u} \int_0^{l_u} \epsilon_{xx}^k(t, \phi^k) dx \\ \bar{\epsilon}_{yy}^k(t) &= \frac{1}{l_u} \int_0^{l_u} \epsilon_{yy}^k(t, \phi^k) dx\end{aligned}\quad (3.14)$$

The average in-plane longitudinal and transverse moduli and Poisson's ratio of the equivalent fill or warp lamina can be calculated as,

$$\begin{aligned}E_{xx}^k(t) &= \frac{\sigma}{\bar{\epsilon}_{xx}^k(t)} \\ E_{yy}^k(t) &= E_{22}(t) \\ \nu_{xy}^k(t) &= -\frac{\bar{\epsilon}_{yy}^k(t)}{\bar{\epsilon}_{xx}^k(t)} \\ \nu_{yx}^k(t) &= \nu_{xy}^k(t) \frac{E_{yy}^k(t)}{E_{xx}^k(t)}\end{aligned}\quad (3.15)$$

Since, all segments are subjected to the same shear strain; the average in-plane shear modulus of the equivalent fill or warp lamina can be obtained as:

Let τ_{xy} be the shear stress acting on the unit cell. The shear strain on each lamina and corresponding shear modulus will be calculated as,

$$\begin{aligned}\mathcal{E}_{xy}^k(t, \phi^k) &= \frac{\tau_{xy}}{G_{xy}^k(t, \phi^k)} \\ G_{xy}^k(t) &= \frac{1}{l_u} \int_0^{l_u} \frac{\tau_{xy}}{\mathcal{E}_{xy}^k(t, \phi^k)} dz = \frac{1}{l_u} \int_0^{l_u} G_{xy}^k(t, \phi^k) dz\end{aligned}\quad (3.16)$$

where,

$$\frac{1}{G_{xy}^k(t, \phi^k)} = \frac{\cos^2 \phi^k}{G_{12}(t)} + \frac{\sin^2 \phi^k}{G_{23}(t)} \quad (3.17)$$

where, $G_{xy}^k(t, \phi^k)$ is the time-dependent shear modulus of the infinitesimal section within equivalent fill or warp lamina along local x, y, z axes. G_{12} and G_{23} are time-dependent shear moduli of the unidirectional lamina along principal directions (1, 2, 6). Since, actual shear strain can not be transformed, engineering shear strain was calculated and used for transformation in following equations.

Using the average in-plane moduli and Poisson's ratio, the stiffness of the equivalent lamina in x, y, Z coordinate system can be calculated as,

$$Q_{ijeq}^k(t) = \begin{bmatrix} E_{xx}^k(t)/(1 - \nu_{xy}^k(t) * \nu_{yx}^k(t)) & \nu_{yx}^k(t) * E_{xx}^k(t)/(1 - \nu_{xy}^k(t) * \nu_{yx}^k(t)) & 0 \\ \nu_{xy}^k(t) * E_{yy}^k(t)/(1 - \nu_{xy}^k(t) * \nu_{yx}^k(t)) & E_{yy}^k(t)/(1 - \nu_{xy}^k(t) * \nu_{yx}^k(t)) & 0 \\ 0 & 0 & 2 * G_{xy}^k(t) \end{bmatrix} \quad (3.18)$$

The corresponding stiffness of equivalent fill and warp laminae in the global coordinate system (X,Y,Z) for a given angle of loading (θ) are obtained using transformation matrix given by equation 3.19,

$$[T^k] = \begin{bmatrix} m^2 & n^2 & 2mn \\ n^2 & m^2 & -2mn \\ -mn & -mn & m^2 - n^2 \end{bmatrix}^k \quad (3.19)$$

where, $m = \cos \theta; n = \sin \theta$ for fill lamina, and, $m = \cos(90 + \theta); n = \sin(90 + \theta)$ for warp lamina. The transformed stiffness of equivalent fill or warp lamina is,

$$Q_{Ijeq}^k(t) = [T^k]^{-1} [Q_{ijeq}^k(t)] [T^k]; \quad (3.20)$$

Using stiffness from equation 3.19 and the classical lamination theory [64], given in *Appendix A*, the stiffness per unit width of the equivalent laminate, i.e. section (2) is determined as,

$$A_{II}^2(t) = \left[\frac{h_0}{4} (Q_{Ijeq}^{fill}(t)) \right]_a + \left[\frac{h_0}{2} (Q_{Ijeq}^{warp}(t)) \right]_b + \left[\frac{h_0}{4} (Q_{Ijeq}^{fill}(t)) \right]_c \quad (3.21)$$

By inverting equation 3.20, compliance matrix for the section (2) is obtained as:

$$[a_{XY}^2(t)] = [A_X^2(t)]^{-1} \quad (3.22)$$

Using equation 3.22, all terms of the compliance matrix in equation 3.23, are determined and used in equation 3.2,

$$[a_{II}^2(t)] = \begin{bmatrix} a_{XX}(t) & a_{XY}(t) & a_{XZ}(t) \\ a_{YX}(t) & a_{YY}(t) & a_{YZ}(t) \\ a_{ZX}(t) & a_{ZY}(t) & a_{ZZ}(t) \end{bmatrix}^2 \quad (3.23)$$

Once, the compliance matrices, given by equations 3.8 and 3.23, for section (1) and section (2) respectively, are determined the total compliance of the entire laminate is

determined using equation 3.2 and the total strain is calculated using equation 3.1. Using the total laminate strain and applied stress, the laminate compliance can be calculated as,

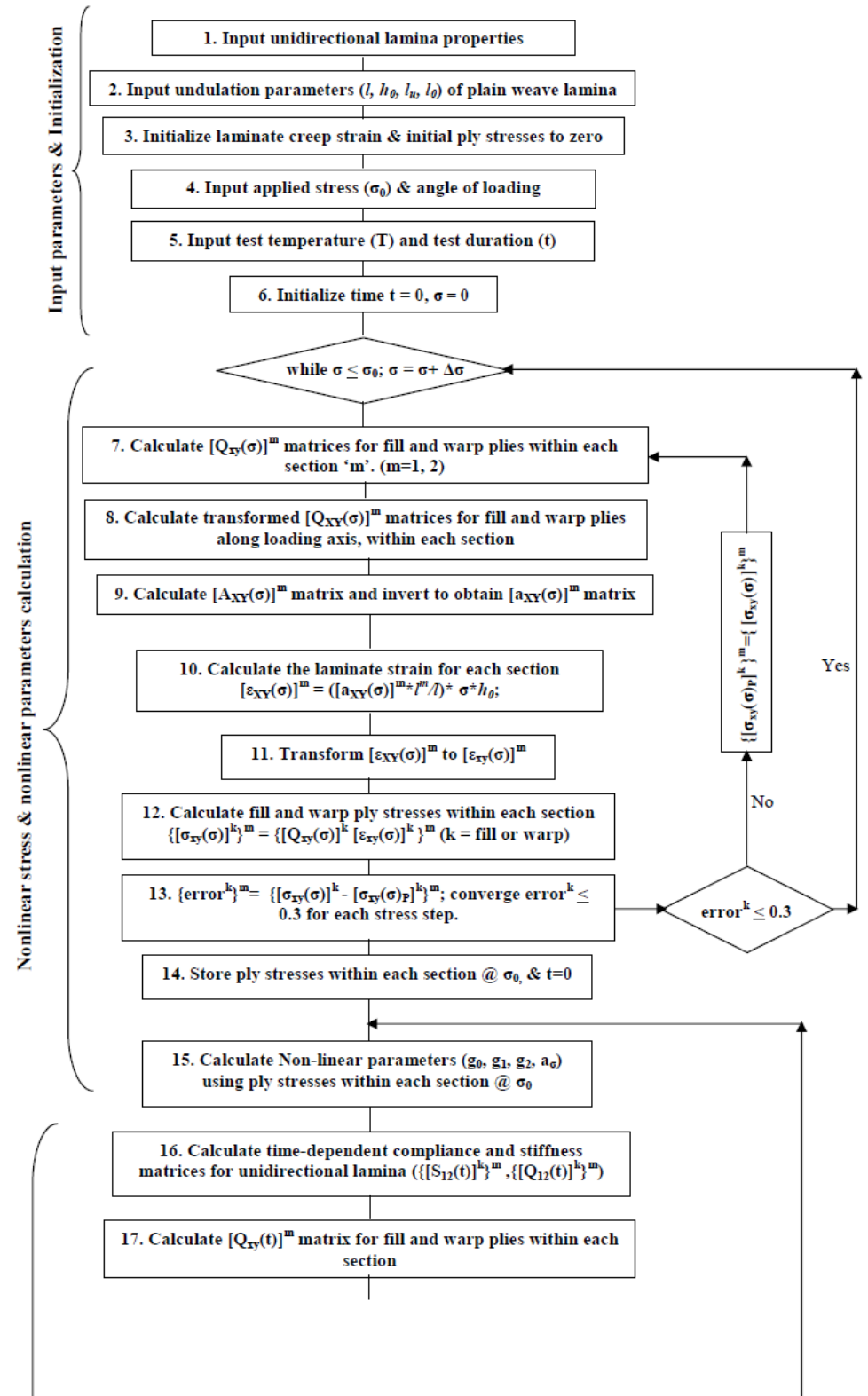
$$[S_{XY}(t)] = \frac{1}{\sigma_0} [\varepsilon_{XY}(t)] \quad (3.24)$$

The time-dependent compliance was simulated as per the procedure discussed in the next section for two different angles of loading, 0^0 , also referred as on-axis loading, and 45^0 , also referred as off-axis loading. The simulated results were compared with experimental results to validate the model.

3.3.3 MATLAB Program for Simulation of Creep of Woven Composites

In order to compute the creep of plain weave composites under tensile loading, a MATLAB based computer program was written. A flow chart outlining the various steps of the program is shown in *Figure 3.7*.

1. Steps 1 to 6 of the program correspond to initialization and input of various parameters. The various inputs are undulation parameters of plain weave fabric, the tensile and creep properties of unidirectional lamina, applied stress, loading angle with respect to fill lamina, test temperature, and test time.
2. Initial strain in the plain weave laminate and the ply stresses within laminate are initialized to be zero. Time is initialized as zero.
3. For a given creep stress applied to the laminate, the laminae stresses at $t = 0$ are calculated using the procedure given in steps 7-15 in *Figure 3.7*. Using the incremental stress step, first the stiffness of fill and warp laminae within each laminate section (1 and 2) are calculated in local coordinate system (x, y, Z) in *step 7*, and then transformed to global coordinate system (X, Y, Z) in *step 8*.



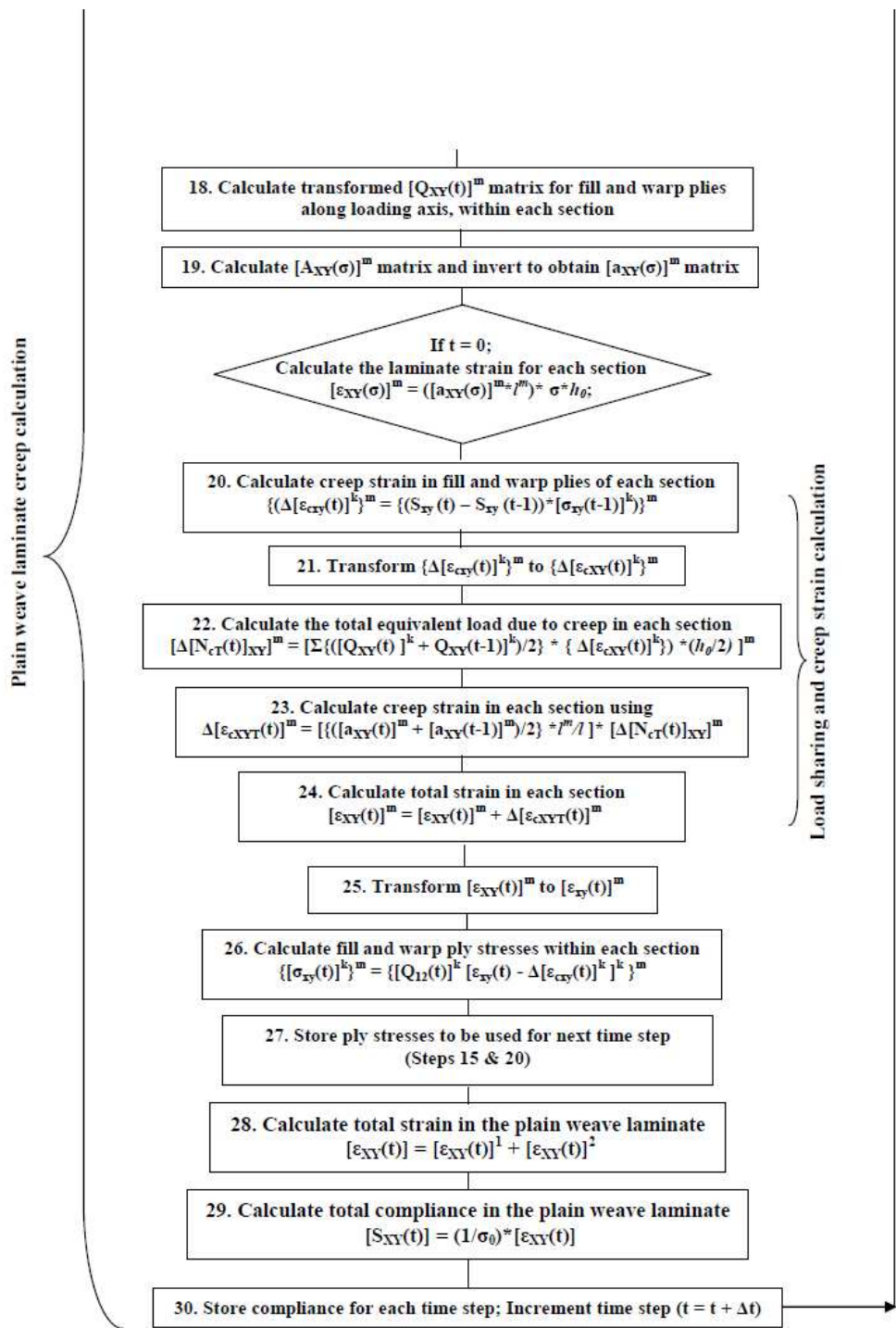


Figure 3.7: Flow chart representing proposed modified equivalent laminate creep model (MELM) for plain weave polymer woven composites.

Laminate stiffness and compliance matrices are calculated and the laminate strains are calculated for each section in *steps 9, 10*. Strains are transformed to local coordinate system in *step 11*, and laminae stresses are calculated in *step 12*. For each stress step, convergence is checked for calculated laminae stresses in *step 13*.

4. First, depending on the applied stress, the nonlinear parameters (g_0 , g_1 , g_2 and a_σ) for unidirectional laminae are calculated in *step 15* at a given test temperature, using the inputs, and the laminae stresses calculated in steps 7-15 for $t = 0$.
5. Using these laminae stresses, nonlinear parameters are calculated at $t = 0$.
6. The time-dependent stiffness and compliance matrices are calculated in steps 16-19 for each section using equations 3.3-3.7 and 3.12-3.22.
7. If $t = 0$ the laminate strain for each section is calculated using the laminate compliance and applied stress.
8. For $t > 0$, the creep strain for each section is calculated in steps 20 to 24.
9. Consider the fabric laminate subjected to a constant tensile load as shown in *Figure 3.8*. Due to the difference in modulus of the fill and the warp laminae, the load distribution between them will be as shown in *Figure 3.9*. Under a constant applied load, load shared by the fill lamina is much higher than the load shared by the warp lamina because of the higher modulus of the former when compared to the latter. During creep, the modulus of each ply changes with time due to the viscoelasticity of the matrix, resulting in constant re-distribution of load shared between the fill and the warp lamina of the plain weave laminate. The load (and

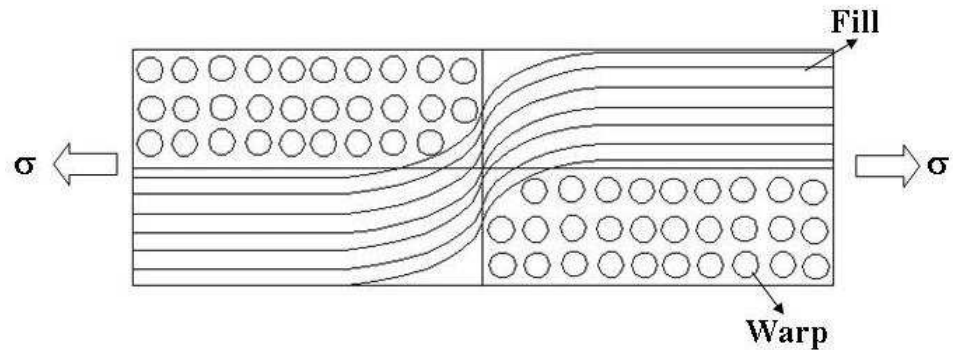


Figure 3.8: Schematic of a plain weave laminate under a constant applied stress.

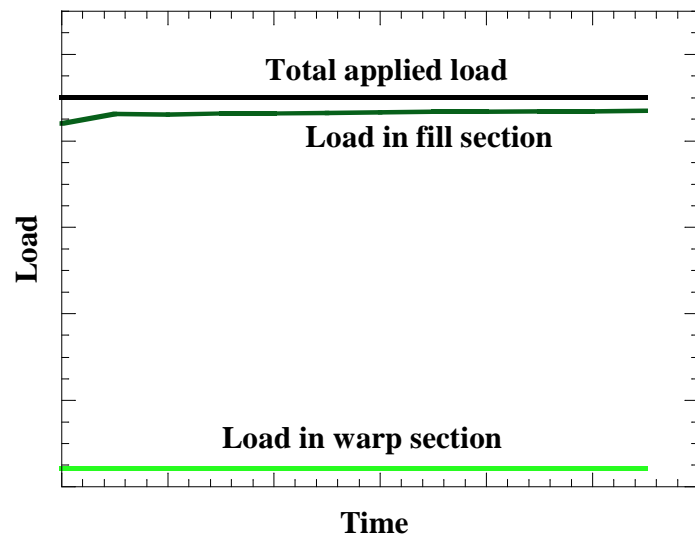


Figure 3.9: A plot of load distribution between fill and warp lamina of a plain weave laminate.

thus the stress) shared by the fill lamina will increase with time while that by the warp lamina will decrease with time.

10. Since the lamina creeps under constraint within a laminate, the unconstrained creep strain will be different from the constrained creep strain of the laminae within the laminate. Hence, creep strain of the laminate is calculated using the unconstrained creep strain of the laminae in steps 20-23. The unconstrained creep strain is calculated in *step 20* using change in lamina compliance for a given time increment and the lamina stresses calculated in previous time step. The load required to cause this incremental elastic strain (equal to the unconstrained creep strain) in each lamina for that time step is then calculated and added in *step 22* to obtain the total incremental load corresponding to the unconstrained creep strain in all laminae of the laminate. This incremental load is used to calculate the incremental creep strain in the laminate for a given time step as shown in *step 23*.
11. In *step 24*, the creep strain obtained in each time step for each laminate section is stored and added to the total strain obtained in previous time step and total strain in each laminate section is determined.
12. Laminae strains in global coordinate system within each section are transformed to local coordinate system in *step 25*.
13. The change in laminae stresses with time influences the creep of the laminae, if the stresses are in the nonlinear viscoelastic region. Additionally, the change in laminae stresses will also result in change in elastic strain. Therefore, the change in laminae stresses with time is monitored, as given by equation in *step 26*. For $t > 0$, the laminae stresses within each section are calculated in *step 26* for current

time step and stored for next time step, *step 27*, for nonlinear parameters calculation given by *step 15*, and to calculate creep strain in *step 20*.

14. The total strains obtained for all laminate sections are added and the total strain for the entire plain weave laminate is determined in *step 28*.
15. Plain weave laminate compliance is calculated using laminate strain and applied stress for each time step in *step 29*.
16. Plain weave laminate compliance for each time step is stored and time step is incremented in *step 30*.

The simulation from the above program was compared with experimental results for both on-axis and off-axis loading. Additionally, the simulations were also compared with simulations using two models available in the literature, namely Crimp Model [50] and Equivalent Laminate model [20]. The relevant equations are provided in *Appendix A*.

4. EXPERIMENTAL & SIMULATION DETAILS

4.1 Introduction

In this chapter, the experimental procedure used for generation of experimental data for the creep of plain weave woven polymer composites is presented. Additionally, the experimental procedure used to generate creep data for unidirectional composites in the nonlinear viscoelastic region is also described. Finally, details of the computer program developed as a part of this thesis and the simulation procedure to predict creep of woven composites are presented and discussed.

4.2 Experimental Details

4.2.1 Material

The composite material used in this thesis consisted of F263-8 epoxy resin reinforced with T300 celion plain weave carbon fabric. The fabric prepreg (W3G-282) was supplied by Hexcel Corporation in the form of 42" wide roll. This material is used in aerospace industries. As mentioned in Chapter 1, this material has been qualified for structural applications in civilian commercial aircrafts [1]. In general, carbon fiber/ epoxy composites have major share in aerospace applications. Hence, this material is representative of these materials. Additionally, the results of this study are generally applicable to all woven composites.

4.2.2 Manufacturing of test coupons

4.2.2.1 Preparation of composite panels

The following steps were adopted to manufacture the woven composite panels.

- i) The prepreg was always stored in a vacuum sealed bag inside a freezer at -25 °C to avoid curing of the resin during storage. Prior to lay-up, the bag containing the prepreg was removed from the freezer and allowed to thaw to room temperature before unsealing the bag.
- ii) *Hand lay-up:* The prepreg was removed from the vacuum bag, cut into 12"x12" sheets. The prepreg sheets were manually laid up to required thickness. The fiber orientation was kept same in all the layers.
- iii) *Vacuum bag Assembly:* Two aluminium tool plates were cleaned with alcohol and coated with a minimum of two coats of Frekote[©], a silicone based release agent supplied by Dexter Corporation, USA. Enough time was allowed between two coats to enable drying. After drying of the coating, stacked layers of the prepreg were placed between tool plates and bagged as shown in *Figure 4.1*. First, a release film, supplied by Hexcel Corporation, USA, was placed on the bottom of tool plate followed by the stack of prepeg layers, another release film and another tool plate on top. The release films were used for easy removal of cured panel after curing. This assembly was covered with a breather clothe to provide a passage for air and volatiles from the stacked prepreg to the vacuum port.

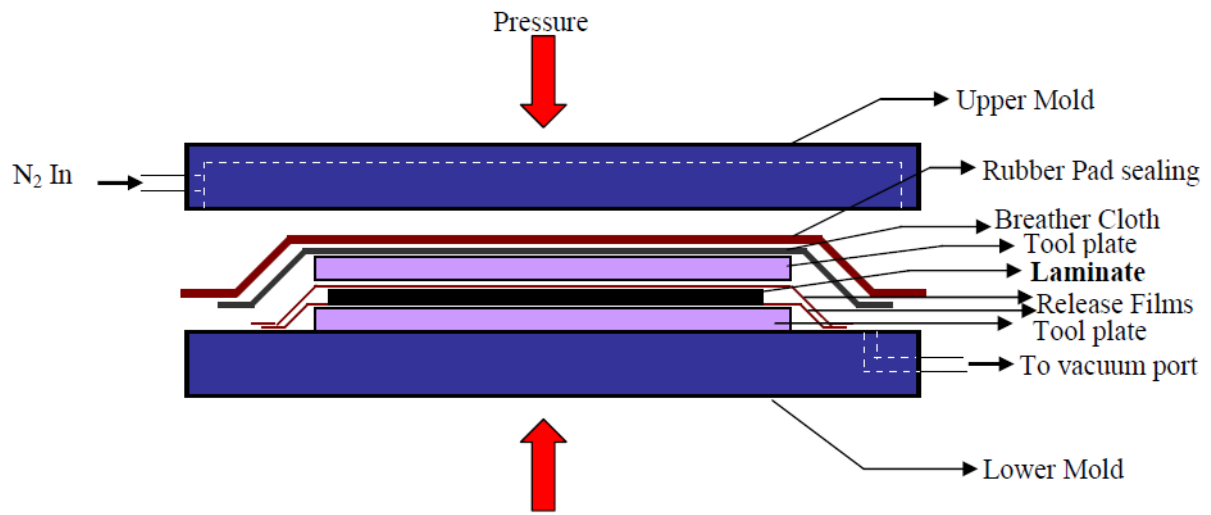


Figure 4.1: Schematic of the mold assembly & vacuum bag used in simulated autoclave curing of composite panels.

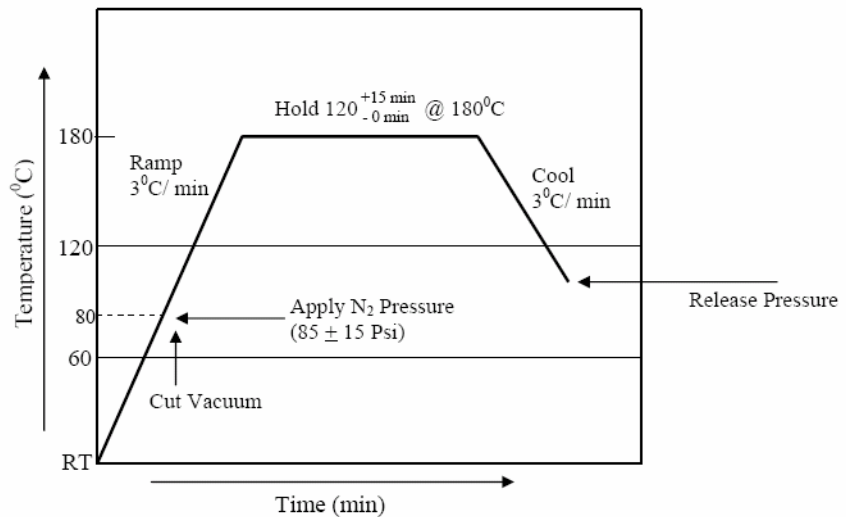


Figure 4.2: Cure cycle used in manufacturing of the composite panels.

- iv) *Autoclave curing:* The prepreg panel was cured in a 50-ton Carver hydraulic hot press using the autoclave cure cycle shown in *Figure 4.2*. The assembly placed on the lower half of a two-piece mold and was covered with a rubber pad to create a vacuum bag between the pad and the lower mold as shown in *Figure 4.1*. This is referred to as vacuum bag in this thesis. The top half was placed over the pad sandwiching the latter between the two halves. This mold assembly was held between heated platens of hydraulic hot press for curing of the prepreg. The mold was heated at a rate of $3^{\circ}\text{C}/\text{min}$ until 177°C and held at that temperature for about 2 hours before cooling down to room temperature. During ramping, vacuum was applied to the vacuum bag assembly to remove entrapped air and volatiles from the prepreg layers. When the temperature reached 85°C , vacuum bag containing the panel was vented to atmospheric pressure and nitrogen gas was introduced into the mold between the pad and the top mold to apply a pressure of 85psi over the vacuum bag and the panel. After the end of the hold period, the mold was cooled down to room temperature and the panel was subsequently removed from the mold.
- v) *Post Cure:* To ensure complete cross-linking of any monomers that did not cross-link during the curing process, post curing of the cured panel was done at 220°C for 4 hours in a convection oven. This temperature was chosen based on prior work by C.V. Iyer [4]. Samples of the post-cured composite were subjected to a ramp test using a Differential Scanning Calorimeter (DSC) No residual exothermic heat was observed, as shown in *Figure 4.3*,

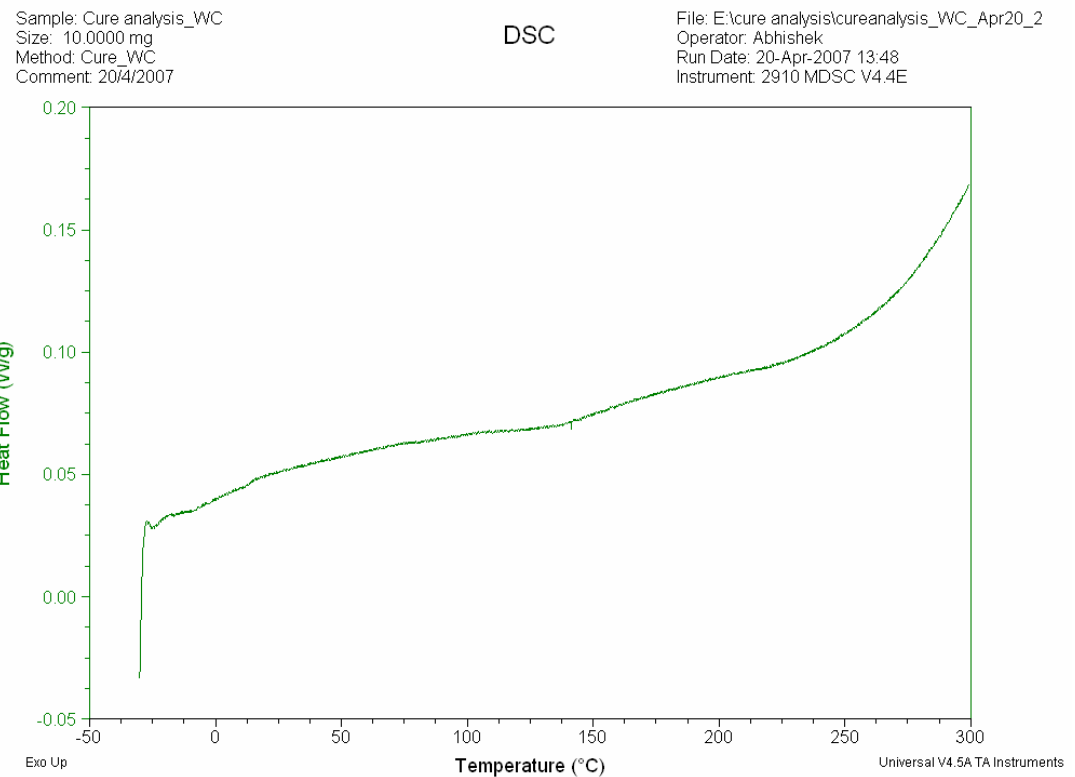


Figure 4.3: DSC plot of thermal analysis of post cured plain weave composite panel.

confirming complete curing of the composite.

4.2.2.2 Volume fraction determination

Creep of polymer matrix composites vary with volume fraction of fiber and matrix [4]. Thus, it is important to determine volume fraction of fibers in the plain weave composite, used in the present study, to predict its creep with accuracy. The volume fraction of plain weave composite was determined using a two-step procedure. The first step was to determine the density of the composite using water displacement method followed by second step to determine the volume fraction of the fiber in the composite using acid digestion method.

i) Water Displacement method

This method, described in ASTM standard D- 792 [72], was used to determine the specific density of the composite. This method consisted of the following steps:

1. Weigh the specimen in air to the nearest 0.1 mg.
2. Weigh a metal wire partially submerged in water.
3. Suspend the specimen using the wire and measure weight of the specimen fully submerged in water with partially submerged wire.
4. Determine the specific density of the specimen at 23 °C using the following formula:

$$\rho = 0.9975x \frac{a}{(a + w - b)} \quad (4.1)$$

where,

ρ = Specific density of composite (g/cm³).

Table 4.1: Summary of fiber volume fraction test results (step 1 & 2) for the manufactured woven composite panel.

Sample	Composite Density (g/cm³)	Fiber Mass fraction (%)	Fiber Volume fraction (%)
1	1.57	70.8	63
2	1.58	72.4	65
3	1.58	72.6	65
4	1.57	71	63.3
5	1.57	71.8	64.2
Average	1.57	72 ± 1	64 ± 1

a = weight of the specimen, in air (g).

b = weight of the fully immersed specimen and partially immersed wire in water (g).

w = weight of partially immersed wire in water (g).

0.9975 is a conversion factor multiplied to convert density from kg/m³ to specific density at room temperature in g/cm³. Specific density results are tabulated in *Table 4.1*

ii) Acid Digestion Method

Acid digestion method was used to determine the volume fraction of the fiber in the composite following the procedure described in ASTM standard D 3171-06 [73]. The digestion procedure consisted of the following steps:

1. A piece (1"x1") of composite taken from the cured panel was dried and weighed.
2. The sample was then heated in a 125ml conical flask containing 30ml of 70% concentrated nitric acid solution in water. The digestion of matrix was carried out for 5 hours at temperature of $75 \pm 1^{\circ}\text{C}$. The flask was connected with a reflex condenser to condense nitric acid vapor and re-circulate the acid back to the flask.
3. The undigested part of the specimen was then filtered using a sintered glass crucible under a vacuum of 16.9Pa (127Torr).
4. The undigested filtered fiber part was washed with acetone and distilled water.
5. The fibers were dried in an air circulated oven at 100°C for 1hour.
6. The fibers were cooled down in a desiccator to prevent any moisture absorption from the surrounding.
7. The dried fibers were weighed to the nearest of 0.1mg.

8. The volume fraction of fiber in the composite sample was calculated using the formula given below:

$$V_f = (M_F / M_I) \times \rho_c / \rho_f \quad (4.2)$$

where,

V_f = volume fraction of reinforcement (fibers)

M_I = initial weight of specimen (g).

M_F = final weight of specimen after digestion (g).

ρ_c = Density of composite specimen (g/cm^3).

ρ_f = Density of the fiber = $1.76\text{g}/\text{cm}^3$.

Five trials were completed to get a good average for measured fiber volume fraction. The results are tabulated in *Table 4.1*. The average volume fraction of all the composite panels was 64%. Mass fraction results are also tabulated in *Table 4.1*.

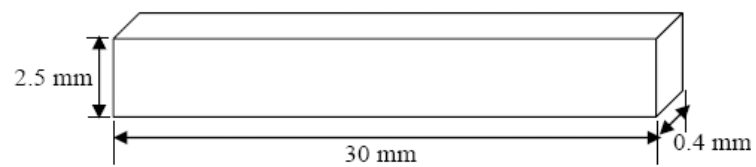
4.2.2.3 Test coupon preparation

The edges of the post cured panels were trimmed to a width of 1.5" to remove resin rich edges. The test coupons for Dynamic Mechanical Analysis (DMA) tests were of dimensions shown in *Figure 4.4a* and were cut using Buehler's Isomet 1000 high precision diamond saw with oil as the coolant. These test coupons were rinsed to remove any remaining oil, dried and stored. Tabs were bonded to the gripped ends of the tensile test coupons to avoid crushing of the ends during gripping. Tabs were made of woven (carbon fiber / epoxy composite) prepreg. The panels for tab were also manufactured as per the procedure discussed in 4.2.2.1. The cured panel was cut into 1.5" wide tab-strips using a diamond saw. One side of strip was tapered to 7^0 angle using a milling machine equipped with a carbide cutter. Tapering was done to avoid any stress concentration in

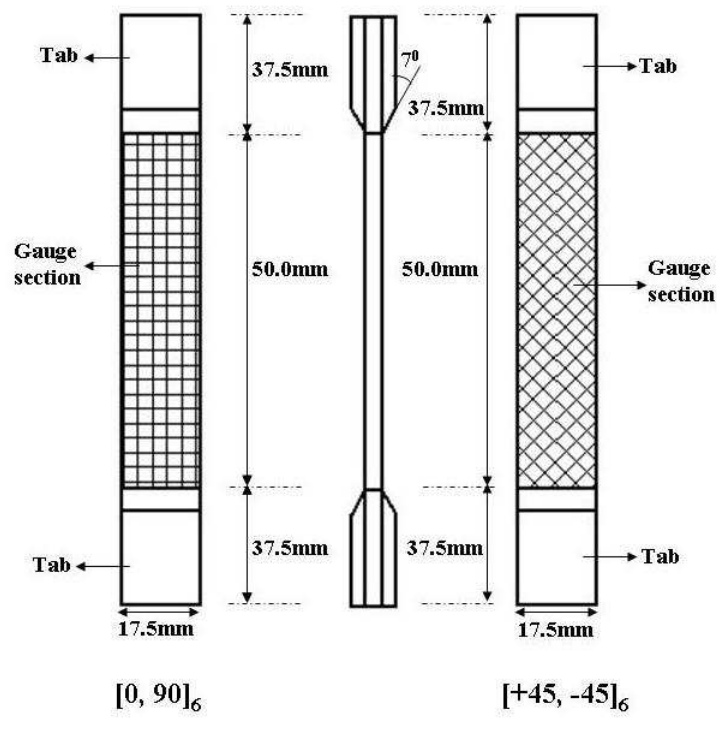
the test coupons at the edge of a tab. The ends of the composite panel and the tab strips were sanded using 180 grit size silicon carbide papers. The sanded surfaces were thoroughly cleaned and wiped using ethyl alcohol to remove all loose particles. Dexter Corporation's BMI 9873 adhesive was used to bond the tab-strips to the ends of composite panel. The panel-adhesive-tab sandwich was heated in a hydraulic press to 177 °C and held for 1 hour under a pressure of 300MPa to allow the adhesive to flow and cure. The panel with edge-bonded tabs was then allowed to cool down to room temperature under pressure. Tensile test coupons for on-axis (0^0) and off-axis (45^0) tests, as shown in *Figure 4.4b*, were cut from the tabbed panels using a slow-speed Buehler Micro-matic diamond precision saw running at a speed of 500 rpm. A table feed rate of 10mm/min was used. A slow feeding rate is desirable to avoid any overheating of the part or saw, and damage to the sample edge. The panel was held on to the cutting platform using double sided tape. The dimensions of test coupons used for both on-axis and off-axis tests are given in *Table 4.2*. DMA test coupons were used for on-axis tests only.

4.2.2.4 Strain gaging

Strain gages from Micro Measurements Group Inc., NC, USA were used to measure the strain during tensile and creep experiments. A plain weave woven structure can be approximated to be made-up of a repeat unit cell, as shown in *Figure 4.5a*. The size of this unit cell for the plain weave composites used in the present study is 2.1mm x 2.1mm. If the strain gage size is less than this size, the measured strain will not be representative of the average strain in the composite and will be inaccurate. Previous researchers have observed this dependence of the average strain on strain gage size and have recommended that the size of strain gage must be larger than the unit cell size [74,



(a)



(b)

Figure 4.4: Test coupon geometry for tests using (a) DMA and (b) Instron testing machine.

Table: 4.2 Test coupon dimensions for on-axis and off-axis tests.

Test	Gage Length (mm)	Width (mm)	Thickness (mm)
Tensile	50 ± 1.00	17.5 ± 1.0	1.0 ± 0.1
Creep – DMA	30 ± 1.00	2.5 ± 0.1	0.4 ± 0.05
Creep– Instron	50 ± 1.00	17.5 ± 1.0	1.0 ± 0.1

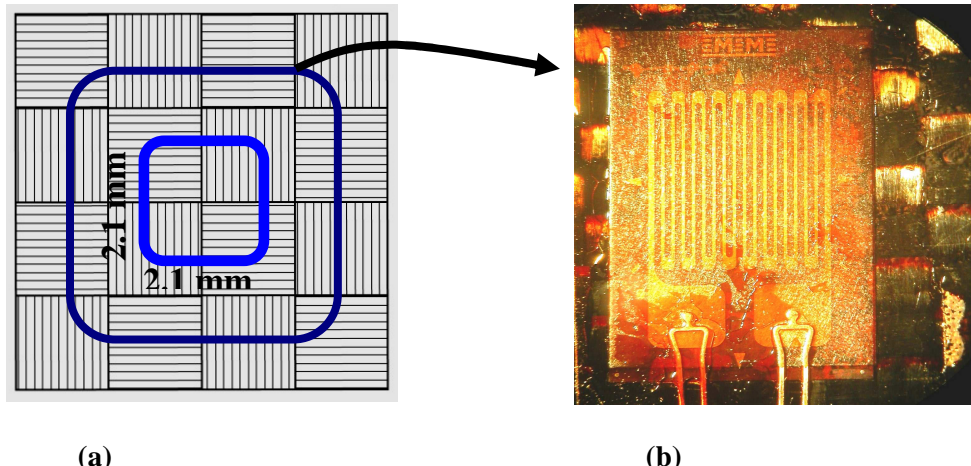
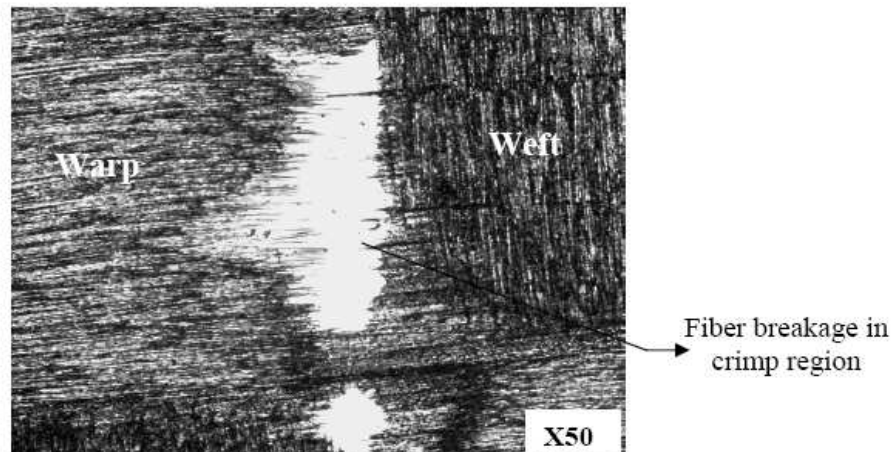
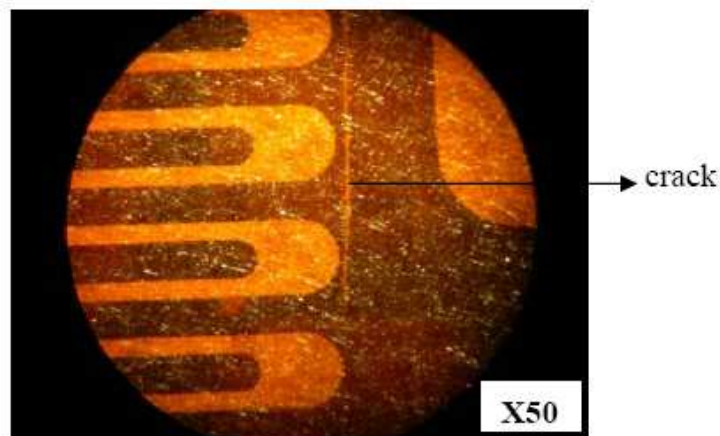


Figure 4.5: (a) Size of unit cell and (b) strain gage size used for experiment.



(a)



(b)

Figure 4.6: (a) Fiber breakage due to surface abrasion and (b) Cracking of strain gage backing during test due to broken surface fibers in the test coupon.

75]. Same has also been recommended by *ASTM standard D6856-03* [76]. Based on this analysis, the strain gages chosen for our experiments were of the size of 6.35mm x6.35mm gage area (more than 2 times of the unit cell size) as shown in *Figure 4.5b*. WA-06-250BF-350 gages were used for the tensile tests and WK-06-250AE-350 gages were used for the creep tests.

As per the strain gage installation procedures, recommended in the manual from Micro Measurement Group Inc. [77], the gage area of a test coupon was abraded in succession using 200, 400 and 600 grit papers, respectively. The abraded area was cleaned using M-prep Conditioner A (alkaline) followed by M-prep Neutralizer B (acidic). The purpose of surface abrasion is to remove any unwanted dirt/oil on the test coupon surface and provide a smooth surface for good bonding of the strain gage to the test coupon surface and get accurate measurement of strain. However, in the case of plain weave composite samples, fiber crimping results in an uneven surface. It was found that surface abrasion caused breakage of the fibers in the crimp region, as observed in *Figure 4.6a*. The stress concentration caused by these broken fibers resulted in pre-mature failure of the backing of the strain gage at stress levels above 30% UTS, as shown in *Figure 4.6b*. Hence, in order to avoid such surface damage, surface abrasion was not used in this study to clean the surface. Instead, a thin coating of M-bond 610 adhesive was applied on the gage area to provide a smooth surface for strain gage installation. The thin adhesive coating was partially cured for 5-10 minutes at 60 °C, in circulated convective oven prior to strain gage installation. The strain gage was then bonded to the test coupon by applying more M-bond 610 adhesive on the previously applied coating and cured under spring-clamp pressure at 180 °C for 2hours. The sample was allowed to cool to room

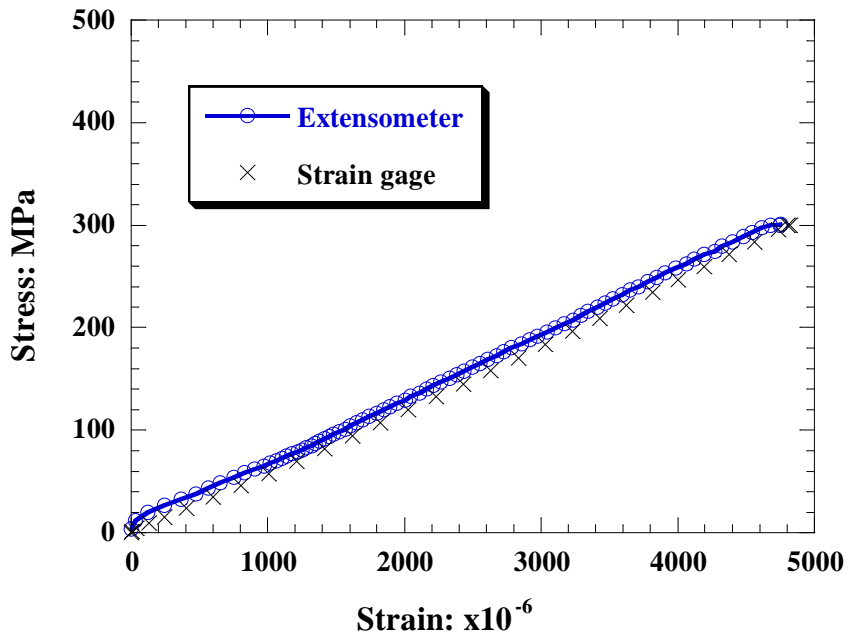


Figure 4.7: Comparison of on-axis tensile test results at a temperature of 120 °C using extensometer and strain gage.

temperature in the oven. The clamp was removed and the sample was post cured at 220 °C for 2hrs to ensure that the adhesive was completely cured and to prevent any residual curing of adhesive during testing. While the new strain gage installation method, described above, improved the capability of the strain gage to remain intact up to 50% UTS under on-axis or off-axis loading, the gages did not survive during the tests conducted at stress levels above 50% UTS. Hence, a dynamic strain gage extensometer (series 2620), supplied by Instron Inc., was used for strain measurement at stress levels beyond 50% UTS, during both on-axis and off-axis testing. The extensometer had a gage length of 1inch and could be used up to a maximum temperature of 200 °C. The extensometer was installed on the test coupon using metallic springs, supplied with an extensometer kit. In order to confirm any difference between the strains measured using the strain gage and extensometer, an on-axis tensile test was done by loading the test coupon to 50% UTS at 120 °C. Stress-strain plot obtained from this experiment is compared in *Figure 4.7* with the stress-strain plot obtained using strain gage for the same test conditions (loading rate and test temperature). Both strain values compared within an error band of $\pm 1\%$, confirming the reliability of extensometer reading.

4.2.2.5 Conditioning of test coupons

The test coupons were used in post-cured condition and were stored at room temperature. Prior to each test, the strain gaged test coupon was heated to 270 °C (glass transition temperature of epoxy matrix) and soaked for 15minutes before cooling to room temperature to erase previous physical aging history of the matrix during storage.

4.2.3 Tensile test

On-axis and off-axis tensile tests were conducted using Instron 8562 servo-electric test frame equipped with 8500 control system, shown in *Figure 4.8*. The test frame was equipped with a $\pm 25\text{kN}$ load cell and an environmental chamber capable of reaching a temperature of 350°C . During ramping up to a desired temperature, the instrument was under load control and was programmed to maintain zero load. However, the load cell temperature was observed to increase due to conduction of heat through the pull rod between the load cell and the test coupon. This temperature rise affected zero load control during ramping. In order to avoid this, load cell temperature was always maintained at room temperature using cooling water circulated through the pull rod during high temperature tests. During temperature ramp, the metallic grips holding the test coupon expand. Difference in thermal expansion coefficients as well as stiffness between metallic grips and the composite coupon caused the test coupon to bend during ramping. In order to avoid this, one end of the test coupon was not clamped during ramp-up to desired temperature to allow free expansion of the grips and the test coupon. Once, the temperature reached the desired value, the environmental chamber was opened and the coupon was clamped at both ends and allowed to equilibrate at desired temperature, before loading. Once, the temperature had equilibrated, the instrument was switched to position control before loading at a test temperature.

On-axis and off-axis tensile tests were conducted to obtain ultimate tensile strength (UTS) and modulus of the material at different test temperatures below the glass-transition temperature of its matrix. Both tensile test plans are shown in *Table 4.3*. A strain rate of 10^{-4} sec^{-1} was used and each test was performed as per ASTM standard D



Figure 4.8: Instron 8562 servo-electric frame with environmental chamber.

Table 4.3: Test plans for on-axis and off-axis tensile tests.

(a) Test plan for on-axis test

Test Temperature($^{\circ}$C)	No. of Samples for testing
Room Temperature	3
80	3
160	3
240	3

(b) Test plan for off-axis test

Test Temperature($^{\circ}$C)	No. of Samples for testing
Room Temperature	3
80	3
100	3
120	3
140	3
160	3

4762-04. The stress and strain data was acquired using SCXI-1000 Data Acquisition System from National Instruments (described in *section 4.2.8*).

4.2.4 Tensile creep tests

Tensile creep tests were conducted using two types of equipment:

(i) *Dynamic Mechanical Analyzer (DMA)*: On-axis creep tests at lower stress levels (up to 7MPa) were performed using DMA 2980 from TA instruments shown in *Figure 4.9*. DMA is desirable for tests at lower stresses due to higher load stability during creep tests. During on-axis creep tests, the creep strain for stresses below 7MPa, within the tested time period, was only 1-2microstrains and hence, DMA is desirable to record this strain accurately. Creep tests were conducted using a film tension clamp. The equipment was capable of exerting a load up to 18N and can be operated in the temperature range of -150 $^{\circ}\text{C}$ to 600 $^{\circ}\text{C}$. A single test coupon was used at each stress level for the entire test temperature range of 80 - 240 $^{\circ}\text{C}$ as per the test plan given in *Table 4.4*. The creep test was performed for 1 hour at each stress and temperature. After each creep test, the test coupon was allowed to recover for 2 hours at the tested temperature. The test temperature was ramped at 20 $^{\circ}\text{C}$ intervals and the test coupons were allowed to equilibrate for 1 hour at each temperature.

(ii) *Instron*: An Instron 5500R screw-driven test machine was used for on-axis and off-axis creep testing at stress levels above 7MPa. Off-axis creep test at 7MPa was also conducted using Instron 5500R. Instron 5500R machine was operated using Bluehill software (version 2.5) and equipped with a \pm 25kN load cell and an environmental chamber, shown in *Figure 4.10*. The chamber could be ramped to 300 $^{\circ}\text{C}$. The instrument was equipped with water cooled pull rod for high temperature tests. Similar to the Instron



Figure 4.9: Dynamic Mechanical Analyzer 2980

Table 4.4: Plan for On-axis creep testing using DMA.

Test	Test Temp. (°C)	Applied Stress (MPa)	No. of Samples/ test	Creep time (hrs/ test)
Creep	80- 240	3- 7	2	1

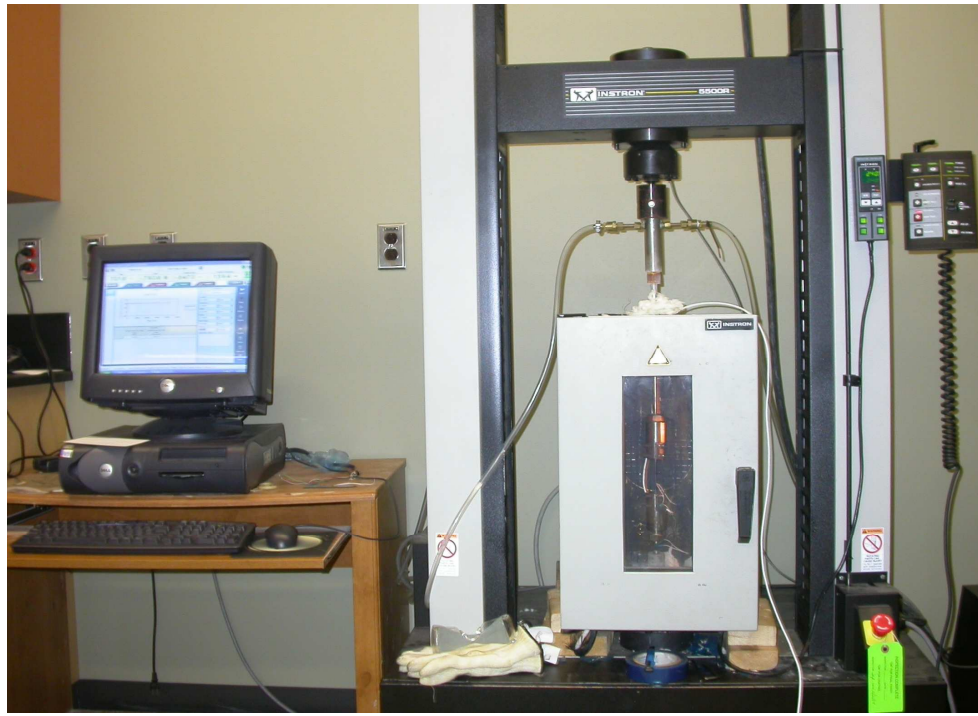


Figure 4.10: Instron 5500R screw- driven tensile and creep test machine.

Table 4.5: Test plans for on-axis and off-axis creep testing using Instron testing machine.

(a) On-axis creep test plan

Test	Test Temp. (°C)	Applied Stress (MPa)	No. of Samples/ test	Creep time (hrs/ test)
Creep	80- 160	100- 450	1	1

(b) Off-axis creep test plan

Test	Test Temp. (°C)	Applied Stress (MPa)	No. of Samples/ test	Creep time (hrs/ test)
Creep	80- 160	7, 50	1	1

8562, the instrument was kept under load control during ramp-up and equilibration. In some cases, the thickness of the test coupon at one tabbed end was found to be different from the thickness at the other end due to difference in thickness of the adhesive bond, which caused bending of the test coupon after clamping at both ends. Such bending of the test coupons was avoided using a thin aluminum shim at one end of the test coupon, before clamping. The instrument was switched to position control mode while loading to a desired creep load. A loading rate of 10^{-4} sec⁻¹ was used. After reaching the desired load, the instrument was switched to load control mode to maintain a constant creep load. On-axis and off-axis creep tests were conducted at different temperatures and stresses as shown in *Table 4.5*. A single test coupon was used at each stress level for the entire test temperature range of 80-160 °C. The creep test was performed for 1 hour at each stress and temperature. After each creep test, the test coupon was allowed to recover for 1 hour at the tested temperature. In addition to the short-term creep tests, long-term creep tests, ranging from 2-5 days, were also conducted using fresh test coupons at different temperatures and stresses under both on-axis and off-axis loading, as desired. The creep strain was measured using strain gages or an extensometer and recorded using National Instruments SCXI data acquisition system. A dummy composite coupon (material, lay-up and strain gage same as test coupon) was used during strain measurements with strain gages, to off-set the effect of temperature and its variation on strains measured using strain gages. The dummy coupon with bonded strain gage was under no load and was very near the test coupon. The two strain gages on dummy and test coupons were connected to DAQ system configured for quarter bridge configuration.

4.2.5 Damage analysis

F263/ T300 epoxy/ carbon fiber plain weave composites used in the present thesis did not develop any process induced vertical cracks after manufacturing as shown in *Figure 4.11a*. However, the cracks developed, when the test coupons were conditioned at its glass transition temperature of 270 °C as shown in *Figure 4.11b*. This conditioning was necessary to erase physical aging of the test coupon during its storage, prior to testing, as described in Section 4.2.2.5. If physical aging is not erased, it would influence the creep strain and complicate the analysis. Thus, conditioning procedure was necessary. The test coupons developed longitudinal edge cracks within the transverse yarn section (warp) of the test coupon as shown in *Figure 4.11b*. This cracking was due to thermal stresses caused by CTE mismatch among the layers (as well as between the fiber and resin) and high ΔT (250 °C) when the material was cooled from 270 °C to room temperature. The CTE mismatch was the maximum in plain weave composites since the warp and weft fibers were orthogonal to each other. This process-induced damage could affect the tensile behavior and creep of composite under on-axis or off-axis tensile loading. Thus, it is necessary to characterize the effect of process-induced damage on these composites under tensile load. The effect of process-induced damage on tensile properties under on-axis and off-axis loading of composite test coupons was analyzed by performing repeated loading - unloading tensile tests at different temperatures using Instron 8562 and Instron 5500R tensile testing machines, and by testing the coupons under load for creep. The microscopic analysis of process-induced damage as well as damage induced during/ after tensile and creep tests was conducted using Nikon's Eclipse



Figure 4.11a: Micrograph of polished edge of post cured $[0, 90]_6$ plain weave composite coupon (X 100).

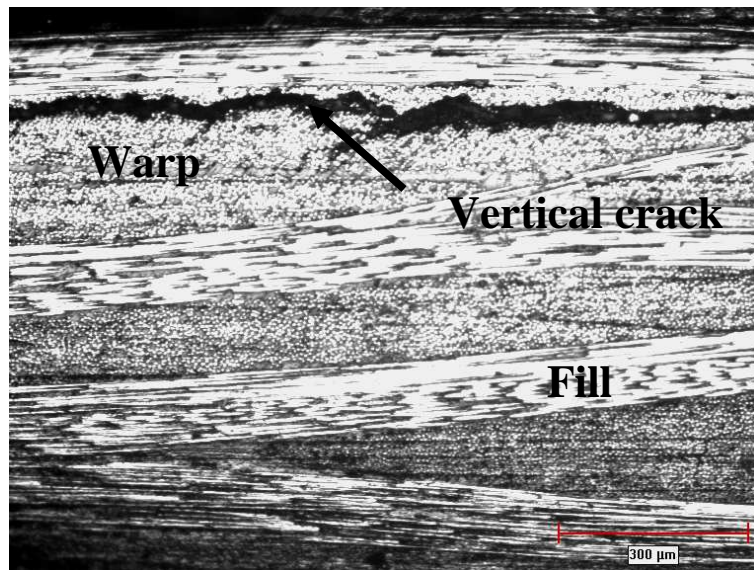


Figure 4.11b: Micrograph of polished edge of post cured and conditioned $[0, 90]_6$ plain weave composite coupon with vertical cracks (X 100).

LV100 optical microscope and Xradia's MicroXCT. Details on process-induced damage and its effect are discussed in section 4.2.8.

4.2.6 Microscopic analysis

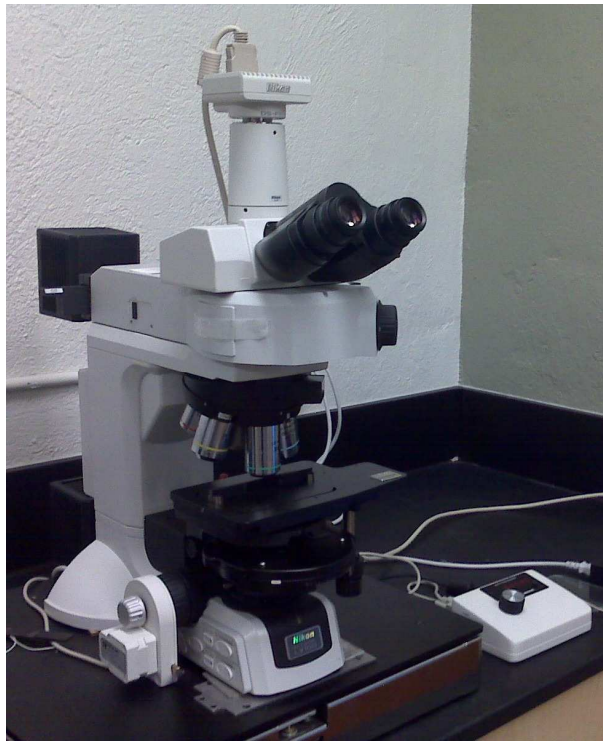
The microstructural and damage analyses of on-axis and off-axis test coupons were performed using Nikon's Eclipse LV100 optical microscope and Xradia's MicroXCT, shown in *Figures 4.12a and b* respectively.

The optical microscope was equipped with objective lenses with magnifications of X2.5- X50 along with an eyepiece with magnification of X10. The microscope was attached to Nikon's DS-Fi1 camera to capture the images of the samples, which were viewed and analyzed using Nikon's NIS-Elements Basic Research- 3.0 image analysis software.

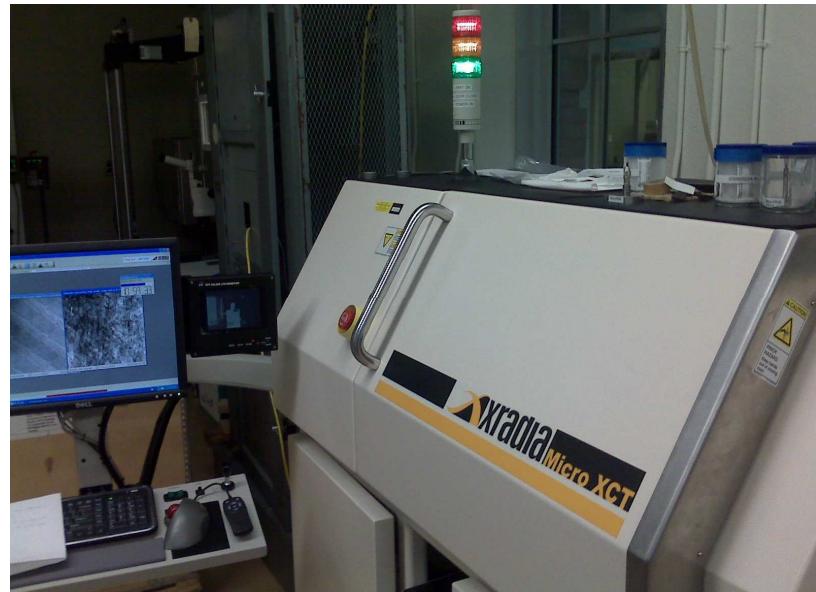
Xradia MicroXCT is a transmission-type full field imaging x-ray microscope operating at energy levels in the range of 40- 150KeV. The instrument consists of an x-ray source of 150kV/ 10W and a thermoelectric cooled CCD detector with magnification in the range of X1- X20. The instrument has a capability for both 2-D transmission imaging and 3-D tomographic imaging. The instrument is supplied with a software package, consisting of a TXM controller, a reconstruction engine, and a 3D viewer, for microscope control and image analysis.

4.2.7 Data Acquisition System (DAQ)

Data collection during tensile and creep tests was performed by a SCXI-1000 Data acquisition system from National Instruments Inc., USA. The system consisted of a SCXI- 1121 signal conditioning module fitted into a SCXI- 1000 chassis and connected



(a)



(b)

Figure 4.12: (a) Nikon's LV100 Eclipse optical microscope, and (b) Xradia MicroXCT microscope.



Figure 4.13: Data acquisition system with Labview software.

to a SCXI-1321 terminal block, shown in *Figure 4.13*. The DAQ unit was connected to a PCIe-6251 multifunctional DAQ board, fitted in to a computer, using a shielded cable. A Labview based program was used for data sampling and logging at different rates during test. The data sampling rate was set to 1000 kHz while the logging rate was varied from 1 data point/ sec to 1 data point/ 300sec. The hardware was programmed to acquire three independent parameters (strain, load and position) simultaneously for each test.

4.2.8 Rationale for selection of creep test parameters

4.2.8.1 Creep test time

The magnitude of creep and the change in curvature of the creep curve with time should be substantial enough to verify the model predictions reliably. Due to the presence of orthogonal fibers, the magnitude of creep and change in curvature of the creep curve is significantly low within the test duration of few hours to few days. Creep rate due to viscoelastic deformation decreases with increase in creep time and hence, the time required for similar magnitude increase in creep compliance would typically increase logarithmically with increase in creep time. For the case of plain weave composites, the orientation of high modulus fibers along the load axis during on-axis loading reduced the creep magnitude significantly. Hence, temperature was used as an accelerating factor to obtain the creep data in a reasonable time period than increasing the creep time at a given temperature. Creep curves beyond the experimental time window were generated through accelerated testing at higher temperatures and TTSP, discussed in Chapter 2. One key requirement for successful superposition is: parts of creep curves at two successive temperatures should overlap; e.g. the end portion of creep curve at T_1 should overlap with beginning portion of creep curve at T_2 as shown in the schematic shown in *Figure 4.14*.

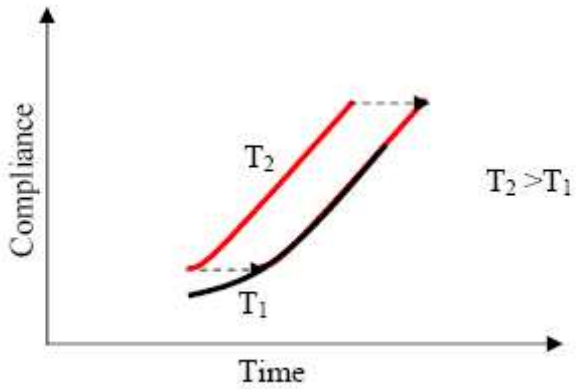


Figure 4.14: Time-Temperature Superposition Principle (TTSP) procedure.

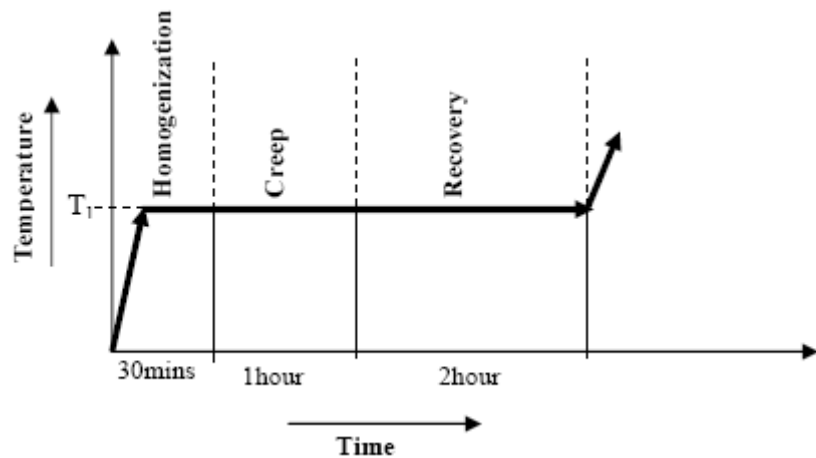


Figure 4.15: Time and steps used for each creep test.

The temperature steps and creep time at a temperature must be carefully chosen such that the above requirement is met. Larger the temperature jump, longer should be the creep time at a temperature. In this study, preliminary experiments were conducted to determine this. Based on this, temperature steps of 20°C and creep time of 1 hour was chosen.

Secondly, the time taken to complete each creep test was about 3.5 hours as shown in *Figure 4.15*. The recovery time was normally twice the creep time to recover all the creep strain upon loading so that the same test coupon could be tested at multiple temperatures. This time would significantly increase if creep time is increased. Additionally, the number of specimens would have also increased. These were also taken into consideration while choosing the test parameters.

Based on the considerations discussed above, the accelerated testing scheme given in *Tables 4.4* and *4.5* was selected.

4.2.8.2 Creep Stress and Temperature

As mentioned in Section 4.2.5, process-induced damage developed in the materials used in this study. Such cracks are termed vertical cracks in the literature [78]. Similar process-induced damage has been reported previously in cross-ply laminates [0/90]_s, made of F263/ T300 epoxy/ carbon fiber unidirectional prepreg [2, 78]. Cross-ply laminate had shown process-induced transverse cracks (along the thickness direction) as well as process-induced vertical cracks (along the length direction), immediately after the manufacturing of the composite panel, as shown in *Figure 4.16*. Even though, one can manufacture a woven composite panel without introducing these vertical cracks after post-curing using different composite material, such cracks in these composite material

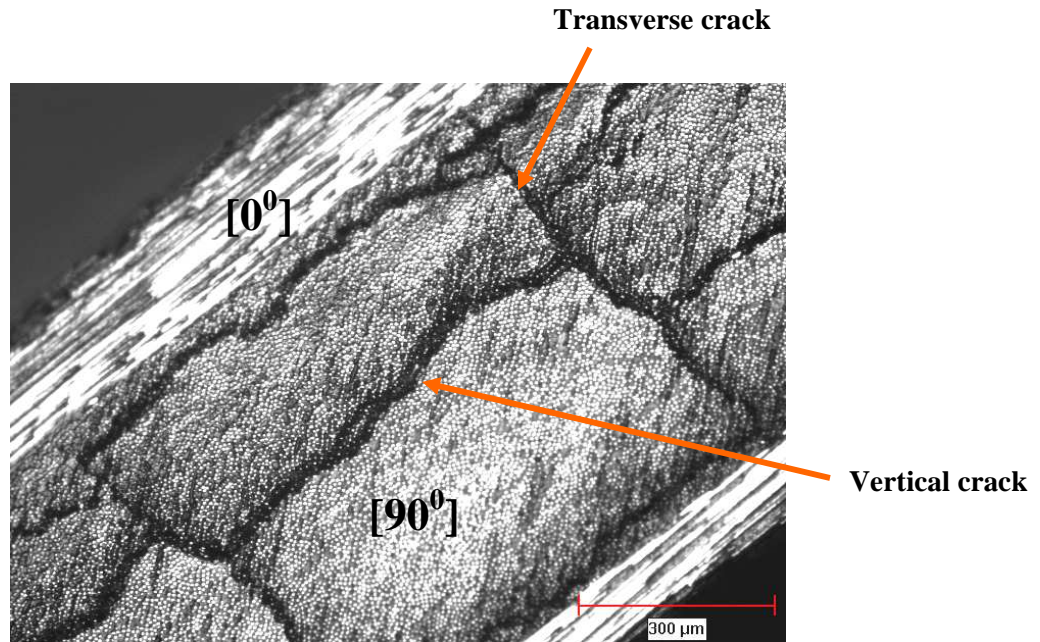


Figure 4.16: Micrograph of cross-ply laminate $[0/90_2]_s$ with transverse and vertical cracks (X 100) [78].

could not be avoided. The primary reason for these cracks were thought to be due to process-induced residual stresses caused by the mismatch in cure shrinkage and thermal expansion coefficients (CTE) between the $[0^0]$ and $[90^0]$ plies of the laminate. Since, woven fabric composites also consists fiber yarns woven in orthogonal directions ($[0^0]$ and $[90^0]$), the mismatch in CTE is believed to be the reason for this cracking. Transverse cracking along the thickness direction of the transverse yarns was not observed. Ahci and Talreja [29] reported transverse cracks in woven composites at higher temperatures and discussed there effect on creep. However, none of the published studies have recorded vertical cracking and its effect on mechanical properties of woven composites. Additionally, the damage can increase during loading to a creep load as well as during creep. Birur et. al [2] have completed a detailed study on such increase in damage in multidirectional non-woven composites as well as their impact on creep rupture.

In the present study, the creep model does not have the capability to predict creep with damage. Thus, in order to make sure that the creep results are not affected by this damage, a thorough preliminary investigation was pursued to examine the impact of such damage on the tensile and creep behavior of plain weave composites used in this study. Based on this investigation, the creep stress and temperature tabulated in *Tables 4.4* and *4.5* were chosen. The investigation was carried out in two steps as follows:

Step 1- Repeated loading-unloading tensile tests (3-4 cycles) were conducted on a single $[0, 90]_6$ test coupon to different stress levels up to its fracture stress. The modulus during the loading cycle and any un-recovered strain upon unloading were recorded. Additionally, the edges of the test coupons were examined after each unloading step using a digital microscope to record any increase in damage. For on-axis loading, no

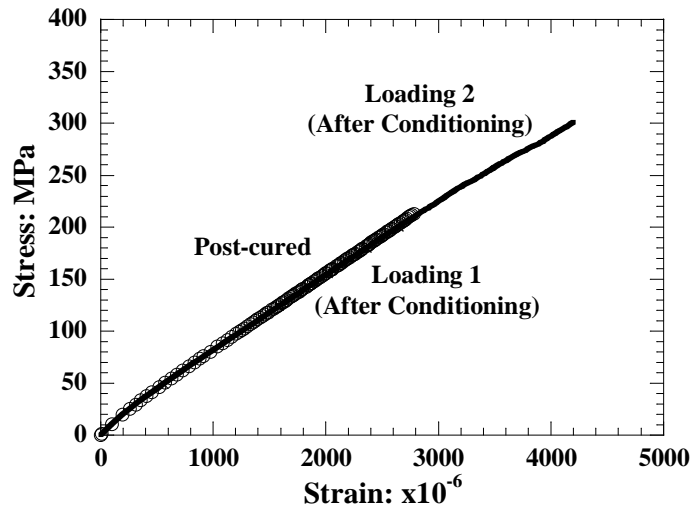


Figure 4.17: Stress-strain plots for $[0, 90]_6$ plain weave composite coupon tested under repeated loading- unloading at room temperature.

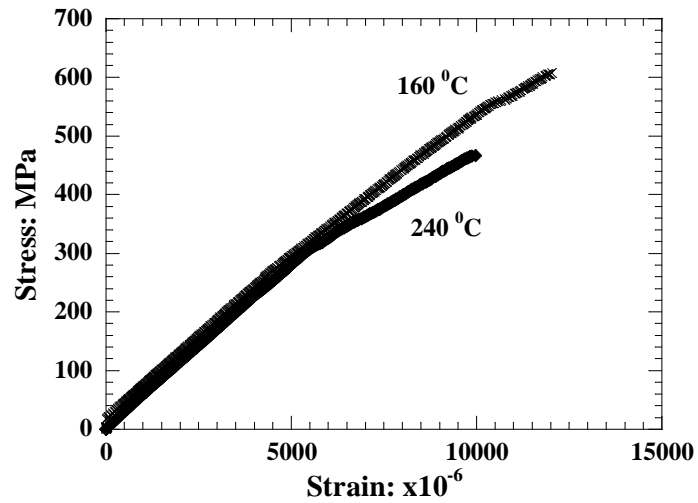


Figure 4.18: Stress-strain plots for $[0, 90]_6$ plain weave composite coupon tested at 160 °C and 240 °C.

permanent strain was recorded. The modulus during the reloading cycle was the same as that of the initial modulus, as illustrated by the stress- strain plot at room temperature in *Figure 4.17*. The test coupon did not show any increase in the number of cracks even after loading to a stress, close to the fracture stress of plain weave composites. These results confirmed that the process-induced damage did not increase further during loading to a creep load at room temperature. Additional tests at higher temperatures confirmed that the process induced damage did not increase during loading to a creep load up to a test temperature of 160 $^{\circ}\text{C}$. However, the coupons tested at 180 $^{\circ}\text{C}$ and above showed additional vertical cracks, away from the fracture surface, when loaded up to fracture stress. The number of vertical cracks was found to increase from 6-8 cracks before test to 15-20 cracks after the test along the length of the coupon. It can be expected that this increase in vertical cracks may cause the reduction in modulus and strength of the composites above 160 $^{\circ}\text{C}$, when loaded close to the fracture stress. This effect can be observed in *Figure 4.18*, tensile test results obtained at 240 $^{\circ}\text{C}$, where the tensile stress-strain curve obtained at 240 $^{\circ}\text{C}$ showed a sudden change in slope, when compared to the stress- strain curve generated at 160 $^{\circ}\text{C}$ at stress levels closer to fracture stress due to an increase in the number of vertical cracks.

Step 2- Based on the results from Step 1, preliminary creep tests were completed at temperatures up to 160 $^{\circ}\text{C}$. These test specimens did not exhibit any un-recovered strain upon loading. However, considerable un-recovered strain was recorded after creep tests at temperatures above 160 $^{\circ}\text{C}$, as shown *Figure 4.19*. The coupons at temperature above 160 $^{\circ}\text{C}$ were found to develop additional vertical cracks as well as inter-laminar cracks along the edges, as shown in *Figure 4.20*. The maximum temperature below which

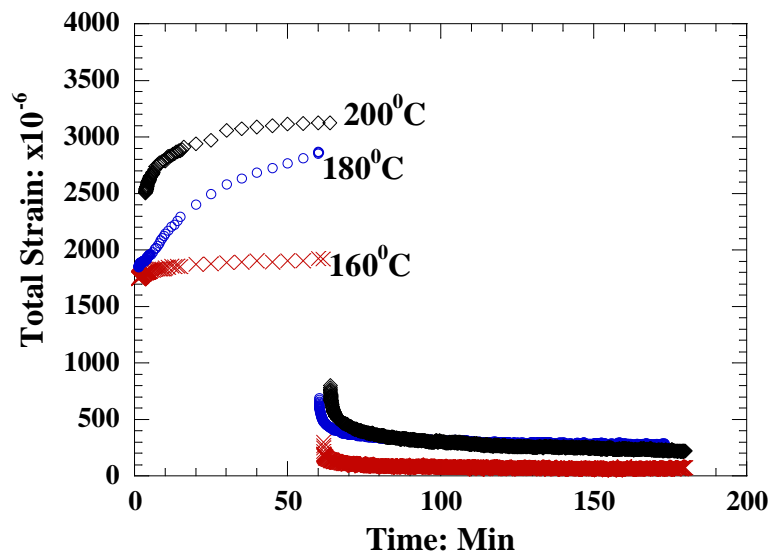


Figure 4.19: Creep-recovery plots for $[0, 90]_6$ plain weave composite coupons subjected to on-axis loading (100MPa) at various temperatures

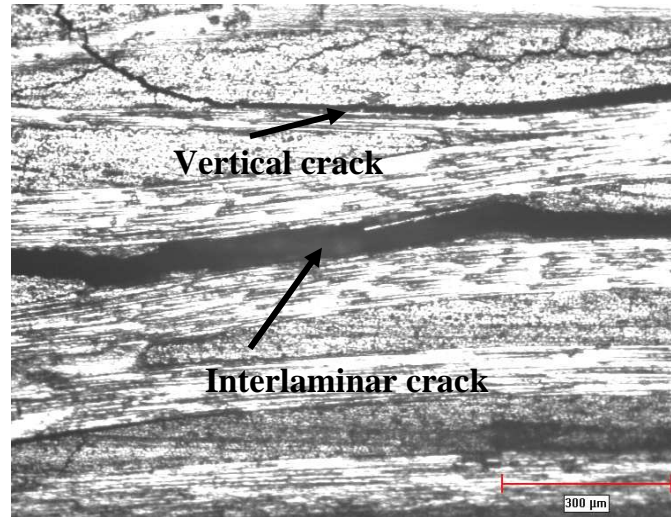


Figure 4.20: Micrograph of polished edge of a $[0, 90]_6$ plain weave composite coupon after creep test at 180°C and 100 MPa stress.

damage did not increase during creep decreased with increase in creep stress level. Based on the above results, the creep test temperature was limited to 160 $^{\circ}\text{C}$ for on-axis and off-axis creep tests, for stress levels of 15- 70% UTS. However, the test temperature was extended up to 240 $^{\circ}\text{C}$ for stress levels below 7MPa for on-axis creep tests, since the preliminary tests did not record any increase in vertical cracks. The maximum creep stress was limited to 70% UTS for the following reason: any further increase in stress decreased the maximum test temperature that can yield creep data without the influence of damage. This, in turn, reduced the time window for the master creep curve, which could not be used to validate the simulation results due to relatively small increase in creep compliance.

4.2.9 Precision, resolution and repeatability of test results

The maximum creep strain measured during on-axis loading at the lowest test stress and temperature was 15microstrains, while that measured at highest test stress and temperature was 600microstrains. Since, the range of the measured creep strain is not very high, it is important to obtain the highest resolution and least fluctuation in the measured strain, resulting in highest precision in the measured strain. The precision in measured strain depends on a number of factors such as resolution and noise in strain measurements, and fluctuations in load and ambient temperature.

In the present work, WK strain gages from Micro Measurements Group Inc. and dynamic strain gage extensometers from Instron Inc. were used for strain measurement during creep tests. The DAQ was set to use for the strain resolution of 1microstrain (gage factor = 2.12; gage resistance = 350ohm; excitation voltage = 3.33V). However, due to noise in the acquired data, a fluctuation of \pm 2.5microstrains was observed, as shown in

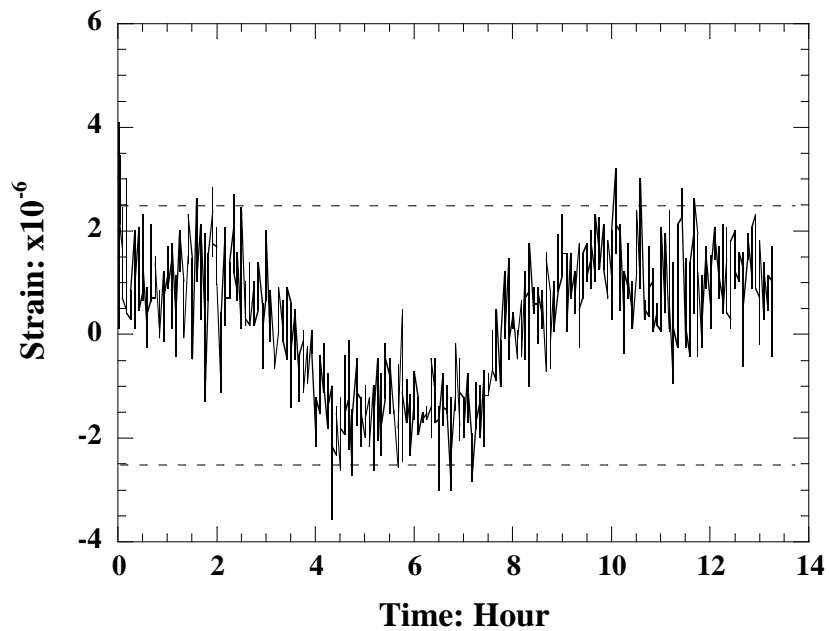
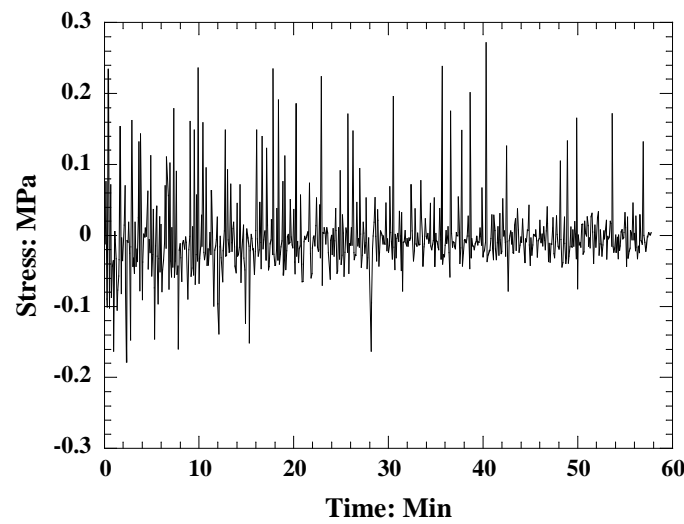
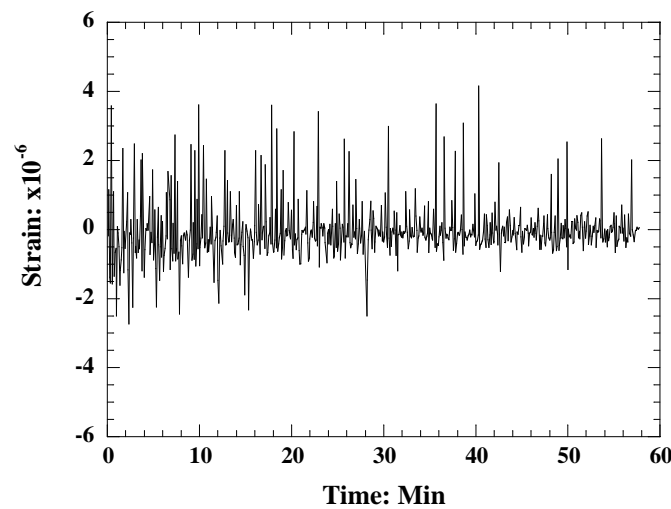


Figure 4.21: Fluctuation in acquired strain data from DAQ



(a) Stress variation



(b) Strain variation

Figure 4.22: Stress and strain variation at a given applied stress and temperature.

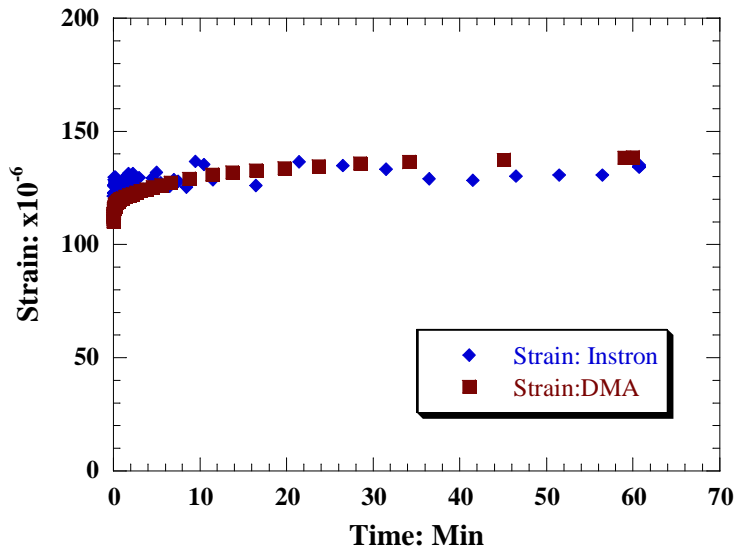


Figure 4.23: Comparison of on-axis strain measured at 7MPa and 80 °C using DMA and Instron testing machine.

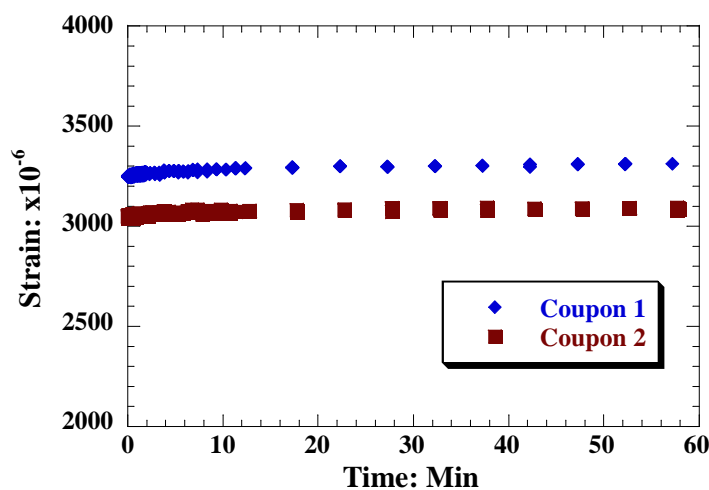


Figure 4.24: Comparison of creep test results at 200MPa and 80 °C using two different test coupons under on-axis loading.

Figure 4.21. This noise was recorded within DAQ system using an in-built program in Labview software (TDM streaming). This noise may be due to a number of factors such as electrical noise in the power supply, noise picked up by the cables, fluctuation in the ambient temperature of the test lab, etc. The test instruments with \pm 25kN load cell, have a capability to maintain the desired load within \pm 0.05% of the applied stress at any given test temperature and stress. The stress fluctuation was recorded through Bluehill software by applying a constant stress on a test coupon for a time period of 1 hour. The stress fluctuation is shown in *Figure 4.22a*. Using this stress fluctuation and composite modulus (65GPa), the corresponding strain fluctuation was calculated, which varied by \pm 3microstrains as shown in *Figure 4.22b*. The magnitude of this is similar to that due to noise in *Figure 4.21*. Thus, even though the resolution of the DAQ system is 1microstrain, the precision in the measured creep strain is about \pm 5microstrains.

Repeatability of creep test results was verified by repeating the test using a second test coupon at select stresses and temperatures. In the present study, DMA and Instron testing machine were used to perform creep experiments. The creep strain measured at 7MPa and 80 $^{\circ}$ C using both instruments, under on-axis loading, is compared in *Figure 4.23*. The measured strain obtained from both instruments compared well within the range of 5-10microstrains. Creep strains from two different test coupons tested at 200MPa and 80 $^{\circ}$ C, under on-axis loading, are compared in *Figure 4.24*. The scatter in instantaneous strain is \pm 3%, variation from one coupon to other. However, the creep strain measured from both the tests compare well with repeatability range of 10-15microstrain or \pm 2.5%. Similar repeatability was also observed in other tests such as

on-axis creep test at 100MPa/ 80 $^{\circ}$ C, off-axis loading tests at 7MPa/ 80 $^{\circ}$ C and 50MPa/ 120 $^{\circ}$ C. These results confirmed repeatability within \pm 2.5%.

4.2.10 Experimental procedure for unidirectional composites

As stated in chapter 3, the creep model for plain weave composites utilizes creep data of unidirectional tape composites. The experimental creep data for unidirectional composites was generated previously [4, 5] in the linear viscoelastic region of its polymer matrix. However, experimental creep data for unidirectional composites in nonlinear viscoelastic region was absent and was generated in the present work. This nonlinear creep data was used to model the creep of unidirectional composites using modified Schapery's model, which will be described in Section 4.3.

Hexcel Corporation's F263-8/T300 epoxy/carbon fiber unidirectional tape composite was used in the study. Longitudinal ($S_{11}(t)$), transverse ($S_{22}(t)$) and shear ($S_{66}(t)$) creep compliance for unidirectional composites in the nonlinear viscoelastic region were generated. Test coupons were prepared using the procedure described in Section 4.2.2. Coupon dimensions and configurations are given in *Table 4.6*. Longitudinal creep compliance ($S_{11}(t)$) was measured using [0]₈ coupons loaded along the fiber direction, as shown in *Figure 4.25*, in the stress range of 15- 50 % UTS. Transverse creep compliance ($S_{22}(t)$) was measured using [90]₈ test coupons loaded perpendicular to the fiber axis, as shown in *Figure 4.25*, in the stress range of 25-80% UTS. Shear creep compliance ($S_{66}(t)$) was measured using [10]₈ test coupons in the stress range of 25- 50% UTS. Shear strain was recorded using two strain gages at an angle of $\pm 45^{\circ}$ to the fiber axis shown in *Figure 4.25*. The difference in strain recorded by

Table 4.6: Test coupon dimensions for various coupon configurations.

Direction	Gage Length (mm)	Width (mm)	Thickness(mm)
[0]₈	50.0 \pm 1.0	12.5 \pm 0.5	1.6 \pm 0.1
[90]₈	50.0 \pm 1.0	12.5 \pm 0.5	1.6 \pm 0.1
Shear [10]₈	50.0 \pm 1.0	12.5 \pm 0.5	1.6 \pm 0.1

Table 4.7: Creep and recovery test scheme for unidirectional composites in nonlinear viscoelastic region of matrix.

Measured Compliance (MPa ⁻¹)	Coupon Configuration	Temperature (°C)	Applied Stress (MPa)	Creep/recovery test time (hrs per temp.)
S ₁₁ (t)	[0]₈	80- 160	200, 400, 800	1/1
S ₂₂ (t)	[90]₈	80- 160	10, 15, 27, 33	1/1
S ₆₆ (t)	[10]₈	80- 160	15, 18, 21, 24	1/1

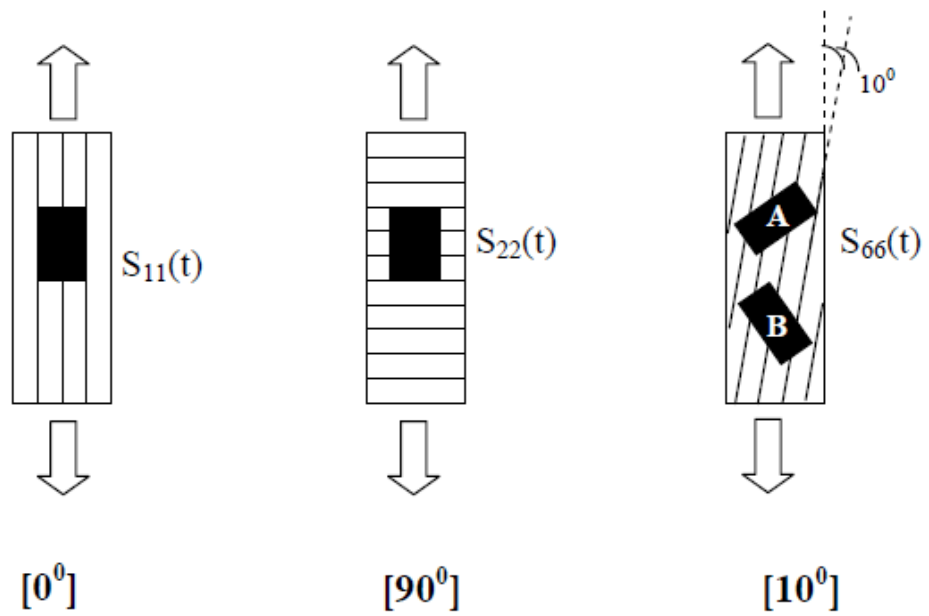


Figure 4.25: Test coupon configurations used to measure $S_{11}(t)$, $S_{22}(t)$ and $S_{66}(t)$.

gages A and B yielded the desired shear strain. Chamis et al. [79] have demonstrated that the 10^0 off-axis test method is an easy and accurate method to characterize in-plane shear properties. Similar procedure was adapted previously [5] to characterize the shear creep compliance (S_{66}) of unidirectional composites in linear viscoelastic region. Each creep test was followed by recovery. The recovery strain was used in the determination of nonlinear parameters. Creep and recovery strain were recorded using WK-06-125BT-350 strain gages from Micro Measurements Group Inc., NC, USA, as discussed in section 4.2.2.4. All creep and recovery tests were performed on Instron 8562 machine at different temperatures and stresses in the nonlinear viscoelastic region of matrix. Strain data was recorded using National Instruments' SCXI- 1000 data acquisition system. Strain rate used for loading to a creep stress was 10^{-4} sec^{-1} . The creep and recovery test scheme is shown in *Table 4.7*.

4.3 Simulation Approach

An analytical model to predict creep of plain weave polymer woven composites under tensile loading is presented in Chapter 3. This model was programmed in MATLAB to simulate the creep, which will be discussed in section 4.3.3. A representative two-dimensional unit cell was used to simulate the creep compliance of plain weave composites. This unit cell was assumed to be made up of unidirectional tape laminae. Creep data of unidirectional tape lamina and microstructural details of the unit cell were input into the MATLAB program. These three components of simulation,

namely the microstructure, creep data for unidirectional lamina, and MATLAB program are discussed below.

4.3.1 Microstructural input parameters

As shown in *Figure 4.26*, the following microstructural parameters were required as input for MATLAB program: length of unit cell (a_0); thickness of the unit cell (h_0) and undulation length (a_u). These parameters were obtained using the micrograph of plain weave composite. A detailed discussion on these parameters is presented in Chapter 5.

4.3.2 Creep data for unidirectional composites

The creep data in the linear viscoelastic region was generated previously [4, 5]. The creep data in the nonlinear viscoelastic region was generated as a part of this thesis work. Despite this, the latter is discussed below rather than in Chapter 5 on ‘Results and Discussion’ because of the author’s desire to dedicate Chapter 5 purely to the discussion on results on creep of plain weave composites.

The experimental creep data of unidirectional tape lamina was fitted and modeled using modified Kohlraush William Watts Equation (KWW equation) [5] given as,

$$S(t) = g_0 S_0 + g_1 g_2 X \left[1 - \exp \left[- \left[\frac{t}{a_\sigma B} \right]^C \right] \right] \quad (4.3)$$

where,

$S(t)$ is the time-dependent compliance,

S_0 is the instantaneous compliance of unidirectional lamina,

t is time in minutes,

X, B and C are the constants,

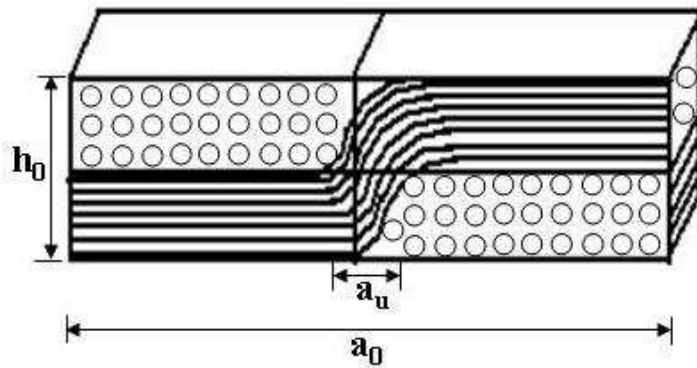


Figure 4.26: Schematic of one - dimensional plain weave unit cell with identified microstructural parameters required as input to the creep model.

Table 4.8: Constants for modified KWW equation used in simulating the time-dependent compliance of unidirectional tape lamina at a reference temperature of 80 °C in linear viscoelastic range of its polymer matrix.

Equation Constants	$S_{11U}(t)$	$S_{22U}(t)$	$S_{66U}(t)$
$S_0 (\text{MPa}^{-1})$	7.115×10^{-6}	122.22×10^{-6}	200×10^{-6}
X	0.004675	0.002675	0.002113
B(min)	1.001×10^{22}	3.882×10^{12}	2.5416×10^7
C	0.3762	0.2863	0.3638

g_0 , g_1 , g_2 and a_σ are the nonlinear parameters defined by Schapery's nonlinear viscoelastic model [35]. These nonlinear parameters are equal to one in the linear viscoelastic region of polymer matrix; however, they are dependent on temperature and stress in the nonlinear viscoelastic region of polymer matrix, as described by equation 4.4.

$$\{g_0, g_1, g_2, a_\sigma\} = \begin{cases} 1, & \text{Linear viscoelastic region} \\ f(\sigma, T), & \text{Nonlinear viscoelastic region} \end{cases} \quad (4.4)$$

Equations 4.3 and 4.4 have been successfully used in the past to model and predict the in-plane creep compliances of unidirectional lamina in the linear viscoelastic region [5]. The model constants, obtained by fitting the experimental creep data for unidirectional lamina, were generated by Iyer [4] and Balachander [5] in the linear viscoelastic region of its matrix, using equation 4.3 are tabulated in *Table 4.8*.

The nonlinear parameters were obtained using experimental creep data generated as a part of this thesis for unidirectional lamina in the nonlinear viscoelastic region. The procedure used to obtain these parameters is described below.

4.3.2.1 Determination of nonlinear parameters

The nonlinear parameters of the Schapery's model [35] were determined following a data reduction method developed by Zaoutsos et al. [80] and Papanicolaou et al. [81, 82], which is described below.

4.3.2.1.1 Theoretical background

For a uniaxial load history, illustrated in *Figure 4.27*, the time-dependent nonlinear viscoelastic response of a unidirectional tape composite will be as shown in *Figure 4.28* and is modeled by Schapery's model [35] as:

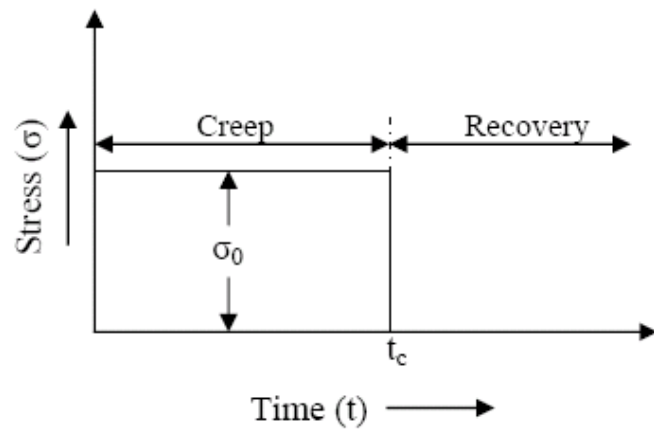


Figure 4.27: Creep and recovery test

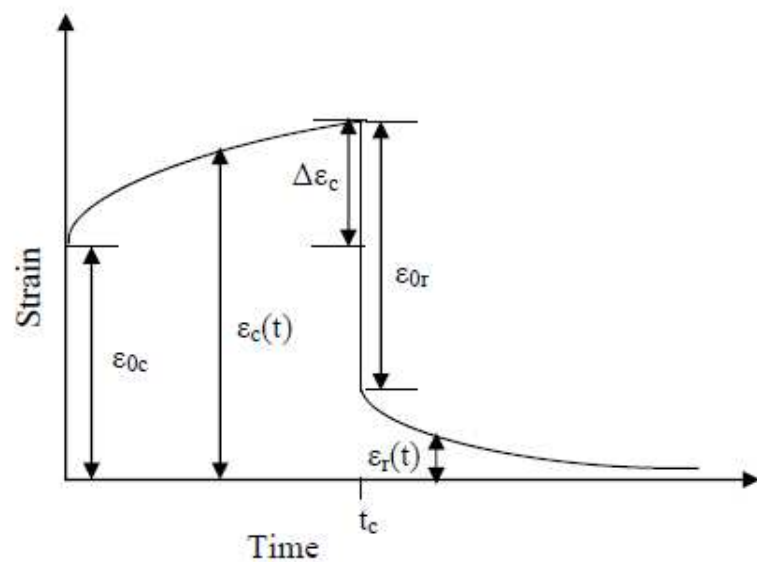


Figure 4.28: A typical strain-time curve generated during a creep-recovery test

$$\varepsilon_c(t) = g_0 S_0 \sigma_0 + g_1 \int_0^t \Delta S(\Psi - \Psi_1) \frac{d(g_2 \sigma)}{d\tau} d\tau \quad (4.5)$$

where, S_0 is the instantaneous compliance and $\Delta S(\psi)$ is the transient time dependent compliance. ψ and ψ_1 are reduced times defined as:

$$\Psi = \int_0^t \frac{dt'}{a_\sigma}; \quad \Psi_1 = \Psi(\tau) = \int_0^\tau \frac{dt'}{a_\sigma} \quad (4.6)$$

g_0 , g_1 , g_2 and a_σ in equation 4.6 are the time-independent nonlinear parameters. g_0 defines the effect of stress and temperature on instantaneous compliance, while, g_1 defines similar effect on creep component of the total compliance. g_2 is the stress and temperature dependent factor considering effect of loading rate during creep. a_σ is the stress shift factor.

Referring to *Figure 4.27*, when a constant stress σ_0 is applied at $t=0$ and subsequently removed at $t=t_c$, the stress history can be given as:

$$\sigma(t) = \sigma_0 [H(t) - H(t - t_c)] \quad (4.7)$$

where $H(t)$ is the Heaviside step function.

By substituting equations 4.6 and 4.7 in to equation 4.5, the time-dependent strain for creep and recovery can be obtained using equations 4.8 and 4.8 respectively,

$$\varepsilon_c(t) = g_0 S_0 \sigma_0 + g_1 g_2 \Delta S \left(\frac{t}{a_\sigma} \right) \sigma_0 \quad \text{for } 0 < t < t_c \quad (4.8)$$

$$\varepsilon_r(t) = [\Delta S \left(\frac{t_c}{a_\sigma} + t - t_c \right) - \Delta S(t - t_c)] g_2 \sigma_0 \quad \text{for } t > t_c \quad (4.9)$$

The viscoelastic creep strain at $t = t_c$ can be calculated by subtracting the instantaneous compliance ($g_0 S_0 \sigma_0$) from the total viscoelastic strain given by equation 4.8, and is given as:

$$\Delta \epsilon_c(t_c) = g_1 g_2 \Delta S \left(\frac{t_c}{a_\sigma} \right) \sigma_0 \quad (4.10)$$

By substituting the value of $(g_2 \sigma_0)$ from equation 4.10 in to equation 4.9, the expression for recovery strain can be written as:

$$\epsilon_r(t) = \frac{\Delta \epsilon_c(t_c)}{g_1} \left[\frac{\Delta S \left(\frac{t_c}{a_\sigma} + t - t_c \right) - \Delta S(t - t_c)}{\Delta S \left(\frac{t_c}{a_\sigma} \right)} \right] \text{ for } t > t_c \quad (4.11)$$

The creep component of the compliance is represented by the modified KWW equation, i.e.,

$$\Delta S(t) = X \left[1 - \exp \left[- \left[\frac{t}{B} \right]^C \right] \right] \quad (4.12)$$

By substituting equation 4.12 into equations 4.8 and 4.11, the following expressions for total viscoelastic strain and recovery strain can be obtained,

$$\epsilon_c(t) = g_0 S_0 \sigma_0 + g_1 g_2 X \left[1 - \exp \left[- \left[\frac{t}{B} \right]^C \right] \right] \sigma_0 \quad \text{for } 0 < t < t_c \quad (4.13)$$

and

$$\varepsilon_r(t) = \frac{\Delta\varepsilon_c(t_c)}{g_1} \left[\frac{\exp\left[-\left[\frac{t-t_c}{B}\right]^C\right] - \exp\left[-\left[\frac{\frac{t_c}{a_\sigma}+t-t_c}{B}\right]^C\right]}{1 - \exp\left[-\left[\frac{t}{B}\right]^C\right]} \right] \quad \text{for } t > t_c \quad (4.14)$$

4.3.2.1.2 Data reduction method

The data reduction method developed by Zaoutsos et al. [80-82] was used to obtain the nonlinear parameters.

Using equation 4.8, the viscoelastic strain at time $t = t_c^-$, the time just before unloading, can be given as:

$$\varepsilon_c(t_c^-) = g_0 S_0 \sigma_0 + g_1 g_2 \Delta S \left(\frac{t_c^-}{a_\sigma} \right) \sigma_0 \quad (4.15)$$

Similarly, the viscoelastic recovery strain at time $t = t_c^+$, the time just after unloading, following equation 4.9, is given as:

$$\varepsilon_r(t_c^+) = g_2 \Delta S \left(\frac{t_c^+}{a_\sigma} \right) \sigma_0 \quad (4.16)$$

Further, the viscoelastic creep strain at $t = t_c^-$ can be obtained from equation 4.10 as:

$$\Delta\varepsilon_c(t_c^-) = g_1 g_2 \Delta S \left(\frac{t_c^-}{a_\sigma} \right) \sigma_0 \quad (4.17)$$

In case of linear viscoelastic behavior, the instantaneous strain response (ε_{0c}) at $t = 0^+$ is equal to the instantaneous strain response (ε_{0r}) at $t = t_c^+$. However, in the case of nonlinear viscoelastic behavior, these two values will be different. Thus, the difference between the two strains corresponding to the time of the instantaneous unloading ($t = t_c^+$) and the time of the instantaneous loading ($t = 0^+$), respectively, can be given as:

$$\Delta\varepsilon_0 = \varepsilon_{0r} - \varepsilon_{0c} \quad (4.18)$$

where, ε_{0r} is determined using equations 4.15 and 4.16 as:

$$\varepsilon_{0r} = \varepsilon_c(t_c^-) - \varepsilon_r(t_c^+) = \varepsilon_c(t_c^-) - g_2 \Delta S \left(\frac{t_c^+}{a_\sigma} \right) \sigma_0 \quad (4.19)$$

and ε_{0c} was obtained by rearranging equation 4.15 as:

$$\varepsilon_{0c}(t_c^-) = g_0 S_0 \sigma_0 = \varepsilon_c(t_c^-) - g_1 g_2 \Delta S \left(\frac{t_c^-}{a_\sigma} \right) \sigma_0 \quad (4.20)$$

Substituting equations 4.19 and 4.20 into equation 4.18,

$$\Delta\varepsilon_0 = g_2(g_1 - 1) \Delta S \left(\frac{t_c}{a_\sigma} \right) \sigma_0 \quad (4.21)$$

$g_2 \Delta S \left(\frac{t_c}{a_\sigma} \right) \sigma_0$ in the above equation can be substituted by values from equation 4.17

yielding an equation for g_1 as:

$$g_1 = \frac{\Delta\varepsilon_c(t_c)}{(\Delta\varepsilon_c(t_c) - \Delta\varepsilon_0)} \quad (4.22)$$

g_1 is calculated using the values of $\Delta\varepsilon_c(t_c)$ and $\Delta\varepsilon_0$, which can be obtained from a creep-recovery experiment as illustrated in *Figures 4.27 and 4.28*.

g_0 is calculated as the ratio of the instantaneous compliance upon loading ($t = 0^+$) in a creep-recovery experiment in the nonlinear creep region to the instantaneous compliance after loading ($t = 0^+$) in a creep-recovery experiment in the linear region, and is given as,

$$g_0 = \frac{(\varepsilon(t_0^+)/\sigma_0)_{nl}}{(\varepsilon(t_0^+)/\sigma_0)_l} \quad (4.23)$$

Once, g_0 and g_1 are calculated for a given creep curve at a stress in nonlinear region, the time shift factor (a_σ) due to applied stress was calculated numerically by fitting the experimental recovery data using equation 4.14.

Finally, g_2 is calculated using equation 4.21 as,

$$g_2 = \frac{\Delta\varepsilon_0}{(g_1 - 1)\Delta S\left(\frac{t_c}{a_\sigma}\right)\sigma_0} \quad (4.24)$$

Once, all nonlinear parameters are obtained, the total viscoelastic strain is calculated using equation 4.13 and the corresponding compliance is calculated as,

$$S(t) = \frac{\varepsilon_c(t)}{\sigma_0} \quad (4.25)$$

4.3.2.2 Results of nonlinear parameters for unidirectional composites

Creep-recovery experiments were completed in this research project at various temperatures and stresses using $[0^0]$, $[90^0]$ and $[10^0]$ unidirectional composites in the nonlinear viscoelastic region, following the procedure described in section 4.2.11. The epoxy matrix in the composites used in the present work has been found to exhibit creep in the linear viscoelastic region up to a stress level of 5MPa and nonlinear creep beyond

5MPa [4]. Thus, the nonlinear parameters were set equal to 1 up to a stress level of 5MPa and were derived as a function of temperature and stress beyond 5MPa using experimental results and following the procedure discussed in the previous section.

Longitudinal Compliance: The creep-recovery data for [0⁰] composites was obtained in the temperature range of 80-160 ⁰C and in the stress range of 15-50 % (200-800MPa) of ultimate tensile strength of [0⁰] composites. The creep curves at different temperatures are plotted in *Figure 4.29*. The creep curves at various temperatures and a constant stress were shifted (using TTSP) to a reference temperature of 80 ⁰C and are plotted in *Figure 4.30*. Since creep of [0⁰] composites is dominated by the fiber, the composite exhibited neither appreciable creep nor any nonlinearity with increase in stress, even when its matrix is in the nonlinear viscoelastic region. Thus, it was concluded that the creep compliance did not change with stress and temperature (within the test range) and hence, values of all four nonlinear parameters were equal to 1 for [0⁰] composites in the nonlinear viscoelastic region of its epoxy matrix.

Transverse Compliance: The creep-recovery data for [90⁰] composites were obtained in the temperature range of 80-160 ⁰C and in the stress range of 25- 80% UTS (10-33MPa). Transverse creep compliance at various stress levels and at a temperature of 80 ⁰C is plotted in *Figure 4.31*. The time for start of creep is longer for higher stresses (15-33MPa) due to longer loading time to reach the desired creep load. Since, transverse creep is matrix dominant, these creep curves show nonlinearity above 5MPa stress. The nonlinear parameters were calculated from each creep-recovery data, obtained at various

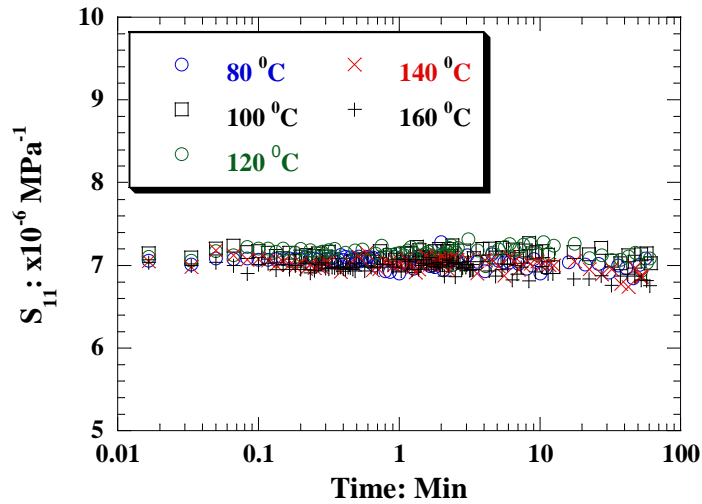


Figure 4.29: Longitudinal creep compliance (S_{11}) plots at various temperatures and at a constant stress of 200 MPa.

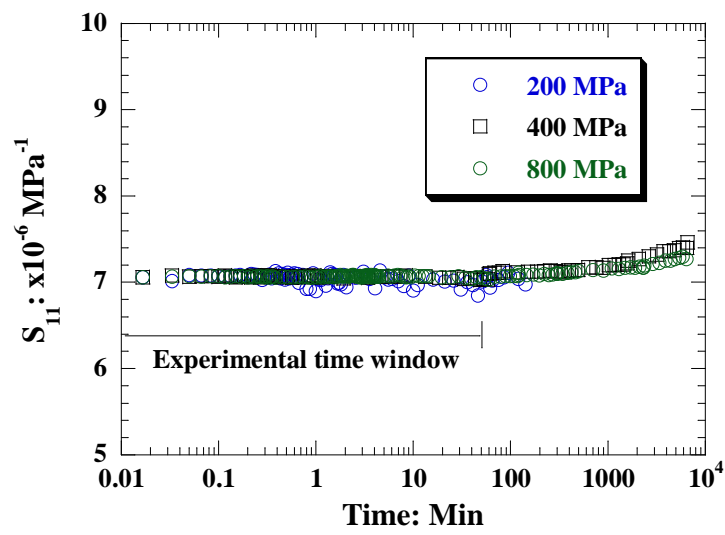


Figure 4.30: Master creep compliance (S_{11}) plots at various stress levels and a reference temperature of 80 °C.

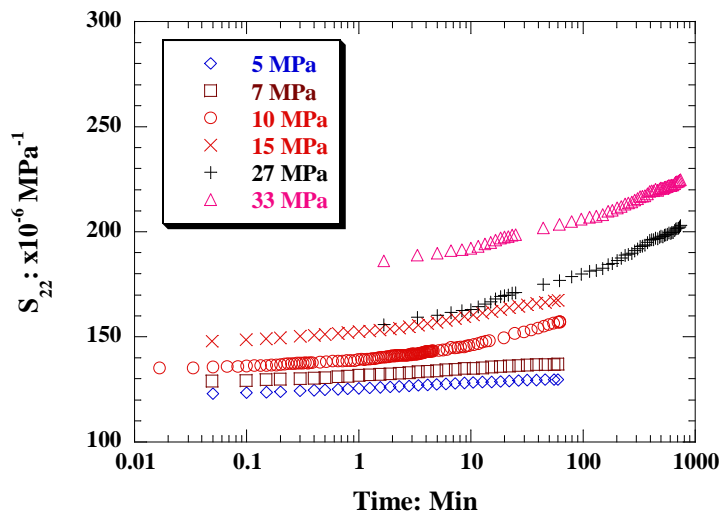


Figure 4.31: Transverse creep compliance (S_{22}) plots at various stress levels and a constant temperature of 80°C .

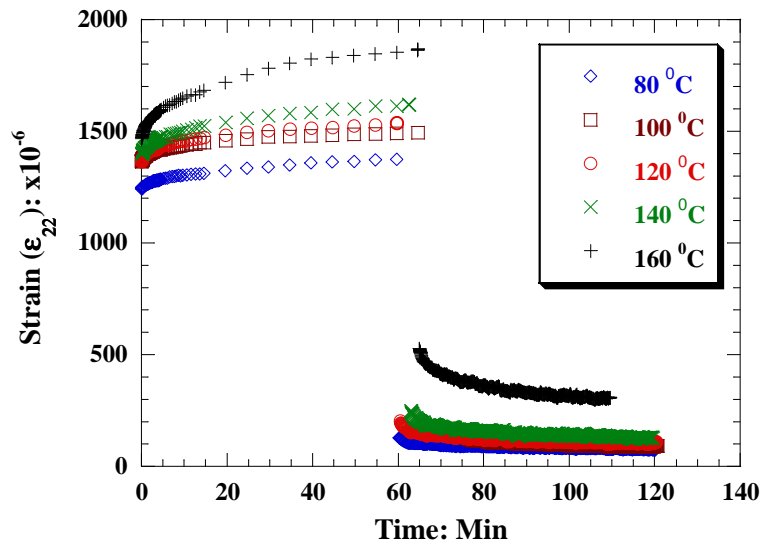


Figure 4.32: Creep and recovery data for $[90^{\circ}]_s$ test coupon at various temperatures ranging $80\text{-}160^{\circ}\text{C}$ and at a stress level of 10MPa .

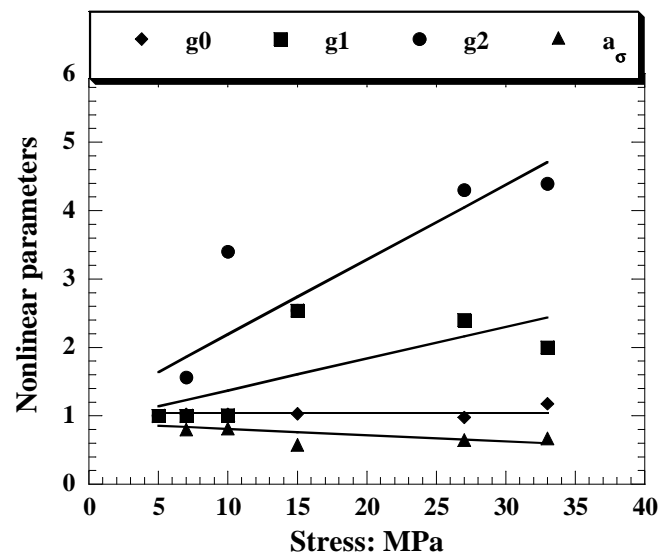
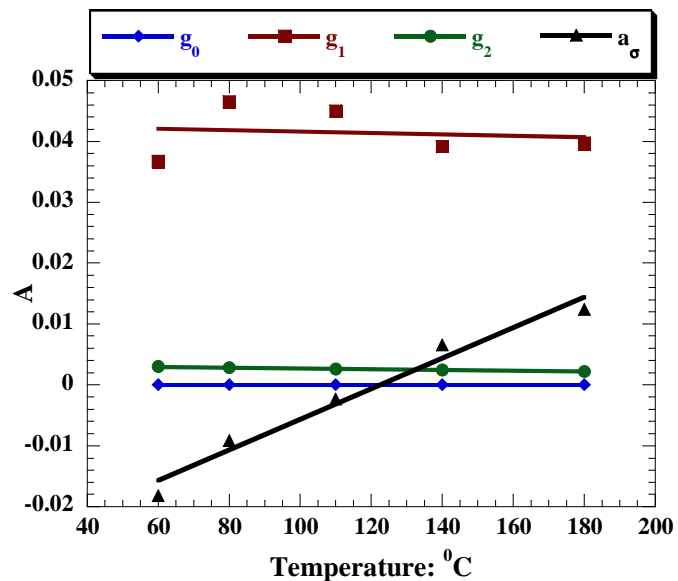
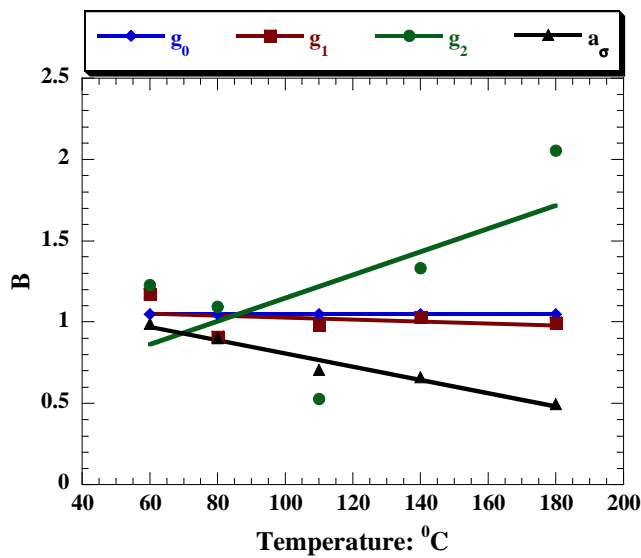


Figure 4.33: Plot of nonlinear parameters for transverse compliance (S_{22}) at various stress levels and a temperature of 80°C .



(a)



(b)

Figure 4.34: Plot of constants A and B at various temperatures and a stress level of 10MPa.

temperatures and stresses. A creep-recovery plot at a stress of 10MPa and various temperatures ranging from 80-160 $^{\circ}\text{C}$ is shown in *Figure 4.32*. The nonlinear parameters obtained using these creep-recovery plots at various stresses and at a constant temperature are plotted in *Figure 4.33*. These parameters were linearly fitted to obtain stress dependent functions ($A*\sigma + B$) at each temperature. g_0 was found to be constant. Previous studies [83- 86] on nonlinear parameters have only focused on deriving these parameters at room temperature. However, in the present study, the temperature dependence of these parameters was also derived. To derive the temperature dependence, slope (A) and constant (B), obtained at different temperatures, were linearly fitted to obtain temperature dependent functions, as shown in *Figures 4.34a* and *4.34b*, respectively. By substituting the temperature dependent functions of A and B to the respective stress dependent equations, nonlinear parameter functions were derived, as given by equation 4.26.

$$g_0 = 1.0414;$$

$$g_1 = 0.0414 * \sigma + 1.0175;$$

$$g_2 = 0.001 * T * \sigma + 0.0143 * \sigma + 0.0071 * T + 0.4391;$$

$$a_{\sigma} = 0.0003 * T * \sigma - 0.0308 * \sigma - 0.0041 * T + 1.2134 \quad (4.26)$$

where temperature is in degree Celsius and stress is in MPa.

The magnitude and variation of the nonlinear parameters for transverse compliance was found to be similar to those observed by other researchers [80-84].

Shear Compliance: The creep-recovery data for [10⁰] composites was obtained in the temperature range of 80-160 $^{\circ}\text{C}$ and in the shear stress range of 25- 50% UTS (15-

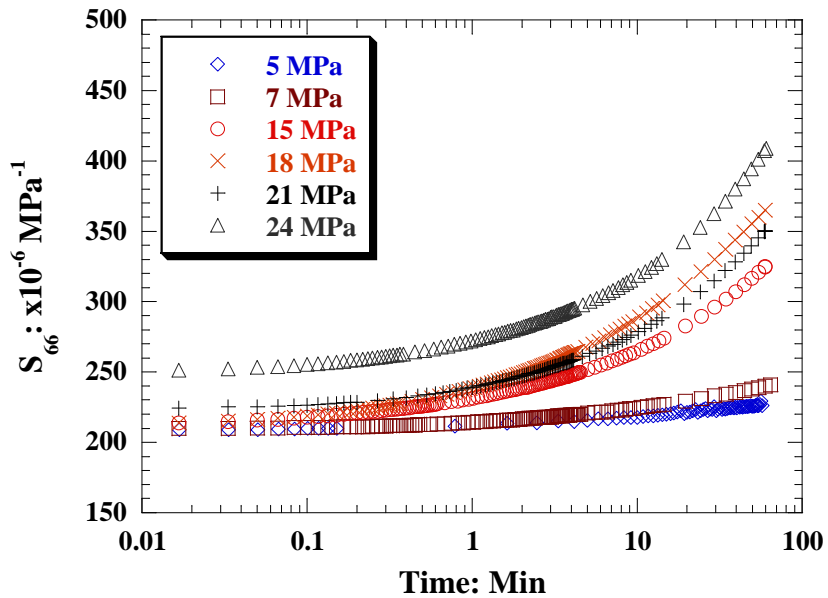


Figure 4.35: Shear creep compliance (S_{66}) plots at various stress levels and at a constant temperature of 80°C .

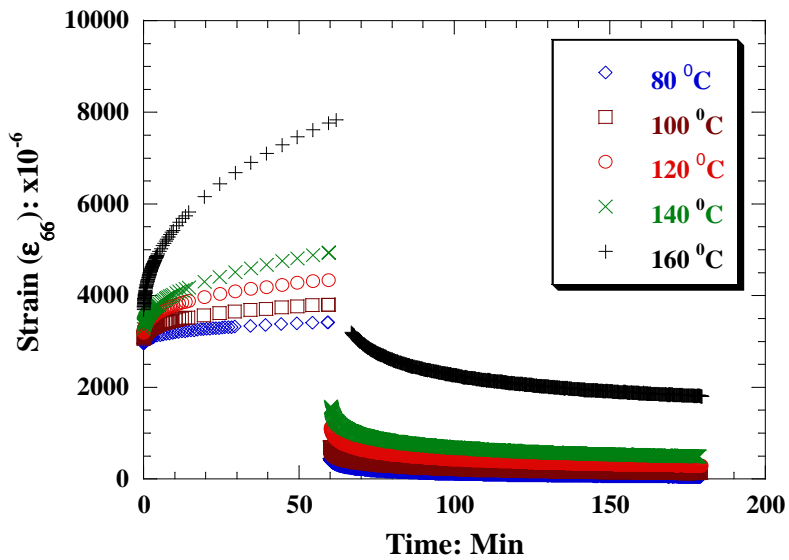


Figure 4.36: Shear creep and recovery data for $[10]_8$ test coupon at various temperatures ranging $80\text{--}160^{\circ}\text{C}$ and at a stress level of 15MPa.

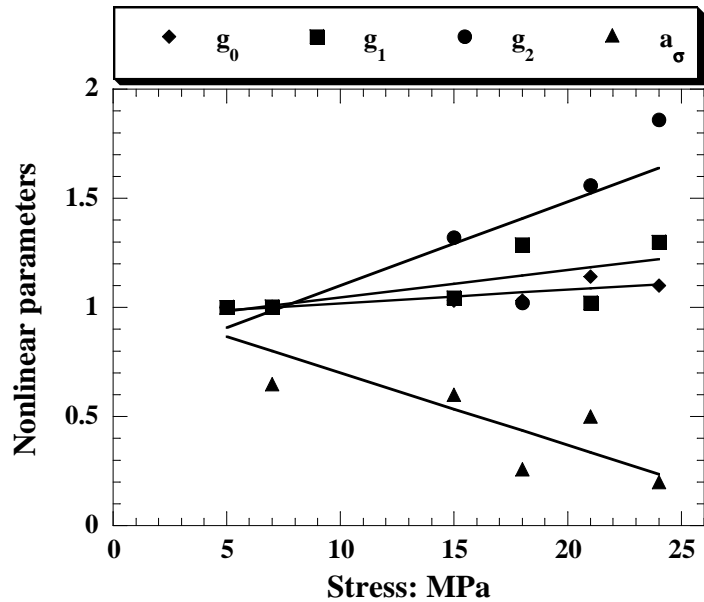
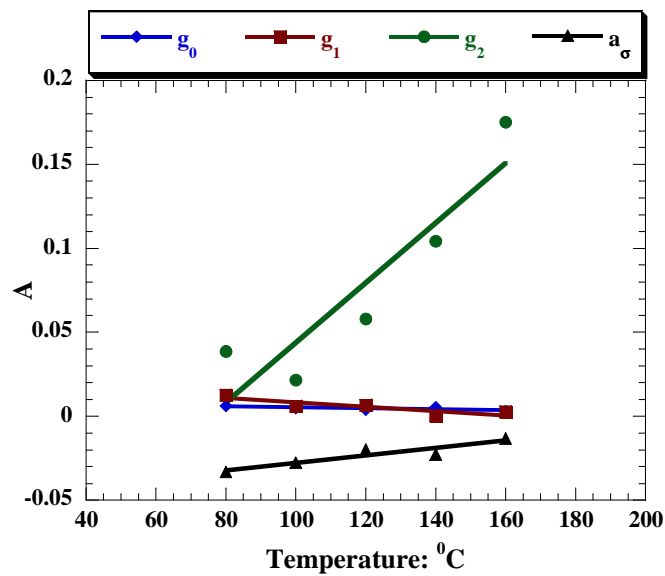
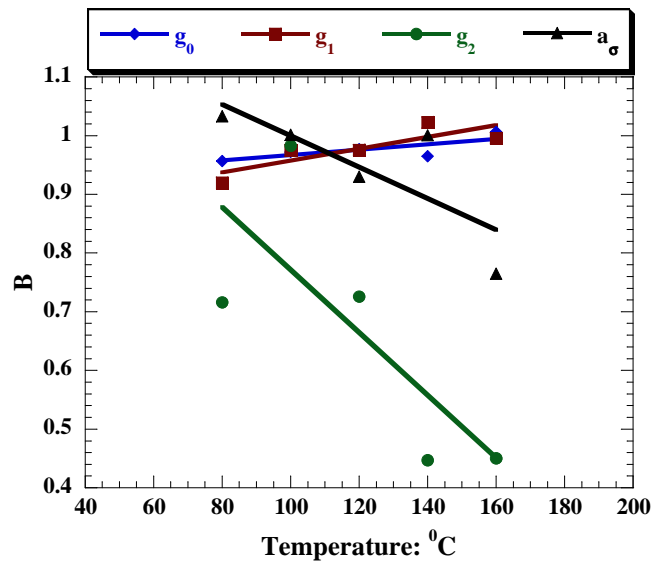


Figure 4.37: Plot of nonlinear parameters for shear compliance (S_{66}) at various stress levels and a constant temperature of 80°C .



(a)



(b)

Figure 4.38: Plot of constants A and B at various temperatures and a shear stress level of 15MPa.

24MPa). Shear creep compliance at various stress levels are plotted in *Figure 4.35* for a constant temperature of 80 $^{\circ}$ C. Shear creep compliance exhibited nonlinearity beyond 5MPa, similar to transverse compliance. The nonlinear parameters were calculated from creep-recovery plot obtained at various temperatures and stresses. Creep-recovery curves obtained at a shear stress of 15MPa and various temperatures ranging from 80-160 $^{\circ}$ C are plotted in *Figure 4.36*. The nonlinear parameters obtained using these creep-recovery plots at various stresses and at a constant temperature are plotted in *Figure 4.37*. Similar to the procedure followed for transverse compliance, these parameters were linearly fitted to obtain stress dependent functions ($A*\sigma + B$) at each temperature. Temperature dependence was then obtained by linearly fitting slope (A) and constant (B), as shown in *Figures 4.38a* and *4.38b*, respectively. By substituting the temperature dependent functions of A and B in the respective stress dependent equations, nonlinear parameter functions were derived, as given by equation 4.27.

$$g_0 = 0.005 * \sigma + 0.9754;$$

$$g_1 = 0.0055 * \sigma + 0.9774;$$

$$g_2 = 0.0018 * T * \sigma - 0.1342 * \sigma - 0.0053 * T + 1.3044;$$

$$a_{\sigma} = 0.0002 * T * \sigma - 0.0502 * \sigma - 0.0027 * T + 1.2676 \quad (4.27)$$

where temperature is in degree Celsius and stress is in MPa.

The magnitude and variation of nonlinear parameters for transverse compliance was found to be similar to those observed by other researchers [80-84].

Table 4.9: Nonlinear parameters for transverse creep at various stresses and temperatures.

Temperature (°C)	Stress (MPa)	g_0	g_1	g_2	a_σ
80	7	1.05	1.31	1.67	0.84
	10	1.05	1.43	1.95	0.82
	15	1.05	1.64	2.42	0.78
	27	1.05	2.14	3.55	0.70
	33	1.05	2.38	4.12	0.66
100	7	1.05	1.31	1.95	0.80
	10	1.05	1.43	2.29	0.80
	15	1.05	1.64	2.86	0.79
	27	1.05	2.14	4.24	0.78
	33	1.05	2.38	4.92	0.78
120	7	1.05	1.31	2.23	0.76
	10	1.05	1.43	2.63	0.77
	15	1.05	1.64	3.31	0.80
	27	1.05	2.14	4.92	0.86
	33	1.05	2.38	5.72	0.89
140	7	1.05	1.31	2.51	0.72
	10	1.05	1.43	2.98	0.75
	15	1.05	1.64	3.75	0.81
	27	1.05	2.14	5.60	0.94
	33	1.05	2.38	6.53	1.01
160	7	1.05	1.31	2.80	0.68
	10	1.05	1.43	3.32	0.73
	15	1.05	1.64	4.19	0.82
	27	1.05	2.14	6.28	1.02
	33	1.05	2.38	7.33	1.13

Table 4.10: Nonlinear parameters for shear creep at various stresses and temperatures.

Temperature (°C)	Stress (MPa)	g_0	g_1	g_2	a_σ
80	7	1.01	1.02	1.00	0.81
	15	1.05	1.06	1.03	0.54
	18	1.07	1.08	1.06	0.44
	21	1.08	1.09	1.09	0.33
	24	1.10	1.11	1.12	0.23
100	7	1.01	1.02	1.10	0.79
	15	1.05	1.06	1.46	0.54
	18	1.07	1.08	1.60	0.45
	21	1.08	1.09	1.74	0.36
	24	1.10	1.11	1.87	0.27
120	7	1.01	1.02	1.24	0.76
	15	1.05	1.06	1.90	0.55
	18	1.07	1.08	2.14	0.47
	21	1.08	1.09	2.39	0.39
	24	1.10	1.11	2.63	0.32
140	7	1.01	1.02	1.39	0.73
	15	1.05	1.06	2.33	0.56
	18	1.07	1.08	2.68	0.49
	21	1.08	1.09	3.04	0.42
	24	1.10	1.11	3.39	0.36
160	7	1.01	1.02	1.53	0.71
	15	1.05	1.06	2.76	0.56
	18	1.07	1.08	3.22	0.51
	21	1.08	1.09	3.69	0.45
	24	1.10	1.11	4.15	0.40

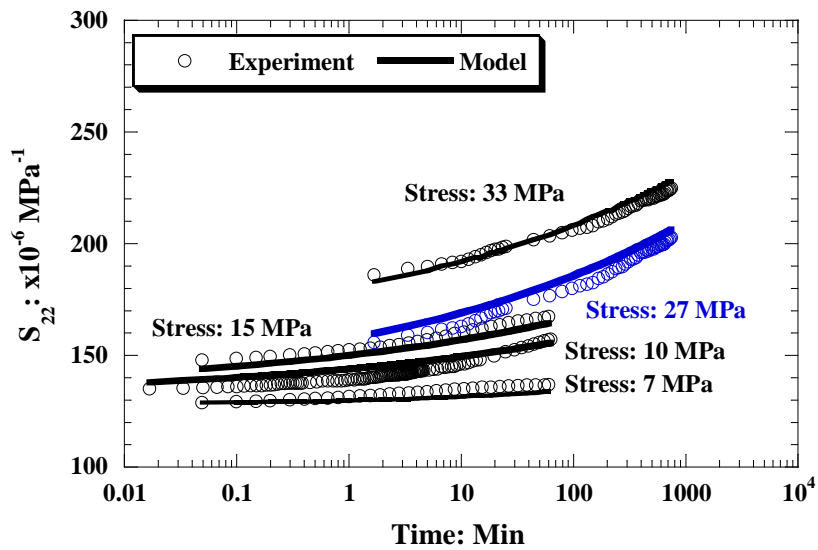


Figure 4.39: Comparison of predicted and experimental transverse creep compliance (S_{22}) at various stresses and at a constant temperature of 140°C .

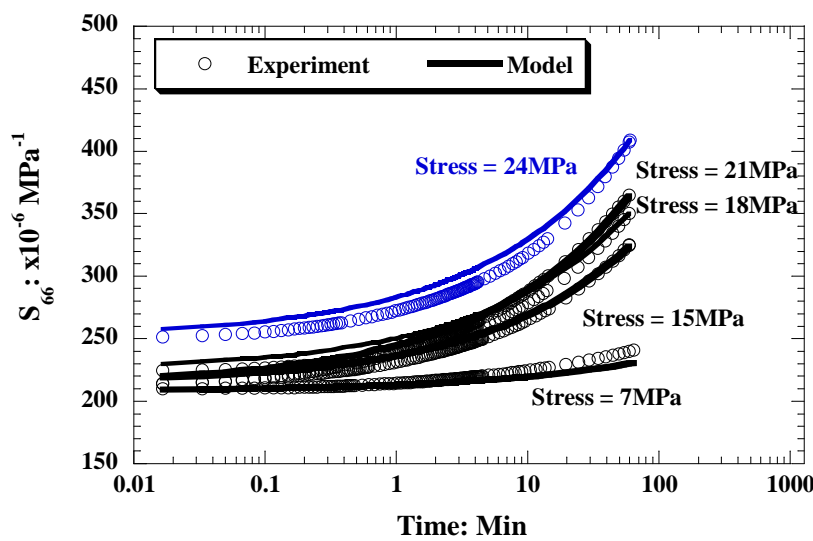


Figure 4.40: Comparison of predicted and experimental shear creep compliance (S_{66}) at various stresses and at a constant temperature of 140°C .

All the nonlinear parameters obtained for transverse and shear creep at various temperatures and stresses, using equations 4.26 and 4.27, are tabulated in *Tables 4.9* and *4.10*, respectively.

In order to verify the simulation and predictive capability of the experimentally determined nonlinear parameters and nonlinear viscoelastic model, the transverse and shear compliances of the unidirectional lamina was simulated at various temperatures and stress levels using the modified KWW equation constants, given in *Table 4.8*, and nonlinear parameters, given in *Tables 4.9* and *4.10*. The simulated as well as predicted transverse and shear compliance curves are compared with experimental results in *Figures 4.39* and *4.40*, respectively. Please note that experimental data at all stress levels except 27MPa in *Figure 4.39* and 24MPa in *Figure 4.40* were used in determining the nonlinear parameters. Hence, the comparisons at these stress levels highlight the quality of simulation using the non-linear parameters within an error range of 2-4%. The predicted transverse compliance curve at 27MPa at 140 $^{\circ}$ C in *Figure 4.39* and predicted shear compliance curve at 24MPa in *Figure 4.40* validates the prediction capability of Schapery's model and nonlinear parameters represented by equations 4.26 and 4.27. These stress and temperature dependent nonlinear functions for transverse and shear compliance were used with equation 4.3 to calculate time-dependent transverse and shear compliance of unidirectional lamina in nonlinear viscoelastic stress range. These were used along with the creep model, as described in Chapter 3, to calculate the creep of plain weave composite at various stress levels at 80 $^{\circ}$ C.

4.3.3 Simulation parameters

The various simulation parameters used in the MATLAB program such as time step size and stress step size affect the accuracy of the simulation. In the current program, the minimum possible time step of $1.01t$ was used. Here ‘ t ’ is current time in minutes. This time step was chosen to minimize the execution error in the program during the run and optimize the execution time for running up to time period of 10^{10} minutes (>30 years). Further a lower time step ($1.0t$) for few cases were also tried to confirm any variation, but no difference was seen.

The stress step size chosen for calculation of ply stresses at time $t=0$ was 1 MPa. Ply stress calculated during an iteration step was assumed to have converged if difference in ply stress between the current and previous iterations was less than 0.3 MPa.

As stated previously, the effect of stress on creep of unidirectional lamina was derived using nonlinear parameters (g_0 , g_1 , g_2 and a_σ). These nonlinear parameters were considered equal to 1 below a stress level of 5 MPa, due to the linear creep behavior of unidirectional lamina. Above 5 MPa, the nonlinear parameters were calculated, as described in section 4.3.2.2 and used to calculate nonlinear creep compliance of unidirectional lamina. It can be seen from *Figures 4.33 and 4.37* that there is a sudden change in these non-linear parameters from the stress increases through 5 MPa.

During creep of plain weave composites, load (stress) shared by fill along loading direction increases, while the load shared by warp, transverse to the loading direction, decreases. In the applied stress range, where warp stress is in nonlinear range, its compliance is calculated using nonlinear parameters derived using equations 4.26 and 4.27. With increase in time, the warp stress on warp ply decreases. Once, warp stress

reduces below 5MPa, the nonlinear parameters are calculated to be 1 according to *Figures 4.33 and 4.37*. A sudden change in one of the nonlinear parameters, a_σ , from a value below 1 to 1 at 5MPa causes a sudden reduction in calculated transverse compliance of warp, leading to fluctuation in calculated compliance of plain weave laminate, as shown in *Figure 4.41*. To avoid such fluctuation in calculated compliance, the nonlinear parameters below 5MPa were calculated using equation 4.26 and 4.27, instead of assuming them to be 1, for both warp and fill laminae. In order to ensure that the calculated unidirectional creep compliance at stresses below 5MPa, using the nonlinear parameters derived from equations 4.26 and 4.27 are accurate, the predicted compliance (S_{22} and S_{66}) of unidirectional composites are compared in *Figures 4.42* and *4.43* with experimental results. The predictions validated well with experimental results.

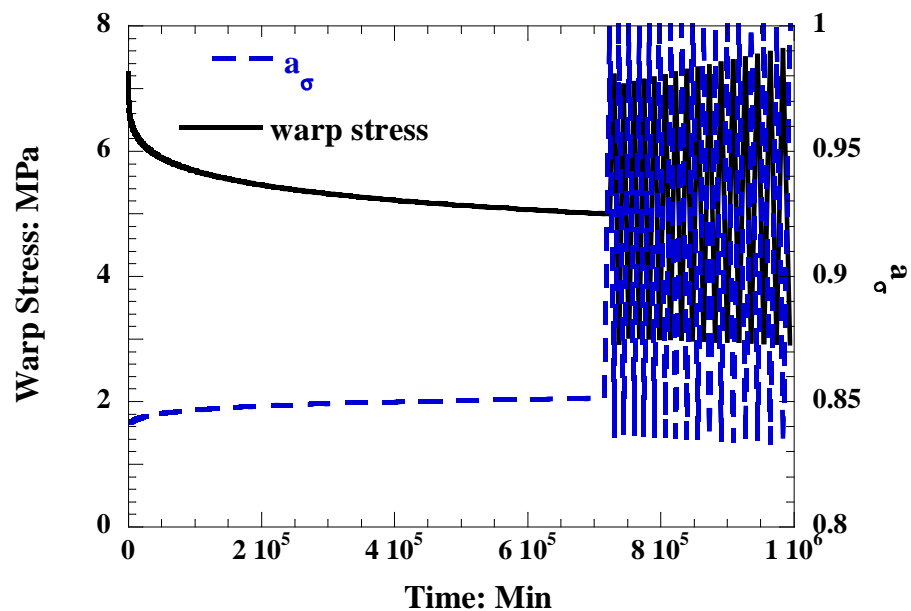


Figure 4.41: Variation of warp stress (σ_{22}) and nonlinear parameter (a_0) with time at applied stress of 100MPa and temperature of 80 $^{\circ}\text{C}$.

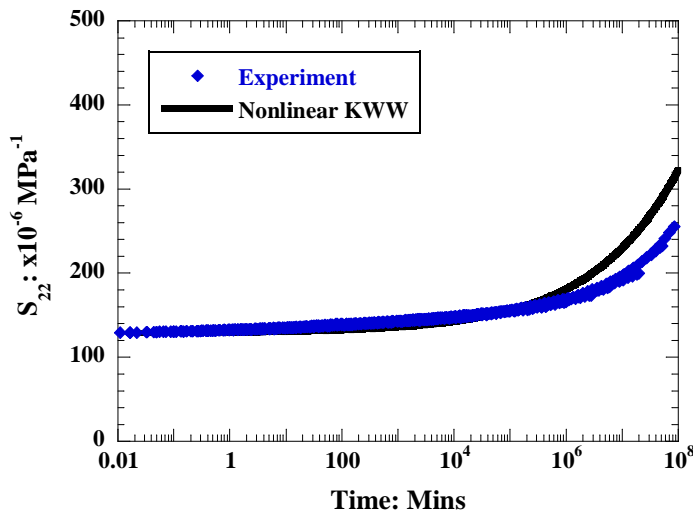


Figure 4.42: Comparison of experimental creep compliance (S_{22}) of unidirectional composites with predicted creep compliance derived using nonlinear parameters and KWW equation at 3MPa and 80 $^{\circ}\text{C}$.

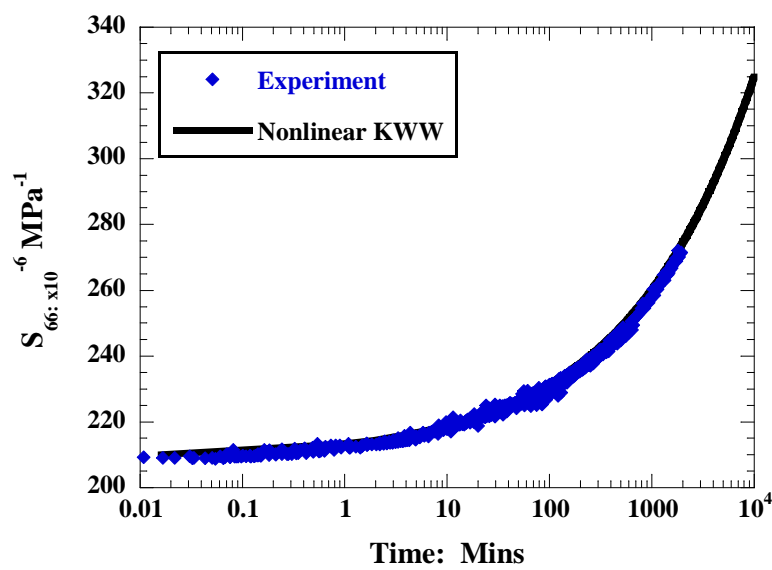


Figure 4.43: Comparison of experimental creep compliance (S_{66}) of unidirectional composites with predicted creep compliance derived using nonlinear parameters and KWW equation at 5MPa and 80 $^{\circ}\text{C}$.

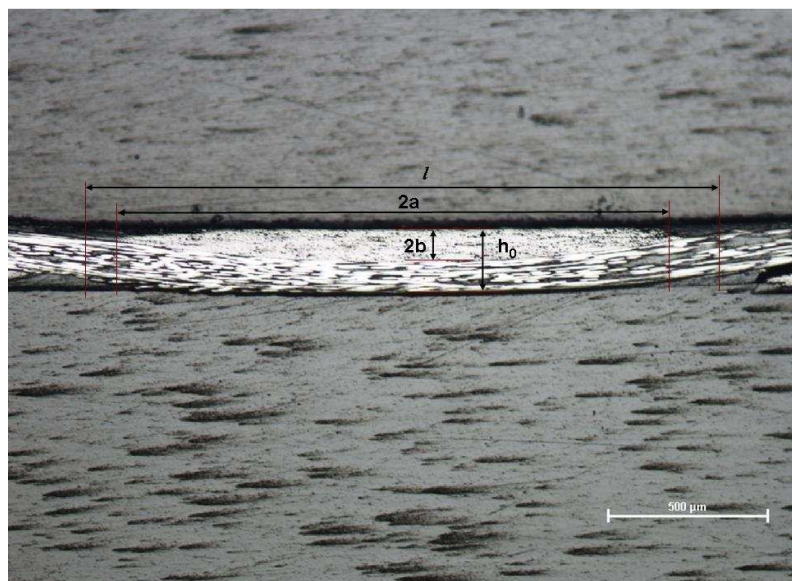
5. RESULTS AND DISCUSSION

5.1 Introduction

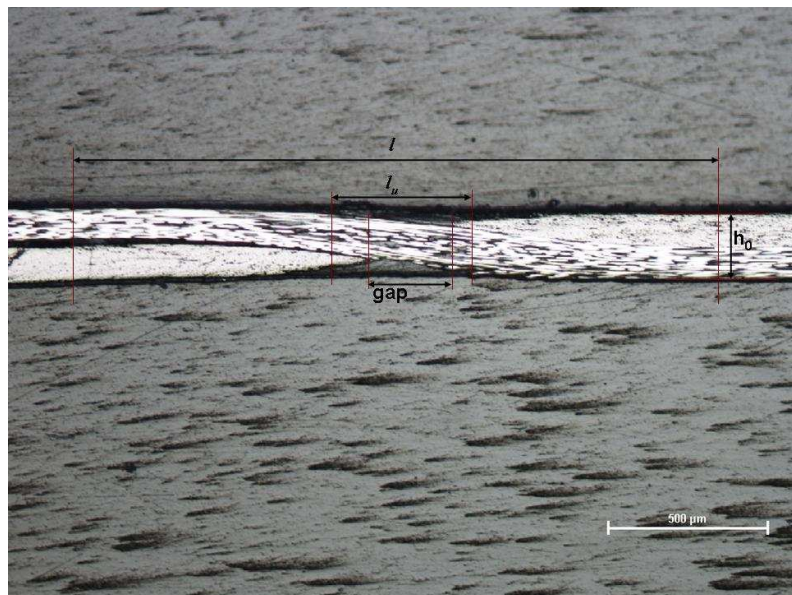
Experimental results on tensile creep of plain weave polymer woven composite material under on-axis and off-axis loading conditions (0^0 and 45^0 loading with respect to the fill direction of the composite) are presented and discussed in subsequent sections. The effect of microstructure of plain weave composites on its creep behavior is analyzed and presented. Predicted creep plots from the creep model, developed as a part of this research project, are compared with the experimental results and the predictive capability of the creep model is evaluated. Finally, the effect of assumptions made in the creep model on the accuracy of simulation is discussed.

5.2 Microstructural characterization of plain weave composites

Various microstructural parameters in a plain weave composite are lamina thickness, yarn's cross-sectional dimensions (width and thickness), undulation or crimp length, undulation angle, and fiber volume fraction within a yarn and the composite. In addition, nesting of plies in a laminate was also studied. The plain weave composite coupons were characterized to determine the average values of these parameters. The influence of these parameters on elastic and creep behavior of plain weave composites was studied parametrically and will be presented in section 5.4.1.4. The microstructural parameters were measured using the micrographs of a single ply lamina as well as a



(a)

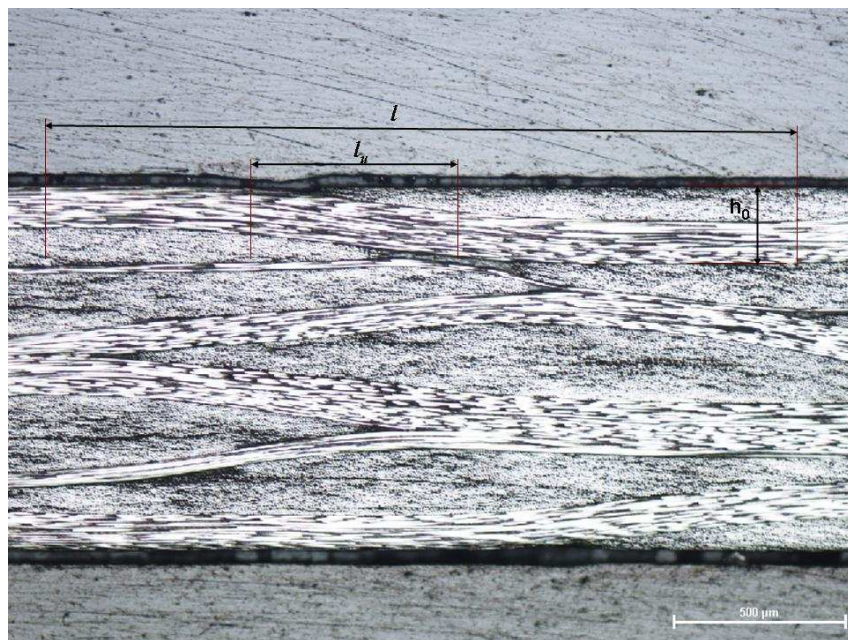


(b)

Figure 5.1: Micrographs of a single-ply lamina used for measurement of undulation parameters (X50).



(a)



(b)

Figure 5.2: Micrographs of a multi-ply laminate used for measurement of undulation parameters (X50).

Table 5.1: Undulation parameters measured using micrograph of a single-ply lamina shown in Figure 5.1.

Single- ply lamina (in mm)						
	<i>l</i>	<i>h</i> ₀	<i>l</i> _u	2 <i>a</i>	2 <i>b</i>	gap
	1.999	0.206	0.520	1.728	0.110	0.266
	2.007	0.200	0.504	1.728	0.110	0.271
	2.000	0.201	0.529	1.722	0.110	0.260
	1.978	0.206	0.510	1.710	0.110	0.220
Average	1.996	0.203	0.516	1.722	0.110	0.254
Std Dev [*]	0.0125	0.003	0.011	0.008	0.000	0.023

^{*}(Standard Deviation – Std Dev)

Table 5.2: Undulation parameters measured using micrographs of multi-ply laminates shown in Figure 5.2.

Multi-ply laminate (in mm)						
	<i>l</i>	<i>h</i> ₀	<i>l</i> _u	2 <i>a</i>	2 <i>b</i>	gap
Batch 1 Coupon 1	2.090	0.225	0.635	1.962	0.104	-
	2.156	0.230	0.591	1.988	0.110	-
	2.094	0.227	0.613	1.950	0.122	-
	2.089	0.211	0.621	1.970	0.116	0.054
	2.159	0.222	0.629	1.991	0.122	-
	2.132	0.203	0.624	1.983	0.113	0.021
	2.197	0.200	0.637	1.994	0.113	-
	2.222	0.208	0.664	0.200	0.113	-
	2.170	0.206	0.621	2.015	0.119	-
	2.150	0.224	0.630	1.980	0.116	-
Average	2.146	0.216	0.627	1.803	0.115	0.038

Table 5.2 Continued...

Std Dev	0.045	0.011	0.019	0.564	0.006	0.0233
Batch 1	2.002	0.214	0.630	1.81	0.105	0.110
	2.053	0.195	0.621	1.91	0.097	0.086
	2.059	0.235	0.605	1.673	0.105	-
	2.029	0.222	0.629	1.820	0.113	-
	2.007	0.216	0.626	1.760	0.113	0.271
	2.056	0.227	0.656	1.972	0.119	0.480
	2.089	0.211	0.610	1.888	0.105	-
	2.040	0.235	0.656	1.796	0.124	0.195
	2.067	0.211	0.613	1.918	0.113	-
	2.071	0.223	0.650	1.899	0.115	-
Average	2.047	0.219	0.630	1.845	0.111	0.228
Std Dev	0.028	0.012	0.019	0.089	0.008	0.159
Batch 2	2.060	0.184	0.670	1.940	0.122	0.076
	2.080	0.168	0.650	1.950	0.113	-
	2.06	0.180	0.690	1.874	0.113	0.206
	2.075	0.176	0.637	1.812	0.119	-
	2.045	0.192	0.624	1.924	0.119	-
	2.013	0.208	0.678	1.758	0.113	-
	2.078	0.181	0.661	1.863	0.111	-
	2.015	0.181	0.670	1.836	0.115	-
	2.075	0.200	0.683	1.836	0.120	-
	2.064	0.197	0.693	1.847	0.119	-
Average	2.057	0.187	0.666	1.865	0.116	0.148
Std Dev	0.025	0.012	0.022	0.060	0.004	0.092

multi-ply laminate (which was used for experiments), shown in *Figure 5.1* and *Figure 5.2* respectively. The following parameters (as highlighted in *Figure 3.5*) were measured using a single-ply and multi-ply laminate: length of a unit cell (l), undulation length (l_u), lamina thickness (h_0), cross-sectional dimensions ($2a$ and $2b$) of fill and warp yarns within a lamina, and gap between two fill or warp yarns. All the measured values and their average are tabulated in *Tables 5.1* and *5.2* for a single ply and a multi-ply laminate, respectively. The multiple measurements were obtained using a single coupon for both single ply and multi-ply laminate. The variation of undulation parameters among multi-ply coupons within a batch as well as between two batches was also captured, as given in *Table 5.2*. The standard deviation was 0.05mm and 0.012mm for undulation length and thickness of laminae in multi-ply laminates, respectively.

It was observed that the microstructural parameters for a single-ply lamina are different from that for a multi-ply laminate. However, the unit cell length of the single-ply lamina was observed to be same ($l = 2.0\text{mm}$) as provided by the fabric manufacturer, Hexcel Incorporation [87]. During curing, consolidation (i.e. overall reduction in thickness of the laminate) of the laminate occurs due to a number of causes such as resin bleeding, removal of air between plies, cure shrinkage, and nesting of the plies. Due to such consolidation, the unit cell length and undulation length were found to be higher and lamina thickness was found to be lower in a multi-ply laminate when compared to a single-ply lamina. Previous studies [7-10] have also reported such decrease in the thickness per lamina with increase in number of laminae in the laminate. The cross-sectional dimensions of the yarn increased slightly resulting in change in the gap between the yarns. The gap length in a single ply was found to be substantially

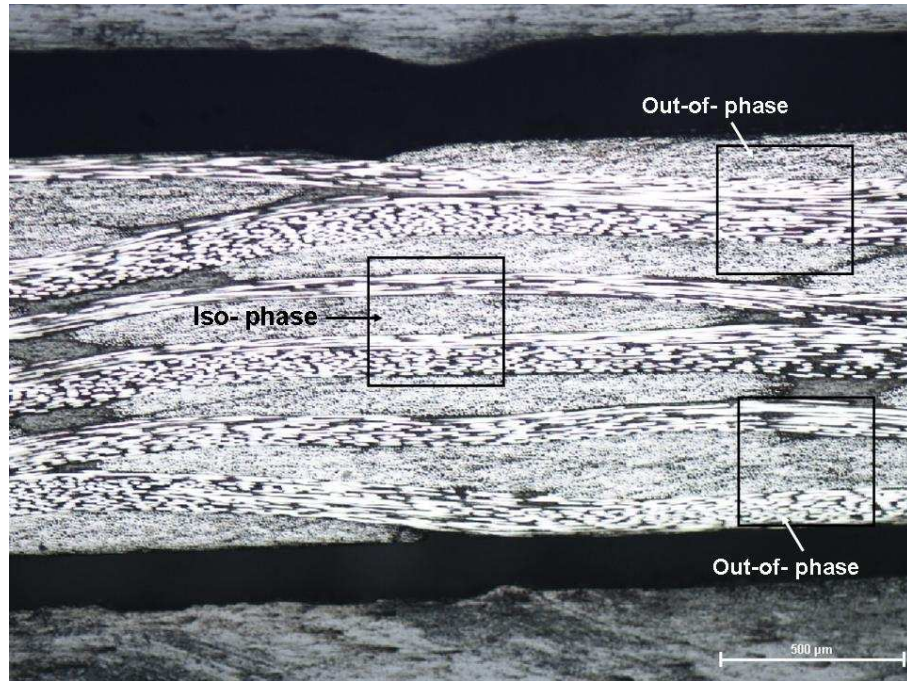


Figure 5.3: Micrograph of a multi-ply laminate showing nesting(X50).

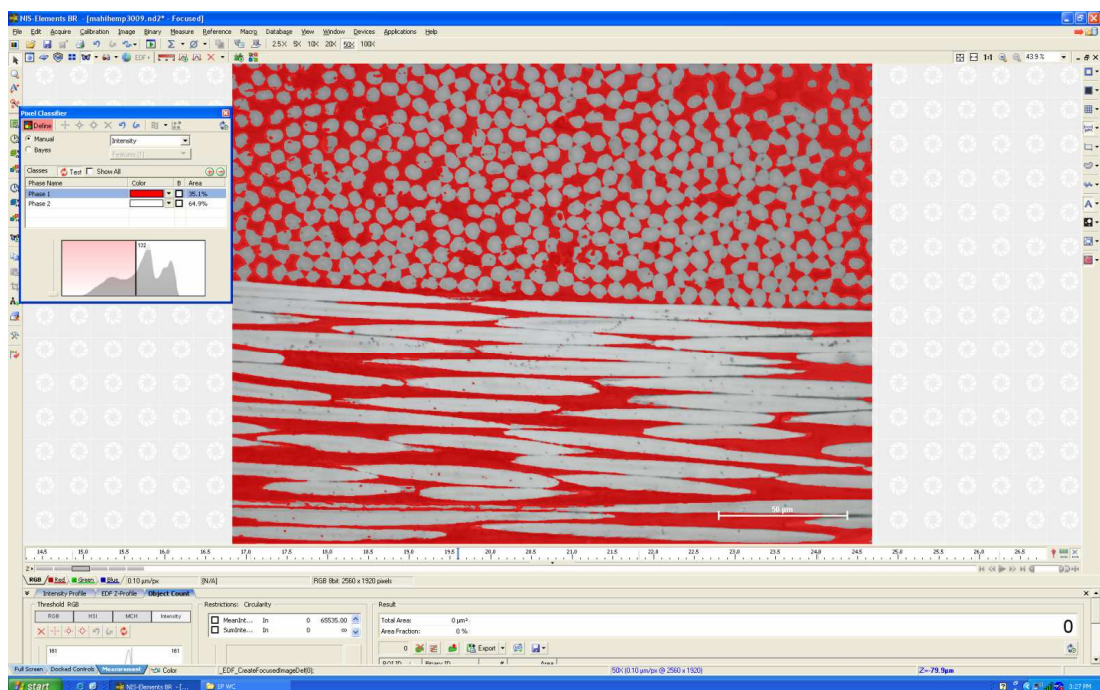


Figure 5.4: Image analysis method used to measure the volume fraction of fiber in plain weave composite coupons using its micrograph at X500.

higher than that in the laminate, apparently due to nesting in the laminate. Because of this, the gap length in the laminate varied by a wide margin from location to location, as observed in *Table 5.2*. In contrast, the gap length was same at all locations in a single-ply lamina. Yarns were found to overlap completely at several locations resulting in zero gap width.

The nesting in multi-ply laminates, characterized by spatial movement of one ply with respect to the other, is shown in *Figure 5.3*. Both iso-phase (relative spatial movement is zero), out-of-phase (relative spatial movement is such that the undulation is out-of-phase) nesting were observed. Nesting of the laminate is caused due to shifting of the plies during lay-up as well as during manufacturing. It is not possible (i.e. practical) to precisely match the position of yarns in one lamina with another so as to get an iso-phase configuration. Even if achieved, the plies may slide past each other due to resin flow and applied pressure during manufacturing. In addition to the random distribution of iso-phase and out-phase configurations, the multidirectional laminate showed nesting in between these two extremes (i.e. relative movement between 0 and 90). This is normally referred to as random phase nesting (or stacking) in the literature. Although, the unit cell length, undulation length and lamina thickness were found to be similar at the locations of iso-phase and out-of-phase stacking, the gap between two yarns was found to be relatively larger in the iso-phase region than in out-of-phase region.

Despite the observed random phase stacking, iso-phase stacking was assumed during creep simulation as a first approximation. The effect of this on the accuracy of simulations will be discussed in section 5.4.3.

The average fiber volume fraction of a unit cell was determined through image analysis of the micrographs of both single-ply lamina and multi-ply laminate. *Figure 5.4* shows the screen shot of analyzed image. The red region corresponds to the resin while the grey region corresponds to the fiber. These regions were accurately delineated and quantified through threshold capability of the NIS element's software for the Nikon microscope. The warp and fill fibers are differentiated by the circular and oblong shapes respectively. The average fiber volume fraction in a unit cell was found to be in the range of 62-66 %. This value is same as the average fiber volume fraction of a woven laminate determined through acid digestion method, in section 4.2.2.2. The creep model assumed that the unit cell of the woven composite is made up of unidirectional tape of similar average fiber volume fraction and used the experimental creep data for the latter. The experimentally determined average fiber volume fraction for the unidirectional tape is 60-62% and is same as that for the woven laminate. This confirms that unidirectional tape data could be used to predict the creep of the woven laminate studied in this thesis.

5.3 Tensile behavior of plain weave composites

5.3.1 On-axis loading

Tensile tests under on-axis loading were conducted to determine the tensile strength and modulus of plain weave composites in the temperature range of 80- 240 $^{\circ}\text{C}$ using [0, 90]₆ test coupons. *Figure 5.5* shows the stress- strain plots obtained from tensile tests conducted at different temperatures. The plots were linear except at higher stresses for 160 $^{\circ}\text{C}$ and 240 $^{\circ}\text{C}$, when a sudden deviation was observed due to increase in damage.

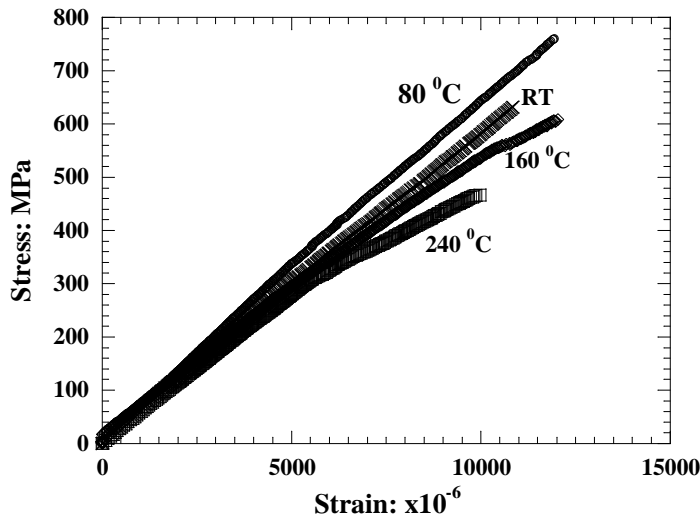


Figure 5.5: Tensile stress- strain plots for $[0, 90]_6$ plain weave composite coupons at various temperatures.

Table 5.3: Tensile test results for $[0, 90]_6$ plain weave composite coupons at various temperatures tested at a strain rate of 10^{-4} sec $^{-1}$.

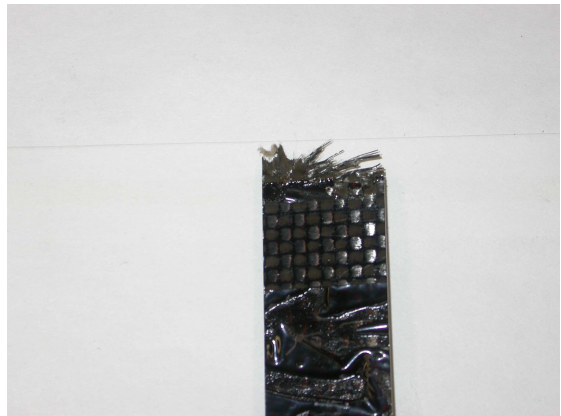
Temperature (°C)	Ultimate Tensile Strength (MPa)	Strain to Failure (%)	Modulus (GPa)
25	634 ± 19	1.1 ± 0.02	67.5 ± 6.4
80	775 ± 5	1.2 ± 0.03	68.7 ± 2.1
160	680 ± 8	1.1 ± 0.03	60.5 ± 0.2
240	600 ± 20	1.1 ± 0.05	54.0 ± 2.0



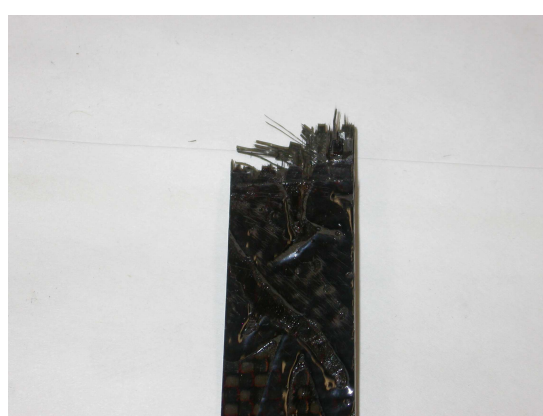
(a) Room temperature



(b) 80 °C



(c) 160 °C



(d) 240 °C

Figure 5.6: Fractured edges of [0, 90]₆ plain weave composite coupons after tensile test at various temperatures.

The ultimate tensile strength (UTS), strain to failure and tensile modulus at various temperatures are tabulated in *Table 5.3*. The tensile strength and the tensile modulus (slope of stress-strain plot) both decreased with increase in temperature. However, the strain to failure was virtually the same for all test temperatures. The micrographs of fractured edges of test coupons at different temperatures are shown in *Figure 5.6*. The specimens showed a brittle fracture. Since, the fracture strength of plain weave composites under on-axis loading is fiber dominant, the fracture mode did not change substantially with temperature. However, the fractured edge at 240 °C was relatively more irregular with pulled-out yarns when compared to a relatively flat fracture surface at RT.

5.3.2 Off-axis loading

Tensile tests under off-axis loading were conducted to determine the tensile strength and modulus of plain weave composites in the temperature range of 80- 160 °C using [+45, -45]₆ test coupons. The stress-strain plots shown in *Figure 5.7* are substantially non-linear when compared to stress – strain plots for on-axis loading due to shear deformation. The ultimate tensile strength (UTS) decreases and the strain to failure increases with increase in test temperatures, as tabulated in *Table 5.4*. While, the strength was lower, the strain was higher under off-axis loading than under on-axis loading, thus resulting in much lower off-axis modulus than on-axis modulus for all temperatures. The tensile modulus decreased with increase in stress and temperature due to enhanced viscoelasticity of the polymer matrix of the composite under off-axis loading. Similar

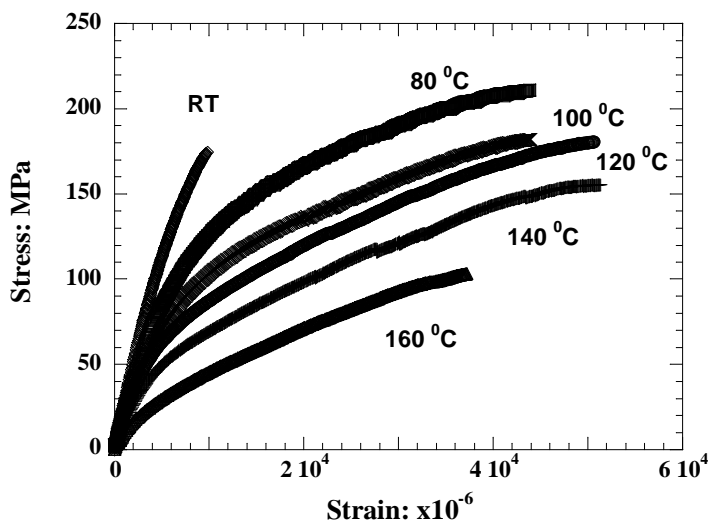
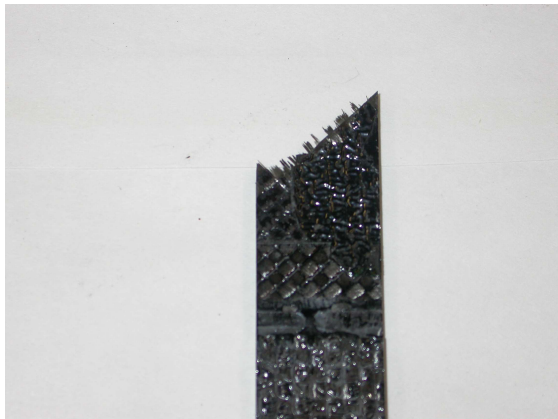


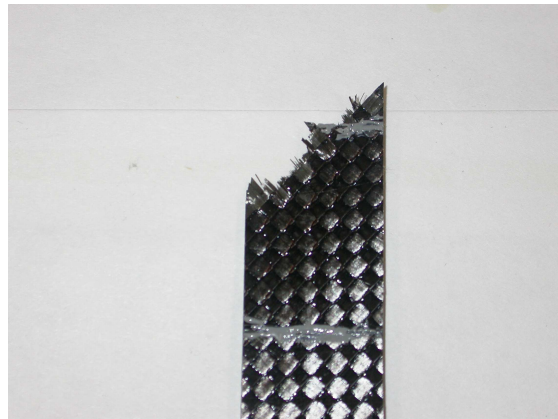
Figure 5.7: Tensile stress- strain plots for $[45, -45]_6$ plain weave composite coupons at various temperatures.

Table 5.4: Tensile test results for $[45, -45]_6$ plain weave composite coupons at various temperatures tested at a strain rate of 10^{-4} sec $^{-1}$.

Temperature ($^{\circ}\text{C}$)	Ultimate Tensile Strength (MPa)	Strain to Failure (%)	Modulus (GPa)
25	224 ± 8	1.43 ± 0.01	26.20 ± 1.1
80	211 ± 8	4.38 ± 0.02	19.91 ± 0.5
100	182 ± 2	4.39 ± 0.03	17.14 ± 1.0
120	180 ± 9	5.06 ± 0.01	16.32 ± 1.0
140	155 ± 4	5.13 ± 0.02	12.50 ± 0.2
160	103 ± 12	3.72 ± 0.02	7.60 ± 0.2



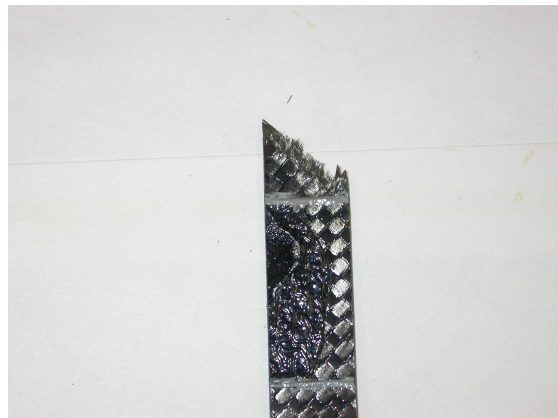
(a) Room temperature



(b) 80 °C



(c) 100 °C



(d) 120 °C



(e) 140 °C



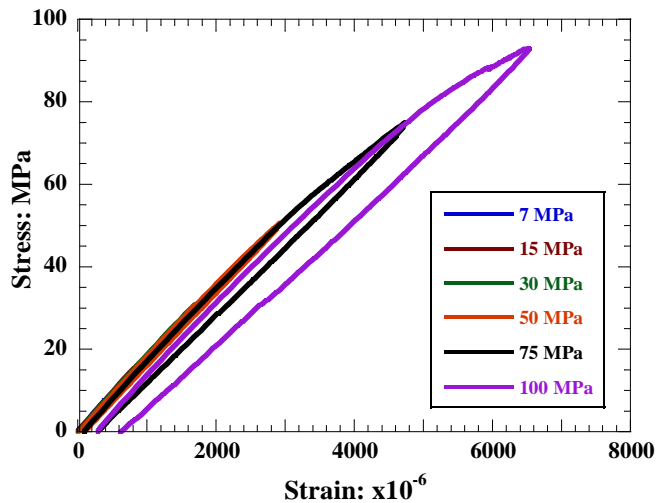
(f) 160 °C

Figure 5.8: Fractured edges of $[+45, -45]_6$ plain weave composite coupons after tensile test at various temperatures.

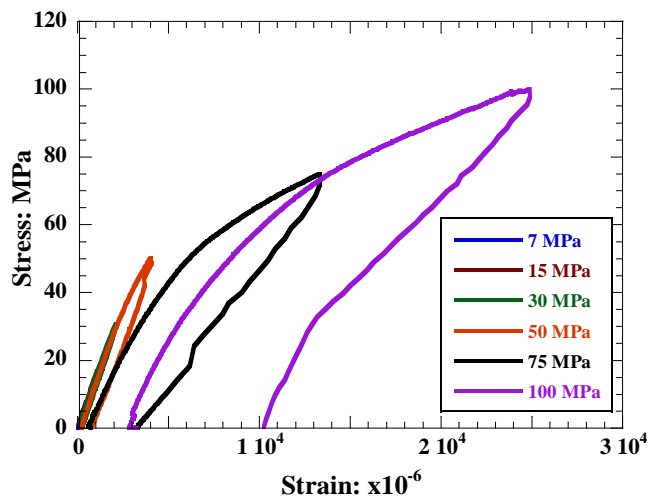
trend in strength and strain to failure with increase in angle between the fill yarn and loading axis has also been observed by other researchers [71, 85, 86]. The micrographs of fractured edge of test coupons fractured at different temperatures are shown in *Figure 5.8*. Unlike the fiber dominated brittle failure mode under on-axis loading, a ductile shear failure mode was observed under off-axis loading at all temperatures.

Similar to the experimental analysis conducted to study the effect of process-induced damage on the tensile behavior of plain weave composites under on-axis loading (discussed in Chapter 4), the effect of process-induced damage (vertical cracking) on tensile behavior of plain weave composites under off-axis loading was also analyzed. Fresh test coupons $[+45, -45]_6$ were tested at three different temperatures of 80, 120 and 160°C by loading and unloading in the stress range of 7- 100MPa. The instantaneous modulus and the permanent strain after loading and unloading from each stress level were recorded. The stress-strain plots from these repeated loading-unloading tests at each temperature are shown in *Figures 5.9a-c* and corresponding instantaneous modulus and permanent recovery strain are tabulated in *Table 5.5*.

The permanent strain increased and the instantaneous modulus decreased with increase in stress at each temperature. The permanent strain also increased with increase in temperature for a test coupon loaded to the same stress level. Even though the tensile strength registered during monotonic tensile test at 160°C was 103MPa, the test coupon fractured at a much lower stress during the loading – unloading tests (during loading to a stress level of 50MPa), as shown in *Figure 5.9c*. This indicates that the damage increased with stress during tensile loading. Further confirmation of increase in damage was obtained using optical and non-destructive inspection after test. Since, the damage in the

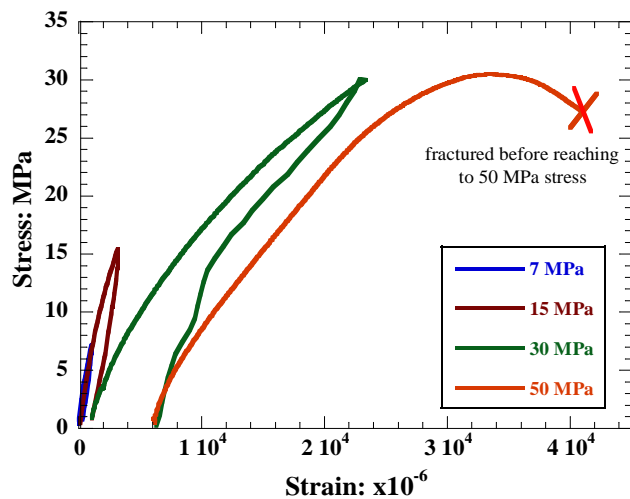


(a) 80°C



(b) 120°C

Continue....

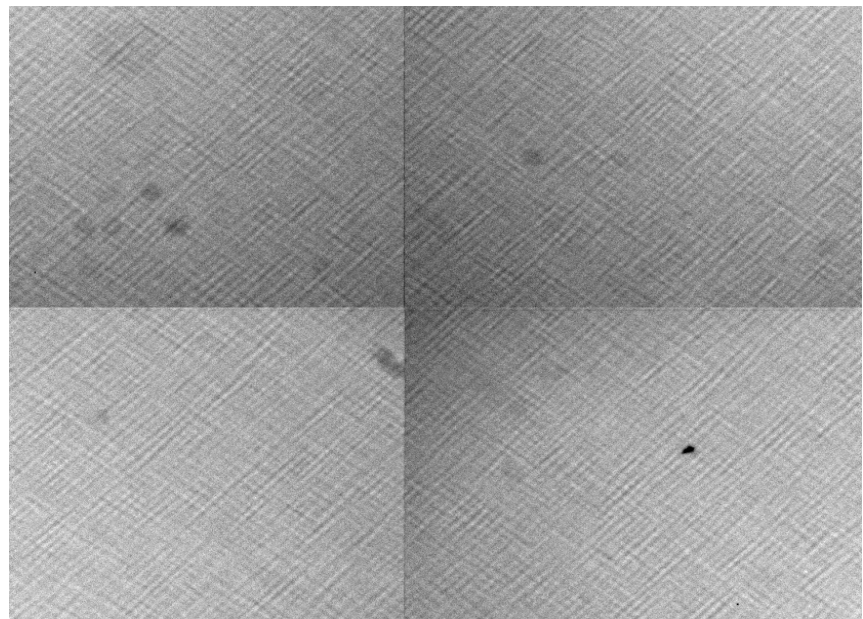


(c) 160°C

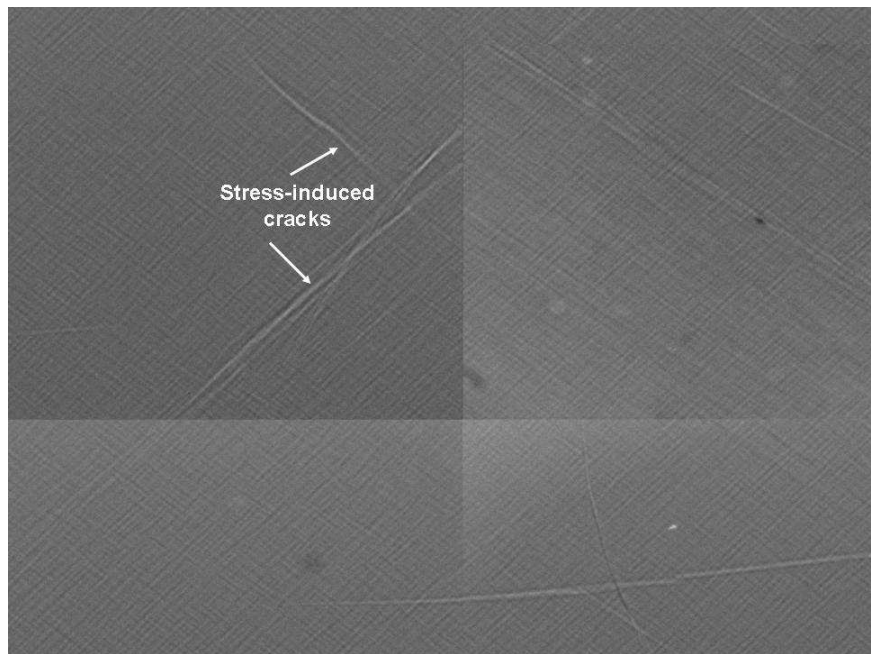
Figure 5.9: Stress-strain plots of loading-unloading tests for $[+45, -45]_6$ plain weave composite coupons at various temperatures.

Table 5.5: Instantaneous modulus and permanent recovery strain in $[+45, -45]_6$ plain weave composite coupons obtained through loading-unloading tests at various temperatures.

Stress (MPa)	T = 80 °C		T = 120 °C		T = 160 °C	
	Instantaneous Modulus (GPa)	Permanent Strain (microstrain)	Instantaneous Modulus (GPa)	Permanent Strain (microstrain)	Instantaneous Modulus (GPa)	Permanent Strain (microstrain)
7	19.2	11	17.1	34	6.8	293
15	18.8	22	16	104	5.1	1043
30	18.2	49	15	229	2.3	7224
50	17.4	101	14.8	801	-	-
75	16.1	300	11	3313	-	-
100	13.8	756	10.3	10246	-	-

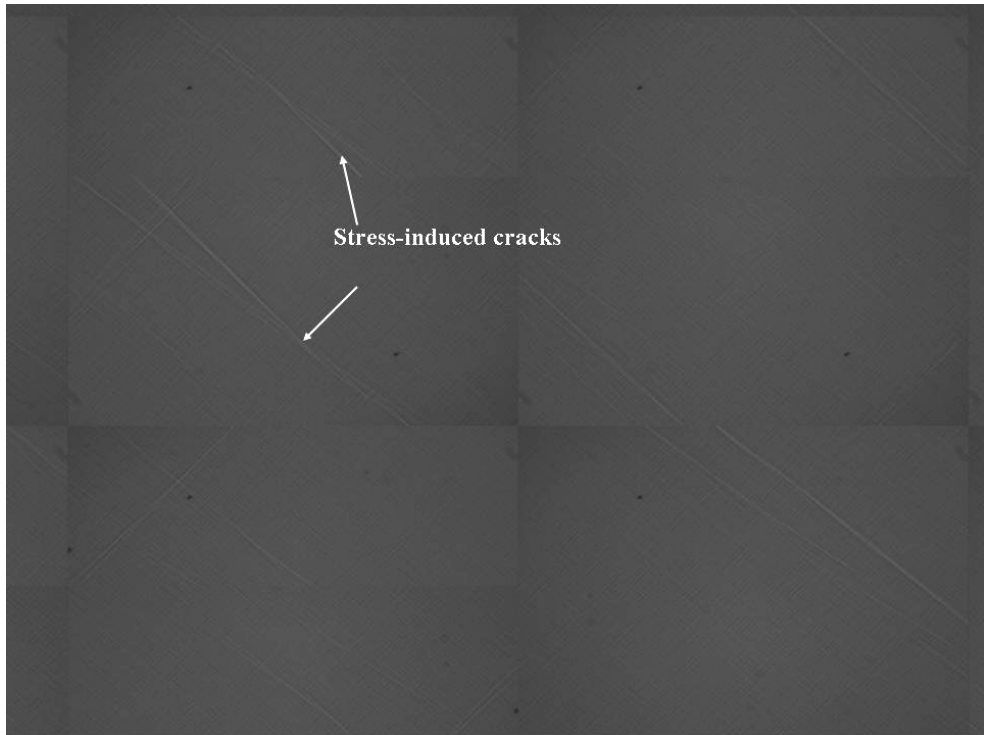


(a) 80°C



(b) 120°C

Continued....



(c) 160°C

Figure 5.10: Radiographs of $[+45, -45]_6$ plain weave composite coupons inspected non-destructively after loading-unloading tests at various temperatures (X10).

form of vertical cracks was found in transverse (warp) yarns, they could not be observed on the polished edge of $[+45, -45]_6$ coupons using optical microscope. Hence, X-radia's Micro XCT was used to inspect the $[+45, -45]_6$ test coupons non-destructively at X10 magnification. No damage was recorded after testing at RT and at 80°C suggesting that this damage either didn't increase or increase to a level that could be detected. However, cracks were observed in the test coupons tested at 120 and 160°C , where the size of the cracks, near the fractured end were of sufficient size to be detected by X-ray. The radiographs of tested coupons at all three temperatures are shown in *Figures 5.10a-c*. These images are two-dimensional mosaic images. The fibers observed in orthogonal direction in these images are fill and warp fibers. As shown in *Figures 5.10b & c*, the cracks could be observed along the fill or warp fiber directions. The parallel cracks correspond to cracking in various plies across the thickness of the laminate. These cracks were not observed before testing. The stress-strain plots and micrographs obtained for $[+45, -45]_6$ coupons indicate that these cracks have considerable affect on the tensile behavior of plain weave composites under off-axis loading.

5.4 Creep of plain weave composites

5.4.1 On-axis loading

The tensile creep tests were conducted for plain weave composites under on-axis loading using $[0, 90]_6$ test coupons. The creep tests were conducted in a wide range of stress, ranging from less than 1% UTS to 70% UTS of the composite, and in the

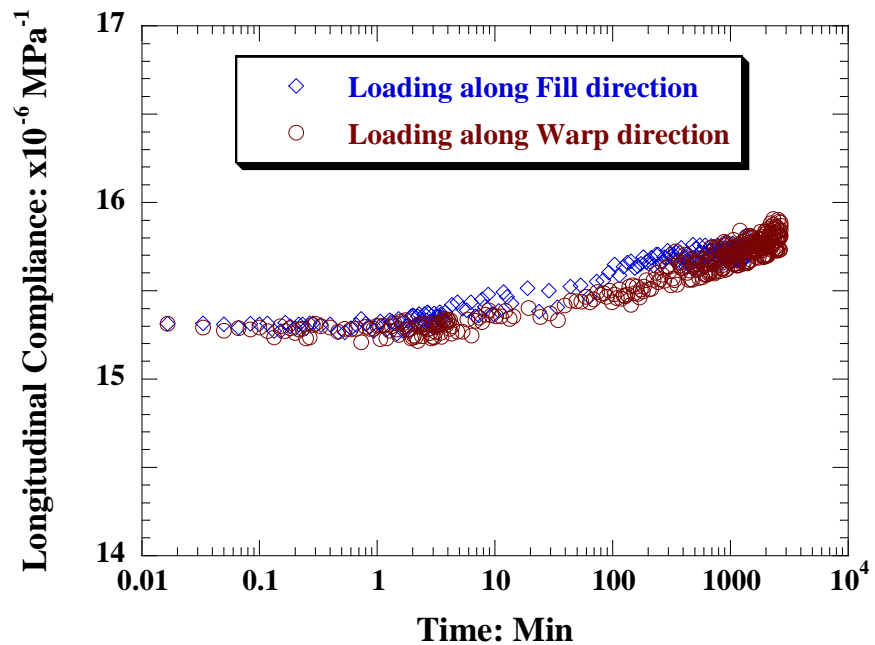


Figure 5.11: Experimental creep results for [0, 90]₆ plain weave composite test coupons loaded to 200 MPa along fill and warp directions at 80 °C.

temperature range of 80- 240 $^{\circ}\text{C}$. The composite exhibited increasing damage above 160 $^{\circ}\text{C}$ during creep tests conducted above 1% UTS (section 4.2.9). Thus, the creep tests above 1% UTS stress were limited up to temperature of 160 $^{\circ}\text{C}$. The experimental results are presented first followed by model results. The fabric used in the present study had the same microstructural parameters (l , h_0 , l_u , $2a$, $2b$) in both fill and warp directions. This suggests that the composite properties would be same in both directions, In order to verify this, two composite coupons were tested under same stress and temperature, by loading along fill and warp directions. The creep plots obtained from these two tests are compared in *Figure 5.11*. The instantaneous compliance as well as creep compliance were the same along fill and warp directions. Thus, all creep test results presented in subsequent sections were generated by loading the coupons along fill direction only.

5.4.1.1 Effect of Temperature

To quantify the effect of temperature on tensile creep of plain weave composites under on-axis loading, creep tests were conducted at various temperatures ranging from 80- 160 $^{\circ}\text{C}$ at stress levels of 100- 450MPa (15- 70% UTS), using [0, 90]₆ test coupons. The creep results at various temperatures and at a stress level of 100MPa are shown in *Figure 5.12*. Similar creep plots are plotted at stress levels of 200, 300, 400 and 450MPa and can be found in *Appendix B*. It was found that the test coupons showed an increase in damage during creep tests, even at 160 $^{\circ}\text{C}$, when tested at 400 and 450MPa. Thus, the creep results at 400 and 450MPa were limited to the temperature of 140 $^{\circ}\text{C}$.

The instantaneous as well as creep compliance of the plain weave composites increased with increase in temperature. However, the magnitude of the increase in compliance was small at any test stress and temperature within test time period of 1hour.

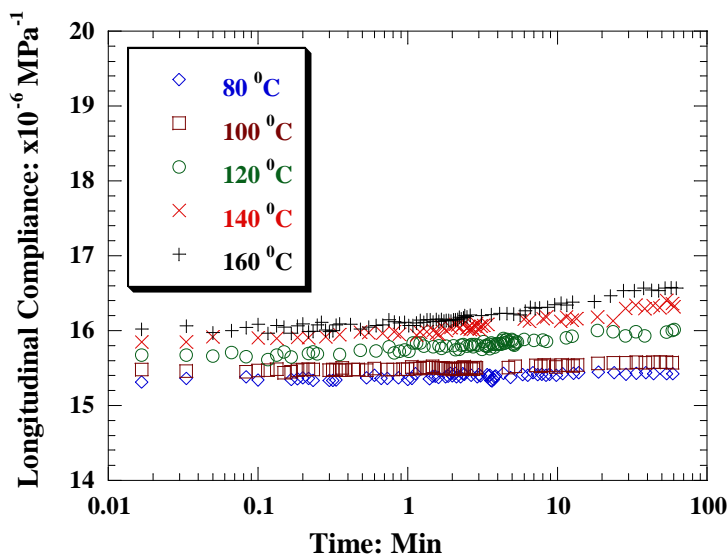


Figure 5.12: Experimental creep results for $[0, 90]_6$ plain weave composite test coupons at various temperatures and at a stress level of 100MPa.

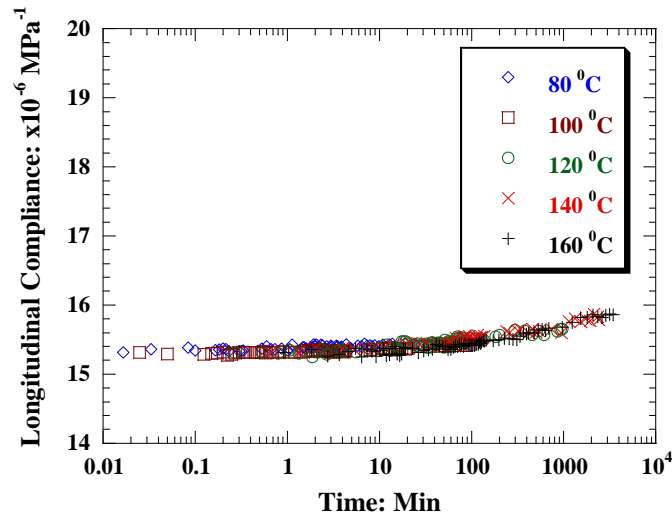


Figure 5.13: Master creep plot for $[0, 90]_6$ plain weave composite test coupons at a reference temperature of 80 °C and at a stress level of 100MPa.

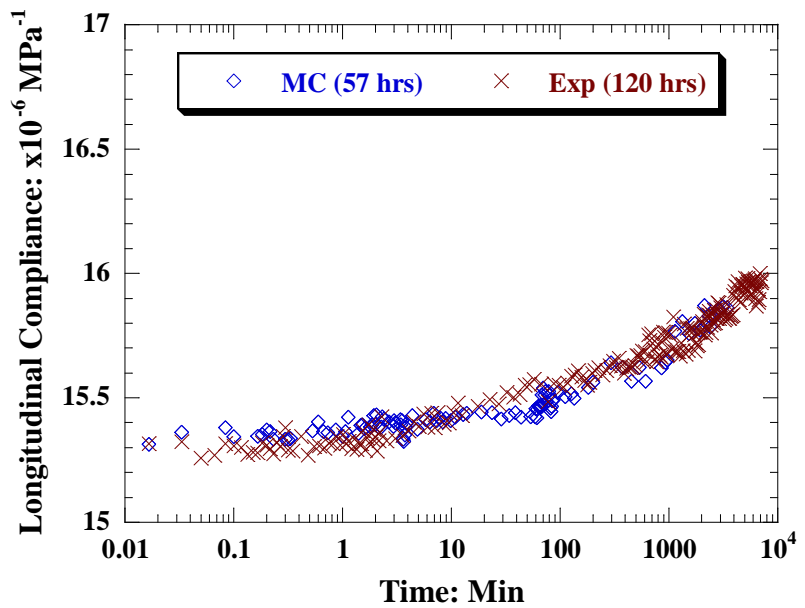


Figure 5.14: Comparison of master creep plot and experimental creep data of $[0, 90]_6$ plain weave composite test coupon at a temperature of 80°C and stress of 100MPa.

The total increase in creep compliance at the highest test stress and temperature was found to be ~ 8% within experimental time window. The plain weave composite consists of fibers in orthogonal direction and was loaded along the fibers in this case. Since the fiber modulus is much higher than that of the polymer matrix in the composite, the composite exhibited less creep within the experimental time window.

As discussed in chapter 2, it is not possible to obtain the creep data for the composite for its entire service life (25- 30years) experimentally. Thus, in practice short-term creep tests are usually conducted at higher temperatures, much beyond the actual service temperature, and within possible experimental time window. The creep data generated at various temperatures is shifted to the actual service temperature (or to a reference temperature) and the creep data is obtained for entire service life of the composite. Such shifting procedure is well known as Time-Temperature Superposition Principle (TTSP) and is discussed in Chapter 2. Normally, this is applied to polymer matrix and unidirectional tape composites. The TTSP procedure was adopted in the present work also to obtain long-term creep data at a reference temperature of 80 $^{\circ}\text{C}$, beyond the experimental time window, in order to verify the predictive capability of the creep model.

The creep plots at different temperatures were shifted to a reference temperature of 80 $^{\circ}\text{C}$ and a master plot was generated. Such a master plot at 100MPa is shown in *Figure 5.13*. Similar master plots were also generated at other stress levels and can be found in *Appendix B*. In order to confirm the validity of the TTSP procedure, a fresh test coupon was tested at 100MPa and 80 $^{\circ}\text{C}$ for the time period of 120 hours (5days), which is two times the maximum shifted creep time for the master plot. The experimental creep

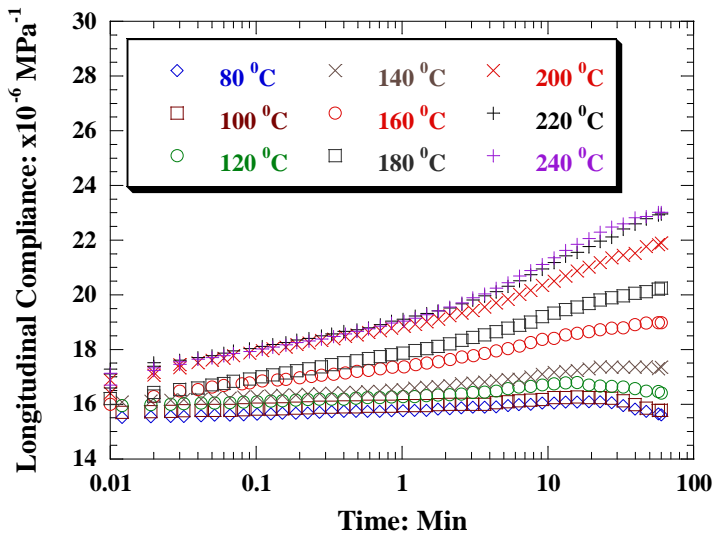


Figure 5.15: Experimental creep plots for $[0, 90]_6$ plain weave composite test coupons at various temperatures and at a stress level of 5MPa.

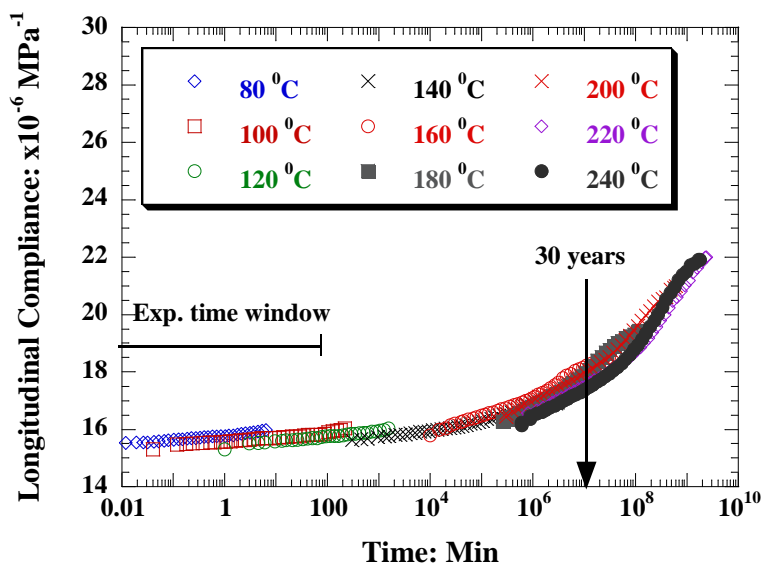


Figure 5.16: Master creep plot for $[0, 90]_6$ plain weave composite test coupon at a reference temperature of 80 °C and at a stress level of 5MPa.

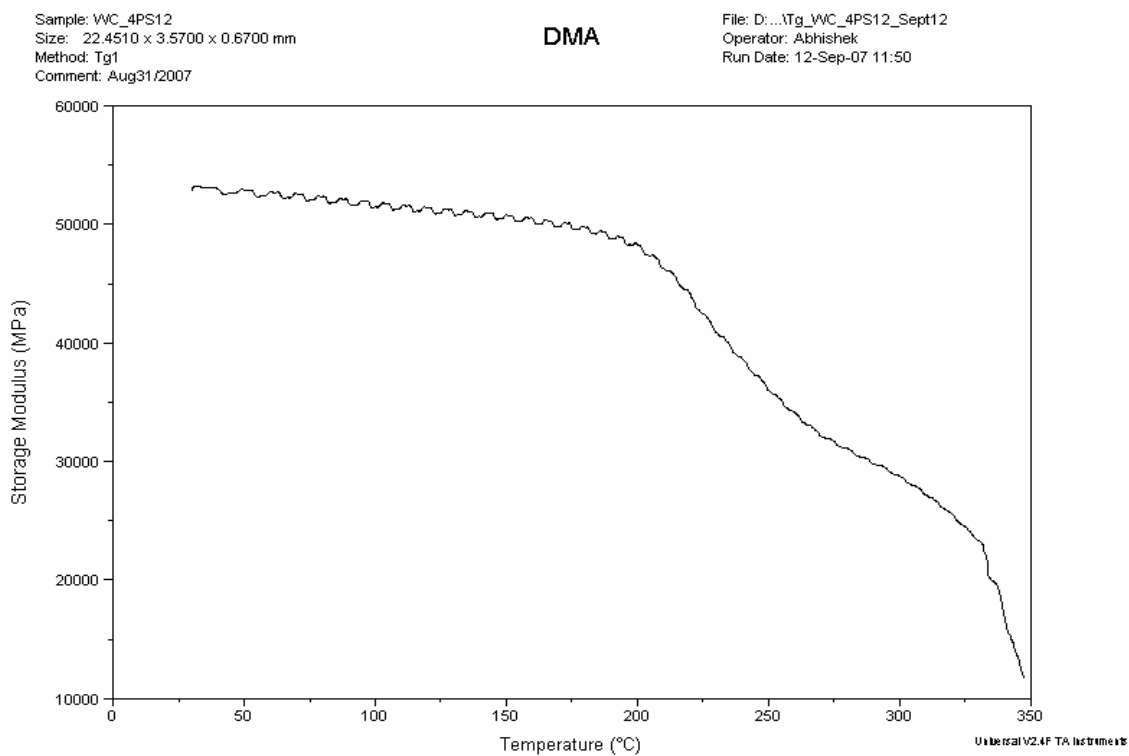


Figure 5.17: Variation of storage modulus of [0, 90] plain weave composites with temperature obtained using DMA at 10Hz frequency.

plot at 100MPa is compared with the master plot obtained using TTSP in *Figure 5.14*. Both the creep plots superpose with each other confirming the applicability of TTSP to obtain the creep data beyond the experimental time window for woven composites. Since, the composite could not be tested beyond the temperature of 160 $^{\circ}\text{C}$, the creep data could not be obtained beyond 2.5days through superposition at the tested stress levels. However, the composite did not show any increase in process-induced damage during creep at lower stress levels (< 1% UTS) above 160 $^{\circ}\text{C}$. Hence, tensile creep tests were conducted at stress levels of 3, 5 and 7 MPa in the temperature range of 80- 240 $^{\circ}\text{C}$. The creep tests at these stress levels were conducted using the Dynamic Mechanical Analyzer (DMA). The creep plots at different temperatures and at 5 MPa are shown in *Figure 5.15*. The creep plots at different temperatures were shifted to a reference temperature of 80 $^{\circ}\text{C}$ and a master plot was generated, as shown in *Figure 5.16*. The creep plots at 3 and 7MPa at different temperatures and master plots at these stresses can be found in *Appendix B*. Using the master plots at these stresses, the creep data was obtained for a longer time period (> 30years).

The instantaneous compliance of the composite increased with increase in temperature. Hence, before applying the TTSP procedure to obtain a master plot (which accounts for shift in time due to temperature), the creep plots at higher temperatures were required a vertical shift to eliminate the increase in instantaneous compliance with temperature. These vertical shift factors were obtained as follows. The change in modulus with temperature was obtained using DMA at a frequency of 10Hz. This high frequency was chosen to eliminate any contribution from viscoelasticity to the modulus. The modulus versus temperature plot is shown in *Figure 5.17*. The instantaneous compliance

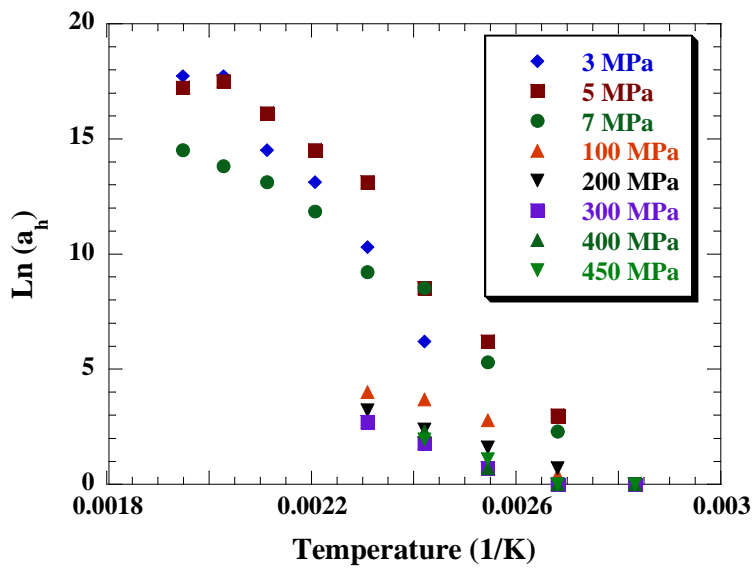


Figure 5.18: Horizontal shift factors for $[0, 90]_6$ plain weave composites as a function of inverse of temperature at various stress levels.

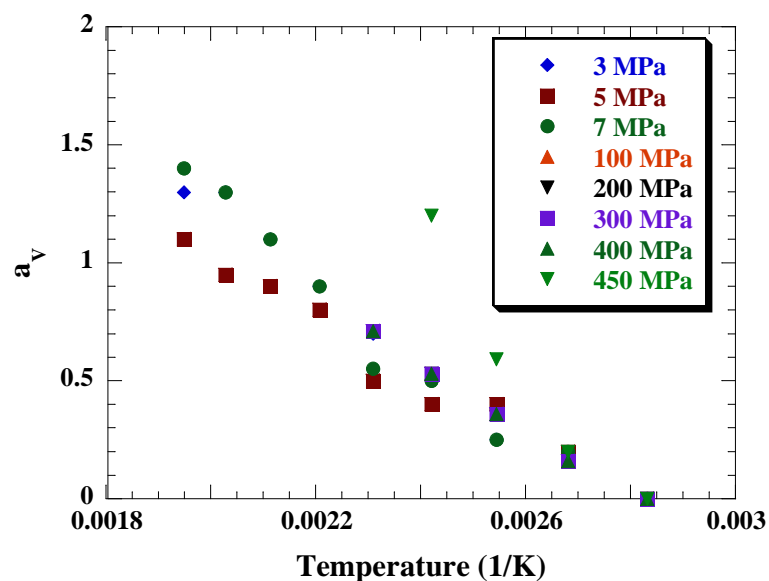


Figure 5.19: Vertical shift factors for $[0, 90]_6$ plain weave composites as a function of inverse of temperature at various stress levels.

Table 5.6: Activation energies and pre-exponential factors for [0, 90]₆ plain weave composites at various stress levels.

Stress (MPa)	Activation Energy (E) KJ/mol	Pre-exponential factor (A)
3	174.21	58.71
5	165.85	57.22
7	134.17	46.39
100	72.08	24.36
200	51.56	17.45
300	44.94	14.87
400	44.95	14.92
450	41.39	13.81

at any temperature was calculated using the equation $S_0 = A + B^* T$, as described in [4], where A is the constant, B is the slope obtained from DMA plot in *Figure 5.17* and T is the temperature in ^0K . The values of A and B are $1.218 \times 10^{-5} \text{ MPa}^{-1}$ and $8.88 \times 10^{-9} \text{ MPa}^{-1} \text{ K}^{-1}$, respectively, obtained from *Figure 5.17*. The vertical shift for a creep plot at T with respect to T_{ref} is given by the difference in instantaneous compliance at these two temperatures. This vertical shift factor was subtracted from the creep plot if $T > T_{\text{ref}}$ and this resulted in shifting down of the creep plot at T. This vertical shift factor is added to the creep plot if $T < T_{\text{ref}}$ and this results in shifting up of the creep plot at T. The horizontal and vertical shift factors for all stress levels are plotted as a function of temperature in *Figure 5.18* and *Figure 5.19*, respectively. The activation energy for the molecular mechanism responsible for the observed creep can be obtained from the slope of the plot of horizontal shift factor vs. temperature and Arrhenius model for the relationship between the horizontal shift factor and temperature, represented by equation 5.1 below:

$$a_T = A \exp\left[\frac{-E}{RT}\right]; \quad \ln(a_T) = \ln(A) - \frac{E}{RT} \quad (5.1)$$

where, a_T = horizontal shift factor; E = activation energy (J/mole); R = gas constant (8.314 J/K.mole); T = Temperature (K); A= pre-exponential constant.

The activation energy and pre-exponential factors obtained at each stress level is tabulated in *Table 5.6*. The activation energy for transverse creep, obtained using unidirectional tape is 125KJ/mole, which is different from the values reported in *Table 5.6*. This is thought to be due to the effect of fibers. In [90 0] composites used in generating transverse creep of unidirectional tape, the fibers are oriented transverse to the loading direction and hence, the measured creep is due to polymer matrix. Hence, the

activation energy from transverse creep can be considered to be representative of the creep mechanism. However, in woven composites the fibers are oriented parallel to the loading axis in addition to their transverse orientation.

Moreover, the activation energy values reported in *Table 5.6* decreases with increase in stress. However, according to thermal activation theory, the activation energy for creep should not change with applied stress. Hence, the activation energy for a woven composite cannot be considered to be corresponding to the mechanism that causes creep. It is to be considered as a constant used in determining the horizontal shift factor for woven composites.

5.4.1.2 Effect of Stress

The creep results at various stresses ranging from 100- 450MPa are plotted in *Figure 5.20* at a temperature of 80 $^{\circ}$ C. Similar creep results at other test temperatures can be found in *Appendix B*. The increase in instantaneous and creep compliance with increase in applied stress was insignificant up to a stress level of 400MPa, superposed within experimental time window. As stated previously, the creep behavior under on-axis loading is dominated by the fiber and hence, increase in applied stress does not accelerate creep. However, the creep results at 450MPa showed an increase in instantaneous as well as creep compliance.

Master creep plots at different stress levels, obtained using the TTSP procedure discussed in the previous section, are plotted together in *Figure 5.21*. Even though the creep plots, for the stress level up to 400MPa, superpose within experimental time window, they deviate beyond that. The probable cause of higher creep at stresses at and

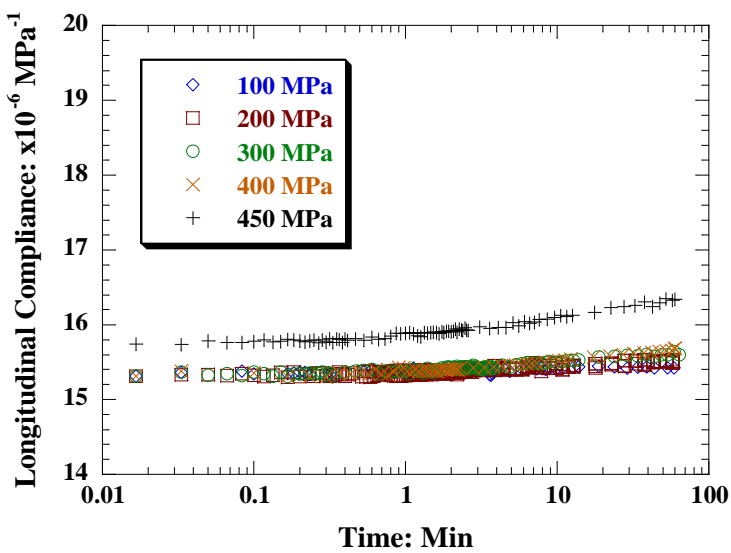


Figure 5.20: Experimental creep results for $[0, 90]_6$ plain weave composite test coupons at various stress levels and at a temperature of 80°C .

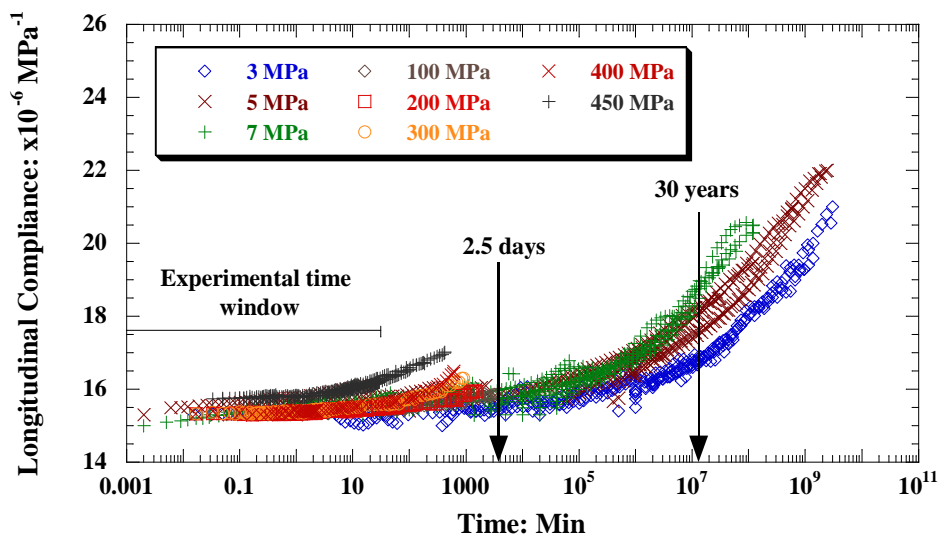


Figure 5.21: Master creep plots for $[0, 90]_6$ plain weave composite test coupons at various stress levels and at a temperature of 80°C .

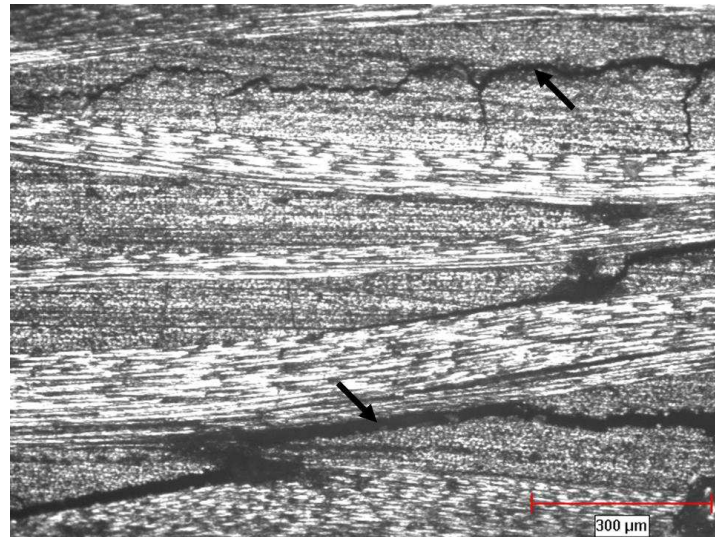


(a) 300MPa, 160 $^{\circ}$ C



(b) 400MPa, 140 $^{\circ}$ C

Continued.....



(c) 450 MPa, 140 °C

Figure 5.22: Micrographs of $[0, 90]_6$ plain weave composite test coupons after creep test at the highest temperature tested for various stress levels.

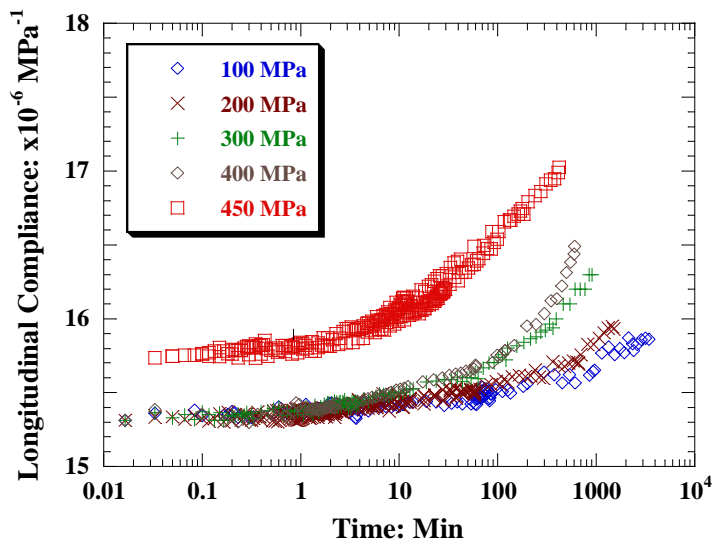


Figure 5.23: Master creep plots for $[0, 90]_6$ plain weave composite test coupons at various stress levels and at a temperature of 80 °C.

beyond 400MPa could be due to time-dependent damage, during creep, at these stresses and higher temperatures. This type of damage is further discussed in following section.

5.4.1.3 Effect of time-dependent damage

As stated in chapter 4, the damage did not increase during tensile loading up to the fracture stress in the temperature range of 80- 160 $^{\circ}\text{C}$. To confirm the same during creep at different stress levels tested, the recovery strain was recorded after each test in addition to the inspection of test coupons under microscope after each test. The test coupons were found to recover completely after creep tests at 100 and 200MPa for the entire test temperature range. However, the test coupons tested at stress levels of 300MPa after 160 $^{\circ}\text{C}$ and at stress levels of 400 & 450MPa after 140 $^{\circ}\text{C}$ were found to have permanent recovery strain of 500-700 μstrain . These test coupons were also observed to have considerable increase in damage, as shown in *Figures 5.22a-c*. These damage modes include vertical cracks, transverse cracks and delamination, indicated by ‘black arrows’ in *Figure 5.22a-c*. The master plots at stress levels from 100-450MPa are plotted in *Figure 5.23*. The time beyond 60-100mins in these plots corresponds to the creep plot obtained at 160 $^{\circ}\text{C}$ for 300MPa and 140 $^{\circ}\text{C}$ for 400 & 450MPa. It can be observed that the slope of creep plot changes beyond 60mins at 300-450MPa stresses. Increase in damage, as observed through micrographs, caused sudden increase in creep rate during creep at these stresses.

5.4.1.4 Creep model results

Creep results for on-axis and off-axis loading of [0, 90]₆ composites were predicted using the MELM creep model presented in Chapter 3 and the average crimp parameters presented in *Table 5.8* and are compared with experimental results in this

section to validate the creep model. First, a parametric study of effect of microstructure on instantaneous (i.e. time-independent) compliance and creep (time-dependent) compliance of plain weave composites is presented. Subsequently, the MELM creep model predictions are compared with experimental results. Predictions using two models available in the literature, the crimp model [50] and the equivalent laminate model [20], are also presented to highlight the merits of the model developed in this thesis.

5.4.1.4.1 Parametric study of effect of microstructure

The experimental characterization of microstructure of a single ply and multi-ply plain weave composite coupons, presented in section 5.2, shows a range of values for the various microstructural parameters. Since, it was not possible to study experimentally the effect of this variation in various microstructural parameters on elastic properties and creep of plain weave composites, a parametric study was conducted to analyze the effect of this variation on the elastic properties and creep of the composite under on-axis loading. This is also used later in interpreting any difference between the experimental and predicted results.

It was observed in section 5.2 that the average length of the unit cell (l) was same (2.0 - 2.1mm) for both single-ply lamina and multi-ply laminate. However, the undulation length (l_u) was higher and lamina thickness (h_0) was lower in multi-ply laminates than a single-ply lamina due to consolidation. Within multi-ply laminate coupons, the range of undulation length (l_u) was found to be 0.6- 0.7mm, while the range of lamina thickness (h_0) was found to be 0.18- 0.22mm. These two parameters define the crimp angle, which can significantly influence the elastic behavior and creep of the plain weave composites.

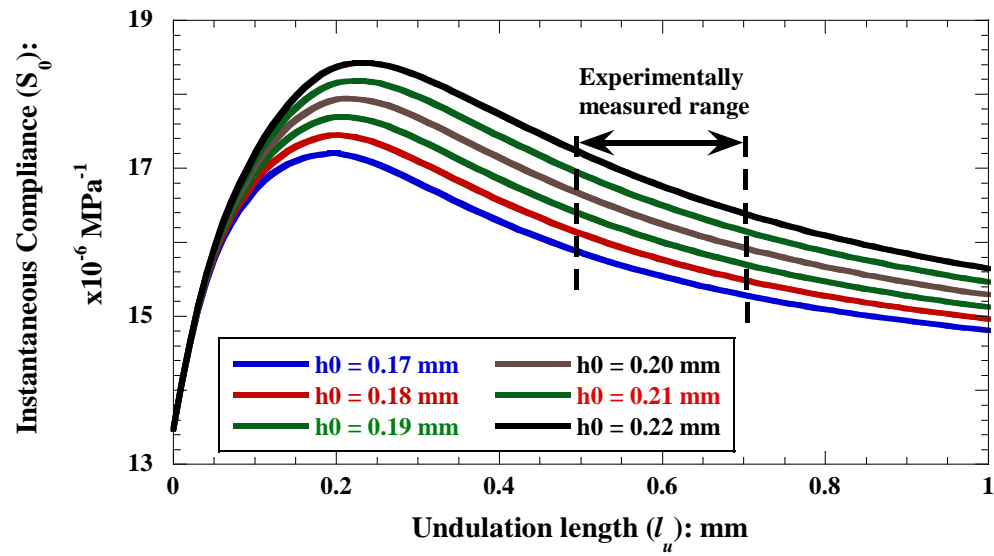


Figure 5.24: Variation of instantaneous compliance of plain weave composites with undulation length (l_u) under on-axis loading.

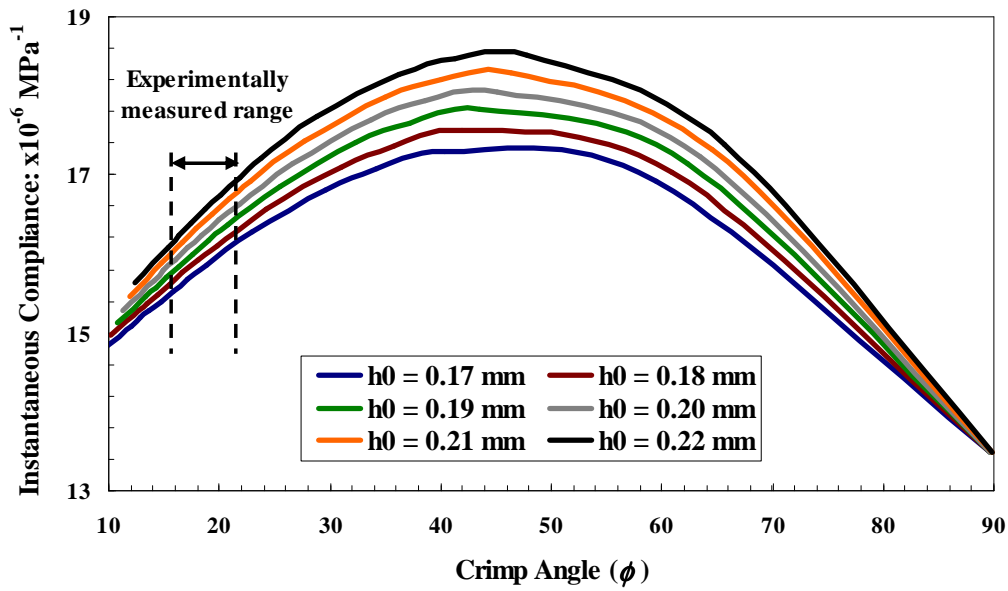


Figure 5.25: Variation of instantaneous compliance of plain weave composites with crimp angle under on-axis loading.

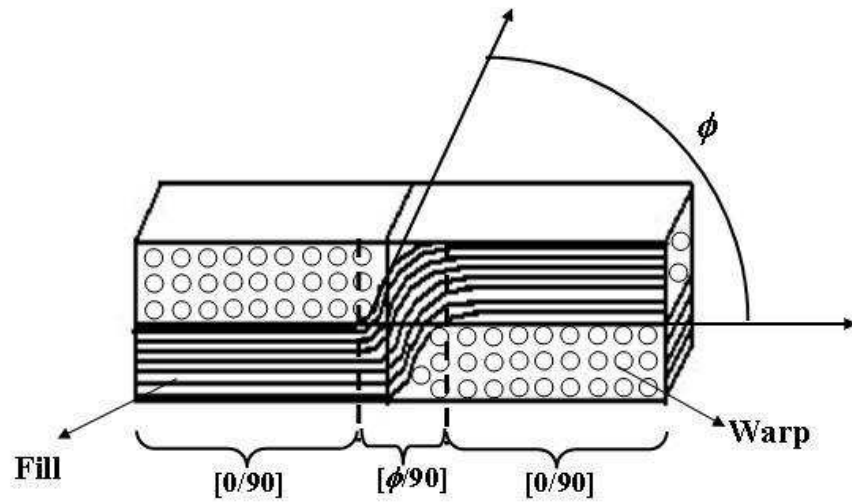


Figure 5.26: Schematic of a plain weave unit cell.

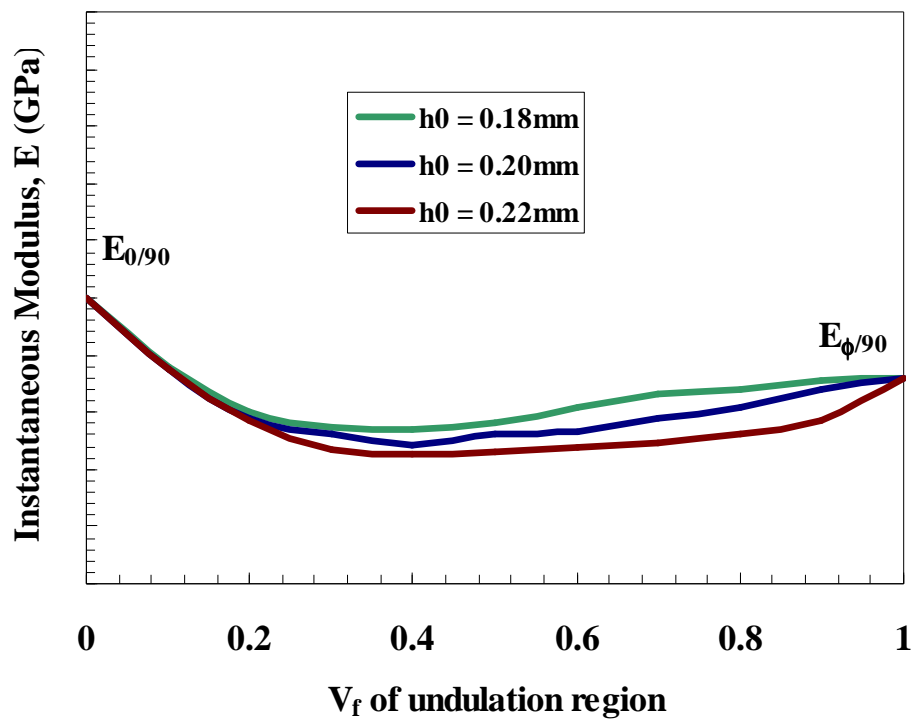


Figure 5.27: Variation of modulus with volume fraction of undulation region in a plain weave composite.

In order to study the effect of undulation length and lamina thickness on predicted compliance of plain weave composites, a range of $l_u = 0$ to 1.0mm and $h_0 = 0.17$ to 0.22mm was selected and the instantaneous compliance was predicted at 80 $^{\circ}\text{C}$, using instantaneous properties of unidirectional composites given in *Table 4.8*. The unit cell length (l) was kept constant as 2.1mm. The predicted instantaneous compliance is plotted in *Figure 5.24* as a function of l_u for various h_0 values. The compliance at $l_u = 0$ corresponds to a cross-ply laminate [0/90]_s with the lowest compliance or highest modulus. The compliance increased with increase in l_u to a maximum at $l_u = 0.2$ mm, beyond which it decreased with further increase in l_u . The compliance also increased with increase in h_0 , for a given l_u . The single and multi-ply woven composites, studied in present work, had l_u in the range of 0.5- 0.7mm and h_0 in the range 0.18- 0.22mm. In this range for l_u & h_0 , the compliance decreases with increase in l_u . The instantaneous compliance is also plotted in *Figure 5.25* as a function of crimp angle for different h_0 (crimp angle = $\tan^{-1}(h_0/l_u)$) and for the entire range of l_u shown in *Figure 5.24*. The compliance increases with increase in crimp angle within the experimentally measured range (13-21 $^{\circ}$) of crimp angles for the single-ply lamina and multi-ply laminate. The change in compliance within experimentally measured undulation parameters range is found to be 5%.

In order to understand these figures, let us consider a schematic of a plain weave unit cell, shown in *Figure 5.26*. For a given unit cell length (l) and thickness (h_0), as undulation length (l_u) increases, the crimp angle (ϕ) of fill yarn decreases. With decrease in crimp angle, the modulus of the fill yarn in the undulation region increases and approaches the modulus of the [0 0] composite. Hence, the compliance of undulation

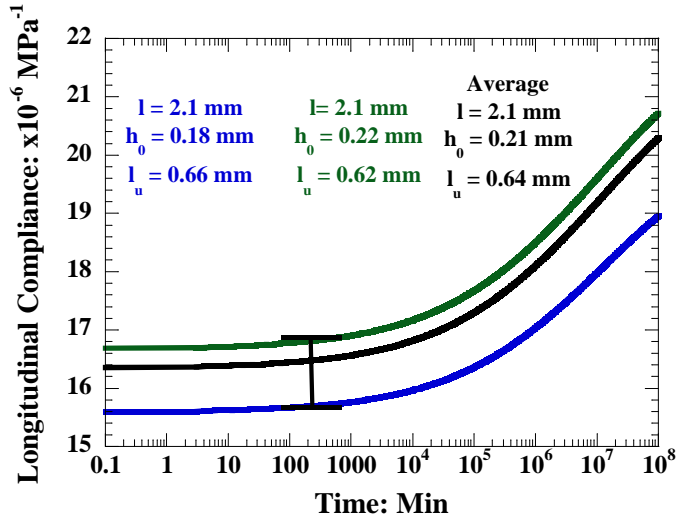
region as well as of overall composite decreases with decrease in crimp angle, as seen in *Figure 5.25* within experimentally measured range for crimp angle (13-21°).

Now, consider the undulated [φ/90] and straight [0/90] portions of the unit cell of the plain weave lamina. With increase in l_u , the volume fraction of [φ/90] laminate section increases, while the volume fraction of [0/90] laminate section decreases. Hence, for a given lamina thickness (h_0), the overall modulus of the composite decreases (i.e. the compliance increases) with increase in l_u due to the increase in volume fraction of [φ/90], as shown in *Figure 5.27*. This trend is opposite to the trend in *Figure 5.24* where the compliance of the plain weave composite decreases with increase in l_u within the experimentally measured range.

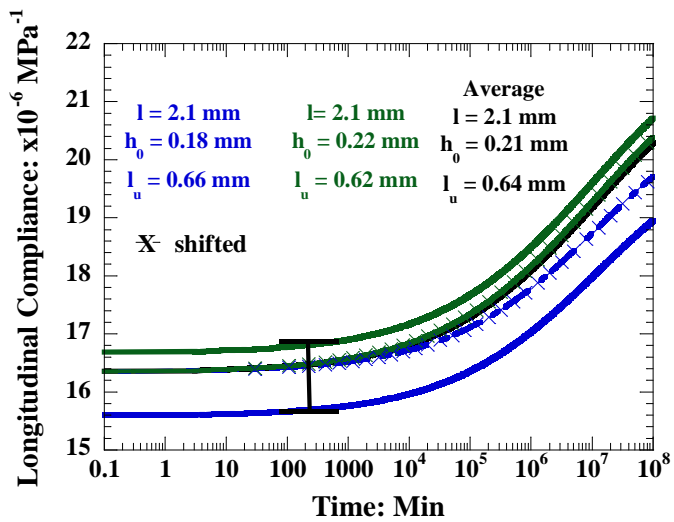
Based on the discussion in the above two paragraphs, it can be concluded that the overall compliance of the unit cell depends on both the crimp angle and the volume fraction of undulated part. Thus, the compliance of the composite, for a given set of undulation parameters, is due to the combined effect of the crimp angle and volume fraction of undulated part of the plain weave composite. At low l_u , the crimp angle is very high and volume fraction of [φ/90] is very low resulting in lower compliance. With increase in l_u , crimp angle decreases and the volume fraction of [φ/90] increases resulting in increase in compliance. However, at higher l_u , the relative effect of crimp angle is much higher than the effect of increase in volume fraction of [φ/90] and thus the overall compliance shows continuous decrease with increase in l_u . Because of these opposing effects, a peak in compliance is observed at $l_u = 0.2\text{mm}$.

Table 5.7: Average, upper bound, and lower bound values for the undulation parameters

Undulation parameters (in mm)			
	l	h_0	l_u
Upper bound	2.1	0.22	0.62
Lower bound	2.1	0.18	0.66
Average	2.1	0.21	0.64



(a)



(b)

Figure 5.28: Predicted creep compliance of plain weave composites under on-axis loading at 80 °C, using three sets of undulation parameters.

For a constant unit cell length and undulation length, as lamina thickness (h_0) increases, the crimp angle increases resulting in increase in the instantaneous compliance as shown in *Figures 5.24 and 5.25*, for the entire range of l_u .

Similar effect of undulation parameters is observed on the creep compliance of the composite. Based on data in *Tables 5.1 and 5.2*, an average value, an upper bound value, and a lower bound value were chosen for the undulation parameters. These are tabulated in *Table 5.7*. The creep predictions using these values are plotted in *Figure 5.28a*. The upper bound of predicted instantaneous compliance is 16.67×10^{-6} MPa $^{-1}$ and lower bound of predicted instantaneous compliance is 15.59×10^{-6} MPa $^{-1}$, while the average instantaneous compliance is predicted as 16.35×10^{-6} MPa $^{-1}$. As shown in *Figure 5.28b*, the creep plots obtained using upper bound and lower bound undulation parameters were shifted by subtracting/ adding the difference between upper bound and lower bound instantaneous compliance with average instantaneous compliance, respectively. This is done to evaluate the effect of undulation parameters on creep rate. It is observed that the predicted creep rate is relatively lower obtained using lower bound undulation parameters (compliance @ 1×10^8 min = 19.71×10^{-6} MPa $^{-1}$), than the predicted creep rate obtained using average undulation parameters (compliance @ 1×10^8 mins = 20.29×10^{-6} MPa $^{-1}$). Similarly, predicted creep rate obtained using upper bound undulation parameters (compliance @ 1×10^8 mins = 20.39×10^{-6} MPa $^{-1}$) is relatively higher than predicted creep rate obtained using average undulation parameters (compliance @ 1×10^8 mins = 20.29×10^{-6} MPa $^{-1}$). As discussed previously, compliance of the composite decreases with increase in undulation length (l_u) and decrease in lamina thickness (h_0). Since, the lower bound undulation parameters have highest l_u and lowest h_0 , the

instantaneous as well as creep compliance is predicted lowest. On the other hand, upper bound undulation parameters have lowest l_u and highest h_0 , the instantaneous and creep compliance is predicted highest.

At any given creep time, the difference between the creep compliance predicted using the average and the two bound values in *Table 5.7* is $\pm 3.5\text{-}4\%$, considering difference between initial compliances and compliance predicted at the highest time shown in *Figure 5.28*. Thus, if the experimental plot compares with the predicted creep cures within $\pm 3.5\text{-}4\%$, the prediction is considered to be accurate in this thesis. The average undulation parameters were used for generation of predicted results presented in the subsequent sections. The error range in prediction, $\pm 3.5\text{-}4\%$, is superposed with the predicted results.

5.4.1.4.2 Creep Model Predictions and Validation

A modified equivalent laminate model (MELM) was used to predict creep of plain weave composites using the average undulation parameters given in *Table 5.7* and unidirectional composite properties given in *Table 4.8*. Predicted results are compared with experimental results in the stress range of 100-450MPa at 80°C , within as well as beyond experimental time window, and validated. As described in section 5.4.1.1, the master plots obtained using experimental creep data at these stress levels could not be obtained beyond 5 days and thus the predicted plots could not be validated for longer time period (e.g. up to 30 years of service life of a composite part). Hence, the creep master plots obtained at 3 to 7 MPa are used to validate the predictions up to 30 years of service life of composite.

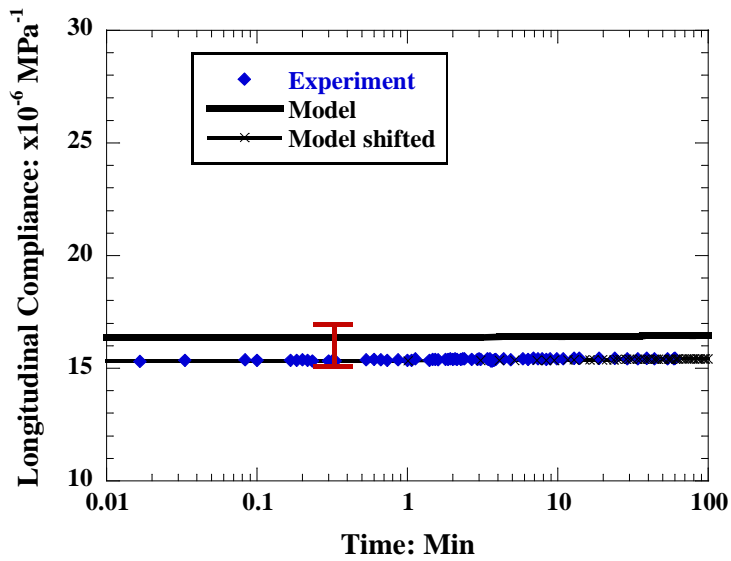


Figure 5.29: Comparison of model predictions with experimental creep results obtained at a stress of 100MPa and temperature of 80 $^{\circ}$ C for plain weave composites under on-axis loading.

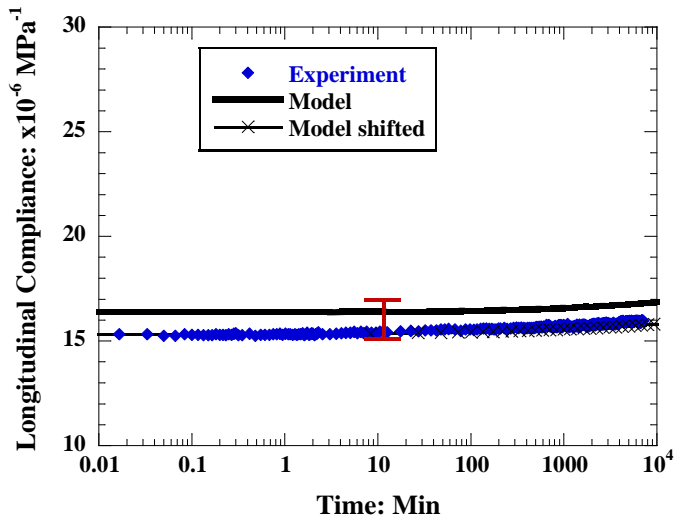


Figure 5.30: Comparison of model predictions with master plot obtained at a stress of 100MPa and temperature of 80 $^{\circ}$ C for plain weave composites under on-axis loading.

Table 5.8: Comparison of on-axis experimental and predicted instantaneous compliance and modulus at various stress levels and at temperature of 80 °C.

Stress (MPa)	Experiment		Predicted	
	On-axis Compliance ($\times 10^{-6}$ MPa $^{-1}$)	On-axis Modulus (GPa)	On-axis Compliance ($\times 10^{-6}$ MPa $^{-1}$)	On-axis Modulus (GPa)
100	15.314	65.30	16.348	61.17
200	15.314	65.30	16.350	61.16
300	15.314	65.30	16.353	61.15
400	15.314	65.30	16.355	61.14
450	15.74	63.50	16.355	61.14

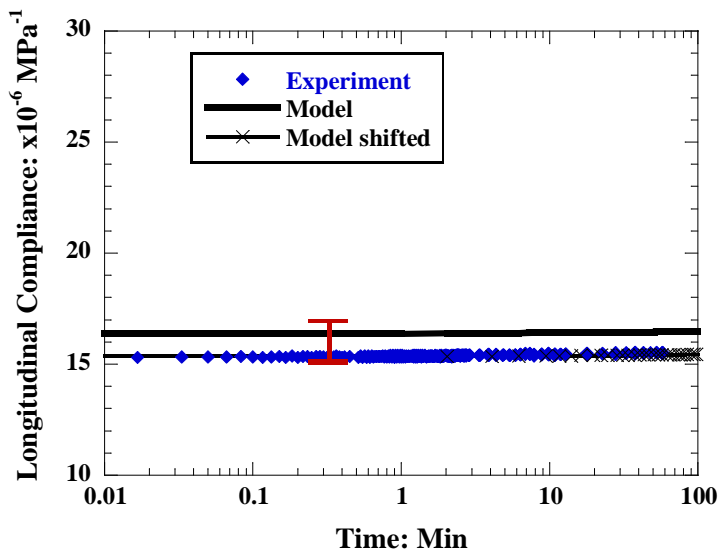


Figure 5.31: Comparison of model predictions with experimental creep results obtained at a stress of 200MPa and temperature of 80 $^{\circ}$ C for plain weave composites under on-axis loading.

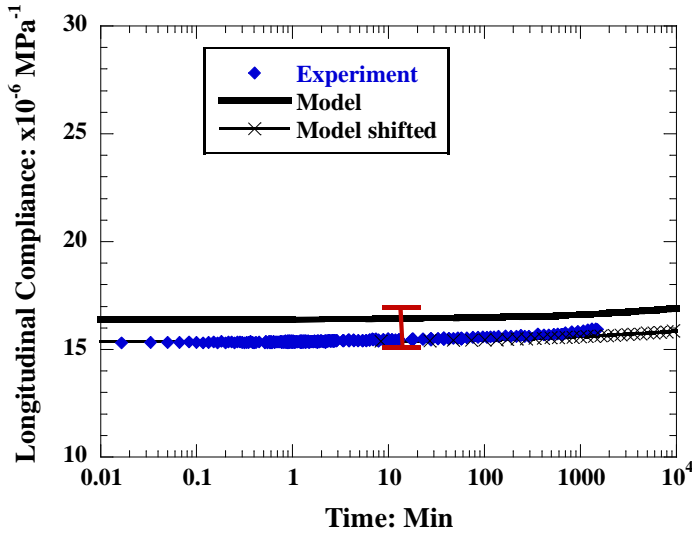


Figure 5.32: Comparison of model predictions with master plot obtained at a stress of 200MPa and temperature of 80 $^{\circ}$ C for plain weave composites under on-axis loading.

Model and experimental creep results at 100MPa and 80 °C are compared within experimental time window of 60mins and shown in *Figure 5.29*. The instantaneous compliance predicted from the model is higher than the instantaneous compliance obtained experimentally. The scatter band in the figure corresponds to the experimentally observed scatter in the undulation parameters. The experimental plots compares with the lower bound of the predicted compliance. The predicted and experimental instantaneous compliance/ modulus at for various applied stresses levels are tabulated in *Table 5.8*. The predicted and experimental increase in creep compliance within experimental time window is 1%. The predicted creep compliance is also higher than experimental creep compliance, due to higher predicted instantaneous compliance than experimental instantaneous compliance. As observed in *Figure 5.29*, the magnitude of increase in compliance within experimental time window is very small and does not show sufficient change in curvature to validate the predictions. Hence, the predictions beyond experimental time window are compared with the creep master plot obtained by applying TTSP to creep plots obtained at various temperatures at 100MPa. The comparison is shown in *Figure 5.30*. The experimental and predictions compare well within time period of master plot (5 days) within an error range of $\pm 3\%$. The predicted compliance shows an increase of 3% while the increase in experimental compliance is 3.5%. By delineating the difference of experimental and predicted instantaneous compliance, the shifted predicted creep plot, as shown in *Figures 5.29* and *5.30*, superpose with experimental plot. This validates the prediction accuracy of MELM model.

Model and experimental results for 200MPa stress at 80 °C are compared within and beyond experimental time window in *Figure 5.31* and *Figure 5.32*, respectively. The

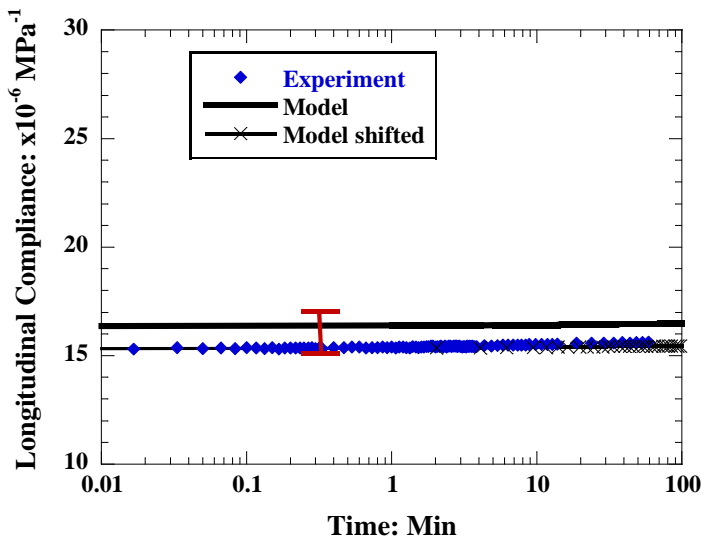


Figure 5.33: Comparison of model predictions with experimental creep results obtained at a stress of 300MPa and temperature of 80 $^{\circ}$ C for plain weave composites under on-axis loading.

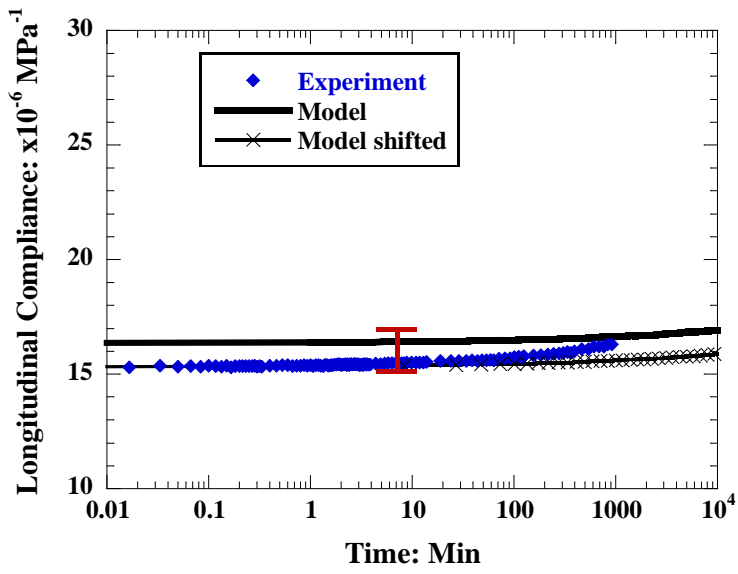


Figure 5.34: Comparison of model predictions with master plot obtained at a stress of 300MPa and temperature of 80 $^{\circ}$ C for plain weave composites under on-axis loading.

predicted and experimental instantaneous compliance/ modulus are given in *Table 5.8*. The experimental instantaneous and creep compliance are equal to the lower bound values of the predicted instantaneous and creep compliance, respectively. The creep predictions within experimental (60mins) as well as master plot time window (1.1days) compares well with experimental results within error range of $\pm 3\%$. The increase in creep compliance within experimental time window is observed to be 1-1.2%, while the increase in compliance within master plot time window is observed to be 2-2.5%. The shifted predicted plots are also shown in figures.

Model and experimental results for 300MPa stress at 80 $^{\circ}\text{C}$ are compared within and beyond experimental time window in *Figure 5.33* and *Figure 5.34*, respectively. The predicted and experimental instantaneous compliance/ modulus are given in *Table 5.8*. The experimental instantaneous and creep compliance are equal to the lower bound values of the predicted instantaneous and creep compliance, respectively. The creep predictions within experimental (60mins) as well as master plot time windows (0.6 days) compare well with experimental results within error range of $\pm 3\%$. The increase in experimental and predicted creep compliance within experimental time window is 1.5-2%. Increase in predicted compliance within the master plot time window is 2.1%, as compare to 4% increase in creep compliance obtained through experimental master plot. The shifted predicted plots are also shown in figures. As shown in *Figure 5.22a*, the test coupons tested at 300MPa and 160 $^{\circ}\text{C}$ exhibited time-dependent damage. Increase in damage at this temperature corresponds to the master plot time window of 365-915minutes (0.25-0.6days) at 300MPa. This increase in damage caused a higher creep rate and experimental creep compliance. Due to lack of consideration of this damage,

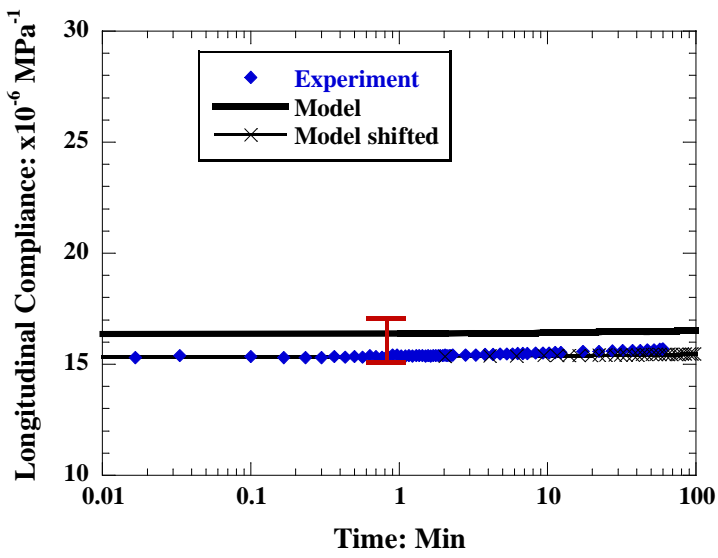


Figure 5.35: Comparison of model predictions with experimental creep results obtained at a stress of 400MPa and temperature of 80 $^{\circ}$ C for plain weave composites under on-axis loading.

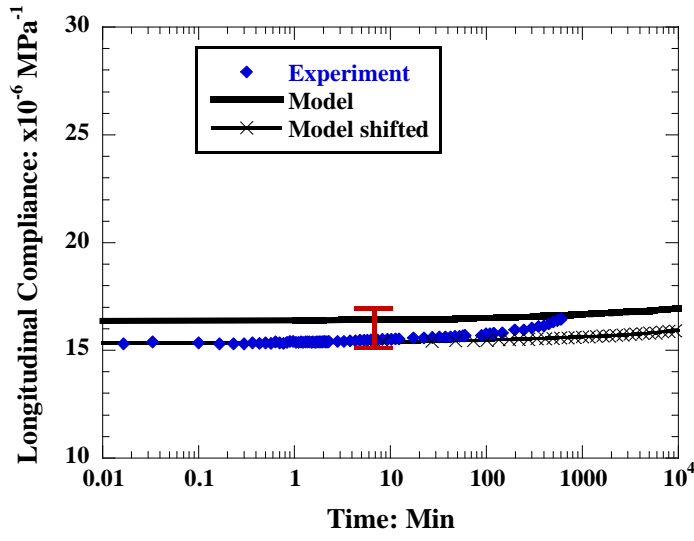


Figure 5.36: Comparison of model predictions with master plot obtained at a stress of 400MPa and temperature of 80 $^{\circ}$ C for plain weave composites under on-axis loading.

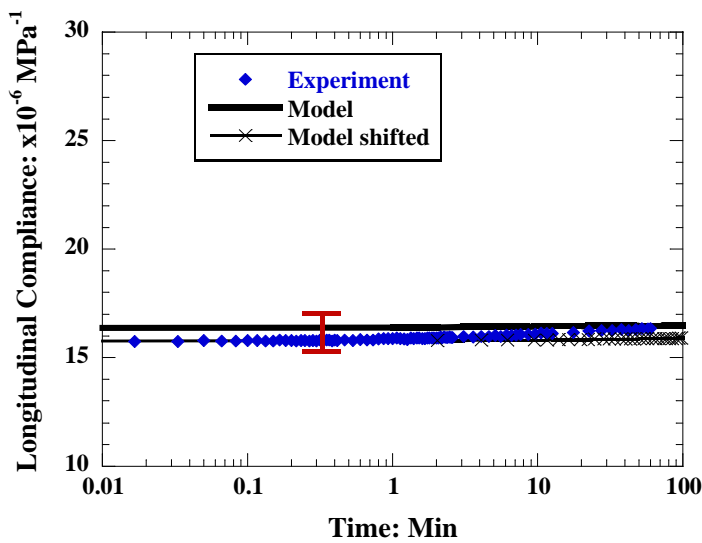


Figure 5.37: Comparison of model predictions with experimental creep results obtained at a stress of 450MPa and temperature of 80 $^{\circ}$ C for plain weave composites under on-axis loading.

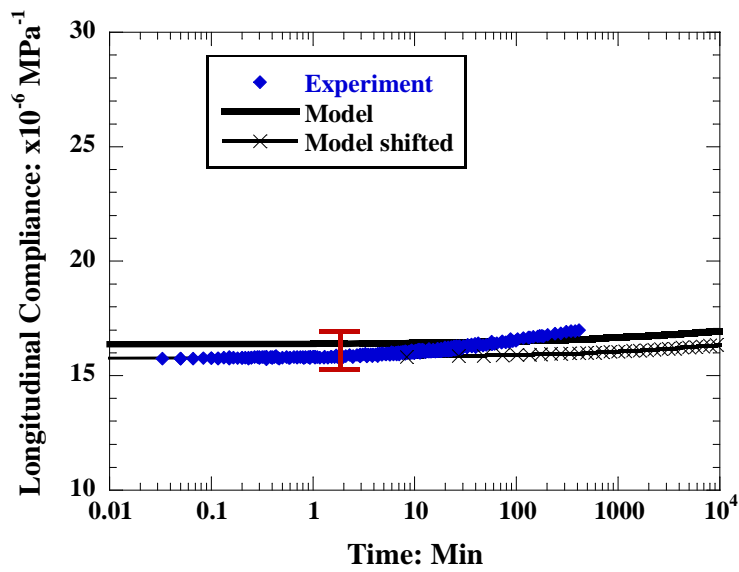


Figure 5.38: Comparison of model predictions with master plot obtained at a stress of 450MPa and temperature of 80 $^{\circ}$ C for plain weave composites under on-axis loading.

predicted creep compliance was lower than the experimental creep compliance within master plot time window.

Model and experimental results for 400MPa stress at 80 $^{\circ}\text{C}$ are compared within and beyond experimental time window in *Figure 5.35* and *Figure 5.36*, respectively. The predicted and experimental instantaneous compliance/ modulus are given in *Table 5.8*. The experimental instantaneous and creep compliance are equal to the lower bound values of the predicted instantaneous and creep compliance, respectively. The creep predictions within experimental (60minutes) as well as master plot time window (0.4 days) compare well with experimental results within an error range of $\pm 3\%$. The increase in experimental and predicted creep compliance within experimental time window is observed to be 1.5-2%. Increase in predicted compliance within master plot time window is observed to be 2.3% as compare to 6% increase in creep compliance obtained through experimental master plot. The shifted predicted plots are also shown in figures. As shown in *Figure 5.22b*, the test coupons tested at 400MPa and 140 $^{\circ}\text{C}$ exhibited time-dependent damage. Increase in damage at this temperature corresponds to the master plot time window of 120- 601minutes (0.1-0.4 days) at 400MPa. This increase in damage caused higher creep rate and experimental compliance. Due to lack of consideration of this damage, the predicted creep compliance was lower than that of the experimental creep compliance, within master plot time window.

Model and experimental results for 450MPa stress at 80 $^{\circ}\text{C}$ are compared within and beyond experimental time window in *Figure 5.37* and *Figure 5.38*, respectively. The predicted and experimental instantaneous compliance/ modulus are given in *Table 5.8*. The experimental instantaneous and creep compliance are equal to the lower bound

values of the predicted instantaneous and creep compliance, respectively. The creep predictions within experimental (60 minutes) as well as master plot time window (0.3 days) compares well with experimental results within an error range of \pm 3%. The increase in predicted creep compliance is observed to be 1.5-2% as compare to 4% increase in experimental creep compliance, within experimental time window. Increase in predicted compliance within master plot time window is observed to be 2.5% as compare to 8% increase in creep compliance obtained through experimental master plot. The shifted predicted plots are also shown in figures. As shown in *Figure 5.22c*, the test coupons tested at 450MPa and 140 $^{\circ}$ C exhibited time-dependent damage. Increase in damage at this temperature corresponds to the master plot time window of 60-414minutes (0.05-0.3days) at 450MPa. This increase in damage caused higher creep rate and experimental creep compliance. Due to lack of consideration of this damage, the predicted compliance was lower than that of experimental compliance within master plot time window.

It can be observed in *Figures 5.29-5.38* that the change in curvature of the master creep plots within the master plot time window were not sufficient enough to validate the model predictions up to the typical service life of an aerospace composite part (30 years). Hence, the master plots at 3-7MPa stress levels were obtained for a time window of 30 years and were used to validate the model predictions for a time period of 30 years.

Model predictions and master plots at 3, 5 and 7 MPa stress levels and at 80 $^{\circ}$ C are compared in *Figures 5.39-5.41*, respectively. The predicted and experimental instantaneous compliance/ modulus at these stresses are tabulated in *Table 5.9*. The experimental instantaneous and creep compliance are equal to the lower bound values of

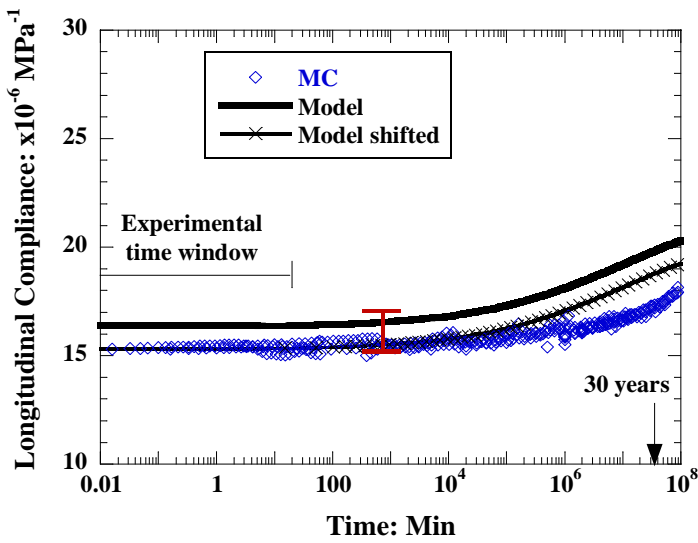


Figure 5.39: Comparison of model predictions with master plot obtained at a stress of 3MPa and temperature of 80 $^{\circ}\text{C}$ for plain weave composites under on-axis loading.

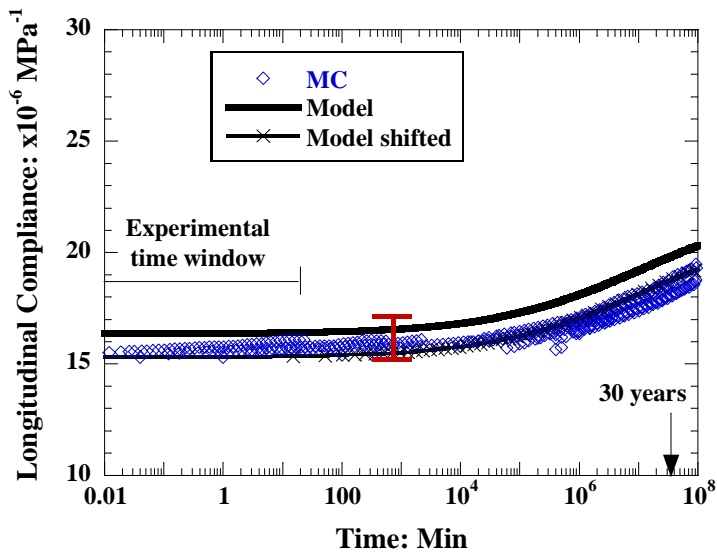


Figure 5.40: Comparison of model predictions with master plot obtained at a stress of 5MPa and temperature of 80 $^{\circ}\text{C}$ for plain weave composites under on-axis loading.

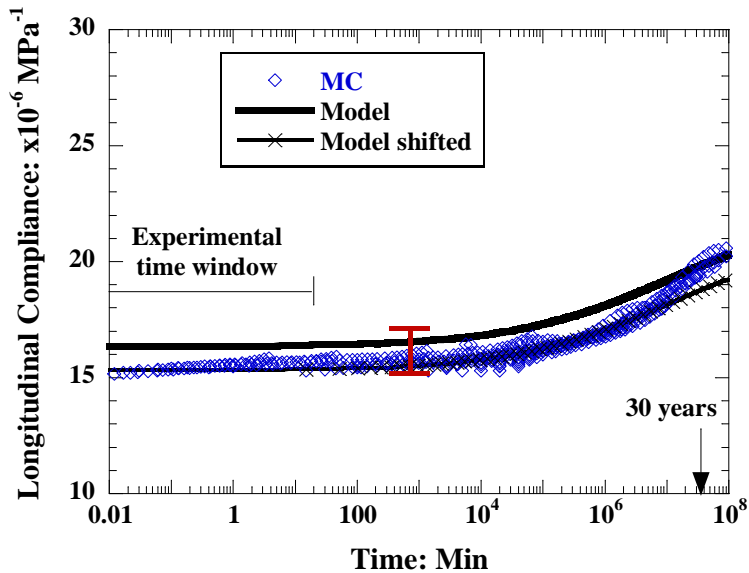


Figure 5.41: Comparison of model predictions with master plot obtained at a stress of 7MPa and temperature of 80 °C for plain weave composites under on-axis loading.

Table 5.9: Comparison of on-axis experimental and predicted instantaneous compliance and modulus at various stress levels and at temperature of 80 °C.

Stress (MPa)	Experiment		Predicted	
	On-axis Compliance ($\times 10^{-6}$ MPa $^{-1}$)	On-axis Modulus (GPa)	On-axis Compliance ($\times 10^{-6}$ MPa $^{-1}$)	On-axis Modulus (GPa)
3	15.31	65.32	16.346	61.18
5	15.31	65.32	16.346	61.18
7	15.31	65.32	16.346	61.18

predicted instantaneous and creep compliance, respectively. The creep predictions within experimental (60minutes) as well as master plot time window (>30years) compare well with experimental results within error range of \pm 3%. The total increase in creep compliance within a time period of 30 years is 30% for both the master creep plot and the predicted creep plot. The shifted predicted plots are also shown in *Figures 5.39-5.41* highlighting the prediction accuracy of MELM model.

In order to highlight the better prediction capability of MELM creep model over prediction capability of other published creep models, derived using crimp model [50] and equivalent laminate model [20], the predictions were obtained using crimp and equivalent laminate creep models and compared with predictions obtained using MELM creep model, for a given stress and temperature. In the crimp model (CM), the undulation in fill yarn of the unit cell is considered and the unit cell was modeled as such, without using an equivalent unit cell with equivalent properties, as discussed in *Appendix A*. In equivalent laminate model (EqM), the undulated fill and warp laminae within entire unit was replaced with an equivalent unidirectional laminae with equivalent properties, as discussed in *Appendix A*. In modified equivalent laminate model (MELM), presented in this thesis, the plain weave unit cell is divided in two sections. The first section simulates creep of straight part of the unit cell, while the second section simulates the creep of undulated part of the unit cell (simulated as equivalent unidirectional laminae with properties obtained by averaging the properties of the crimp section.).

Creep plots at 3MPa and 80 $^{\circ}$ C predicted using all three models with experimental results in *Figure 5.42*. Instantaneous compliance predicted by all three models was higher than the experimental value due to use of average undulation parameters. However, the

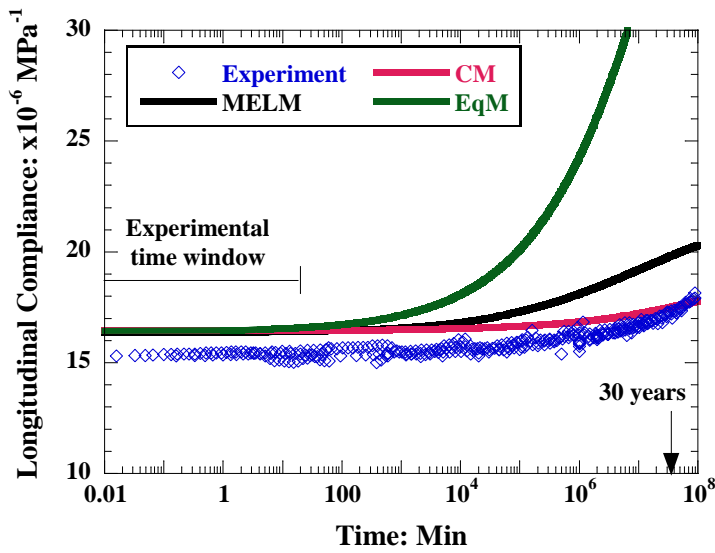


Figure 5.42: Comparison of MELM, CM and EqM model predictions with master plot obtained at a stress of 3MPa and temperature of 80 $^{\circ}\text{C}$ for plain weave composites under on-axis loading.

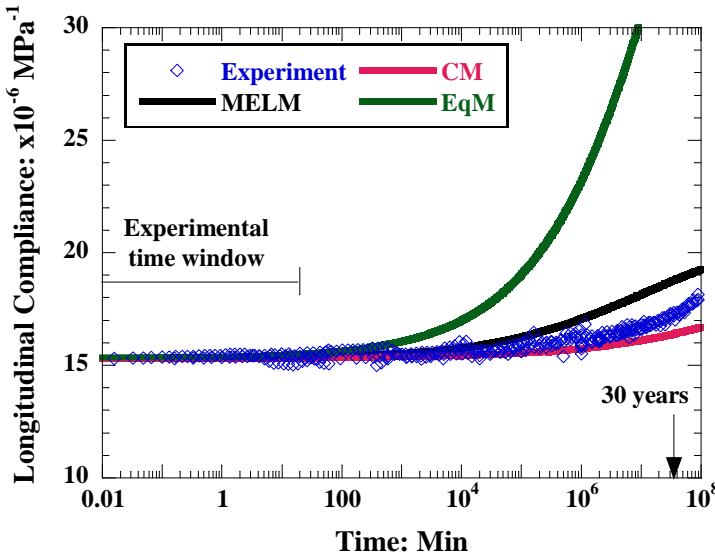


Figure 5.43: Comparison of shifted MELM, CM and EqM model predictions with master plot obtained at a stress of 3MPa and temperature of 80 $^{\circ}\text{C}$ for plain weave composites under on-axis loading.

curvature of the predicted creep plots varied significantly among themselves and from the curvature of the experimental master plot. In order to highlight this, the predicted plots in *Figure 5.42* are re-plotted in *Figure 5.43* by vertically shifting them by a magnitude equal to the difference in instantaneous compliance between the predicted and experimental values. It is very clear from the *Figure 5.43* that the predictions using crimp model deviate from the experimental results at longer time. Predictions using the Equivalent laminate model (EqM) deviate from the experimental master plot with increase in creep time. The prediction using Modified equivalent laminate model (MELM), developed in this thesis, superposed with experimental master plots very well, i.e. the curvature of both plots were same as shown in *Figure 5.43*. This model extended the approach of equivalent laminate model by considering creep of straight section and undulated section separately. Only the undulated section is simulated as made of equivalent unidirectional laminae, similar to the equivalent laminate model. Thus, the model simulates geometry of the plain weave fabric better than the EqM model and thus gives better predictions. These results highlight the merits of the MELM developed in this thesis, over the published models, in predicting the creep of plain weave composites under on-axis loading with accuracy.

Among the three models, only EqM and MELM can be used to predict the off-axis behaviour and these are discussed below.

5.4.2 Off-axis loading

The tensile creep of $[0, 90]_6$ plain weave composites under off-axis loading of 45° was generated by tensile loading of $[45, -45]_6$ test coupons. The creep tests were conducted at stress levels of 7, 50 and 100MPa (3-50% UTS) and in the temperature

range of 80- 160 $^{\circ}\text{C}$. The experimental and predicted creep results for various test conditions are presented and compared in the following sections.

5.4.2.1 Effect of time-independent and time-dependent damage

As discussed in section 5.3.2, plain weave composites showed an increase in damage during off-axis loading to desired creep load. These damages resulted in permanent strain in the composite. In order to study possible increase in damage during creep, the test coupons were allowed to recover after unloading from creep load for each creep test. The creep-recovery plots for each stress level and temperature tested are shown in *Figures 5.44, 5.45, and 5.46* for creep stresses of 7, 50 and 100MPa at 80 $^{\circ}\text{C}$. These stresses correspond to 3-50% of UTS at 80 $^{\circ}\text{C}$. Creep time was 60mins while recovery time was 120mins. Single test coupon was used for creep- recovery tests for all temperatures at each stress level.

It is observed that the test coupon tested at 7MPa did not recover completely after testing at 160 $^{\circ}\text{C}$. Test coupon tested at 50MPa showed recovery after testing at 80 $^{\circ}\text{C}$, but did not recover completely at higher test temperatures. The test coupon tested at 100MPa did not recover even at 80 $^{\circ}\text{C}$. The permanent strain, after recovery, was recorded for all temperatures and stress levels and is tabulated in *Table 5.10*. This permanent strain is compared with the permanent strain obtained after tensile loading to the creep stress but before creep, which is tabulated in *Table 5.5*. Any difference between the two is indicative of increase in damage during creep. It is observed from *Table 5.10* that the amount of permanent strain did not change during creep for a stress of 7MPa at all temperatures, except at 160 $^{\circ}\text{C}$. The permanent strain in the composite, at 7MPa and

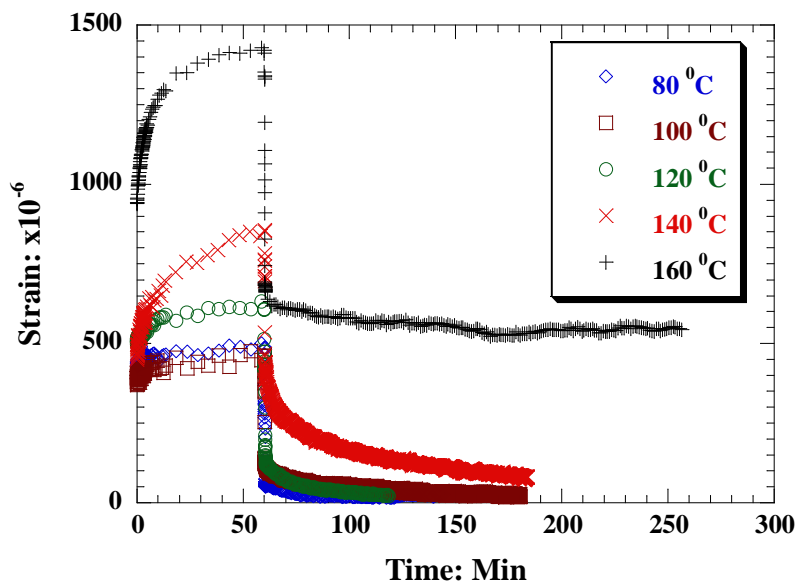


Figure 5.44: Creep-recovery plot for $[+45, -45]_6$ plain weave composite test coupon at various temperatures and a stress level of 7MPa.

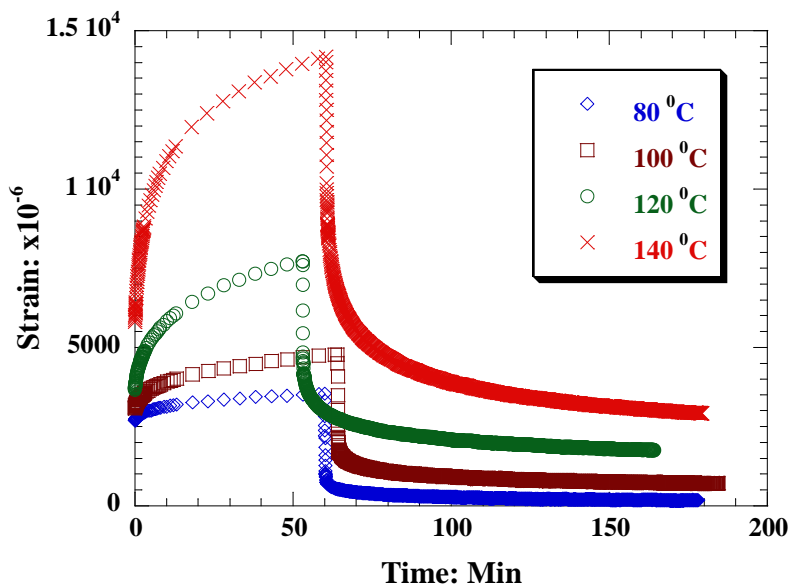


Figure 5.45: Creep-recovery plot for $[+45, -45]_6$ plain weave composite test coupon at various temperatures and a stress level of 50MPa.

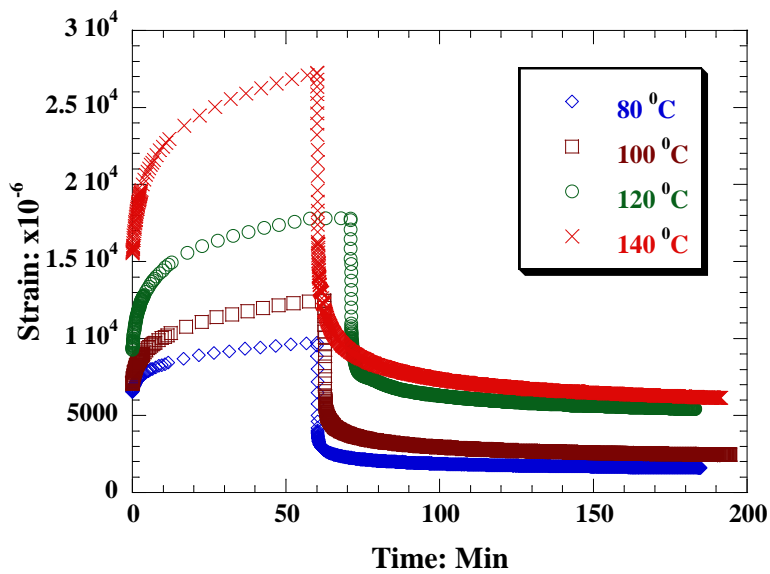


Figure 5.46: Creep-recovery plot for $[+45, -45]_6$ plain weave composite test coupon at various temperatures and a stress level of 100MPa.

Table 5.10: Recovery strain after creep tests at various stresses and temperatures for $[+45, -45]_6$ plain weave composite test coupons.

Temperature ($^{\circ}\text{C}$)	Stress = 7 MPa	Stress = 50 MPa	Stress = 100 MPa
	Recovery Strain (microstrain)	Recovery Strain (microstrain)	Recovery Strain (microstrain)
80	26	183	1615
100	23	524	2351
120	30	1049	5425
140	76	1160	6039
160	500	-	-

160 $^{\circ}\text{C}$, increased from 300 μstrain before creep to 500 μstrain after creep. This confirms that the damage had increased further during creep.

While the increase in permanent strain during creep at 50MPa and 80 $^{\circ}\text{C}$ was 80 μstrain , at higher temperatures, it was more than two times the magnitude at 80 $^{\circ}\text{C}$. This clearly indicates that the damage had considerably increased during creep at 50MPa for temperatures higher than 80 $^{\circ}\text{C}$.

Further, the permanent strain after creep at 100MPa was much higher than that recorded for 50MPa, at all test temperatures. Since the effect of time-dependent damage was not focused in this study, creep without damage could not be recorded at any test temperature at this stress level. Hence, creep tests under off-axis loading were limited to stress levels below 100MPa. Additionally, the temperature of testing at 7 and 50MPa were limited to 160 $^{\circ}\text{C}$ in order to avoid any time-dependant damage. This severely restricted the time window of the master plot. Hence, creep tests were done at both these stress levels at a single test temperature of 80 $^{\circ}\text{C}$ for two days. These results were used in validating the predicted results.

The test coupons were inspected before and after each creep test using X-radia Micro XCT; but, the damage could not be imaged. It is believed that the size of the cracks were too small to be imaged at the resolution used to image the maximum possible area of the sample (X10).

5.4.2.3 Effect of temperature and stress

To quantify the effect of temperature on tensile creep of plain weave composites under off-axis loading, creep tests were conducted at various temperatures ranging from 80 - 160 $^{\circ}\text{C}$ at 7MPa (3% UTS) using [+45, -45]₆ test coupons. The creep results at

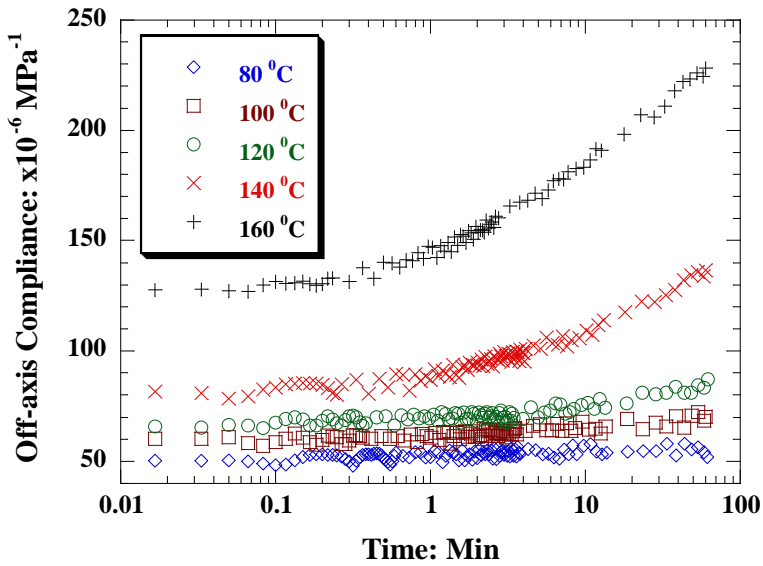


Figure 5.47: Compliance of $[+45, -45]_6$ plain weave composites at 7MPa and at various test temperatures.

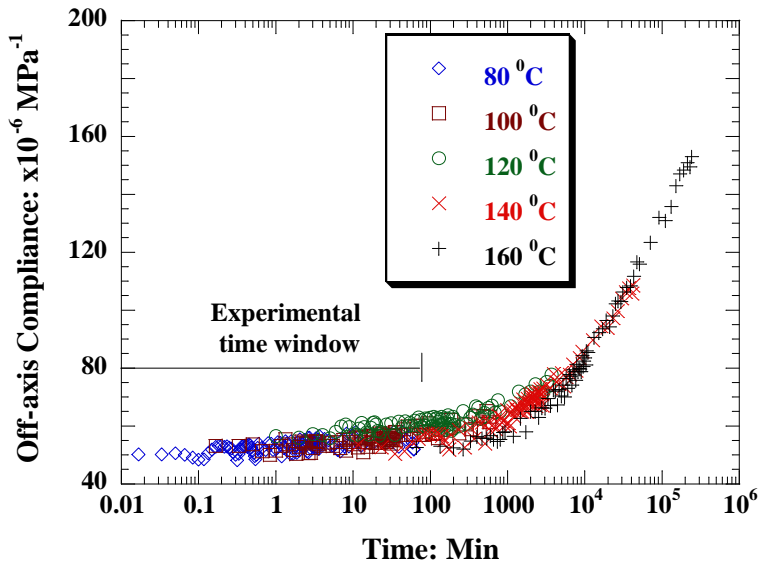


Figure 5.48: Master creep plot for $[+45, -45]_6$ plain weave composites at a reference temperature of 80 °C and at a stress level of 7MPa.

various temperatures are shown in *Figure 5.47*. The instantaneous as well as creep compliance of the plain weave composite, under off-axis loading, increased with increase in temperature. The maximum increase in creep compliance at 7MPa was 80% for the temperature range tested, within the experimental time window of 1 hour. As stated before, high permanent strain was recorded after the test at 160 $^{\circ}\text{C}$ at 7MPa.

In order to obtain the long-term creep data beyond the experimental time window, the experimental creep data at different temperatures were shifted along the time axis to a reference temperature of 80 $^{\circ}\text{C}$, following the TTSP procedure, described previously in section 5.4.1.1. The master plot obtained for 7MPa is shown in *Figure 5.48*. The master plot corresponds to a creep time of 156days at 7MPa. However, it is observed in *Figure 5.48* that the master plot shows sudden change in slope (increase in creep rate) beyond 1000mins (0.7days), corresponding to the data obtained at 160 $^{\circ}\text{C}$. As stated previously that the test coupon had shown very high permanent strain (500 μ strain) after creep test at 160 $^{\circ}\text{C}$, relative to the permanent strain obtained after creep tests at temperatures below 160 $^{\circ}\text{C}$. This indicates that the time-dependent damage in the test coupon during creep caused higher creep rate at 160 $^{\circ}\text{C}$. In order to confirm occurrence of this damage, a fresh test coupon was tested at 7MPa and 80 $^{\circ}\text{C}$ for 2880mins (2days) and experimental data is plotted with master plot in *Figure 5.49*. The experimental plot beyond 100mins shows much lower creep rate than obtained through master plot. The test coupon tested for 2days shows permanent strain of 50 μ strain only after the test. This confirms that time-dependent damage has occurred in the test coupon tested at 160 $^{\circ}\text{C}$, during creep. The time-dependent damage could not be accounted in TTSP procedure for plotting master

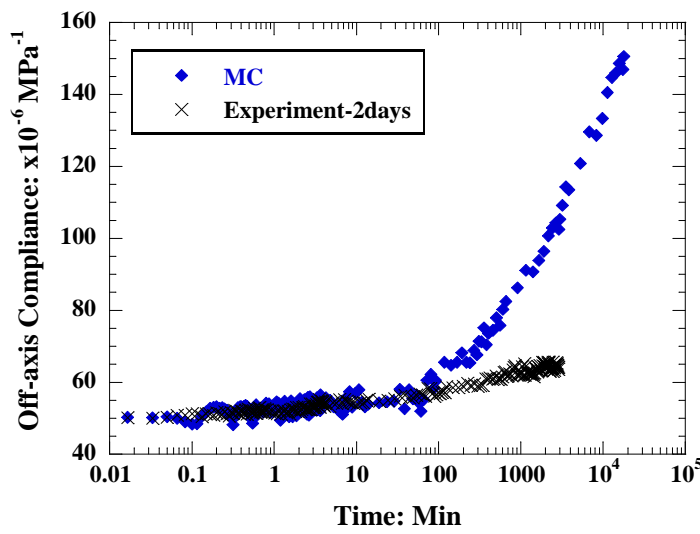


Figure 5.49: Comparison of master creep plot and 2-days experimental creep plot for $[+45, -45]_6$ plain weave composites at a reference temperature of 80°C and at a stress level of 7MPa.

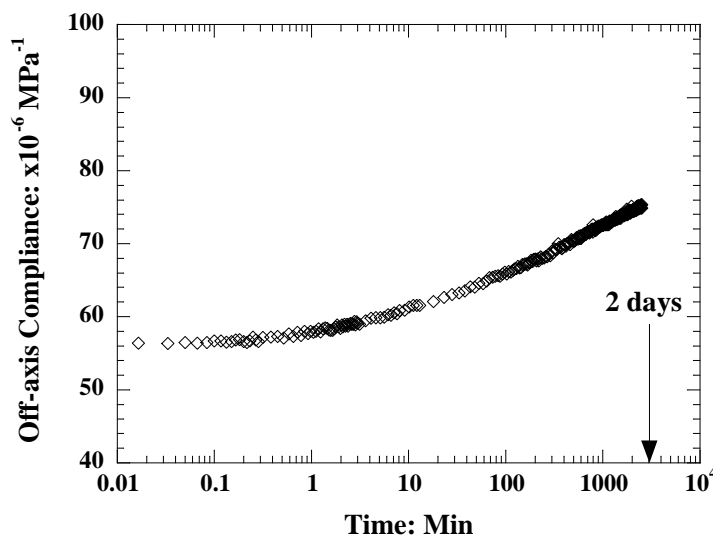


Figure 5.50: Experimental creep plot for $[+45, -45]_6$ plain weave composites at a temperature of 80°C and at a stress level of 50MPa for 2 days.

plot, the master plot data beyond 100mins could not be for the purpose of obtaining long term data and using for validation of creep model. Instead, experimental data obtained for 2days, as shown in *Figure 5.49*, is decided to use for validation of model results.

As discussed previously, the composite showed increase in damage during creep at 50MPa for test temperatures above 80 $^{\circ}\text{C}$, which caused additional increase in instantaneous as well as creep compliance, along with the increase in compliance due to temperature only. Hence, the creep results at temperatures above 80 $^{\circ}\text{C}$ were not used to obtain long-term creep data beyond experimental time window at 80 $^{\circ}\text{C}$, since the TTSP procedure can only be used to delineate the effect of temperature on compliance. Therefore, the creep test was conducted up to 2days at 50MPa and 80 $^{\circ}\text{C}$ using [+45, -45]₆ test coupon. The creep time was chosen to yield a creep plot with adequate change in curvature and compliance so that the results could be used to validate the model predictions reliably. The creep plot obtained at 50MPa and 80 $^{\circ}\text{C}$ is shown in *Figure 5.50*. The total increase in creep was found to be 33% within a time period of 2 days.

To recognize the effect of stress on creep of plain weave composites under off-axis loading, creep plots, generated at 7MPa and 50MPa at 80 $^{\circ}\text{C}$ for 2days are compared and shown in *Figure 5.51*. The instantaneous compliance increased substantially with stress, which is to be expected based on tensile test results presented and discussed in section 5.3.2. When the plots are superposed in *Figure 5.51*, accounting for this difference in instantaneous compliance, it can be observed that the creep compliance for 50MPa increases relatively rapidly with time than the creep compliance at 7MPa. This clearly demonstrates that the polymer matrix of the composite is in the non-linear viscoelastic region at 50MPa and the creep model developed in this thesis account for

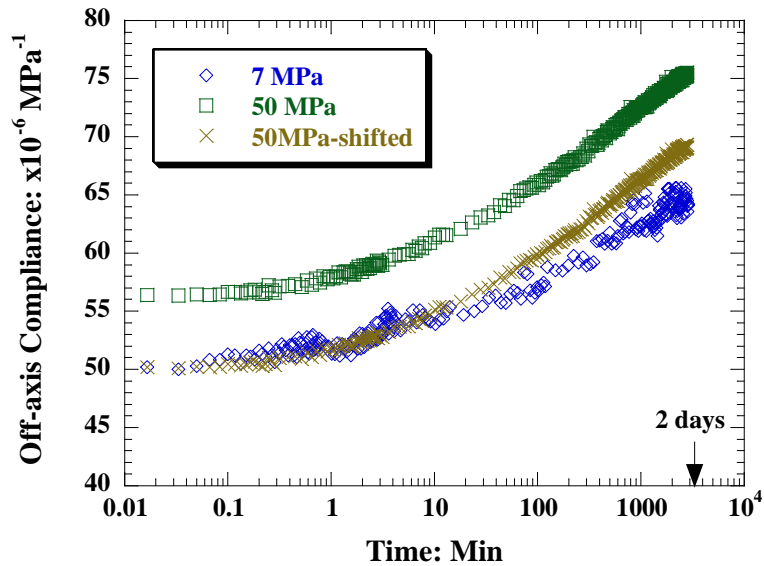


Figure 5.51: Comparison of long-term creep of $[+45, -45]_6$ plain weave composites at 7 & 50MPa stress levels and at a temperature of 80°C .

such viscoelastic non-linearity. Similar non-linear behavior has been observed previously [5] for unidirectional composites under off-axis loading.

5.4.2.4 Model results

The experimental off-axis tensile creep results, obtained using [45, -45]₆ plain weave test coupons at various stresses and temperatures, are used to validate the creep model, presented in Chapter 3. The predicted creep results are compared with experimental results and validated in this section. First, a parametric study of effect of microstructure on off-axis elastic (time-independent) properties and creep (time-dependent) of plain weave composites is presented. Following sub-sections presents comparison of MELM creep model results with experimental results as well as comparison with equivalent laminate model [20] predictions for creep.

5.4.2.4.1 Parametric study on effect of microstructure

Similar to the previous study on effect of microstructure presented in section 5.4.1.4.1 for plain weave composites under on-axis loading, the effect of microstructural parameters such as undulation length and lamina thickness on the instantaneous and creep compliance of composite under off-axis loading was studied and presented here.

Using the undulation length (l_u) in the range of 0-1.0mm and lamina thickness (h_0) in the range of 0.17- 0.22mm, and the unidirectional composite properties given in *Table 4.8*, the instantaneous compliance was predicted and is plotted in *Figure 5.52*, as a function of l_u for various values of h_0 . The unit cell length (l) was kept constant as 2.1mm. The compliance at $l_u = 0$ corresponds to a [+45/-45]_s laminate with the lowest compliance or highest modulus. Similar to the behavior observed under on-axis loading, the compliance increased with increase in l_u to a maximum at $l_u = 0.2\text{mm}$, beyond which

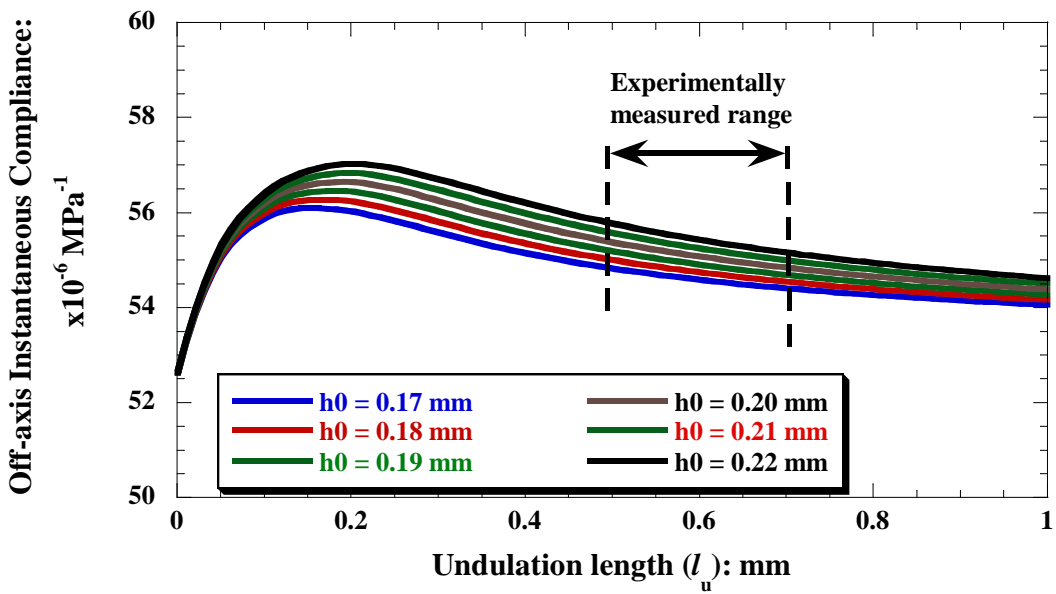


Figure 5.52: Variation of instantaneous compliance with undulation length for plain weave composites under 45^0 off-axis loading.

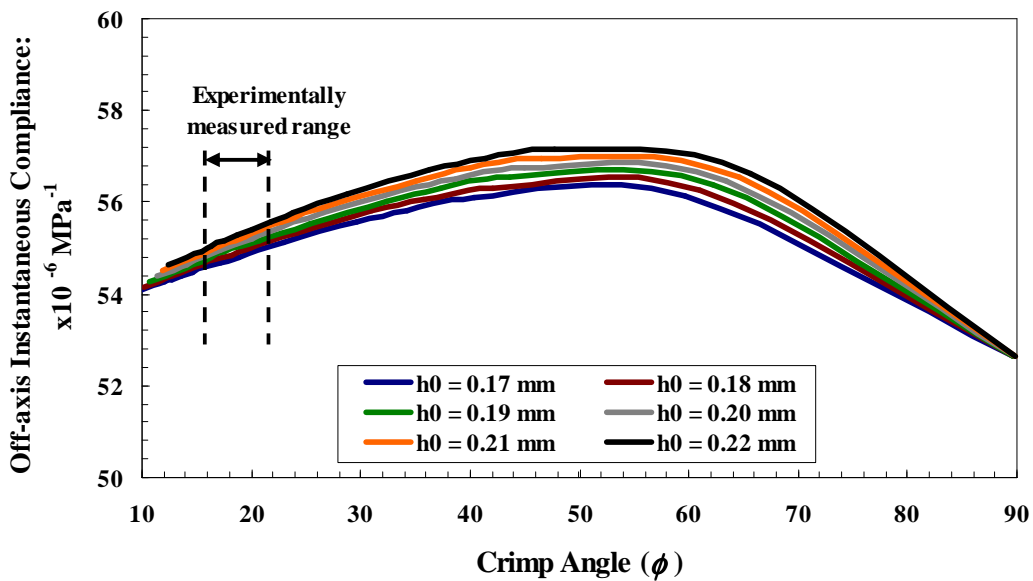
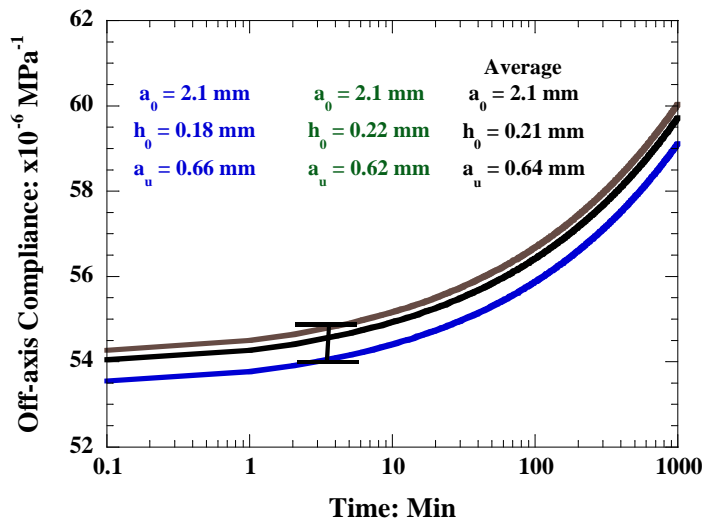


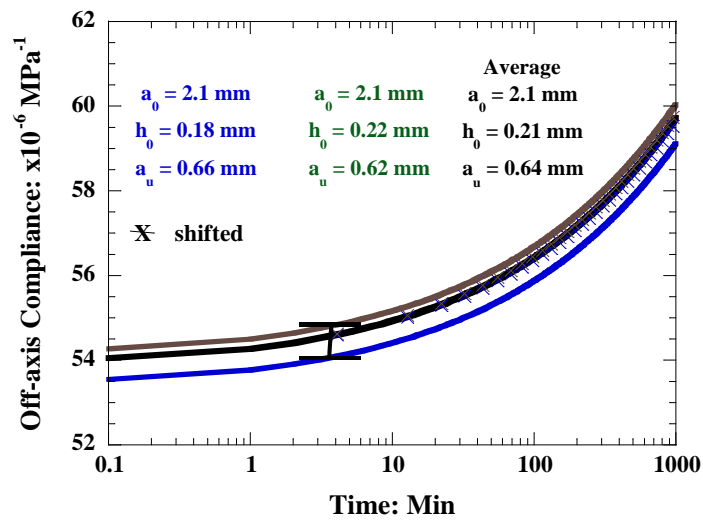
Figure 5.53: Variation of instantaneous compliance of plain weave composites with crimp angle under 45^0 off-axis loading.

it decreased with further increase in l_u . The reason for this trend in compliance with increase in l_u has been discussed previously in section 5.4.1.4.1. The compliance also increased with increase in h_0 , for a given l_u . In the experimentally measured range of l_u & h_0 , the compliance decreases with increase in l_u . The instantaneous compliance is also plotted in *Figure 5.53* as a function of crimp angle for different h_0 (crimp angle = $\tan^{-1}(h_0/l_u)$) and for the entire range of l_u shown in *Figure 5.52*. The compliance increases with increase in crimp angle within the experimentally measured range ($13\text{-}21^\circ$) of crimp angle.

For a constant unit cell length and undulation length, as lamina thickness (h_0) increases, the crimp angle increases resulting in increase in the instantaneous compliance as shown in *Figures 5.52 and 5.53*, for the entire range of l_u . In order to determine the error introduced in model predictions due to experimentally observed scatter in undulation parameters, the average, upper bound, and lower bound values given in *Table 5.7* were used to predict the off-axis compliance and plotted in *Figure 5.54a*. The upper bound of predicted instantaneous compliance is 54.08×10^{-6} MPa $^{-1}$ and lower bound of predicted instantaneous compliance is 53.36×10^{-6} MPa $^{-1}$, while the average instantaneous compliance is predicted as 53.86×10^{-6} MPa $^{-1}$. As shown in *Figure 5.54b*, the creep plots obtained using upper bound and lower bound undulation parameters were shifted by subtracting/ adding the difference between upper bound and lower bound instantaneous compliance with average instantaneous compliance, respectively. This is done to evaluate the effect of undulation parameters on creep rate. It is observed that the predicted creep rate is relatively lower obtained using lower bound undulation parameters (compliance @



(a)



(b)

...Continue

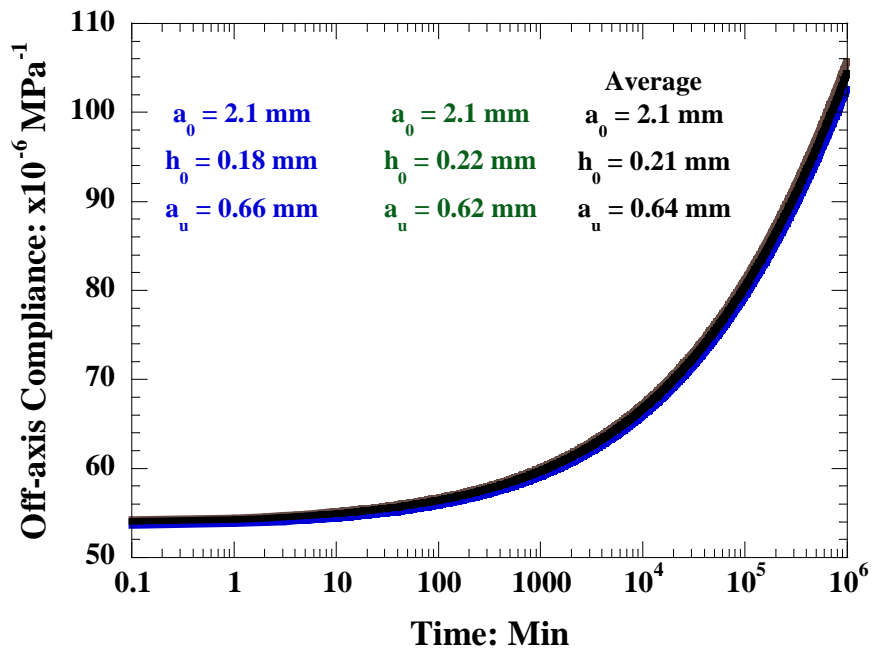


Figure 5.54: Predicted creep compliance of plain weave composites under off-axis loading for three sets of undulation parameters.

1×10^6 mins = 103.15×10^{-6} MPa $^{-1}$), than the predicted creep rate obtained using average undulation parameters (compliance @ 1×10^6 mins = 104.38×10^{-6} MPa $^{-1}$). Similarly, predicted creep rate obtained using upper bound undulation parameters (compliance @ 1×10^6 mins = 105.54×10^{-6} MPa $^{-1}$) is relatively higher than predicted creep rate obtained using average undulation parameters (compliance @ 1×10^6 mins = 104.38×10^{-6} MPa $^{-1}$). In *Figures 5.54a* and *5.54b*, the time range is plotted only up to 1000mins to show distinguish all three creep plots clearly. Creep plots up to 1×10^6 mins (2years) are plotted in *Figure 5.54c*. As discussed in section 5.4.1.4.1, compliance of the composite decreases with increase in undulation length (l_u) and decrease in lamina thickness (h_0). Since, the lower bound undulation parameters have highest l_u and lowest h_0 , the instantaneous as well as creep compliance is predicted lowest. On the other hand, upper bound undulation parameters have lowest l_u and highest h_0 , the instantaneous and creep compliance is predicted highest.

At any given creep time, the difference between the creep compliance predicted using the average and the two bound values in *Table 5.7* is $\pm 1\text{-}1.5\%$, considering difference between initial compliances and compliance predicted at the highest time shown in *Figure 5.54c*. Thus, if the experimental plot compares with the predicted creep cures within $\pm 1\text{-}1.5\%$, the prediction is considered to be accurate in this thesis. The average undulation parameters were used for generation of predicted results presented in the subsequent sections. The error range in prediction, $\pm 1\text{-}1.5\%$, is superposed with the predicted results.

5.4.2.4.2 Creep Model Predictions and Validation

Modified equivalent laminate model (MELM) was used to predict the off-axis creep of plain weave composites using undulation parameters given in *Table 5.7* and unidirectional composite properties given in *Table 4.8*. Predicted results are compared with experimental results, obtained for 2days, in the stress range of 7-50MPa at 80 °C.

Model and experimental creep results at 7MPa and 80 °C are compared within experimental time window of 2days shown in *Figure 5.55*. The instantaneous compliance predicted from the model (53.86×10^{-6} MPa $^{-1}$) is higher than the instantaneous compliance obtained experimentally (50.22×10^{-6} MPa $^{-1}$). The predicted compliance shows increase of 16% when compared to the increase in experimental compliance of 20%, within 2days. Predicted creep plot compares well with experimental creep plot within error range of \pm 1%. The predicted plot is plotted up to 30years.

Model and experimental creep results at 50MPa and 80 °C are compared in *Figure 5.56* for a time period of 2days. The instantaneous compliance predicted from the model (56.66×10^{-6} MPa $^{-1}$) is similar to the instantaneous compliance obtained experimentally (56.3×10^{-6} MPa $^{-1}$). The experimental and predictions compare well within time period of 2days within error range of \pm 1%. The predicted compliance shows increase of 20% when compared to the increase in experimental compliance of 30%, within 2days. The predicted plot is plotted up to 30years.

Further, the equivalent laminate model (EqM) predictions were compared with predictions obtained using MELM model for a given stress and temperature, under off-axis loading. Predictions from both models are compared in *Figures 5.57* and *5.58* with experimental creep data at 7 and 50MPa and 80 °C, respectively. The predictions using EqM model exhibited a rapid increase in creep rate with increase in creep time and the

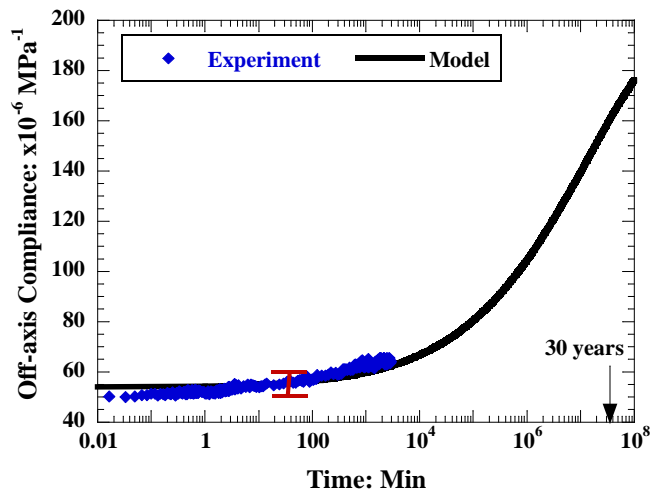


Figure 5.55: Comparison of model predictions with experimental creep plot obtained at a stress of 7MPa and temperature of 80 $^{\circ}\text{C}$ for plain weave composites under off-axis loading.

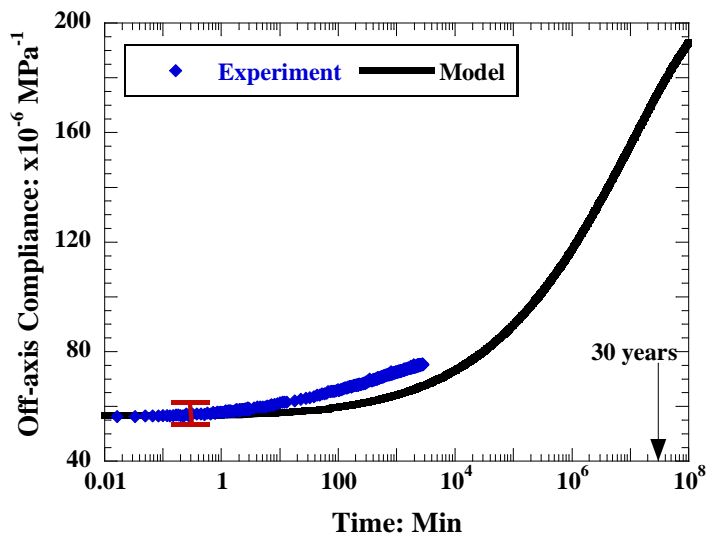


Figure 5.56: Comparison of model predictions with experimental results obtained at a stress of 50MPa and temperature of 80 $^{\circ}\text{C}$ for plain weave composites under off-axis loading.

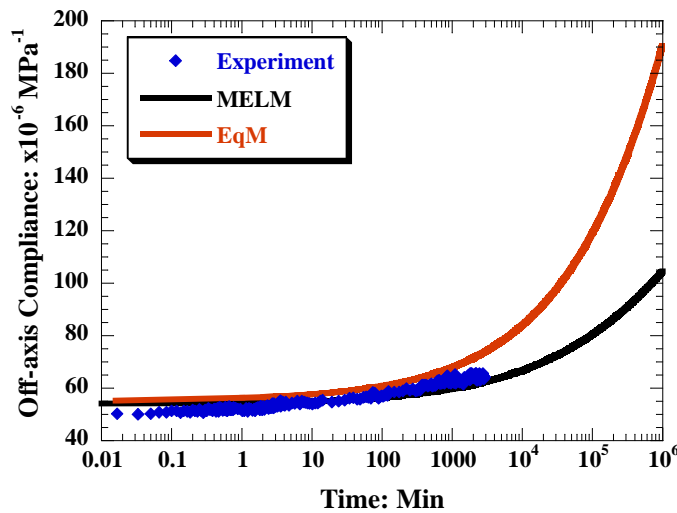


Figure 5.57: Comparison of MELM and EqM model predictions with experimental results obtained at a stress of 7MPa and temperature of 80 $^{\circ}$ C for plain weave composites under off-axis loading.

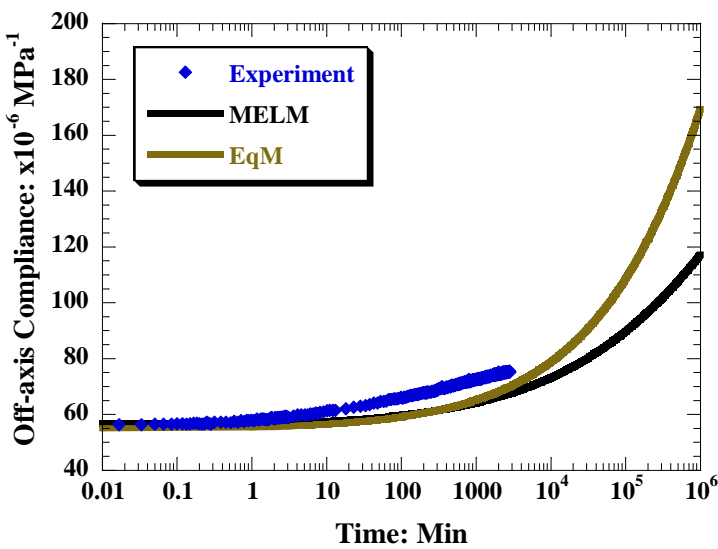


Figure 5.58: Comparison of MELM and EqM model predictions with experimental results obtained at a stress of 50MPa and temperature of 80 $^{\circ}$ C for plain weave composites under off-axis loading.

predictions deviated rapidly from the experimental results. In contrast, the predictions using MELM, developed in this thesis, predicts the change in curvature of the creep plots very well. The above comparisons highlight the better prediction capability of MELM model over EqM model under off-axis loading.

5.4.3 Discussion

5.4.3.1 Effect of crimp and microstructural parameters

To recognize the effect of crimp on creep of plain weave composites, creep plots for $[0^0]$ composite, $[90^0]$ composite, $[0/90]$ cross-ply laminate and $[0,90]$ plain weave laminate are compared, at 3MPa and 80°C , in *Figure 5.59*, under on-axis loading. $[0^0]$ composite does not creep due to loading along fiber direction. Since, fibers do not creep and share the major portion of the applied load, $[0^0]$ composite does not creep and exhibit lowest compliance. On the other hand, creep in $[90^0]$ composite is matrix dominant and thus show highest instantaneous and creep compliance. Plain weave composite consist fibers in 0^0 and 90^0 directions, the compliance of the composite lies between these two extremes. As observed in *Figure 5.59*, the instantaneous compliance of $[0, 90]$ plain weave composite is higher than instantaneous compliance of $[0/90]$ cross-ply laminate. Due to presence of crimp in a plain weave composite, the compliance of the composite is higher than the compliance of cross-ply laminate. Plain weave composite shows higher creep (10%) than creep of cross-ply laminate (1%) for a given time period, due to presence of crimp region. This comparison demonstrates the effect of crimp on creep of composites.

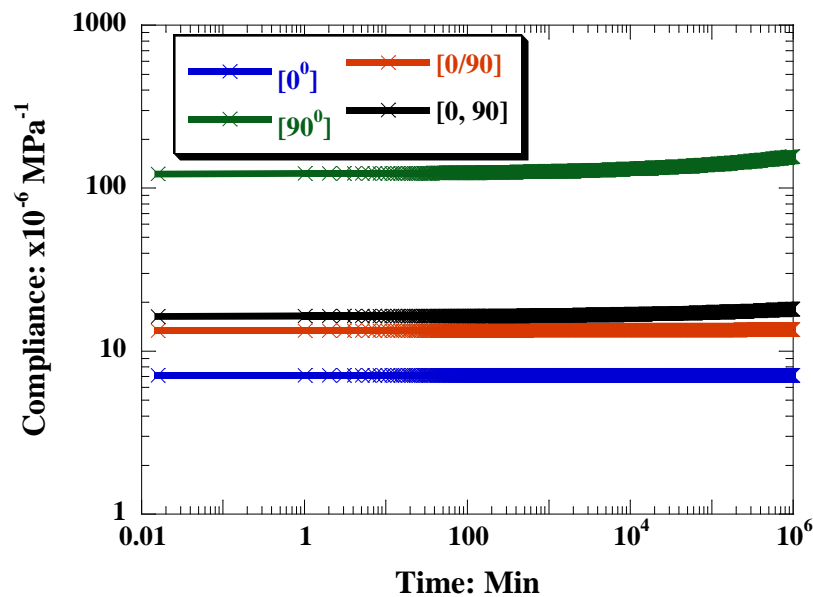


Figure 5.59: Comparison of creep of $[0^0]$, $[90^0]$, $[0/90]$ cross-ply and $[0, 90]$ plain weave composite to illustrate effect of crimp.

In sections 5.4.1.4.1 and 5.4.2.4.1, the effect of undulation parameters on creep of plain weave composites under on-axis and off-axis loading was discussed, parametrically. Such effect has been studied previously for instantaneous compliance, as discussed in Chapter 2; the study was extended here for the first time for creep of plain weave composites. The results of parametric studies, plotted in *Figures 5.28b* and *5.54b*, suggest that effect of experimentally observed scatter in the undulation parameters on creep is relatively lower than its effect on time-independent modulus/ compliance.

5.4.3.2 Effect of orientation of loading axis

In order to highlight the effect of orientation of the load axis on the creep behavior of plain weave composites, the creep results obtained using $[0, 90]_6$ composite coupons are compared with the creep results obtained using $[45, -45]_6$ composite coupons in *Figure 5.60* for a stress level of ~20% UTS and 80°C . The instantaneous and creep compliance increased with increase in angle of orientation of load axis with respect to the fill or warp fiber direction. The total increase in creep compliance of plain weave composites under 45^0 loading was found to be 31%, much higher than the 1% increase in compliance of plain weave composites under 0^0 loading. Since, the fibers are elastic, the creep of plain weave composite was due to creep of the polymer matrix. For on-axis loading, fibers oriented along the load axis will share the major portion of the applied load, in addition to constraining the deformation of the polymer matrix. Due to high modulus of the fibers, the overall creep deformation of the plain weave laminate under on-axis loading is very low. With increase in angle of loading with respect to the fiber direction, the load shared by the fibers as well as the constraint on the deformation decrease and the creep of the laminate increases. Under on-axis loading, the creep is

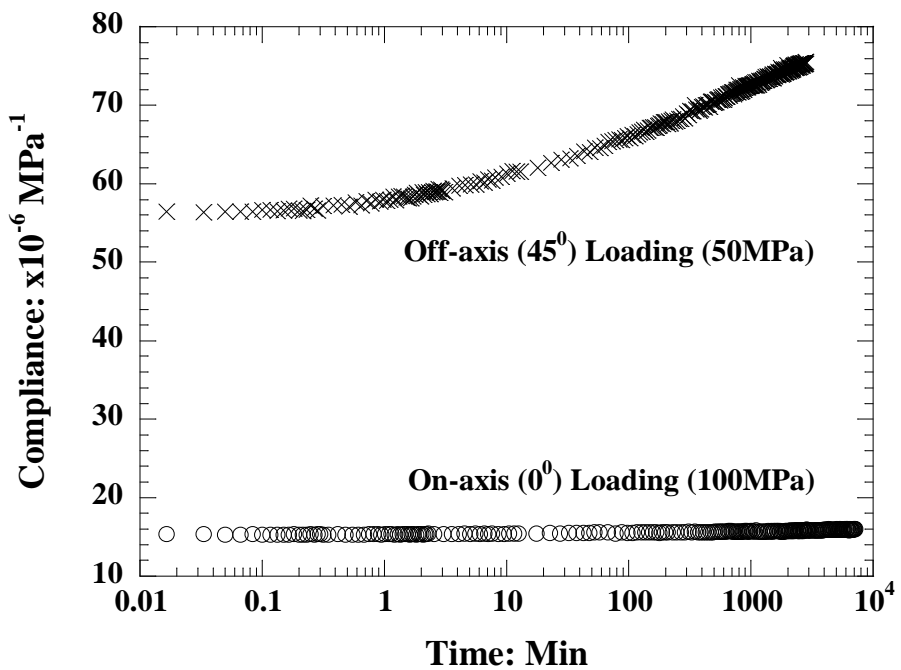


Figure 5.60: Comparison of experimental creep of plain weave composites under on-axis (0^0) loading and off-axis (45^0) loading at a stress of 20% UTS and a temperature of 80°C .

mainly due to normal stresses while under off-axis loading, the creep is due to both normal and shear stresses introduced in the polymer matrix, due to orientation of the applied load with respect to fiber axis. Since shear creep compliance of a unidirectional composite and its polymer matrix is higher than their transverse creep compliance, the magnitude of contribution from shear creep increases with increase in orientation angle, due to increase in shear stress for a given applied stress. The maximum contribution occurs at angle of 45^0 and hence, the observed creep magnitude in $[45,-45]_6$ test coupons is the maximum possible creep, for a given applied stress, creep time, and test temperature. For orientations between 0^0 and 45^0 , the creep magnitude will be in between the values for these two orientations. Hence, these two orientations were chosen for validation of the creep model in this thesis.

5.4.3.3 On Creep Model

A new creep model, Modified equivalent laminate model (MELM), has been developed as a part of thesis and has been validated using experimental results for the creep of plain weave composites.

As discussed in Chapter 3, Section 3.2, previous creep models [39-49] have used elastic properties of fibers, creep of resin and a micromechanical model to predict creep of woven composites, which was referred to as the “first approach” in that section. However, in the present research project, creep of unidirectional composites, obtained experimentally, was used to predict creep of woven composites, referred to as the “second approach”. In order to validate that the second approach is better than the first approach, creep of plain weave composites was also predicted using creep of resin, elastic properties of fibers and a micromechanical model. Creep of unidirectional

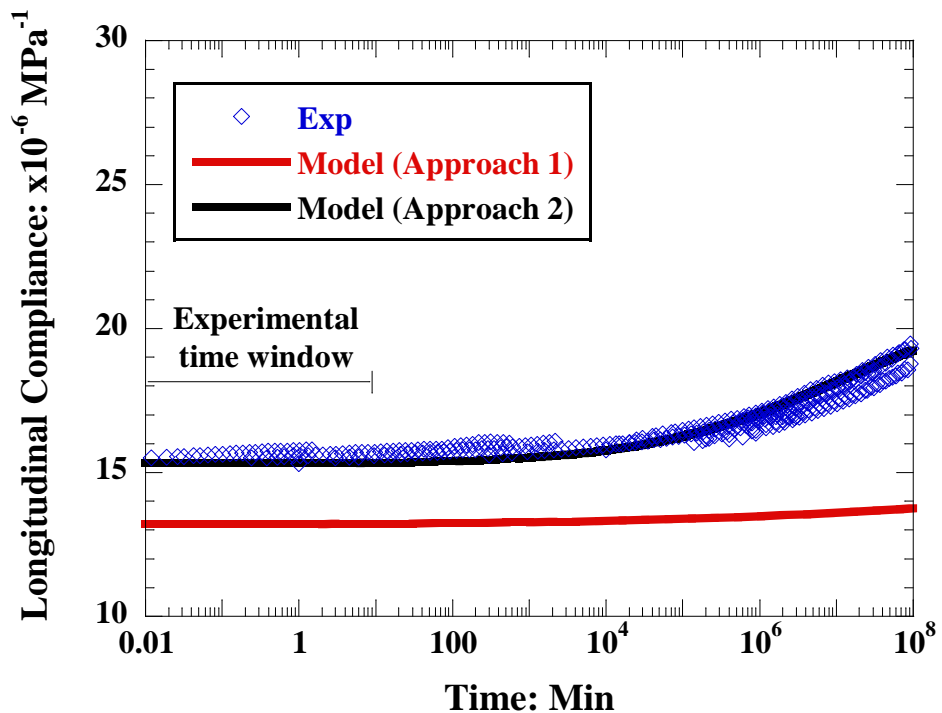


Figure 5.61: Comparison of experimental and predicted creep results obtained using approach 1 and approach 2 for plain weave composites under on-axis loading at 5MPa and 80 $^{\circ}\text{C}$.

composites was first simulated using elastic properties of fiber and creep of resin by employing a modified rule of mixtures [51]. The predicted creep of unidirectional composites was then used as the input to the MELM, developed in this thesis, to calculate creep of plain weave composites. The predicted creep results from these two approaches are compared with experimental creep results in *Figure 5.61*. It can be observed that predicted compliance from the first approach is lower than experimental compliance, within as well as beyond experimental time window. *Shortriya and Sottos* [41, 42] used the first approach for predicting creep of woven composites, which did not correlate well with experimental results. On the other hand, the predicted compliance obtained using the second approach compared well with experimental compliance. This validates the modeling approach opted in this research project over modeling approaches opted by other researchers.

The model predicts the on-axis and off-axis creep of plain weave composites within an error range of $\pm 3\%$ and $\pm 1\%$ respectively. Predictive capability of this model for both on-axis as well as off-axis loading, is the first in the literature since most of the previous studies have been focused mainly on the on-axis loading. Additionally, this study has validated the model over a wide range of stresses, unlike any other published study. The model predictions have been validated using experimental master plots for 30 years, at lower stress levels under on-axis loading. However, it was not possible to validate the prediction capability of the model for longer time periods at higher stresses, due to increase in damage at higher stresses and temperatures. Hence the prediction capability of the model should be validated in the future using a different composite system that does not show time-dependent damage at higher stress levels. Further, the

prediction capability of modified equivalent laminate model (MELM) was compared with crimp model (CM) and equivalent laminate model (EqM), available in literature. As observed in *Figures 5.42, 5.57 and 5.58*, MELM predicts the experimental results, under both on-axis and off-axis loading, better than both CM and EqM. It should be noted that CM could not be used to predict the creep under off-axis loading.

5.4.3.4 On model assumptions

As discussed in sections 5.4.1.4.2 and 5.4.2.4.2, the error range between model predictions and experimental results is $\pm 1\text{-}3\%$. Possible causes can be various assumptions made while developing the creep model and simulating the creep. Validity of these assumptions and error introduced due to these assumptions are presented and discussed in this section. Various assumptions made are:

- (a) The creep model presented in Chapter 3 assumed that the creep of unidirectional lamina determined experimentally under uni-axial loading could be used to determine the creep of the lamina under bi-axial state of stress encountered within the plain weave laminate. Experimental validation of this using a biaxial creep test of a unidirectional lamina was not performed. There are many published studies [88, 89] that have successfully predicted the off-axis creep of unidirectional lamina using this assumption. Good correlation obtained between the experimental creep data for woven composites and model predictions using this assumption, confirms the validity of this assumption.
- (b) The microstructural characterization of plain weave composite coupons showed that the undulation parameters varied within a multi-ply composite test coupon used for experiments. However, a constant average value of undulation parameters was used

to calculate the creep of entire composite and thus the effect of variation of undulation parameters within a composite was not captured. The range of undulation parameters obtained through microstructural characterization and the range of predicted compliance using these parameters was presented and discussed previously in sections 5.4.1.4.1 and 5.4.2.4.1 for on-axis and off-axis loading, respectively. As discussed in these sections, the variation of undulation parameters could be one of the possible reasons for variation between experimental and predicted results.

- (c) The microstructural characterization of plain weave composites also has shown the random-phase nesting of various plies of the laminate, as shown in *Figure 5.3*. The test coupons were found to have both iso-phase and out-of-phase laminae stacking with random distribution of each type of stacking. Ito and Chou [18] have studied the effect of nesting on elastic modulus of plain weave laminates. They have shown that the iso-phase stacking results in lower modulus (i.e. higher compliance) than out-of-phase and random stacking, due to relatively higher tension- transverse shear coupling effect. Considering the stiffness matrix for the crimp section in equation 5.1,

$$Q_{ij} = \begin{bmatrix} Q_{xx} & Q_{xy} & Q_{xz} \\ Q_{yx} & Q_{yy} & Q_{yz} \\ Q_{zx} & Q_{zy} & Q_{zz} \end{bmatrix} \quad (i, j = x, y, z) \quad (5.1)$$

In case of iso-phase stacking, there will not be any coupling effect, so Q_{xz} , Q_{yz} , Q_{zx} , and Q_{zy} will be zero. However, out-of-phase and random stacking will have tension-transverse coupling and thus Q_{xz} , Q_{yz} , Q_{zx} , and Q_{zy} will be non-zero, leading to higher modulus (lower compliance) of the plain weave composites. Moreover, the coupling

effect is a function of crimp angle, increasing with increase in crimp angle. The present creep model assumes iso-phase stacking with no tension- transverse shear coupling. While iso-phase assumption enabled ease of modeling, the assumption of zero tension – transverse shear coupling allowed prediction of a behavior that is closest to observed random phase stacking, since the coupling effect for the latter is minimal. Also, Ito and Chou have shown that the coupling is large in a single ply woven lamina when compared to a multi-ply laminate. Hence, the tension –transverse shear coupling is assumed to be zero in the current creep model. Hence, these assumptions are realistic and believed to have resulted in minimal error in the predictions.

- (d) Due to weave pattern, a gap between two warp yarns was observed in the micrograph of a single-ply lamina shown in *Figure 5.1b*. The gap was measured in a single-ply lamina as well as multi-ply laminates and tabulated in *Tables 5.1* and *5.2*. However, the gap was found only at few locations in multi-ply laminates and the size of gap was much smaller than the gap measured from single-ply lamina. When the gap between warp section increases, the volume fraction of fiber would decrease for a given unit cell. Previous researchers [18-24] considered this gap in their analytical models to predict the elastic properties of woven composites. During optical examination, the gaps were found only in few locations of the multi-ply laminate. As evidenced from *Table 5.2*, the size of this gap was very small. Hence, the gap between two warp (or two fill) yarns is assumed to be zero in the creep model developed in this thesis. The error in the prediction due to this assumption is believed to be negligible.

(e) In the present creep model, the unit cell was idealized to have an average volume fraction of 64%, based on the experimental volume fraction analysis discussed in Chapter 4. However, due to weave pattern, fiber volume fraction within a warp or a fill yarn can be higher than the average volume fraction of the unit cell considered for the modeling. Consider a section of unit cell of plain weave with the warp yarn having an elliptical cross-section as shown in *Figure 5.62*. The elliptical warp yarns have higher fiber volume fraction than the average fiber volume fraction in the unit cell. The surrounding region is resin-rich region, as illustrated. The major length ($2a$) and width ($2b$) of the elliptical cross- section of the warp yarn was measured and tabulated in *Tables 5.1* and *5.2*. Using the average values for these two parameters, area of the ellipse and the entire unit cell was calculated. The warp and fill yarns of the plain weave composite used in this thesis consist of 3000 carbon fiber filaments of diameter of $7.5\mu\text{m}$. Using the above values, the fiber volume fraction within the warp yarn was calculated to be 80.5%, while the volume fraction of resin-rich region was 19.5%. Using the % area of elliptical section and volume fraction of fiber within elliptical section, volume fraction of fibers was calculated within entire unit cell. The overall fiber volume fraction within unit cell was calculated to be 63.3%, which is similar to the experimentally determined average fiber volume fraction. Thus, consideration of an equivalent unit cell with no resin-rich gap would result in the same volume fraction within equivalent unit cell, as measured.

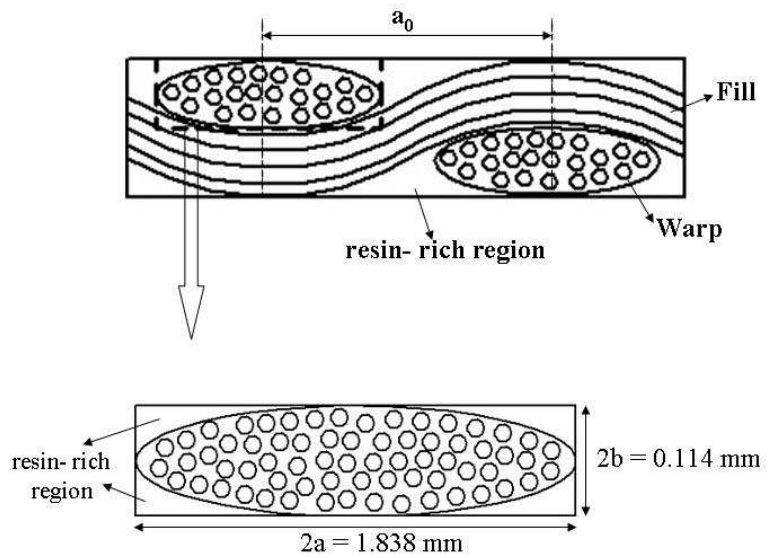


Figure 5.62: Schematic of a section of unit cell of plain weave composite used to calculate the fiber volume fraction.

6. CONCLUSIONS, THESIS CONTRIBUTIONS & RECOMMENDATIONS FOR FUTURE WORK

A creep model, the Modified Equivalent Laminate Model (MELM), was developed and validated using experimental results for creep of plain weave composites. The MELM was used along with the creep of unidirectional composites, characterized *independently* by two other researchers [4, 5] of the Composite Materials and Structures Research Group at the University of Manitoba, to predict the creep of plain weave composites. The predictions compared well with experimental results within an error range of $\pm 3\%$ and $\pm 1\%$ for on-axis and off-axis loading, respectively, for a wide range of applied stress. This demonstrates the predictive capability of MELM developed in this thesis. The experimental and analytical study of creep of plain weave composites under off-axis loading is the first study of this kind since most of the previous studies have been focused mainly on the on-axis loading. Additionally, this study has validated the developed model over a wide range of stresses and has examined parametrically the effect of microstructure on creep of plain weave composites, which has not been previously studied. Therefore, it is concluded that all the four objectives of this thesis, stated in 2.5, have been successfully achieved.

A summary of accomplished tasks are presented below.

- A Modified Equivalent Laminate Model (MELM) was developed to predict the tensile creep of plain weave polymer woven composites, subjected to loading at

varying orientations to the fill or warp fibers, using creep of unidirectional composites.

- To validate the creep model developed in this thesis, experimental creep results were generated using F263/ T300 carbon fiber/ epoxy plain weave composites, subjected to on-axis (0^0) and off-axis (45^0) tensile loading to the fill or warp fibers. Creep experiments under on-axis loading were conducted in the temperature range of $80\text{--}240\ ^0\text{C}$ (below glass-transition temperature of polymer matrix) and a stress range of 1- 70% UTS. Creep experiments under off-axis loading were conducted in the temperature range of $80\text{--}160\ ^0\text{C}$ and a stress range of 3-25% UTS.
- Creep of plain weave composites was found to increase with increase in temperature under both on-axis and off-axis loading conditions. However, the increase in creep under on-axis loading was found to be 1%, much lower than the 31% increase recorded for off-axis loading, for a given temperature and stress. Since the elastic fibers share a major portion of the applied load, the creep of plain weave composites under on-axis loading (0^0) did not accelerate with increase in stress up to 60% UTS, within experimental time window of 60 minutes. However, with further increase in stress, the composite showed accelerated creep. Creep of plain weave composite under off-axis loading (45^0) was found to be dominated by creep of its polymer matrix. Thus, creep accelerated with increase in stress within as well as beyond experimental time window, under off-axis loading.
- The microstructure of plain weave composite coupons was characterized experimentally to obtain the scatter in the values for the undulation parameters.

Using these values, a parametric study was performed using MELM to understand the effect of microstructure of plain weave composites on its on-axis and off-axis creep. The undulation parameters were observed to affect both instantaneous compliance and creep rate (i.e. curvature of the creep plot). However, the effect on the former was significantly more than the effect on the latter.

- The creep predictions were obtained using different sets of undulation parameters under on-axis and off-axis loading. Creep in plain weave composites decreased with increase in undulation length and increased with increase in lamina thickness, within range of undulation parameters, obtained experimentally. Additionally, the upper bound, the lower bound and the average set of values of undulation parameters were used to predict the creep of plain weave composites. The variation in creep due to this scatter was found to be $\pm 3.5\text{-}4\%$ for on-axis loading and $\pm 1\text{-}1.5\%$ for off-axis loading.
- The MELM was validated by comparing the predictions with experimental creep results within and beyond experimental time window. The predictions under on-axis loading were validated up to time period of 30 years and were found to be in very good agreement with experimental creep results within $\pm 3\%$. Similarly, predictions under off-axis loading were validated up to 2 days and was found to be in very good agreement with experimental creep results within $\pm 1\%$.
- The MELM was found to have better prediction capability than creep models based on crimp model [50] and equivalent laminate model [20], for both on-axis and off-axis creep.

- Under on-axis loading, the experimental master creep plot was generated for a time period of 30 years at stress levels up to 1% of UTS and used to validate the model predictions. However, master creep plot at higher stress levels could not be generated for a time period longer than 5 days, due to increase in time-dependent damage with increase in stress and temperature.

Major thesis contributions from this research project are:

- Development of MELM to predict the tensile creep of plain weave polymer woven composites, for any orientation of the load with respect to the orientation of the fill and warp fibers, using the creep of unidirectional lamina. The ability of the model to predict creep for any orientation of the load is a “first” in this area. Thus, creep of plain weave composites made of any material can be predicted using this model provided unidirectional creep data for that material is known. The primary advantage of this is in eliminating the need for extensive creep characterization of the woven composites. Additionally, this approach may be extended with additional modification to the model/ program to predict the creep of woven composite of any fiber architecture using the creep of unidirectional lamina.
- Generation of experimental data for the creep of plain weave composites over a wide range of stress and temperature. Generation of knowledge on the effect of microstructure on creep of plain weave composites is first such study. Additionally, this thesis has also generated knowledge on time-dependent damage

in woven composites and its effect on creep and tensile properties and their prediction. This is not available in the published literature.

Recommendations for future work:

- A different composite material that does not develop time-dependent damage at higher stresses and temperatures should be used to generate master creep plots for several years at higher stress levels and to validate the model predictions at these higher stress levels for longer periods of time. Similarly, creep data for off-axis loading could also be generated for several years using a different composite material and could be used to validate model predictions for longer time periods under off-axis loading.
- The creep model can be further extended to account for the effect of time-dependent damage during creep, as well as for different weave patterns.

REFERENCES

1. Chovil D.V., S.T. Harvey, J.E. MacCarty, O.E. Desper, E.S. Jamison, H. Syder, Advanced composite elevator for Boeing 727 aircraft, Volume-1 Technical summary, *NASA Contractor Report 3290, Langley Research Centre, NASA*, 1981.
2. Birur A., A. Gupta, J. Raghavan, Creep-rupture of multi-directional polymer composite laminates-Influence of Time-dependent damage, *Journal of Engineering Materials & Technology*, v124, n4, 2006, pp 611-617.
3. Poe C.C., Jr., H.B. Dexter, I.S. Raju, A review of the NASA textile composites research, *American Institute of Aeronautics and Astronautics, Inc., NASA- AIAA-97-1321*, 1997.
4. Iyer C.V., Individual and Interactive influence of temperature, stress, physical aging, moisture and fiber volume fraction on creep, creep-rupture and fracture of epoxy matrix and its composites, *M.Sc. Thesis, University of Manitoba, Canada*, 2001.
5. Balachander M.A., On prediction of creep in multi-directional polymer composites, *M.Sc. Thesis, University of Manitoba, Canada*, 2001.
6. Ito M., T.W. Chou, Elastic moduli and stress field of plain weave composites under tensile loading, *Composites Science and Technology*, v57, 1997, pp787-800.
7. Saunders R.A., C. Lekakou, M.G. Bader, Compression and microstructure of fiber plain woven cloths in the processing of polymer composite, *Composites part A*, v29A, 1998, pp443-454.

8. Saunders R.A., C. Lekakou, M.G. Bader, Compression and processing of polymer composite. 1. A mechanical and microstructural study for different glass fabrics and resins, *Composites Science and Technology*, v59, 1999, pp983-993.
9. Chen B., T.W. Chou, Compaction of woven fabric preforms: nesting and multilayer deformation, *Composites Science and Technology*, v60, 2000, pp2223-2231.
10. Chen B., E. J. Lang, T. W. Chou, Experimental and theoretical and theoretical studies of fabric compaction behavior in resin transfer molding, *Materials Science & Engineering*, vA317, 2001, pp188-196.
11. Lomov S.V., I. Verpoest, Compression of woven reinforcements: a mathematical model, *Journal of Reinforced Plastics and Composites*, v20, n2, 1999, pp179-191.
12. Lomov S.V., I. Verpoest, T. Peeters, D. Roose, M. Zako, Nesting in textile laminates: geometrical modeling of the laminate, *Composites Science and Technology*, v63, 2003, pp993-1007.
13. Yurgartis S.W., K. Morey, Measurement of yarn shape and nesting in plain-weave composites, *Composites Science and Technology*, v46, 1993, pp39-50.
14. Yurgartis S.W., Techniques for the quantification of composite mesostructure, *Composites Science and Technology*, v53, 1995, pp145-154.
15. Ishikawa T., M. Matsushima, Y. Hayashi, Experimental confirmation of the theory of elastic moduli of fabric composites, *Journal of Composite Materials*, v19, 1985, pp443-458.
16. Whitcomb J., G. Kondagunta, K. Woo, Boundary effects in woven composites, *Journal of Composite Materials*, v29, n4, 1995, pp507-524.

17. Woo K., J. Whitcomb, Effect of fiber tow misalignment on the engineering properties of plain weave textile composites, *Composite Structures*, v37, n3/4, 1997, pp343-355.
18. Ito M., T.W. Chou, An analytical and experimental study of strength and failure behavior of plain weave composites, *Journal of Composite Materials*, v32,n1, 1998, pp2-29.
19. Naik N.K., V.K. Ganesh, An analytical method for plain weave fabric composites, *Composites*, v26, 1995, pp281-289.
20. Sottos N.R., J.M. Ockers, M. Swindeman, Thermoelastic properties of plain weave composites for multilayer circuit board applications, *Journal of electronic packaging*, v127, 1999, pp37-43.
21. Naik N.K., V.K. Ganesh, Failure behavior of plain weave fabric laminates under on-axis uniaxial tensile loading: I-Laminate geometry, *Journal of Composite Materials*, v30, n16, 1996, pp1748-1778.
22. Naik N.K., V.K. Ganesh, Failure behavior of plain weave fabric laminates under on-axis uniaxial tensile loading: II-Analytical predictions, *Journal of Composite Materials*, v30, n16, 1996, pp1779-1822.
23. Ganesh V.K., N.K. Naik, Failure behavior of plain weave fabric laminates under on-axis uniaxial tensile loading: III-Effect of fabric geometry, *Journal of Composite Materials*, v30, n16, 1996, pp1823-1856.
24. Ganesh V.K., N.K. Naik, Failure behavior of plain weave fabric laminates under in-plane shear loading: effect of fabric geometry, *Composite Structures*, v30, 1995, pp179-192.

25. Onal L., S. Adanur, Modeling of elastic, thermal, and strength/failure analysis of two-dimensional woven composites- a review, *Applied Mechanics Reviews*, v60, 2007, pp37-49.
26. Ishikawa T., T.W. Chou, Stiffness and strength behavior of woven fabric composites, *Journal of Materials Science*, v17, 1982, pp3211-3220.
27. Ishikawa T., T.W. Chou, Nonlinear behavior of woven fabric composites, *Journal of Composite Materials*, v17, 1983, pp399-413.
28. Osada T., A. Nakai, H. Hiroyuki, Effect of nesting of fiber bundles on micro fracture of laminated woven fabric composite, *American Society of Mechanical Engineers, Textile Engineering Division*, v2, 2002, pp37-40.
29. Ahci E., R. Talreja, Characterization of viscoelasticity and damage in high temperature polymer matrix composites, *Composites Science & Technology*, v66, 2006, pp 2506-2519.
30. Iyer C.V., M.A. Balachandar, J. Raghavan, Long-term durability of polymer composites, *Proceedings of International SAMPE Symposium and Exhibition*, v46, n1, 2001, pp704-717.
31. Yeow Y.T., The time temperature behavior of graphite epoxy laminates, *Ph.D. Dissertation, Virginia Polytechnic Institute & State University, Blacksburgh, USA*, 1978.
32. Griffith W.I., The accelerated characterization of viscoelastic composite materials, *Ph.D. Dissertation, Virginia Polytechnic Institute and State University, VA, USA*, 1979.

33. Brinson H.F., D.H. Morris, D. Dillard, Environmental effects and viscoelastic behavior of laminated graphite/ epoxy composites, *Environmental degradation of engineering materials in aggressive environment, Proceedings of 2nd International Conference of Environmental Degradation of Engineering Materials*, 1981, pp445- 453.
34. Crossman F.W., D.L. Flaggs, LMSC- D33086, *Lockheed Palo Alto Research Laboratory*, Nov. 1978.
35. Schapery R.A., On the characterization of nonlinear viscoelastic materials, *Polymer Engineering and Science*, v9, n4, 1969, pp 295-310.
36. Struik L.C.E., Physical aging in plastics and other glassy materials, *Polymer Engineering & Science*, v17, n3, 1978, pp165-173.
37. Brinson L.C., T.S. Gates, Effect of Physical Aging on long term creep of polymers and polymer matrix composites, *International journal of solids and structures*, v32, n6-7, 1995, pp827-846.
38. Sullivan J.L., Creep and physical aging of composites, *Composite Science & Technology*, v39, 1990, pp207-232.
39. Govindarajan S., N.A. Langrana, G.J. Weng, An Experimental and Theoretical Study of Creep of a Graphite/ epoxy Woven Composite, *Polymer Composites*, v17, n3, 1996, pp353-361.
40. Govindarajan S., N.A. Langrana, G.J. Weng, Modeling Creep behavior in Polymer Woven Composites, *Advances in Computer-aided Engineering (CAE) of Polymer Processing*, ASME, v283, 1994, pp281-296.

41. Shrotriya P., N.R. Sottos, Creep and relaxation behavior of woven glass/ epoxy substrates for multilayer circuit board applications, *Polymer Composites*, v19, n5, 1998, pp567-578.
42. Shrotriya P., N.R. Sottos, Viscoelastic response of woven composite substrate, *Composite Science & Technology*, v65, 2005, pp621-634.
43. Zhu Q., P. Shrotriya, N.R. Sottos, P.H. Geubelle, Three-dimensional Viscoelastic simulation of woven composite substrates for multilayer circuit boards, *Composite Science & Technology*, v65, 2005, pp1971-1983.
44. Bathgate R.G., F. Pang , C.H. Wang, Effects of temperature on the creep behavior of woven and stitched composites, *Composite Structures*, v38, 1997, pp435-445.
45. Pang F., C.H. Wang, R.G. Bathgate, Creep response of woven- fiber composites and the effect of stitching, *Composite Science & Technology*, v57, 1997, pp91-98.
46. Pang F., C.H. Wang, A predictive creep model for un-stitched and stitched woven composites, *Composite Science & Technology*, v60, 2000, pp255-261.
47. Gupta V., S. Roy, L.R. Dharani, Micromechanics modeling of long- term interlaminar properties of woven fabric polymer composites, 42nd *AIAA/ASME/ASCE/AHS/ASC Structures, Structural Dynamics and Materials Conference, USA*, 2001, pp1-11.
48. Gupta V., S. Roy, L.R. Dharani, Multi-scale modeling of long- term mechanical behavior in polymer composite laminates with woven fiber architecture, *Polymers & Polymer Composites*, v9, n5, 2001, pp297-317.
49. Chan A., X.L. Liu, W.K. Chiu, Viscoelastic interlaminar shear modulus of fibre reinforced composites, *Composite Structures*, v75, 2006, pp185-191.

50. Chou Tsu- Wei, Microstructural design of fiber composites, *Cambridge University press, New York*, 1992.
51. Whitney J.M., R.L. McCullough, Micromechanical material modeling, *Applied Mechanics Reviews*, v43, n11, 1990, pp263.
52. Lee J.W., C.E. Harris, A micromechanics model for the effective young's modulus of a piecewise- isotropic laminate with wavy patterns, *Journal of Composite Materials*, v22, 1988, pp717-741.
53. Raju I.S., J.T. Wang, Classical Laminate Theory models for Woven Fabric Composites, *Journal of Composite Science, Technology & Research*, v16, n4, 1994, pp289-303.
54. Pang F., C.H. Wang, Creep rupture failure of woven composites, *Journal of Reinforced Plastics & Composites*, v19, n15, 2000, pp1201-1217.
55. Whitcomb J.D., K. Woo, S. Gundapaneni, Macro finite element analysis of textile composites, *Journal of Composite Materials*, v287, 1994, pp607-618.
56. Whitcomb J.D., W. Kyeongsik, Enhanced direct stiffness method for finite element analysis of textile composites, *Composite Structures*, v28, 1994, pp385-390.
57. Dasgupta A., R.K. Agarwal, S.M. Bhandarkar, Three-dimensional modeling of woven- fabric composites for effective thermo-mechanical and thermal properties, *Composites Science and Technology*, v56, 1996, pp209-223.
58. Thom H., Finite element modeling of plain weave composites, *Journal of Composite Materials*, v33, n16, 1999, pp1491-1510.

59. Vandeurzen Ph., J. Ivens, I. Verpoeast, A three-dimensional micromechanical analysis of woven-fabric composites: II. Elastic analysis, *Composites Science and Technology*, v56, 1996, pp1317-1327.
60. Naik N.K., P.S. Shembekar, Elastic behavior of woven fabric composites: I- Lamina analysis, *Journal of Composite Materials*, v26, n15, 1992, pp2196-2225.
61. Naik N.K., P.S. Shembekar, Elastic behavior of woven fabric composites: II- Laminate analysis, *Journal of Composite Materials*, v26, n15, 1992, pp2226-2246.
62. Naik N.K., P.S. Shembekar, Elastic behavior of woven fabric composites: III- Laminate design, *Journal of Composite Materials*, v26, n17, 1992, pp2522-2541.
63. Hahn H.T., R. Pandey, A micromechanics model for thermoelastic properties of plain weave fabric composites, *Journal of Engineering Materials and Technology*, n116, 1994, pp517-523.
64. Daniel I.M., O. Ishai, Engineering Mechanics of Composite Materials, *Oxford University Press, New York*, 1994.
65. Aboudi J., Micromechanical characterization of the non-linear viscoelastic behavior of resin matrix composites, *Composites Science and Technology*, v38, 1990, pp371-386.
66. Yancey R., M.J. Pindera, Micromechanical analysis of the creep response of unidirectional composites, *Journal of Engineering Materials and Technology*, v112, 1990, pp157-162.
67. Chung I., C.T. Sun, Micromechanics modeling of orthotropic creep behavior in fiber composites, *Advanced Structural Fiber Composites. Proceedings of Topical*

Symposium III on Advanced Structural Fiber Composites of the 8th CIMTEC-World Ceramics Congress and Forum on New Materials, 1995, pp735-742.

68. Wen Y.F., R.F. Gibson, J.L. Sullivan, Prediction of momentary transverse creep behavior of thermoplastic polymer matrix composites using micromechanical models, *Journal of Composite Materials*, v31, n21, 1997, pp2124-2145.
69. Chun H.J., I.M. Daniel, Transverse creep behavior of a unidirectional metal matrix composite, *Mechanics of Materials*, v25, 1997, pp37-46.
70. Megnis M., J. Varna, Micromechanics based modeling of nonlinear viscoplastic response of unidirectional composite, *Composites Science and Technology*, v63, 2003, pp19-31.
71. Woo K., Y.W. Suh, J.D. Whitcomb, Effect of phase shift on engineering properties of $[\pm \theta]$ plain weave laminates, *Journal of Composite Materials*, v39, n6, 2005, pp479-495.
72. Standard test methods for density and specific gravity (relative density) of plastics by displacement, *ASTM D 792-00*, v08.01, 2001.
73. Standard test methods for constituent content of composite materials, *ASTM D3171-06*, v15.03, 2000.
74. Masters J.E., P. G. Ifju, Strain gage selection criteria for textile composite materials, *Journal of Composites Technology & Research*, v19, n3, 1997, pp 152-167.
75. Lang E.J., Tsu-Wei Chou, The effect of strain gage size on measurement errors in textile composite materials, *Composites Science & Technology*, v58, 1998, pp 539-548.

76. Standard guide for testing fabric-reinforced textile composite materials, *ASTM standard D6856-03*, 2003.
77. Measurements Group, Catalog 500, This catalog includes strain gage listing and installation procedure. Available at internet, <http://www.vishay.com>.
78. Gupta A., A. Birur, V. Kaushik, J. Raghavan, Process- induced damage in a multi-directional polymer composite, *Proceedings of the International Conference on Recent Advances in Composite Materials*, v1, 2004, pp 21-27.
79. Chamis C.C., J. H. Sinclair, 10^0 off-axis tensile test for intralaminar shear characterization of fiber composites, *NASA technical note D-8215*, 1976.
80. Zaoutsos S.P., G.C. Papanicolaou, A.H. Cardon, On the non-linear viscoelastic behavior of polymer-matrix composites, *Composite Science & Technology*, v58, 1998, pp 883-889.
81. Papanicolaou G.C., S.P. Zaoutsos, A.H. Cardon, Prediction of the non-linear viscoelastic response of unidirectional fiber composites, *Composite Science & Technology*, v59, 1999, pp 1311- 1319.
82. Papanicolaou G.C., S.P. Zaoutsos, A.H. Cardon, Further development of a data reduction method for the nonlinear viscoelastic characterization of FRPs, *Composites: Part A*, v30, 1999, pp 839-848.
83. Lou Y.C., R.A. Schapery, Viscoelastic characterization of a nonlinear fiber-reinforced plastic, *Journal of Composite Materials*, v5, 1971, pp 208-234.
84. Tuttle M.E., H.F. Brinson, Prediction of the long-term creep compliance of general composite laminates, *Experimental Mechanics*, v26, n1, 1986, pp 89-102.

85. Naik N.K., P.S. Shembekar , M.V. Hosur, Failure behavior of woven fabric composites, *Journal of Composite Technology and Research*, v13, n2, 1991, pp107-116.
86. Kawai M., T. Taniguchi, Off-axis fatigue behavior of plain weave fiber/epoxy fabric laminates at room and high temperature and its mechanical modeling, *Composites: Part A*, v37, 2006, pp243-256.
87. Hexcel Incorporation, 282 Carbon Fabric Product Data, www.hexcel.com.
88. Ogihara S., S. Moriwaki, Tensile creep deformation in unidirectional carbon/epoxy laminates under off-axis loading, *Journal of Materials Science*, v39, 2004, pp3465-3467.
89. Falahatgar S.R., M. Salehi, M.M. Aghdam, Nonlinear viscoelastic response of unidirectional fiber reinforced composites in off-axis loading, *Journal of reinforced Plastics and Composites*, v28, n15, 2009, pp1793-1811.

APPENDIX

Appendix A.....	251
Appendix B.....	261

APPENDIX A

A-1 Classical Lamination theory

Considering an orthotropic laminate (made of unidirectional laminae) under a constant applied stress, the average laminate load and deformation along loading axis can be represented as,

$$\begin{Bmatrix} N \\ M \end{Bmatrix} = \begin{bmatrix} A & B \\ B & D \end{bmatrix} \begin{Bmatrix} \varepsilon \\ \kappa \end{Bmatrix} \quad (\text{A.1})$$

Here, [N] and [M] are average resultant force and moment per unit length (on a plane perpendicular to the loading axis), respectively. ε and κ are the strain and curvature of the laminate at the mid-plane, respectively. [A], [B] and [D] are the stiffness matrices of the laminate, which can be written in terms of stiffness of unidirectional lamina, as,

$$(A_{ij}, B_{ij}, D_{ij}) = \sum_{k=1}^n \int_{h_{k-1}}^{h_k} (1, z, z^2) (Q_{ij})_k dz \quad (i, j = 1, 2, 6) \quad (\text{A.2})$$

where, Q_{ij} is the stiffness matrix corresponding to the unidirectional lamina defined by h_k and h_{k-1} in the thickness direction. [A] is the extensional stiffness, [B] is the bending-extension stiffness and [D] is the bending stiffness.

By inverting the equation A.1,

$$\begin{Bmatrix} \varepsilon \\ \kappa \end{Bmatrix} = \begin{bmatrix} a & b \\ b & d \end{bmatrix} \begin{Bmatrix} N \\ M \end{Bmatrix} \quad (\text{A.3})$$

where, a, b and d are the compliance matrices of laminate, which were obtained from inversion of stiffness matrices (A, B and D).

A-2 Crimp model

In crimp model, the two-dimensional unit cell of plain weave fabric is idealized as one-dimensional unit cell, as shown in *Figure A.1*. The undulation geometry of fill and warp fiber along x-axis can be given as,

$$h_1 = \begin{cases} 0 & (0 \leq x \leq a_1) \\ [1 + \sin\left\{\left(x - \frac{l}{2}\right)\frac{\pi}{l_u}\right\}]h_0/4 & (a_1 \leq x \leq a_2) \\ h_0/2 & (a_2 \leq x \leq l) \end{cases}$$

(A.4)

$$h_2 = \begin{cases} h_0/2 & (0 \leq x \leq a_1) \\ [1 - \sin\left\{\left(x - \frac{l}{2}\right)\frac{\pi}{l_u}\right\}]h_0/4 & (a_1 \leq x \leq l/2) \\ -[1 + \sin\left\{\left(x - \frac{l}{2}\right)\frac{\pi}{l_u}\right\}]h_0/4 & (l/2 \leq x \leq a_2) \\ -h_0/2 & (a_2 \leq x \leq l) \end{cases}$$

h_1 and h_2 are the height of the fill and the warp section respectively; h_0 is the total thickness of the unit cell and l is the length of the unit cell. The parameters $a_1 = (l - l_u)/2$ and $a_2 = (l + l_u)/2$ were determined using the undulation length l_u of the fill section.

Assuming, lamination theory is applicable to each infinitesimal piece of this unit cell, the time-dependent stiffness of the unit cell [$A_{ij}(t)$] can be calculated in terms of time-dependent stiffness of fill and warp laminae as,

$$A_{ij}(t) = \frac{1}{l} \left[\int_{x=0}^{x=l/2} \left\{ \int_{h_{1x}-(h_0/2)}^{h_{1x}} Q_{ij}^F(t, \phi) dz + \int_{h_{1x}}^{h_{2x}} Q_{ij}^W(t) dz \right\} dx + \int_{x=l/2}^{x=l} \left\{ \int_{h_{2x}}^{h_{1x}-(h_0/2)} Q_{ij}^W(t) dz + \int_{h_{1x}-(h_0/2)}^{h_{1x}} Q_{ij}^F(t, \phi) dz \right\} dx \right]$$

(A.5)

After integration, the time-dependent stiffness of the entire unit cell was obtained as,

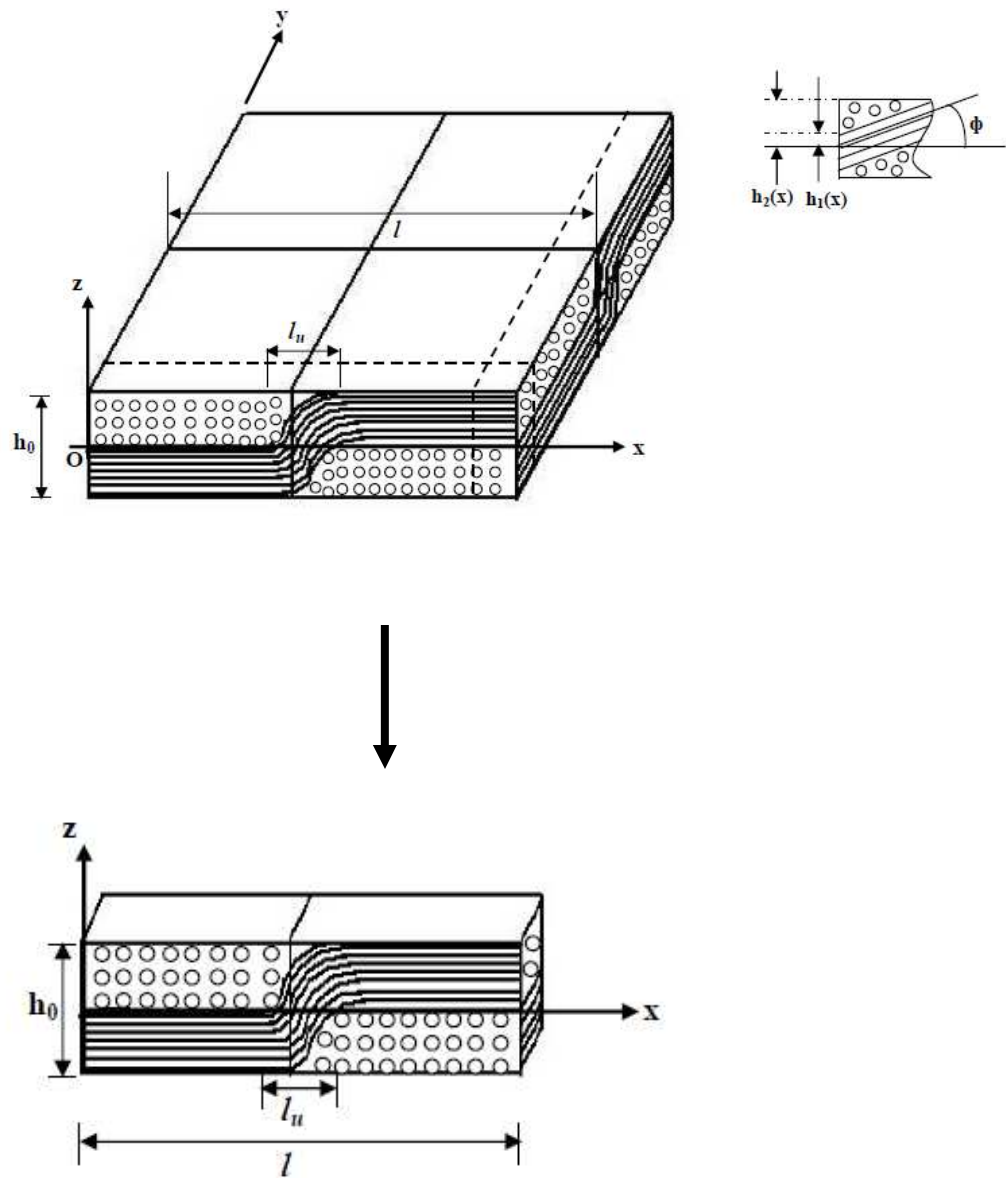


Figure A.1: 2-dimensional and 1-dimensional representation of the plain weave unit cell for crimp model.

$$A_{ij}(t) = \frac{h_0}{2} (2Q_{ij}^F(t, \phi) - Q_{ij}^W(t)) \quad (\text{A.6})$$

The undulation angle (ϕ), the local off-axis angle of the fill section with respect to the x-axis, is given as,

$$\tan(\phi) = \frac{\partial h_i(x)}{\partial x} \quad (\text{A.7})$$

The stiffness matrix of fill section along x-axis at a given undulation angle ϕ is calculated as,

$$[Q_{ij}^F(\phi, t)] = \begin{bmatrix} E_{xx}(\phi, t)/D_\nu & \nu_{yx}(\phi, t)E_{xx}(\phi, t)/D_\nu & 0 \\ \nu_{yx}(\phi, t)E_{xx}(\phi, t)/D_\nu & E_{yy}(\phi, t)/D_\nu & 0 \\ 0 & 0 & G_{xy}(\phi, t) \end{bmatrix} \quad (\text{A.8})$$

$$D_\nu = 1 - (\nu_{yx}(\phi, t))^2 E_{xx}(\phi, t) / E_{yy}(\phi, t)$$

$$\begin{aligned} \frac{1}{E_{xx}(\phi, t)} &= \frac{\cos^4 \phi}{E_{11}(t)} + \left(\frac{1}{G_{12}(t)} - \frac{2\nu_{21}}{E_{22}(t)} \right) \cos^2 \phi \sin^2 \phi + \frac{\sin^4 \phi}{E_{22}(t)} \\ E_{yy}(\phi, t) &= E_{22}(t) \\ \frac{1}{G_{xy}(\phi, t)} &= \frac{\cos^2 \phi}{G_{12}(t)} + \frac{\sin^2 \phi}{G_{23}(t)} \\ \nu_{yx}(\phi, t) &= \nu_{21}(t) \cos^2 \phi + \nu_{32} \sin^2 \phi \end{aligned} \quad (\text{A.9})$$

$E_{11}(t)$, $E_{22}(t)$, $G_{12}(t)$, $G_{23}(t)$, $\nu_{21}(t)$ and ν_{32} are the time-dependent properties of unidirectional composites, determined experimentally in Chapter 4.

Using the time-dependent stiffness, as given in equation A.6, the time-dependent strain and compliance are determined.

A-3 Equivalent laminate model (EqM)

A schematic overview of the equivalent laminate model is presented in *Figure A.2*. A 3-D representation of a unit cell is shown in *Figure A.2a*. The creep of this unit cell is determined using an equivalent laminate, consisting of an equivalent fill lamina sandwiched between two equivalent warp laminae as shown in *Figure A.2e*. If the crimp geometry in *Figure A.2a* is approximated to a sinusoidal curve, there will not be a coupling between the in-plane and out-of-plane components (i.e. $B_{ij} = 0$). In order to fulfill this requirement, the equivalent laminate in *Figure A.2e* is considered to be symmetric. Unlike the crimp in the fill and warp unidirectional lamina in *Figure A.2a*, the equivalent fill and warp laminae in *Figure A.2e* do not have any crimp. Their properties, equivalent to the laminae in *Figure A.2a* are calculated as follows.

Consider the unit cell oriented at an angle θ , to the X- axis, as shown in *Figure A.2*. X, Y, Z represents global coordinate system while x, y, Z represents local coordinate system. l is the length of the unit cell, l_u is the undulation length, and h_0 is the thickness of the unit cell. Let this unit cell be subjected to a tensile stress of σ along X- axis.

The crimp geometry of fill and warp laminae, shown in *Figure A.2b* are defined using equations A.10 & A.11 respectively,

$$h_f = \begin{cases} 0 & (0 \leq x \leq a_1) \\ [1 + \sin\{(x - \frac{l}{2}) \frac{\pi}{l_u}\}] h_0 / 4 & (a_1 \leq x \leq a_2) \\ h_0 / 2 & (a_2 \leq x \leq l) \end{cases} \quad (\text{A.10})$$

and,

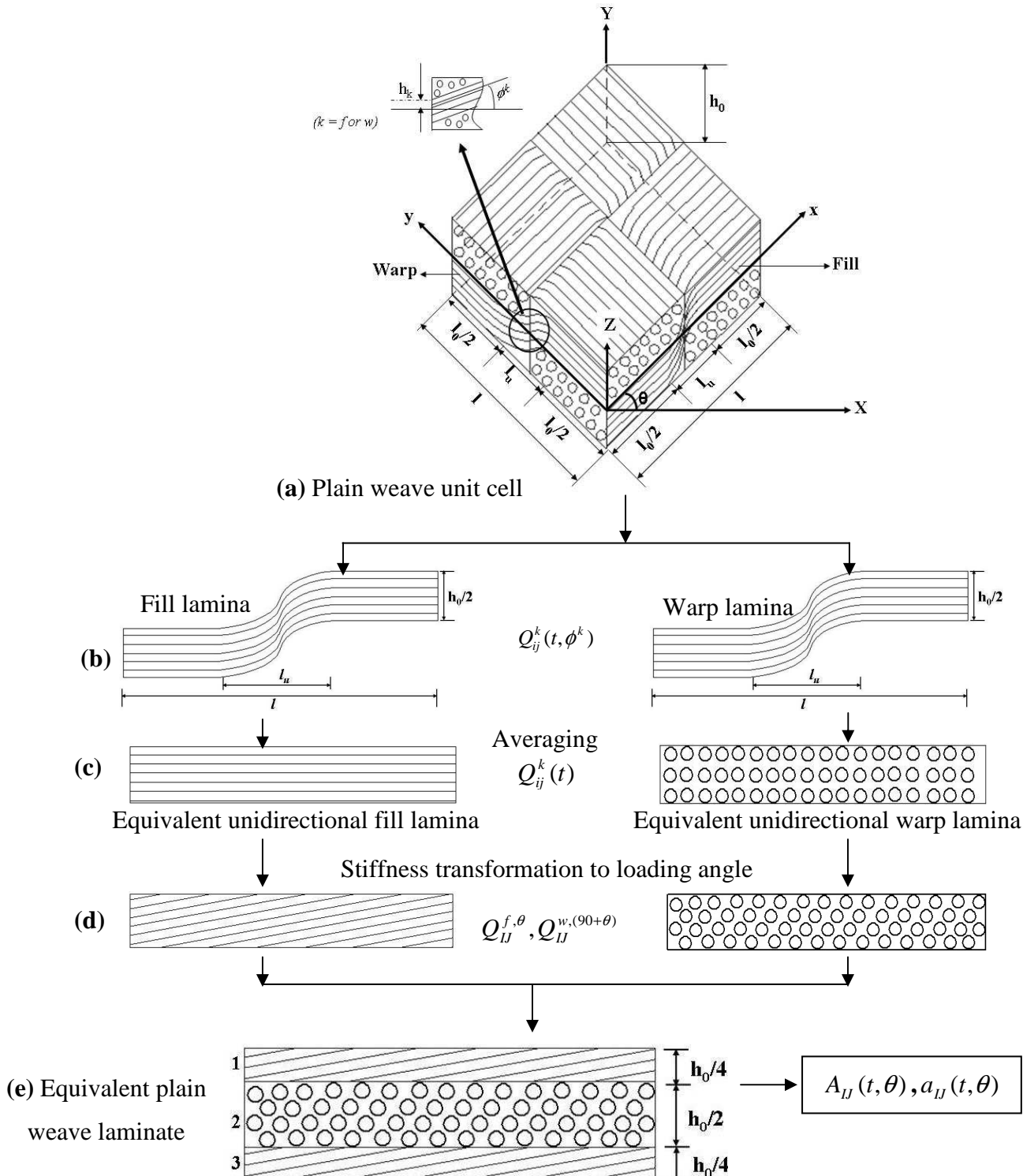


Figure A.2: Schematic overview of equivalent laminate model for predicting creep of plain weave composites.

$$h_w = \begin{cases} 0 & (0 \leq y \leq a_1) \\ [1 + \sin\left\{\left(y - \frac{l}{2}\right)\frac{\pi}{l_u}\right\}]h_0/4 & (a_1 \leq y \leq a_2) \\ h_0/2 & (a_2 \leq y \leq l) \end{cases} \quad (\text{A.11})$$

where, subscript ‘f’ and ‘w’ denotes fill and warp lamina, respectively. h_f and h_w are the Z coordinates of the centre of the fill and warp laminae, respectively. The parameters a_1 and a_2 are determined as $a_1 = (l - l_u)/2$ and $a_2 = (l + l_u)/2$.

The undulation angle (ϕ) at any location along x or y, for fill and warp laminae, are calculated using h_f and h_w as,

$$\tan(\phi^f) = \frac{\partial h_f(x)}{\partial x}; \quad \tan(\phi^w) = \frac{\partial h_w(y)}{\partial y} \quad (\text{A.12})$$

Consider the equivalent lamina in *Figure A.2c* subjected to a tensile stress along x- axis. If this lamina is divided into infinitesimal sections along its length, the stress on each section will be same since they will be in series. However, the strain will be different. The strain in each segment (k = fill or warp) is given as,

$$\begin{aligned} \varepsilon_{xx}^k(t, \phi^k) &= \frac{\sigma}{E_{xx}^k(t, \phi^k)} \\ \varepsilon_{yy}^k(t, \phi^k) &= -\nu_{xy}^k(t, \phi^k) \frac{\sigma}{E_{xx}^k(t, \phi^k)} \end{aligned} \quad (\text{A.13})$$

where,

$$\frac{1}{E_{xx}^k(t, \phi^k)} = \frac{\cos^4 \phi^k}{E_{11}(t)} + \left(\frac{1}{G_{12}(t)} - \frac{2\nu_{21}}{E_{22}(t)} \right) \cos^2 \phi^k \sin^2 \phi^k + \frac{\sin^4 \phi^k}{E_{22}(t)}$$

$$\begin{aligned}
E_{yy}^k(t, \phi^k) &= E_{22}(t) \\
\nu_{yx}^k(t, \phi^k) &= \nu_{21}(t) \cos^2 \phi^k + \nu_{32} \sin^2 \phi^k \\
\nu_{xy}^k(t, \phi^k) &= \nu_{yx}^k(t, \phi^k) \frac{E_{xx}^k(t, \phi^k)}{E_{yy}^k(t, \phi^k)}
\end{aligned} \tag{A.14}$$

Thus, the total average strain in the equivalent lamina over its entire length (l) along x-direction will be,

$$\begin{aligned}
\bar{\epsilon}_{xx}^k(t) &= \frac{1}{l} \int_0^l \epsilon_{xx}^k(t, \phi^k) dx \\
\bar{\epsilon}_{yy}^k(t) &= \frac{1}{l} \int_0^l \epsilon_{yy}^k(t, \phi^k) dx
\end{aligned} \tag{A.15}$$

The average in-plane longitudinal and transverse modulus and poisson's ratio of the equivalent lamina can be calculated as,

$$\begin{aligned}
E_{xx}^k(t) &= \frac{\sigma}{\bar{\epsilon}_{xx}^k(t)} \\
E_{yy}^k(t) &= E_{22}(t) \\
\nu_{xy}^k(t) &= -\frac{\bar{\epsilon}_{yy}^k(t)}{\bar{\epsilon}_{xx}^k(t)} \\
\nu_{yx}^k(t) &= \nu_{xy}^k(t) \frac{E_{yy}^k(t)}{E_{xx}^k(t)}
\end{aligned} \tag{A.16}$$

Since, the segments are subjected to same shear strain, the average in-plane shear modulus of the equivalent lamina can be obtained as,

$$\begin{aligned}
\epsilon_{zz}^k(t, \phi^k) &= \frac{\sigma}{G_{xy}^k(t, \phi^k)} \\
G_{xy}^k(t) &= \frac{1}{l} \int_0^l G_{xy}^k(t, \phi^k) dx
\end{aligned} \tag{A.17}$$

where,

$$\frac{1}{G_{xy}^k(\phi^k)} = \frac{\cos^2 \phi^k}{G_{12}(t)} + \frac{\sin^2 \phi^k}{G_{23}(t)} \quad (\text{A.18})$$

Thus, the stiffness matrix of the equivalent lamina can be written as,

$$Q_{ij}^k(t) = \begin{bmatrix} E_{xx}^k(t)/(1-\nu_{xy}^k(t)*\nu_{yx}^k(t)) & \nu_{yx}^k(t)*E_{xx}^k(t)/(1-\nu_{xy}^k(t)*\nu_{yx}^k(t)) & 0 \\ \nu_{xy}^k(t)*E_{yy}^k(t)/(1-\nu_{xy}^k(t)*\nu_{yx}^k(t)) & E_{yy}^k(t)/(1-\nu_{xy}^k(t)*\nu_{yx}^k(t)) & 0 \\ 0 & 0 & G_{xy}^k(t) \end{bmatrix} \quad (\text{A.19})$$

$E_{xx}^k(t, \phi^k)$, $E_{yy}^k(t, \phi^k)$, $G_{xy}^k(\phi)$, and $\nu_{yx}^k(\phi^k)$ are the time-dependent properties of infinitesimal section within fill or warp along x, y, z axes. $E_{11}(t)$, $E_{22}(t)$, $G_{12}(t)$, $G_{23}(t)$, $\nu_{21}(t)$ and ν_{32} are the time-dependent properties of unidirectional lamina along its principle axes (1, 2, 6), which were obtained experimentally and discussed in chapter 4.

The average time-dependent stiffness, determined using equation A.19 is the time-dependent stiffness of equivalent laminae in *Figure A.2c* for the principal (i.e. local) coordinate system. The corresponding stiffness in the global coordinate system for a given angle of loading (θ) are obtained using transformation matrix given in equation A.20,

$$[T] = \begin{bmatrix} m^2 & n^2 & 2mn \\ n^2 & m^2 & -2mn \\ -mn & -mn & m^2 - n^2 \end{bmatrix} \quad (\text{A.20})$$

where, $m = \cos \theta$; $n = \sin \theta$ for fill lamina, and, $m = \cos(90 + \theta)$; $n = \sin(90 + \theta)$ for warp lamina. The transformed stiffness of fill and warp laminae are,

$$Q_{IJ}^{f,\theta}(t) = [T]^{-1}[Q_{ij}^f(t)][T]; \quad Q_{IJ}^{w,(90+\theta)}(t) = [T]^{-1}[Q_{ij}^w(t)][T]; \quad (\text{A.21})$$

(I, J = X, Y, Z; and i, j = x, y, Z)

Using stiffness from equation A.21 and classical lamination theory [64], the stiffness per unit width of the equivalent laminate shown in *Figure A.2e* is calculated as,

$$A_{IJ}(t, \theta) = \left[\frac{h_0}{4} (Q_{IJ}^{f,\theta}(t)) \right]_1 + \left[\frac{h_0}{2} (Q_{IJ}^{f,(90+\theta)}(t)) \right]_2 + \left[\frac{h_0}{4} (Q_{IJ}^{f,\theta}(t)) \right]_3 \quad (\text{A.22})$$

Using the time-dependent laminate stiffness, time-dependent laminate strain and compliance can be determined.

APPENDIX B

Introduction

In Appendix B, additional experimental creep results obtained for plain weave composites under on-axis and off-axis loading are plotted. These results are discussed in Chapter 5.

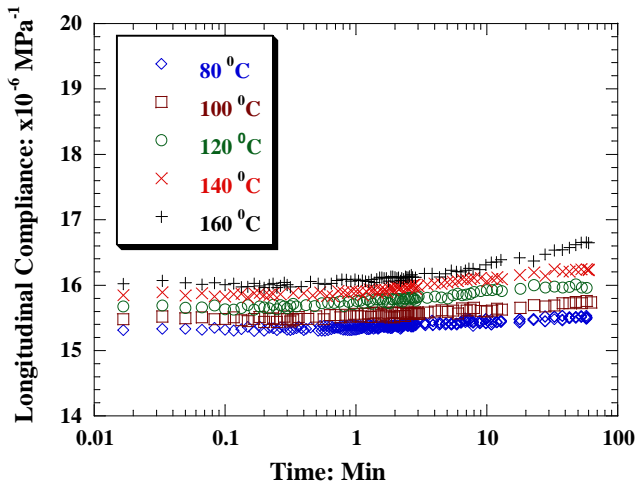


Figure B.1: Experimental creep results for $[0, 90]_6$ plain weave composite test coupons at various temperatures and at a stress level of 200MPa.

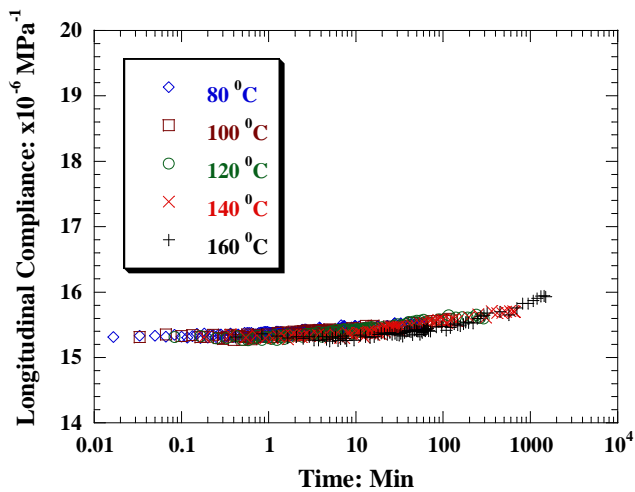


Figure B.2: Master creep curve for $[0, 90]_6$ plain weave composite test coupons at a reference temperature of $80\text{ }^\circ\text{C}$ and at a stress level of 200MPa.

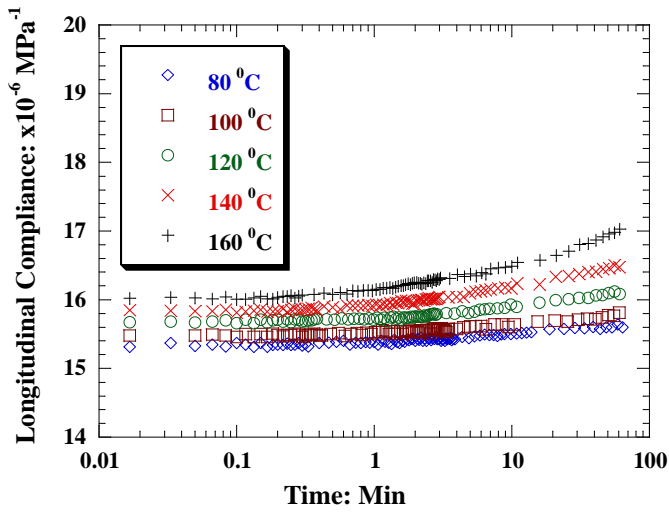


Figure B.3: Experimental creep results for $[0, 90]_6$ plain weave composite test coupons at various temperatures and at a stress level of 300MPa.

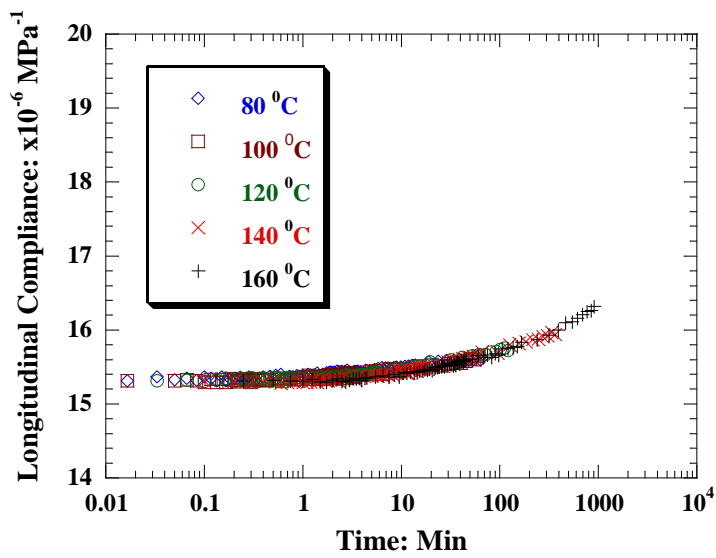


Figure B.4: Master creep curve for $[0, 90]_6$ plain weave composite test coupons at a reference temperature of $80\text{ }^\circ\text{C}$ and at a stress level of 300MPa.

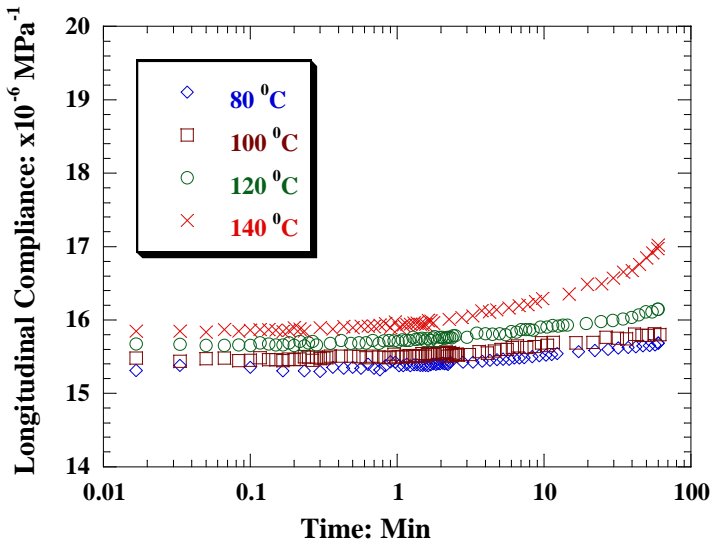


Figure B.5: Experimental creep results for $[0, 90]_6$ plain weave composite test coupons at various temperatures and at a stress level of 400MPa.

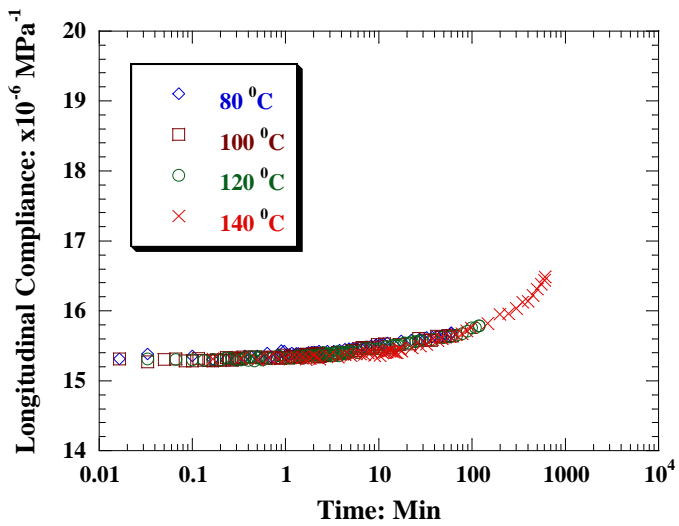


Figure B.6: Master creep curve for $[0, 90]_6$ plain weave composite test coupons at a reference temperature of 80 °C and at a stress level of 400MPa.

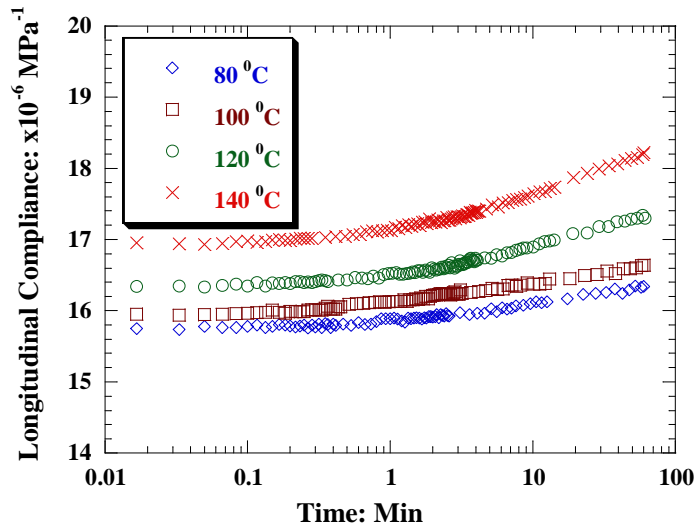


Figure B.7: Experimental creep results for $[0, 90]_6$ plain weave composite test coupons at various temperatures and at a stress level of 450MPa.

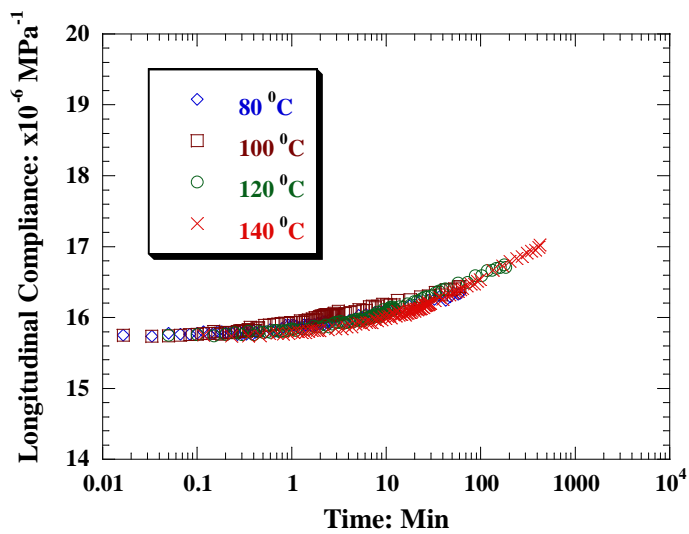


Figure B.8: Master creep curve for $[0, 90]_6$ plain weave composite test coupons at a reference temperature of $80\text{ }^\circ\text{C}$ and at a stress level of 450MPa.

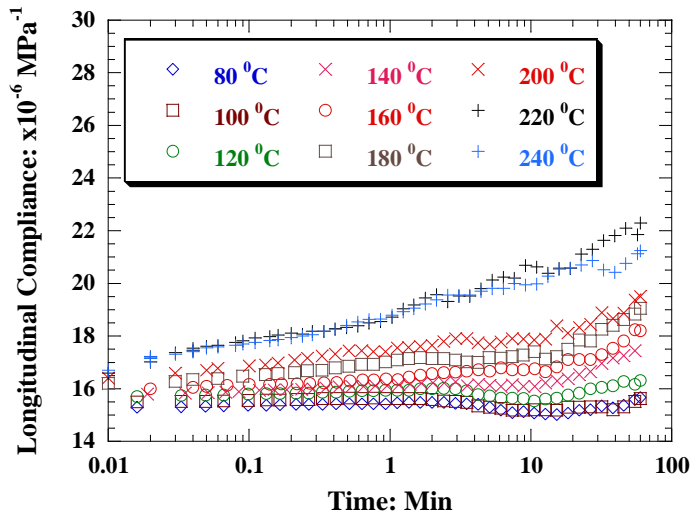


Figure B.9: Experimental creep results for $[0, 90]_6$ plain weave composite test coupons at various temperatures and at a stress level of 3MPa.

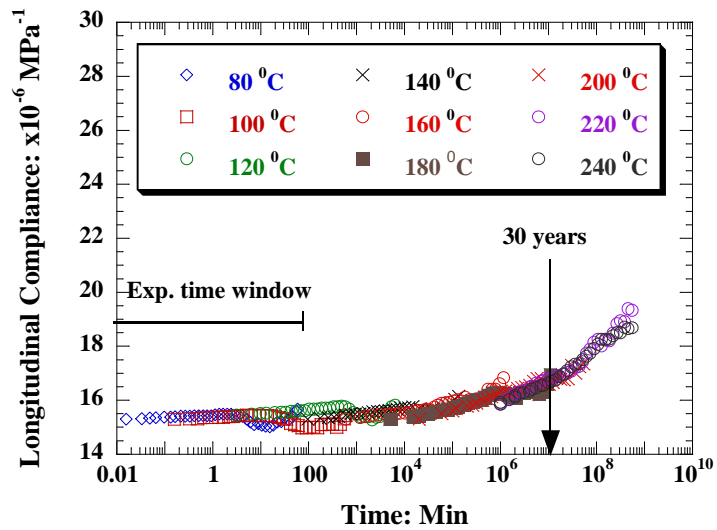


Figure B.10: Master creep curve for $[0, 90]_6$ plain weave composite test coupons at a reference temperature of 80 °C and at a stress level of 3MPa.

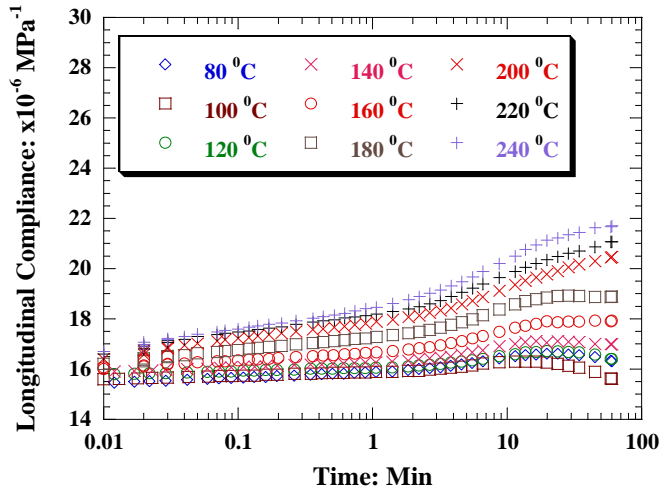


Figure B.11: Experimental creep results for $[0, 90]_6$ plain weave composite test coupons at various temperatures and at a stress level of 7MPa.

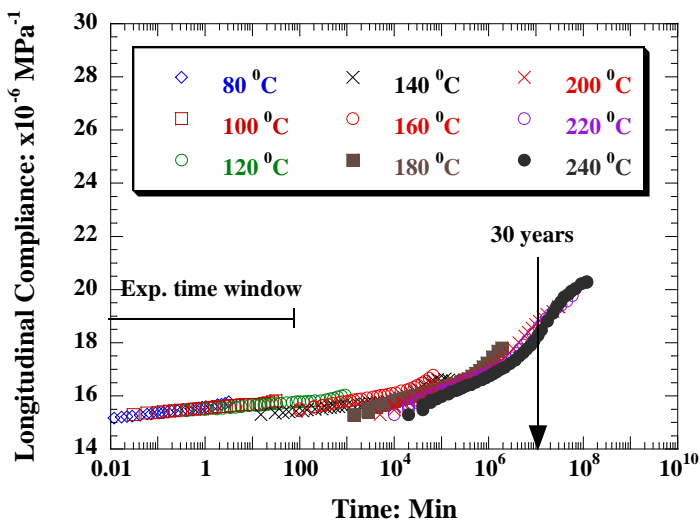


Figure B.12: Master creep curve for $[0, 90]_6$ plain weave composite test coupons at a reference temperature of 80 °C and at a stress level of 7MPa.

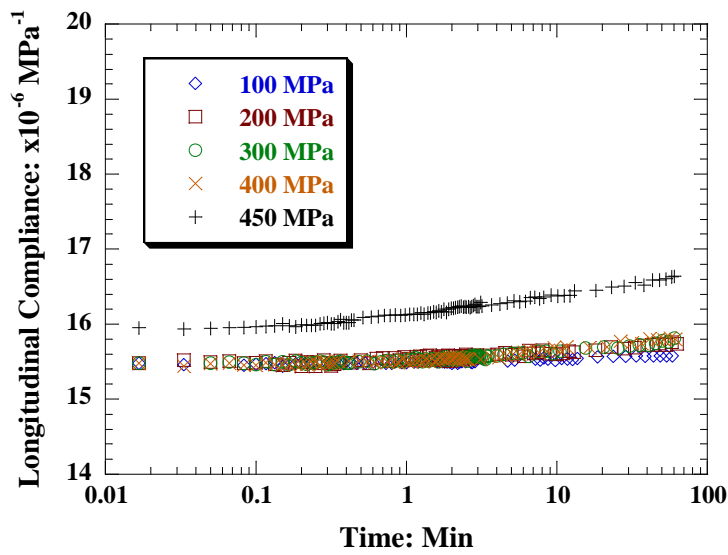


Figure B.13: Experimental creep results for $[0, 90]_6$ plain weave composite test coupons at various stress levels and at a temperature of 100°C .

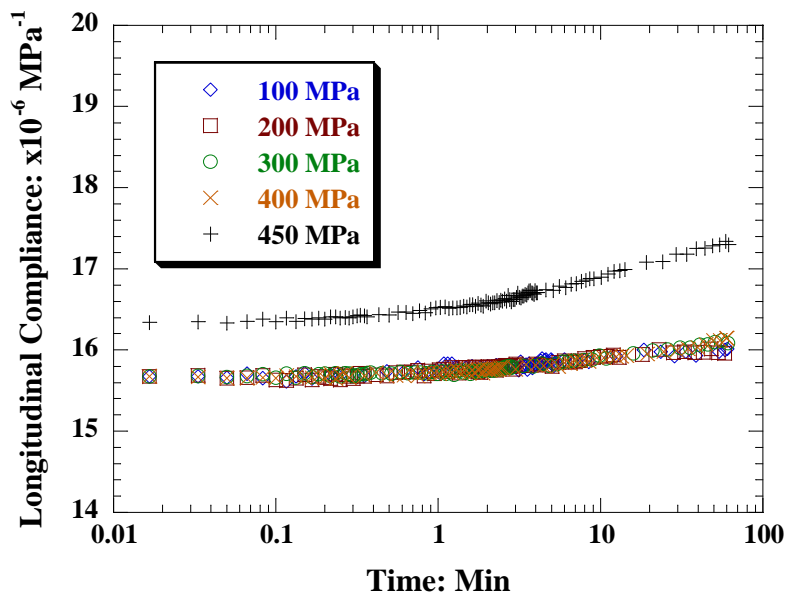


Figure B.14: Experimental creep results for $[0, 90]_6$ plain weave composite test coupons at various stress levels and at a temperature of 120°C .

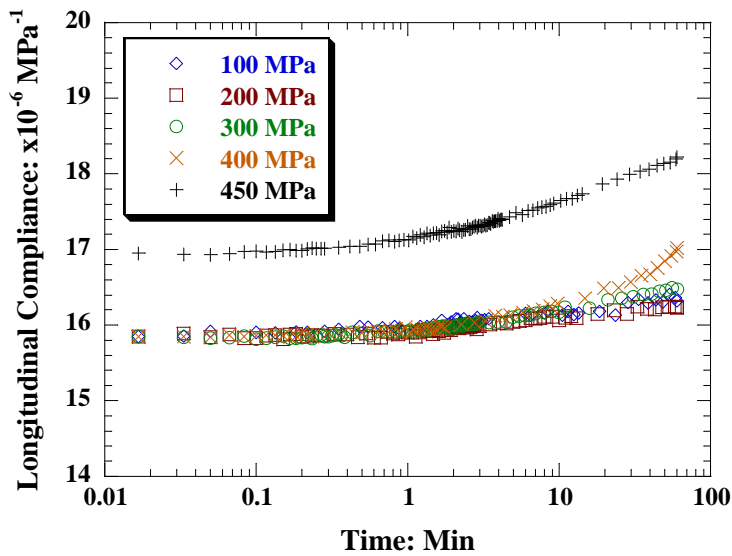


Figure B.15: Experimental creep results for $[0, 90]_6$ plain weave composite test coupons at various stress levels and at a temperature of 140°C .

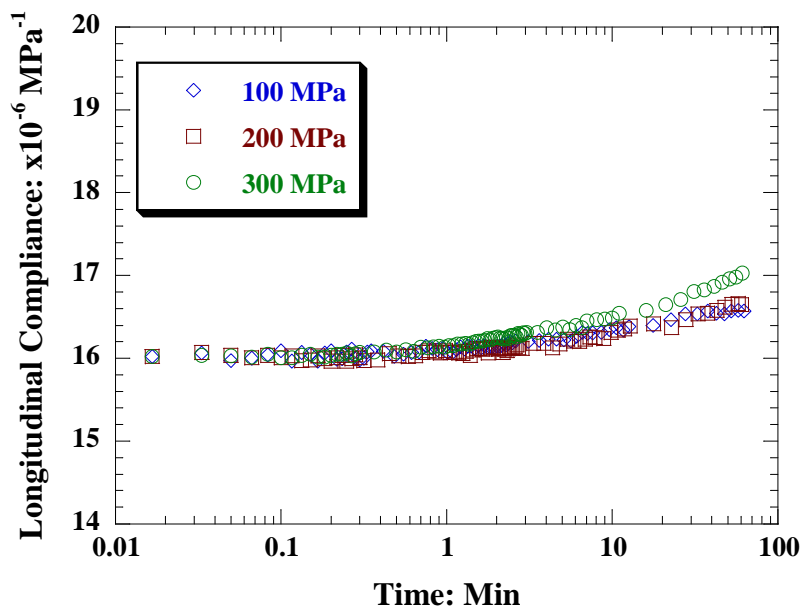


Figure B.16: Experimental creep results for $[0, 90]_6$ plain weave composite test coupons at various stress levels and at a temperature of 160°C .